

## ABSTRACT

Title of Dissertation: CRITICAL BEHAVIOR OF SUPERCONDUCTORS  
AND ELECTRICAL TRANSPORT PROPERTIES  
OF CARBON NANOTUBE THIN FILMS

Hua Xu, Doctor of Philosophy, 2007

Dissertation directed by: Professor Steven M. Anlage  
Department of Physics

With AC microwave measurements from 10 MHz up to 50 GHz and DC nano-volt level measurements we have investigated the superconducting phase transition of  $\text{YBa}_2\text{Cu}_3\text{O}_{7-\delta}$  films in zero magnetic field and electrical transport properties of single walled carbon nanotube networks.

We studied the microwave conductivity of  $\text{YBa}_2\text{Cu}_3\text{O}_{7-\delta}$  thin films around  $T_c$  for different incident microwave power and observed that the microwave fluctuation conductivity deviates from scaling theory at low frequency around  $T_c$ . We systematically investigated the length scales involved in AC measurements and found the probed length scale depends on both frequency and current. At low current density  $J$  but high frequency  $\omega$ , we observed critical behavior without hindrance from finite-size effects. However, at low current density  $J$  and low frequency  $\omega$ , the experimentally probed length scale  $L_{AC}$  may approach the thickness  $d$  of the sample, and then the critical behavior will be destroyed by finite-size effects. In this regime, we can not observe the phase transition.

With very small applied microwave power, specifically -46dBm, and high frequency data, we have investigated the critical fluctuations of  $\text{YBa}_2\text{Cu}_3\text{O}_{7-\delta}$  thin films around  $T_c$ . It is shown that the determination of  $T_c$  is crucial for obtaining critical exponents. Improved temperature stability and conductivity calibration allow us to take high quality data at small temperature intervals (50mK). This improves the conventional data analysis method and allows a new method of extracting exponents to be developed. With these two methods, consistent values of  $T_c$  and the critical exponent were precisely determined. Experiments on 6 samples have been done and the results give a dynamical scaling exponent  $z = 1.55 \pm 0.15$ . The scaling behavior of the fluctuation conductivity is also established.

We have also investigated fluctuation effects of  $\text{YBa}_2\text{Cu}_3\text{O}_{7-\delta}$  by doing frequency-dependent microwave conductivity measurements and dc current-voltage characteristics on the same film. The dc measurement verified that the applied microwave power -46dBm in our ac measurement is small enough for the correct determination of  $T_c$  and critical exponents. For both dc and ac experiments the scaling behavior of the data was investigated. We found that the dc measurement could be affected by disorder. For high quality YBCO films and crystal, the critical exponent  $z$  is also around 1.5, which is consistent with ac measurement.

Finally, using our broadband experimental technique and DC current-voltage characteristic measurement system, we measured the transport properties of single-walled carbon nanotube films. Based on the real and imaginary parts of the microwave conductivity, we calculated the shielding effectiveness for various film thickness. Shielding effectiveness of 43 dB at 10 MHz and 28 dB at 10 GHz is found for films with 90% optical transmittance, which suggests that single walled carbon nanotube(SWCNT) films are promising as a type of transparent microwave shielding material. We also investigated the frequency and electric field dependent conductivity of single walled carbon nanotube networks of various densities. We found the ac conductivity as a function of frequency follows the extended pair approx-

imation model and increases with frequency above an onset frequency  $\omega_0$  which varies over seven decades with a range of film thickness from sub-monolayer to 200 nm. The nonlinear electric field-dependent conductivity shows strong dependence on film thickness as well. Measurement of the electric field dependence of the resistance  $R(|\vec{E}|)$  allows for the determination of the localization length scale  $\mathbf{L}$  of localized states, which is found to systematically decrease with increasing film thickness. The onset frequency  $\omega_0$  of enhanced ac conductivity and the localization length scale  $\mathbf{L}$  of SWCNT networks are found to be correlated, and an empirical formula relating them has been proposed. Such studies will help the understanding of transport properties and broaden the applications of this novel material system.

CRITICAL BEHAVIOR OF SUPERCONDUCTORS  
AND ELECTRICAL TRANSPORT PROPERTIES  
OF CARBON NANOTUBE THIN FILMS

by

Hua Xu

Dissertation submitted to the Faculty of the Graduate School of the  
University of Maryland at College Park in partial fulfillment  
of the requirements for the degree of  
Doctor of Philosophy  
2007

Advisory Committee:

Professor Steven M. Anlage, Chairman  
Professor Christopher J. Lobb  
Professor Richard L. Greene  
Professor Michael S. Fuhrer  
Professor Lourdes G. Salamanca-Riba

© Copyright by

Hua Xu

2007

## DEDICATION

To my parents

## ACKNOWLEDGEMENTS

Earning a Ph. D degree is about learning and the pursuit of knowledge. However, for myself, it is much more than that. Not only a process of learning knowledge, is it a process of developing my ability to analyze and solve complex problems independently, a process of annealing my willpower that keeps pursuing hope even in despair, a process of building my personalities of honesty, preciseness and maturity. During the past five years in University of Maryland, many, many people helped and supported me, without whose help I would never have finished this thesis. I feel that I am extremely fortunate to have been learning and working in such an intellectually rich, stimulating and friendly environment.

First, I would like to acknowledge my advisor, Professor Steven Anlage, for guiding me through all the phases of my research at University of Maryland. I appreciate having an advisor who is actively interactive with his students, and who is extremely experienced with almost every aspects of the experimental physics and also deep theoretical knowledge. In addition, I really appreciate being allowed to freely develop my own independent ideas and to work on them.

Second, and also first, I must thank my another advisor, Professor Christopher J. Lobb, for taking me into the lab as a first year graduate student. He always supported me in what I wanted to do and the aspects of research that I found

interesting, even if it was not what he had planned or intended. Chris Lobb has a deep knowledge and love of physics, especially experimental physics, and I have learned much about the pursuit of scientific knowledge from him.

I also wanted to acknowledge Dr. Matthew C. Sullivan, for his patiently teaching me a lot, almost everything about the fluctuation experiment. I have to owe my experimental expertise to him. I have benefitted a lot from many other close collaborations throughout my thesis work. Of particular significance has been my collaboration with Su Li, who was actively involved in sample deposition, preparation and dc measurement. Most important, lots of discussion between us stimulated the progress of my fluctuation work. I have also learned a lot from my close interaction with my fellow high frequency group members, Dragos Mircea, Michael Ricci and Sameer Hemmady. I would also like to thank the undergraduate student who worked in our lab, Monica Lilly and Diqui He for the considerable help they have provided.

Another persons I have to acknowledge is Liangbing Hu and his advisor George Grüner. I would not have the chapter about the electronic properties of SWCNT films without discussion with Liangbing and support of his advisor.

Other people in other labs in center for superconductivity research helped me a lot for completing this thesis. I would like to make special thanks to members in Greene's lab. Weiqiang Yu, Bing Liang, Pengcheng Li and Josh Higgins etc, they gave me support, ideas and suggestions both professionally and personally. I also want to thank Shixiong Zhang, Hanhee Paik, David Tobias and Sudeep Dutta.

I would also like to thank the faculty of the Center for Superconductivity Research, who provided a wealth of experience and knowledge about an incredibly broad range of subjects. In particular, Richard Greene, I spent a lot of time in his lab and attended his regular group meeting for quite a long time. I also received valuable technical assistance from Brian Straughn and Doug Bensen. Additionally, I received support from the staff of the Center's main office: Belta Pollard, Grace



Sewlall, Cleopatra White, and Brain Barnaby.

In particular I would like to thank the members of my Dissertation Committee, Professors Steven M. Anlage, Christopher J. Lobb, Richard L. Greene, Michael S. Fuhrer and Lourdes G. Salamanca-Riba.

My parents were invaluable for their support and understanding. My father was always ready to offer me advices when I needed and my mother ensured my healthy mood when life and emotional ups and downs in the past years. I owe to them my ambition and the self confidence necessary to achieve my goals.

Finally, I would like to thank all my friends. Your cares, your helps, your suggestions and your encourages and much more, all of these are all really important for my pursuing this Ph. D. I could not have accomplish it without my friends. In the future, I will keep moving forward and never let anyone who cares me down.

# TABLE OF CONTENTS

<b>List of Tables</b>		<b>x</b>
<b>List of Figures</b>		<b>xi</b>
<b>1 Introduction</b>		<b>1</b>
1.1 Introduction to Superconductivity . . . . .		1
1.2 Superconducting Phase Transitions . . . . .		3
1.2.1 Type I Superconductors . . . . .		5
1.2.2 Type II Superconductors . . . . .		8
1.2.3 The Vortex-Glass Transition . . . . .		10
1.3 Fluctuations in Conventional Superconductors . . . . .		12
1.3.1 Zero-dimensional Superconductors . . . . .		14
1.3.2 Fluctuations Above $T_c$ – Equilibrium Properties . . . . .		16
1.3.3 Fluctuations Above $T_c$ – Paraconductivity . . . . .		21
1.3.4 Fluctuations Below $T_c$ . . . . .		24
1.3.5 Summary . . . . .		24
1.4 Fluctuations in High $T_c$ Superconductors . . . . .		25
1.4.1 Universality . . . . .		25
1.4.2 Static Critical Phenomena . . . . .		27
1.4.3 Dynamical scaling . . . . .		31
1.5 Summary . . . . .		34

<b>2</b>	<b>Corbino Reflection Measurement Technique</b>	<b>36</b>
2.1	Overview of the Spectroscopy . . . . .	36
2.2	Impedance Measurement in the Microwave Frequency Range . . . . .	42
2.3	Experimental Setup of the Corbino Reflection Measurement . . . . .	44
2.3.1	Advantages of the Corbino Geometry . . . . .	44
2.3.2	History of the Corbino Technique . . . . .	45
2.3.3	Our Experimental Setup . . . . .	47
2.4	Calibration—Room Temperature . . . . .	52
2.5	Calibration at Cryogenic Temperature – Standards . . . . .	56
2.5.1	Low Temperature Standards: Short . . . . .	59
2.5.2	Low Temperature Standards: Open . . . . .	61
2.5.3	Low Temperature Standards: Load . . . . .	62
2.5.4	Cryogenic Re-calibration Methods . . . . .	66
<b>3</b>	<b>Theory of Superconducting Fluctuation Effects</b>	<b>70</b>
3.1	Ginzburg-Landau Theory . . . . .	70
3.2	Gaussian Fluctuation . . . . .	75
3.2.1	Direct Contribution—Aslamazov-Larkin term . . . . .	75
3.2.2	Indirect Contribution— MT-term . . . . .	79
3.2.3	Ginzburg Criterion . . . . .	80
3.3	Scaling theory . . . . .	82
3.3.1	Scaling Theory and Universality . . . . .	82
3.3.2	DC scaling . . . . .	85
3.3.3	AC Conductivity Fluctuations . . . . .	90
3.4	Finite Size Effect . . . . .	94
<b>4</b>	<b>AC Experiment And Data Discussion</b>	<b>96</b>
4.1	Sample Preparation And Characterization . . . . .	96
4.1.1	The Material: YBCO Thin Film . . . . .	96

4.1.2	Film Growth via Pulsed Laser Deposition . . . . .	98
4.1.3	Film Characterization . . . . .	101
4.1.4	Sample Preparation and Measurement . . . . .	112
4.2	The Complex Resistivity Near $T_c$ in YBCO Films . . . . .	114
4.3	The Fluctuation Conductivity Near $T_c$ . . . . .	116
4.4	The Conventional Analysis Method and its Improvement . . . . .	118
4.5	New Data Analysis Method . . . . .	123
4.6	Discussion . . . . .	127
<b>5</b>	<b>Power Dependence of the Microwave Fluctuation Conductivity</b>	<b>131</b>
5.1	Power Dependent Measurements . . . . .	131
5.2	Power Dependent Fluctuation Conductivity Phenomena . . . . .	134
5.2.1	Nonlinearity Effects of Microwave Fluctuation Conductivity $\sigma_{fl}$ –High Power End . . . . .	134
5.2.2	Low Frequency Downward Curvature of Fluctuation Conduc- tivity $ \sigma_{fl}(\omega) $ . . . . .	136
5.2.3	Confidence Check of the Downturn Behavior . . . . .	137
5.2.4	Power Dependent Fluctuation Conductivity at Low Frequency	139
5.2.5	Applied Current Amplitude . . . . .	139
5.3	Analysis and possible explanation . . . . .	143
5.3.1	Current-induced Length Scale . . . . .	145
5.3.2	Frequency-induced Length Scale . . . . .	147
5.3.3	Power and Frequency Dependent Fluctuation Conductivity . .	149
<b>6</b>	<b>DC and AC Conductivity Measurements on the Same Sample</b>	<b>155</b>
6.1	DC scaling . . . . .	156
6.2	Experimental Procedure . . . . .	157
6.2.1	Introduction to the DC Experiment . . . . .	157
6.2.2	Procedure of Combined AC and DC Experiments . . . . .	159

6.3	Experimental Results and Discussion . . . . .	162
6.3.1	DC experimental results . . . . .	162
6.3.2	Comparison with the AC Experimental Results . . . . .	165
6.3.3	Other DC Experimental Results . . . . .	167
<b>7</b>	<b>Electronic Transport Properties of Single-walled Carbon Nanotube Films</b>	<b>175</b>
7.1	Introduction . . . . .	175
7.2	Microwave Shielding of Transparent and Conducting Single-walled Carbon Nanotube Films . . . . .	177
7.3	Frequency and electric field dependent conductivity of single walled carbon nanotube networks of varying density . . . . .	185
7.3.1	Frequency dependent conductivity for various film thicknesses	187
7.3.2	Electric field dependent conductivity for various film thicknesses	191
7.3.3	Discussion of the frequency and electric field dependent con- ductivity . . . . .	195
<b>8</b>	<b>Conclusion and future work</b>	<b>197</b>
8.1	Results and Conclusions . . . . .	197
8.2	Future Work . . . . .	199
<b>A</b>	<b>Current-Induced Length Scale (Notes Due to Prof. C. J. Lobb)</b>	<b>201</b>
A.1	Initial considerations . . . . .	201
A.2	A More Realistic Model for $\epsilon(r)$ . . . . .	204
<b>B</b>	<b>Fitting of microwave conductivity for sample xuh139 in different frequency ranges</b>	<b>208</b>
	<b>List of Abbreviations</b>	<b>226</b>

## LIST OF TABLES

1.1	Previous theoretical predictions and numerical simulations on critical exponent $z$ in zero field . . . . .	33
4.1	Quadratic fit result of $\log( \sigma_{fl} )$ vs. $\log(f)$ and linear fit result of $\phi_{fl}$ vs. $\log(f)$ for sample xuh139 in the frequency range 0.4 to 10GHz . .	122
4.2	Linear fit slope of $\log \sigma_{fl} $ vs. $\log(f)$ and average of $\phi_{fl}$ for sample xuh139 from 0.4 to 10GHz and corresponding value of $z$ . . . . .	123
4.3	critical temperature $T_c \pm \Delta T_c$ and exponents determined for different YBCO film samples . . . . .	129
6.1	Comparison of results for both AC and DC experimental measurements on the same films . . . . .	167
6.2	Results of DC measurement on NGO substrate . . . . .	168
6.3	Results of DC measurement on YBCO samples on STO substrate and YBCO crystals . . . . .	171
A.1	Analogy between wire loop and vortex loop . . . . .	206
B.1	Sign of the coefficient of $(\log f)^2$ of quadratic fit for $\log \sigma_{fl} $ vs. $\log(f)$ in different frequency ranges for different temperatures for sample xuh139. . . . .	209
B.2	Sign of the slope of linear fits to $\phi_{\sigma}(\omega)$ vs. $\log f$ for different frequency ranges for different temperatures for sample xuh139. . . . .	210

## LIST OF FIGURES

1.1	Phase diagram of a type I superconductor. . . . .	6
1.2	Phase diagram of a type II superconductor . . . . .	9
1.3	Phase diagram of a type II superconductor with the vortex-glass transition . . . . .	11
1.4	Diamagnetic susceptibility of aluminium powders . . . . .	15
1.5	Measured fluctuation magnetization above $T_c$ versus temperature and field of a bulk cylindrical sample of indium. . . . .	17
1.6	Universal behavior of scaled fluctuation magnetization at $T_{c0}$ versus scaled field for a number of materials. . . . .	18
1.7	Measured heat capacity of an individual thin film. . . . .	20
1.8	Universal variation of the measured excess conductance per square due to fluctuations with reduced temperature $t$ above $T_c$ . . . . .	22
1.9	$\tilde{\alpha}_{b-a} = \alpha_b - \alpha_a$ versus temperature $T$ and reduced temperature $T - T_c$ . . . . .	29
1.10	3DXY critical behavior of the superfluid density in the superconducting state of a sample annealed to $YBa_2Cu_3O_{6.92}$ . . . . .	30
2.1	Ranges of the electromagnetic spectrum in which the different radiation sources are applicable. Adapted from [119] Page 211. . . . .	38
2.2	Operating frequency ranges of detectors. Adapted from [119] Page 213. . . . .	39
2.3	Scheme of the Corbino geometry. . . . .	45
2.4	Schematic of the Corbino experiment setup on YBCO measurement. . . . .	47

2.5	Schematic of the sample and the interface of sample and connector. . .	50
2.6	The Agilent N4693A MW electronic calibration (ECal) . . . . .	51
2.7	General Error model for a microwave reflection measurement . . . . .	53
2.8	Magnitude of the error coefficients vs. frequency. . . . .	55
2.9	Magnitude and phase of $S_{11}$ vs. frequency for a silver disk after calibration. . . . .	57
2.10	Magnitude and phase of $S_{11}$ vs. frequency when the center pin is inserted and the house is assembled after calibration. . . . .	58
2.11	Magnitude of the reflection coefficient of a superconducting YBCO film on NGO substrate and silver disk at 80 K . . . . .	60
2.12	Amplitude of measured reflection coefficient for some open standards.	63
2.13	Amplitude of measured reflection coefficient at room temperature af- ter calibration for different attached insulators. . . . .	64
3.1	Free energy density difference in GL theory . . . . .	72
3.2	Schematic of expected $E - J$ curves . . . . .	87
3.3	Schematic of expected $\partial \log(E)/\partial \log(J)$ vs $J$ . . . . .	89
3.4	Schematic of expected data collapse . . . . .	90
3.5	Phase and magnitude of Dorsey's scaling function $S(y)$ above $T_c$ for different D and z . . . . .	95
4.1	Unit cell of YBCO . . . . .	97
4.2	$T_c$ vs. doping in YBCO . . . . .	98
4.3	Schematic of PLD . . . . .	99
4.4	Schematic of the AC susceptibility measurement . . . . .	102
4.5	AC susceptibility of a good sample . . . . .	103
4.6	AC susceptibility four different samples . . . . .	105
4.7	X-ray diffraction patterns showing a-axis . . . . .	108
4.8	SEM pictures showing a-axis outgrowths . . . . .	110



4.9	AFM image of a typical film . . . . .	111
4.10	Complex resistivity of YBCO film xuh139 around $T_c$ . . . . .	115
4.11	Measured fluctuation conductivity vs. frequency at different temperatures near $T_c$ . . . . .	117
4.12	Data Collapse of magnitude of microwave conductivity vs. frequency for one data set and different sets of parameters. . . . .	120
4.13	Scaling of phase and magnitude of fluctuation conductivity to determine $\omega_0(T)$ and $\sigma_0(T)$ . . . . .	124
4.14	$\omega_0(T)$ vs. $t$ and $\sigma_0(T)$ vs. $t$ for different assumed $T_c$ . . . . .	125
4.15	Data collapse as a check for $T_c$ , critical exponent $z$ and $\nu$ for xuh139 .	128
5.1	Sketch of the power region for frequency dependent fluctuation conductivity. . . . .	132
5.2	Magnitude $ \sigma_{fl} $ and phase $\phi_\sigma$ vs. frequency for various temperatures.	135
5.3	$ \sigma_{fl} $ vs. frequency at different temperature for input a fixed power and at a fixed temperature for different power. . . . .	137
5.4	$ \sigma_{fl} $ vs. incident microwave power at different frequencies at a fixed temperature of 89.087 K for sample xuh139. . . . .	140
5.5	Corresponding current density vs. incident microwave power for a film thickness 1300 Å in the Corbino geometry with $\hat{S}_{11} \approx -1$ . . . .	142
5.6	Sketch of the power, frequency and thickness relation in frequency dependent fluctuation conductivity. . . . .	143
5.7	Plot of current density and frequency at which the current-induced and frequency-induced length scales are equal. . . . .	151
5.8	Summary of length scales and finite size effects in AC measurements of fluctuation conductivity. . . . .	154
6.1	YBCO bridge pattern ( $8\mu m \times 40\mu m$ ) for sample xuh112. YBCO is black and the substrate is grey. . . . .	158

6.2	Schematic of the patterned bridge for DC measurement on samples after AC measurement . . . . .	160
6.3	E-J isotherms for sample xuh139, performed after the AC experiment.	163
6.4	Derivative plot for xuh139 in zero magnetic field. . . . .	164
6.5	Obtained value of $z$ vs. $T_c$ for different YBCO samples on NGO substrates . . . . .	169
6.6	Obtained value of $z$ vs. $T_c$ for different YBCO samples . . . . .	170
6.7	Schematic of heating and the finite size effect influence on the derivative E-J plot. . . . .	172
7.1	Schematic of the sample and experimental setup . . . . .	178
7.2	Real and imaginary parts of the microwave conductivity at different temperatures and frequencies . . . . .	180
7.3	Shielding effectiveness and transmittance of SWCNT films. . . . .	182
7.4	Sketch of conductivity of SWCNT film in a broad frequency range: from DC to visible. . . . .	184
7.5	SEM of two samples with different densities. . . . .	186
7.6	Ac conductance for samples with different densities and the onset frequencies vs dc conductance. . . . .	188
7.7	Master scaling curve showing the ac conductivity for samples with different densities. . . . .	189
7.8	The onset frequency vs. dc conductance for different nanotube networks. The three solid lines all have slope one. . . . .	190
7.9	Resistance vs electric field and extracted localization length scale for a very thin film (sample 5). . . . .	193
7.10	Comparison of the localization length scale obtained from electric field depend conductivity data and the estimated localization length scale from frequency dependent conductivity measurement. . . . .	194

# Chapter 1

## Introduction

In the field of condensed matter physics, one of the important feature of matter are their electronic properties. In my work, I developed a broadband frequency measurement system, which can measure electrical conductivity of a sample from DC to 50 GHz and from room temperature to cryogenic temperature. With this setup, along with DC nano-volt level measurements, I investigated the superconducting phase transition of  $\text{YBa}_2\text{Cu}_3\text{O}_{7-\delta}$  films in zero magnetic field. More than that, I also measured the transport properties of single-walled carbon nanotube films, and these studies will help the understanding of transport properties and broaden the applications of this novel material system, single walled carbon nanotube(SWCNT) films. The superconducting phase transition is the focus of my research, and this chapter will serve as its introduction.

### 1.1 Introduction to Superconductivity

Superconductivity was first discovered in 1911 by the Dutch physicist Heike Kamerlingh Onnes.[1] After liquifying helium in 1908, Kamerlingh Onnes obtained the refrigeration technique to reach temperatures of a few degrees kelvin. In 1911, Kamerlingh Onnes began to investigate the electrical properties of metals at extremely cold temperatures. He measured mercury's resistance and saw that at 4.2

K (-269 °C), the resistance vanished abruptly. Below 4.2 K, an electrical current could pass without dissipation through the sample. According to Kamerlingh Onnes, "Mercury has passed into a new state". Kamerlingh Onnes called this newly discovered state, Supraconductivity. In 1913, Onnes was awarded the Nobel Prize for "his investigations on the properties of matter at low temperatures which led, inter alia, to the production of liquid helium".

The next hallmark to be discovered was perfect diamagnetism, found by Walther Meissner and R. Ochsenfeld in 1933.[2] They found that not only a magnetic field is excluded from entering a superconductor, which could be explained by perfect conductivity, but also that a field in an originally normal sample is expelled when it is cooled through  $T_c$ . This effect, called the Meissner Effect, causes a phenomenon that is a very popular demonstration of superconductivity.

Whenever a new scientific discovery is made, researchers must strive to explain why it happens. In 1935, the brothers F. and H. London gave a description of these two basic electrodynamic properties of superconductors.[3] After that there was not much progress until the 1950s, at which time some remarkably complete and satisfactory theoretical pictures came out. They are the phenomenological mean-field theory of Ginzburg and Landau (GL) in 1950,[4] and the fundamental microscopic theory of J. Bardeen, L. N. Cooper and J. R. Schrieffer(BCS) in 1957.[5] Very soon, Gor'kov(1959) showed that the GL theory could be derived from the BCS theory in the appropriate limit of parameter space[6], and then the basic understanding of the theory of superconductivity was complete.

In 1986, Georg Bednorz and Alex Muller at IBM in Zurich Switzerland found superconductivity at 35 K, a startling 12 K above the old record for a superconductor, when they were experimenting with a particular class of metal oxide ceramics called perovskites.[7] Soon after that in February of 1987, a perovskite ceramic material was found to superconduct at 90 K. Because these materials superconduct at significantly higher temperatures they are referred to as high tem-

perature superconductors(HTSC).[8, 9, 10] Since then scientists have experimented with many different forms of perovskites producing compounds that superconduct at temperatures over 130 K.

These new superconductors seem to obey the same phenomenology as the classical superconductors, but the basic microscopic mechanism might be different. The high critical temperature and short coherence length of HTSC make fluctuation effects much larger than those in conventional superconductors.[11, 13] This makes GL theory incomplete to describe the behavior of HTSC. Since the discovery of HTSC, a great deal of work has been done in this field investigating the phase transition in both zero and non-zero magnetic field.[14] Understanding the effects of fluctuations is also important for applications of HTSC, such as high-field magnets and passive microwave devices.

Currently, a great effort is put in investigating high temperature superconductors. The ease of cooling the new superconductors has greatly influenced the development of new materials, material fabrication, and increased the number of applications of superconductors. Thanks to the increased cryocooler reliability and decreased cost associated with cooling devices at temperatures greater than 20 K, electric power applications, high-field magnets and passive microwave devices made from high temperature superconductors are gradually becoming practical. The history of superconductors is only just now beginning.

## 1.2 Superconducting Phase Transitions

Over the years the basic theoretical understanding of superconductivity has been developed in a series of stages. Among these theories, Ginzburg and Landau theory is not very complex in its mechanics, but still powerful in phenomenological insight and provides a convenient foundation for understanding the basic phenomena of superconductivity.

In Ginzburg Landau theory, a complex order parameter,  $\psi(\mathbf{r}) = |\psi(\mathbf{r})|e^{i\varphi(\mathbf{r})}$ , is introduced, where the density of superconducting electrons is given by  $n_s(\mathbf{r}) = |\psi(\mathbf{r})|^2$ . This order parameter is assumed to go to zero at  $T_{c0}$ . Note that  $T_{c0}$  is the mean-field transition temperature, which can be different from the actual transition temperature,  $T_c$ . GL theory requires that the order parameter  $\psi(\mathbf{r})$  is small in magnitude and varies slowly in space and in time so that the free energy density can be expanded in powers of  $|\psi|$  and  $|\nabla\psi|$ . This is not the case very close to  $T_c$ , where fluctuations can cause the order parameter (and the density of superconducting electrons) to vary greatly over small distances and short times, which means  $|\nabla\psi|$  is large and comparable to  $|\psi|$ . However, all discussions of superconductivity begin here and we can still get important results for thermal fluctuations based on GL theory.

In GL theory, the free energy density is given by[15, 17, 16]

$$f_s(T) = f_n(T) + \alpha|\psi|^2 + \frac{\beta}{2}|\psi|^4 + \frac{\hbar^2}{2m^*}|\left(\frac{\hbar}{i}\nabla - q^*A\right)\psi|^2 + \frac{\mu_0 H^2}{8\pi} \quad (1.1)$$

where  $f_n(T)$  is the normal state free energy density at temperature  $T$  in zero field, and  $\alpha$  and  $\beta$  are material parameters. The parameter  $m^*$  determines the energy cost associated with gradients in  $\psi(r)$ . It has dimensions of mass, and it plays the role of an effective mass for the quantum system with macroscopic wave function  $\psi(r)$ .  $q^*$  is effective charge.

In zero field, considering that the order parameter varies in space, for this case,  $\psi(\mathbf{r})$  will minimize the free energy. According to the variational method we can find that the free energy will be a minimum when[15, 17, 18]

$$-\frac{\hbar^2}{2m^*\alpha_0\frac{T-T_{c0}}{T_{c0}}}\nabla^2\psi + \frac{\beta}{\alpha_0\frac{T-T_{c0}}{T_{c0}}}|\psi|^2\psi + \psi = 0. \quad (1.2)$$

Here we Taylor expanded  $\alpha$  about  $T_{c0}$  to the lowest order  $\alpha(T) = \alpha_0\frac{T_{c0}-T}{T_{c0}}$ . Eq 1.2 predicts that changes in  $\psi$  occur over a characteristic length  $\xi$ . A detailed discussion

of this characteristic length  $\xi$  will be given in chapter 3. Here I just give the result:

$$\xi_+ = \sqrt{\frac{\hbar^2 T_{co}}{2m^* \alpha_o |T - T_{co}|}} \quad \text{for } T > T_{co}, \quad (1.3)$$

$$\xi_- = \sqrt{\frac{\hbar^2 T_{co}}{4m^* \alpha_o |T - T_{co}|}} \quad \text{for } T < T_{co}. \quad (1.4)$$

This length scale is identified as the correlation length. This is the characteristic length over which the order parameter  $\psi$  is uniform. In a pure superconductor far below  $T_c$ ,  $\xi(T) \approx \xi(0)$ , which is the temperature independent Pippard coherence length; however near  $T_c$ ,  $\xi(T)$  diverges as  $(T_{co} - T)^{-1/2}$ .

Since the penetration depth  $\lambda$  also diverges as  $(T_{co} - T)^{-1/2}$  near  $T_c$ , the ratio of the two characteristic lengths  $\xi$  and  $\lambda$  is approximately independent of temperature. This ratio is the famous dimensionless Ginzburg-Landau parameter  $\kappa$ :

$$\kappa \equiv \frac{\lambda(T)}{\xi(T)} = \frac{2\sqrt{2}\pi H_c(T)\lambda^2(T)}{\Phi_0}, \quad (1.5)$$

here  $\lambda(T)$  is the penetration depth,  $\xi(T)$  is the GL correlation length,  $H_c(T)$  is the critical field and  $\Phi_0 = \frac{h}{2e}$  is magnetic flux quantum. In the classic pure superconductors,  $\kappa \ll 1$  (type I), but in dirty superconductors or in the high-temperature superconductors,  $\kappa$  may be much greater than 1 (type II). The value  $\kappa = 1/\sqrt{2}$  separates superconductors of type I and II.[15]

### 1.2.1 Type I Superconductors

The first discovered superconductors, such as mercury, lead and indium, are all type I superconductors. The Type I superconductors are mainly comprised of metals and metalloids that show good conductivity at room temperature. The thermodynamic phase diagram of Type I superconductors is relatively simple, and is shown in Fig. 1.1.[15]

When subjected to an increasing external magnetic field, the magnetic field remains zero inside a type-I superconductor until suddenly the superconductivity

is destroyed. The field at which this happen is called the critical field,  $H_c$ . Fig. 1.1 sketches the critical field for different temperatures,  $H_c(T)$ .  $H_c(T)$  separates the normal (resistive) state from the superconducting state (resistance  $R = 0$ ). For type I superconductors, below  $H_c(T)$  the material is always in the Meissner state, and the magnetic field inside always remains zero.

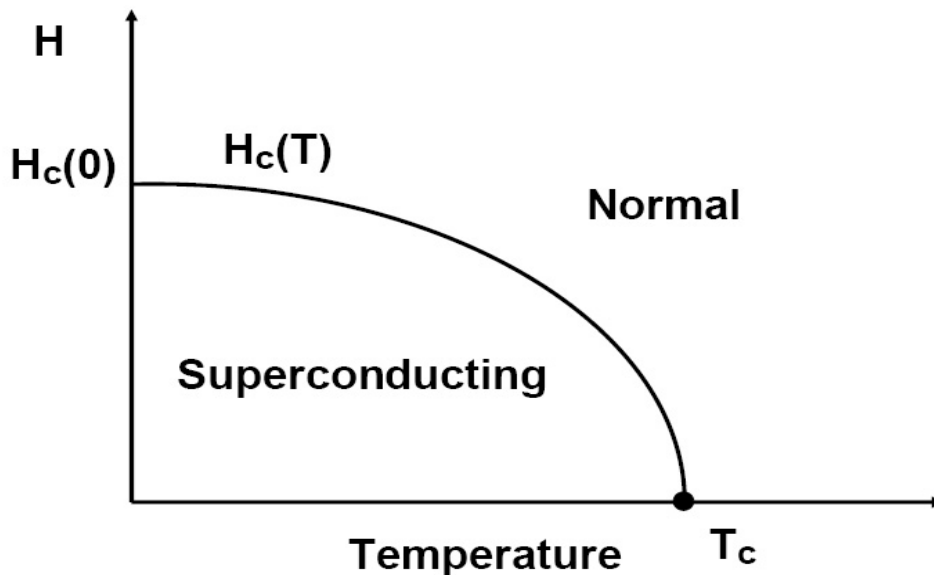


Figure 1.1: Phase diagram of a type I superconductor. The critical point at zero applied magnetic field is a second-order transition.

For any point,  $H > H_c(T)$  (however,  $T < T_c$  and  $H < H_c(0)$ ), in the phase diagram of type I, as the temperature is lowered, the superconductor will change from the normal state to the superconducting state and expel all the magnetic field inside itself. This is a phase transition. Because this procedure will require additional energy – a latent heat – the transition is first order.

Ehrenfest made the first attempt to classifying phase transitions. The Ehrenfest classification scheme labeled phase transitions by the lowest derivative of the free energy that is discontinuous at the transition. The phase transitions that exhibit a



discontinuity in the first derivative of the free energy with a thermodynamic variable is first order transition. The various solid/liquid/gas transitions are classified as a first-order transitions because they involve a discontinuous change in density, which is the first derivative of the free energy with respect to chemical potential.

If the first order derivatives of the free energy are continuous, however, and the second derivative of the free energy has a discontinuity, then the phase transition is a second order. The second order phase transitions include the ferromagnetic phase transition in materials such as iron, where the magnetization, which is the first derivative of the free energy with the applied magnetic field strength, increases continuously from zero as the temperature is lowered below the Curie temperature. The magnetic susceptibility, the second derivative of the free energy with the field, changes discontinuously.

Under the Ehrenfest classification scheme, there could in principle be third, fourth, and higher-order phase transitions. The Ehrenfest scheme is the first attempt of classifying phase transitions. It does not take into account the case where a derivative of free energy diverges, or that some  $n^{th}$  derivatives may be continuous while others are not. The Ehrenfest scheme is an inaccurate method of classifying phase transitions. In the modern classification scheme, phase transitions are divided into two broad categories: first-order phase transitions and continuous phase transitions., also called second-order phase transitions.

First-order phase transitions are those that involve a latent heat. During such a transition, a system either absorbs or releases a fixed amount of energy. Because energy cannot be instantaneously transferred between the system and its environment, first-order transitions are associated with "mixed-phase regimes" in which some parts of the system have completed the transition and others have not. Many important phase transitions fall in this category, including the solid/liquid/gas transitions.

The second class of phase transitions are the continuous phase transitions, also

called second-order phase transitions. These have no associated latent heat. In these transitions, the first derivative of the free energy (and the entropy) is continuous. Since there is no additional energy required to switch phases, small variations in energy can cause local changes in the phase of the material. These variations are called fluctuations, which will be discussed in detail later in this dissertation.

For type I superconductors, the phase transition from normal state to superconducting state is first order, except for one point that is at zero applied magnetic field. There is no magnetic field to expel and no latent heat involved in the process and so the transition in zero field is second order. The point in the phase diagram is called the critical point.

### 1.2.2 Type II Superconductors

Type II superconductors behave differently from type I superconductors. They have a more complicated and controversial phase diagram. The simplest model phase diagram is shown in Fig. 1.2.<sup>1</sup>

In this simplest theory of type II superconductors, there are two different critical fields, denoted  $H_{c1}$ , the lower critical field, and  $H_{c2}$  the upper critical field. For smaller values of applied field, below  $H_{c1}$ , type II superconductors behave similarly to type I and they are superconducting ( $R = 0$ ) and expel magnetic fields (Meissner state). However, for a type II superconductor, once the field exceeds  $H_{c1}$ , magnetic flux does start to enter the superconductor. As the applied field  $H$  is increased, the magnetic flux density increases gradually. Finally at  $H_{c2}$ , the superconductivity is destroyed and the material goes into the normal state.

Between the two critical fields, in which type II superconductors differ significantly from type I,  $H_{c1} < H < H_{c2}$ , magnetic flux penetrates the superconductor in small tubes and each tube carries a quantized amount of magnetic flux,

---

<sup>1</sup>Basic information on type II superconductors is from Refs. [15] and [19].

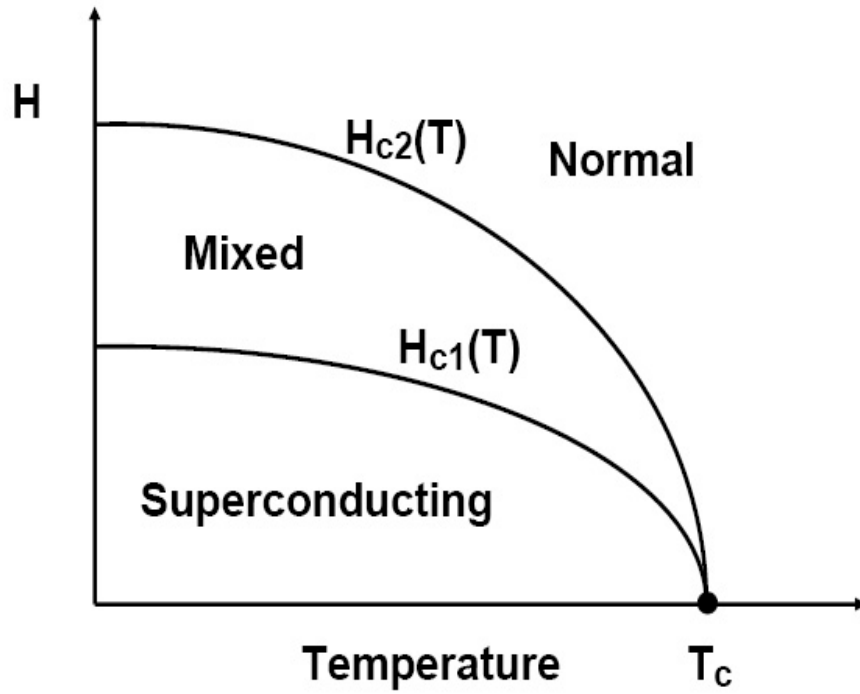


Figure 1.2: Phase diagram of a type II superconductor. Both  $H_{c1}(T)$  and  $H_{c2}(T)$  are second-order phase transitions. The critical point at zero applied magnetic field is also second-order.

$\Phi_0 = h/2e = 2.07 \times 10^{-15} \text{ T-m}^2$ . The center of these magnetic flux tubes act in many ways as a small piece of normal state material. The electrons outside the cores are in the superconducting state. The normal cores are surrounded by circulating supercurrents. Because of long-range interactions the normal cores and these circulating supercurrents often form a flux-line lattice.[18] A normal core with a circulating supercurrent is also called a "vortex". As the vortices enter a superconductor, it forms a "mixed" state. Without defects, when an external current is applied, the vortices will move and the normal electrons in the cores can dissipate energy and the resistance (defined as  $\frac{V}{I}$ ) does not vanish. So in the strict sense of zero resistance, the mixed state is not a superconducting state. In practice because

of pinning on defects in the material, the vortices often move very slowly and make the resistance immeasurably small in the mixed state. However, the early theories incorporating sample imperfections still predicted that  $\frac{V}{I}$  approaches a constant as  $I$  vanishes for all non-zero temperatures.[20, 21, 22] Thus the early theories did not predict the mixed state to be superconducting.

In the area of  $H_{c1} \leq H \leq H_{c2}$ , the superconducting electrons are correlated over all length scales in a pure defect-free superconductors. So in terms of the definition of long-range electronic coherence, the mixed state is superconducting. In this simple conventional model, there is a phase transition at  $H_{c2}$ . Upon approaching  $H_{c2}(T)$  from below, the field inside the superconductor smoothly approaches the applied field, making  $H_{c2}(T)$  a second-order transition. Besides in typical type II superconductors,  $H_{c1}(T)$  is also a second-order phase transition separating a superconducting ( $R = 0$ ) from the non-superconducting mixed state. However, in low- $\kappa$  systems,  $H_{c1}$  can be a first-order transition.<sup>2</sup>

### 1.2.3 The Vortex-Glass Transition

In 1986, a new type of superconductor,  $La_{2-x}Ba_xCuO_4$  (LBCO) with  $T_c = 35K$  was discovered.[7] Very soon, a big jump to  $T_c$  of 90 K followed with the discovery of  $Y_1Ba_2Cu_3O_{7-\delta}$  (YBCO).[8, 9, 10] In these HTSC materials, the effects of thermal fluctuations are much larger than the conventional superconductors due to their higher critical temperature, shorter coherence length, larger magnetic penetration depth and quasi-two-dimensionality.[54]

The extraordinarily enhanced fluctuation effects in HTSC attracted researchers to review the phase diagrams of the type II superconductors. Based on renormalization-group and scaling ideas, Fisher, Fisher and Huse (FFH) made a important modification of the type II phase diagram. They proposed that there are two different

---

<sup>2</sup>See p. 157 of Ref. [15].

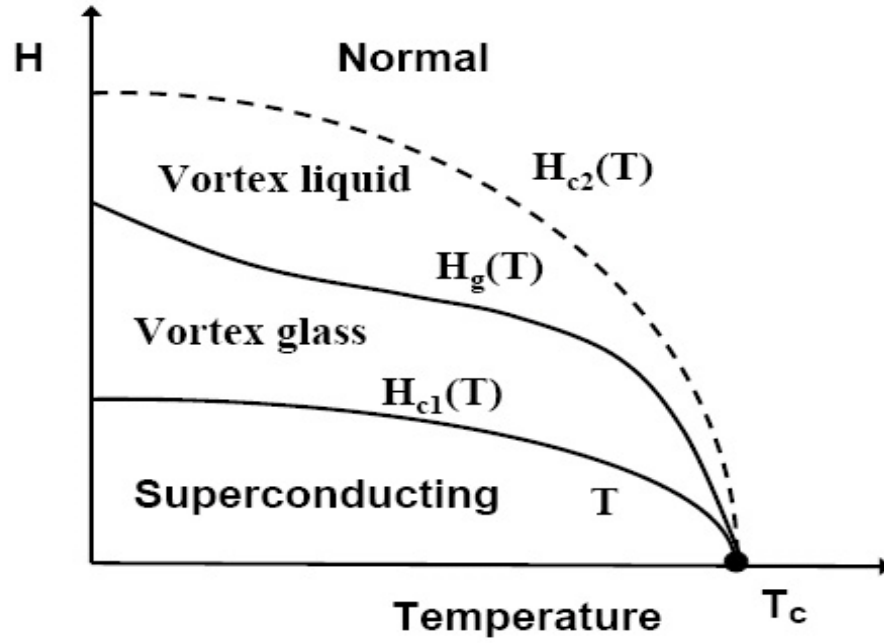


Figure 1.3: Phase diagram of a type II superconductor with the vortex-glass transition. The proposed phase transition within the mixed state ( $H_g(T)$ ) is predicted to be second order.  $H_{c2}(T)$  is no longer a phase transition, but rather a broad crossover from vortex-liquid to normal states. There is still a critical point at  $H = 0$ .

states between lower and higher critical fields instead of a single mixed state. These new states are the vortex glass and vortex liquid. The new phase diagram is shown in Fig. 1.3.[54]

Above  $H_{c1}(T)$  there are vortices inside superconductors. However, at low temperatures, the vortices are pinned and not able to move, so there is no dissipation, corresponding to a superconducting (zero-resistance) state in the mixed state. As the temperature increases, the vortices will start to move and are able to dissipate energy, corresponding to a vortex liquid state. The name of vortex glass and vortex liquid partially tell their characteristics, unmovable and movable. A line, called  $H_g(T)$ , separates the vortex-glass from vortex-liquid phases, and also the supercon-

ducting state from the normal state. Because the vortices are not expelled from the superconductor and there is no energy cost here, the vortex-glass transition is expected to be second-order. (Maybe first order transition in some limit, low- $\kappa$  systems) In this phase diagram, the  $H_{c2}(T)$  does not correspond to any phase transition, but a broad, continuous crossover to the normal state.

After the FFH theory of the vortex-glass phase diagram, lots of work has been done to investigate the phase transition of HTSC. A consensus was gradually reached that the vortex-glass transition does exist. D.R. Strachan, a former student in our group, investigated this transition, discussed the validity of how researchers determine the parameters governing the transition, and called into question whether the vortex-glass transition exists or not.[95] On the other hand, in zero field the existence of a second-order phase transition is not in doubt and at least in principle the critical parameters for this transition are well known. M. C. Sullivan, another former student in our group, investigated the normal-superconducting phase transition in zero field and hoped to clarify the controversial vortex-glass transition with the zero field result. In spite of many of experiments done to determine the critical exponents in both zero field and in finite magnetic field, there is still no consistent interpretation.

### 1.3 Fluctuations in Conventional Superconductors

At any non-zero temperature, fluctuations occur because a system can borrow an energy  $kT$  from its environment. For  $T < T_c$ , this makes it possible to temporarily increase the energy of a small volume of the superconductor, perhaps enough to drive the small volume into the normal state. For  $T > T_c$ , the opposite can happen and a small volume of normal state can go to the superconducting state. Simply speaking, the effect of thermodynamic fluctuations allows us to observe some quasi normal state properties below  $T_c$  and some quasi superconducting state properties

above  $T_c$  and round off the sharp corners and discontinuities which otherwise would be expected to occur at  $T_c$ . More concretely, above  $T_c$ , fluctuations towards the superconducting state lead to the appearance of excess conductivity, diamagnetism, specific heat, and tunneling currents; below  $T_c$ , fluctuations towards the normal state lead to the appearance of resistance in thin wires and the breakdown of fluxoid quantization in small rings.

In conventional superconductors, these fluctuation effects are generally small, but they are still measurable experimentally, particularly in superconducting samples of reduced dimensionality (on the scale of the Ginzburg-Landau coherence length), such as thin films, whisker crystals, and powders.[51]

In high- $T_c$  superconductor, the effects of thermal fluctuations are dramatically enhanced due to their high critical temperature, short coherence length, larger magnetic penetration depth and quasi-two-dimensionality.[54] Close to  $T_c$ , there is a regime where the fluctuations are large and dominate the properties of the superconductors, called the critical regime. The critical regime and the properties of superconductors in this regime will be discussed in detail in chapter 3. The large thermal fluctuations enhanced the critical regime of high  $T_c$  superconductor compared to conventional superconductors. Take YBCO for example, although different estimation methods give a critical regime ranging from  $0.01K$  to  $5K$  wide around  $T_c$ , they all agree that this region is experimentally accessible since good laboratory measurement stability in temperature is of the order of millikelvin. This permits study of fluctuations in far greater detail and provides the opportunity to measure critical behavior near the superconducting phase transition.

Although we are more interested in the fluctuations in the HTSC, fully understanding fluctuations in the conventional superconductors is necessary, which is helpful and illuminating for the research of HTSC. Ginzburg and Landau theory is powerful in phenomenological insight and provides a convenient foundation for understanding the basic phenomena of superconductivity. GL theory and its extension

describe well fluctuation effects in conventional superconductors. In this section, we will review some experimental phenomena and theoretical work on fluctuations in the conventional superconductors.

### 1.3.1 Zero-dimensional Superconductors

Zero-dimensional means the size of the particle is less than the correlation length  $\xi$ . In this case the order parameter  $\psi$  can be seen as uniform and there is no need to consider the spatial variation of the order parameter. For a zero-dimensional particle of volume  $V$ , the GL free energy relative to the normal state is simply:

$$F = (\alpha|\psi|^2 + \frac{1}{2}\beta|\psi|^4)V \quad (1.6)$$

Because of thermal fluctuation, the values of the order parameter with  $F - F_0 \leq k_B T$  should also occur. The magnitude of the fluctuations of the order parameter,  $\delta\psi$  can be estimated[51]:

$$(\delta\psi)^2 \approx k_B T / (2|\alpha|V) \quad T < T_c \quad (1.7)$$

$$(\delta\psi)^2 \approx k_B T / (\alpha V). \quad T > T_c \quad (1.8)$$

Fluctuations get large near  $T_c$  ( $\alpha \rightarrow 0$ ) or for very small particles (small  $V$ ).

Because of fluctuations the value of  $|\psi|^2$  is not fixed, the measurable quantity is  $\langle |\psi|^2 \rangle$ , which is the average of  $|\psi|^2$  over time. An exact solution for  $\langle |\psi|^2 \rangle$  can be found by taking a direct thermodynamic average over all possible values of the order parameter:

$$\langle |\psi|^2 \rangle = \frac{\int |\psi|^2 \exp(-F/k_B T) d^2\psi}{\int \exp(-F/k_B T) d^2\psi} \quad (1.9)$$

This result was first obtained by V. V. Shmidt in 1967[27] and was later re-derived by Parkinson and Muhlschlegel *et al.* in 1972[24, 25].

For a zero-dimensional sample, the most direct measure of  $\langle |\psi|^2 \rangle$  is the diamagnetic susceptibility. The first experimental observation of the diamagnetic susceptibility due to fluctuations was first done by Buhrman and Halperin in 1973.[23]



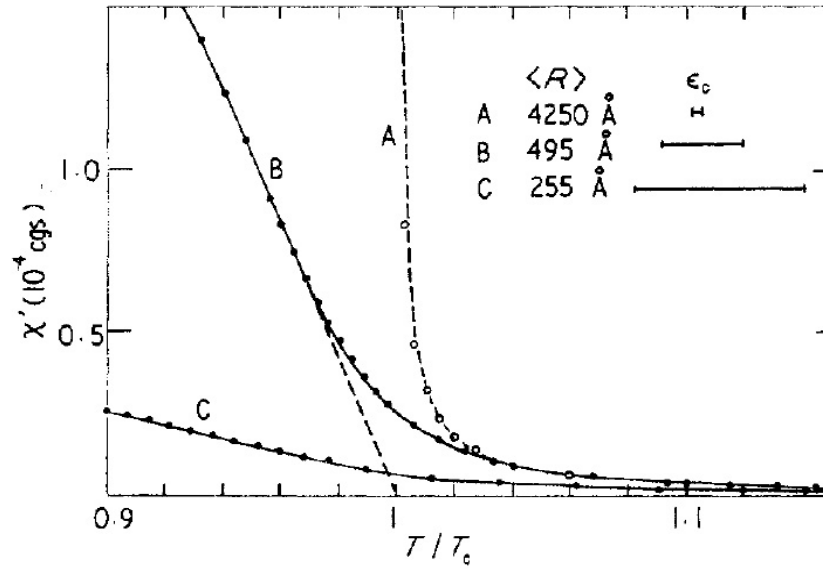


Figure 1.4: Measured diamagnetic susceptibility of aluminium powders with different mean particle sizes. The full curves are the GL theory including fluctuation effects, averaged over the known particle distributions. (Adapted from Buhrman and Halperin [23])

They used a SQUID magnetometer to measure the diamagnetic susceptibility of aluminium powders formed by evaporating aluminium in an inert gas atmosphere. These curves are shown in Fig. 1.4.

The superconducting contribution to the specific heat can also be calculated exactly.[26] Unfortunately the results are hard to test by experiment because it is extremely difficult to achieve thermal equilibrium among a sufficient number of isolated tiny particles.

### 1.3.2 Fluctuations Above $T_c$ – – Equilibrium Properties

#### Diamagnetism

In the Meissner state a bulk superconductor develops a diamagnetic magnetization  $M = -H/4\pi$  which reduces  $B$  to zero inside the superconductor everywhere except in a small surface layer of thickness  $\lambda$  (the penetration depth). For temperatures above  $T_c$ , there is still a small diamagnetic magnetization  $M'$  which comes from fluctuations. This diamagnetic magnetization  $M'$  above  $T_c$  may be calculated from the excess free energy per unit volume according to the usual thermodynamic relation:

$$M' = \partial < F > / \partial B \quad (1.10)$$

The free energy density in Eq. 1.10 can be determined via the partition function  $Z$  of the system and is given by:

$$< F > = -k_B T \ln Z = k_B T \frac{eB}{\pi \hbar c} \int \frac{dk_z}{2\pi} \sum_{n=0}^{\infty} \ln\left(\frac{\pi k_B T}{E_{nk_z}}\right) \quad (1.11)$$

where

$$E_{nk_z} = (\hbar^2/2m^*)(k_z^2 + \xi^{-2}) + (n + \frac{1}{2})\hbar\omega_H, \quad (1.12)$$

with  $\omega_H = e^* H/m^* c$ , the index  $n$  being over the degeneracy of the Landau levels.

A. Schmid calculated the average free energy density to second order in  $B$  and obtained the zero-field susceptibility:[28]

$$\chi' = -\frac{\pi}{6} \frac{k_B T}{\Phi_0^2} \xi(T) \quad (1.13)$$

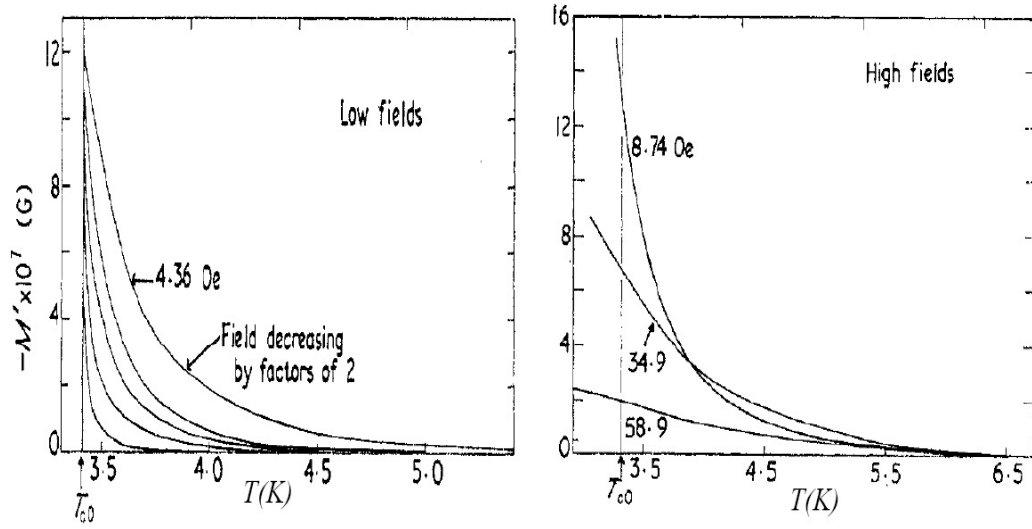


Figure 1.5: Measured fluctuation magnetization above  $T_c$  versus temperature and field of a bulk cylindrical sample of indium. At large fields the magnetization is suppressed. (Adpted from Gollub *et al.*[29])

The first experimental measurement of fluctuation diamagnetism was made by Gollub *et al.* in 1969.[29] They found that in lead samples the fluctuation diamagnetism was still detectable even at approximately twice  $T_c$ . Some typical data are shown in Fig. 1.5. Here any value of  $M'$  other than zero is a sign of fluctuations.

In larger magnetic fields, the fluctuations should be smaller and weaker than in the zero field limit Eq. 1.13.[51] Prange showed the fluctuation magnetization  $M'$  could be written in the form  $M'/H^{1/2}T = f(x)$  where  $f$  is a universal function of  $x = (T - T_{c0})/(T_{c0} - T_{c2}(H))$ . [30] However, the experimental results systematically fell below the GL 'universal curve' when they were scaled. This disagreement was found to be a result of the various limitations of the GL theory due to the slow- variations approximation. To deal with this, Patton *et al.* proposed the introduction of a cut-off energy for short-wavelength fluctuations and got a new universal function  $f'(x, H/H^*)$ , where  $H^* \approx H_{c2}(0)$ .

Then Gollub *et al.* found that such a scaling procedure could indeed eliminate

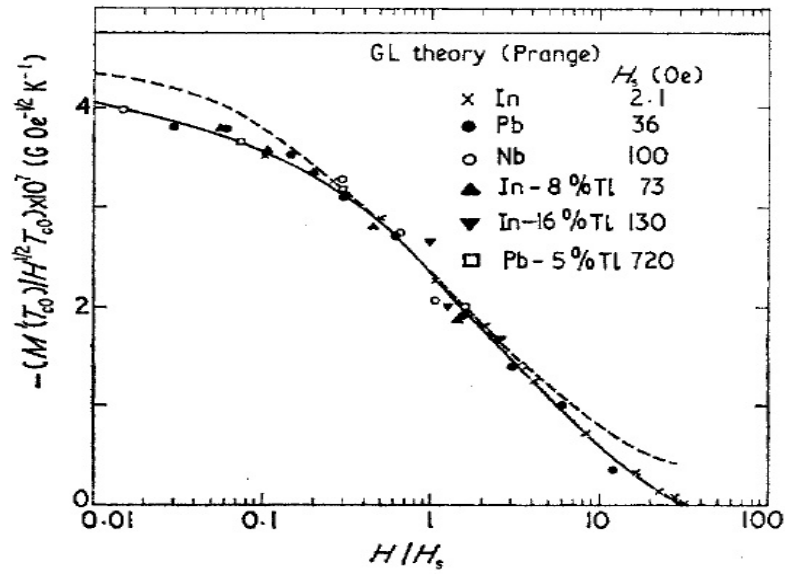


Figure 1.6: Universal behavior of scaled fluctuation magnetization at  $T_{c0}$  versus scaled field for a number of materials. The broken curve is the clean-limit microscopic theory and the solid curve is the scaled experimental results. (Adpted from Gollub *et al.* [29])

the material dependence of their results in 1970.[32] Fig. 1.6 shows the remarkable universal behavior for different materials.

However, in clean materials with long mean free path, the scaling field  $H_s$  (empirically defined as the field at which  $M'$  at  $T_{c0}$  falls to half the GL prediction) is much smaller than predicted by Patton *et al.* This discrepancy was discussed later by Lee and Payne(LP)[34], Kurkijarvi *et al.*(KAE)[35] and Maki *et al.*[36] They found that the effects of non-locality become important at much lower fields than  $H_{c2}(0)$ , and therefore account for the smaller scaling fields. This is in good agreement with the dirty-limit microscopic calculations, for which the non-locality is unimportant.

In sum, the study of fluctuation diamagnetism in bulk samples has not only demonstrated the existence of superconducting fluctuations far above  $T_c$ , but more over has proven useful for exploring the limits of the GL theory.

### Specific Heat

The fluctuation contribution to the specific heat can be calculated similarly by computing the partition function and average free energy similar to the diamagnetism calculation. If there are no fields we can write the free energy as:

$$F = \sum_k (\alpha + \hbar^2 k^2 / 2m^*) |\psi_k|^2. \quad (1.14)$$

where  $\psi_k$  is a term of the Fourier series expansion of  $\psi(r) = \sum_k \phi_k \exp(ik \cdot r)$ . Using the thermodynamic relation for the specific heat  $C_V = -\frac{T}{V} \frac{\partial^2}{\partial T^2} < F >$ , we can get the specific heat result of the fluctuation part for bulk materials[33]:

$$C_V = (k_B / 8\pi \xi^3(0)) t^{-1/2}, \quad (1.15)$$

where  $t$  is reduced temperature  $t = \frac{T - T_c}{T_c}$ . Unfortunately this is too small compared to the mean-field jump in the specific heat at  $T_c$  in typical clean materials until very close to  $T_c$ ,  $t \cong 10^{-11}$ . Even for very dirty materials, in which  $\xi(0)$  is small, it is still too small to be observable.

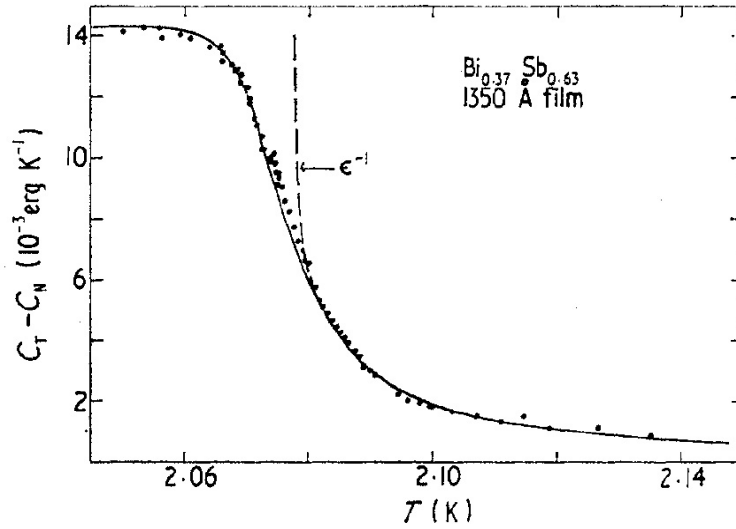


Figure 1.7: Measured heat capacity of an individual thin film. The  $T_{c0} \approx 2.075\text{K}$  broken curve shows the  $t^{-1}$  contribution from fluctuations expected neglecting the critical region near  $T_{c0}$ . The full curve is a two-parameter fit of a theory which takes the critical region into account. (Adapted from Zally and Mochel[37])

However, for two-dimensional thin films or in larger magnetic field, the fluctuation specific heat can be enhanced so that it can be measured. Zally and Mochel were able to measure the heat capacity of individual amorphous Bi-Sb alloy films using AC calorimetry techniques.[37] In Fig. 1.7 results for one of their thin films are shown. We see that far away from  $T_c$  (outside the critical region) the data shows  $t^{-1}$  dependence. Close to the  $T_c$  (inside the critical region), the  $t^{-1}$  dependence fails to describe the data. Gunther and Gruenberg[38] and Grossmann *et al.*[40] extended the theory into the critical region by using a Hartree-type approximation, in which they replaced  $\psi^4$  by  $2 \langle \psi^2 \rangle \psi^2 - \langle \psi^2 \rangle^2$  in a self-consistent way. We see an excellent fit has been achieved in the full curve in Fig. 1.7.

### 1.3.3 Fluctuations Above $T_c$ – Paraconductivity

The first-discovered and most striking aspect of superconductors is their infinite DC conductivity below  $T_c$ . Historically and realistically, conductivity phenomena are always important in studying superconductors. So it is natural to study how conductivity is affected by fluctuations. For temperatures above  $T_c$ , there is excess conductivity due to fluctuations, often called 'paraconductivity' in analogy with 'paramagnetism'.

Paraconductivity above  $T_c$  was first derived from the microscopic theory by Aslamzov and Larkin [55] and then from GL theory by Abrahams and Woo[41] and Schmid in 1968[42]. Here are the results:

$$\sigma_{3DAL}^{DC} = \frac{1}{32} \frac{e^2}{\hbar \xi(0)} t^{-1/2} \quad (1.16)$$

$$\sigma_{2DAL}^{DC} = \frac{1}{16} \frac{e^2}{\hbar d} t^{-1} \quad (1.17)$$

$$\sigma_{1DAL}^{DC} = \frac{\pi}{16} \frac{e^2 \xi(0)}{\hbar S} t^{-3/2} \quad (1.18)$$

$$(1.19)$$

where  $\xi(0)$  is the coherence length at 0 K and  $t = |T/T_c - 1|$ ;  $d$  is the thickness  $d \ll \xi$ ;  $S$  is the cross-section area  $S \ll \xi^2$ . Moreover, for samples of intermediate thickness, we can interpolate between the above forms and get the results. These predictions were found to be in good agreement with experimental results on dirty superconductors[122]. Some experimental results are shown in Fig. 1.8.

However, for cleaner films, the predicted universal behavior was not observed. Maki and Thompson investigated the difference between the AL prediction and the experimental results and proposed that it comes from the indirect effect of the fluctuations on the quasiparticle conductivity.[56, 57] The AL contribution comes from the direct acceleration of the fluctuation-induced superconducting pairs. These superconducting fluctuations then decay into pairs of quasi-particles of nearly opposite momenta. By time-reversal symmetry, the quasi-particles remain in a state of small

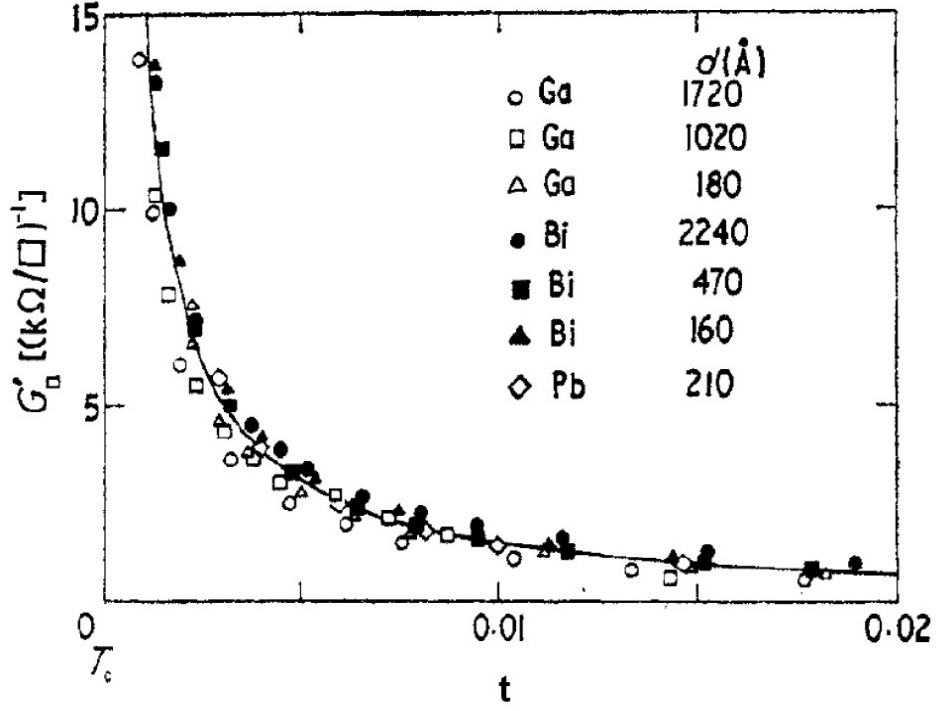


Figure 1.8: Universal variation of the measured excess conductance per square  $G'_\square[(k\Omega/\square)^{-1}]$  due to fluctuations with reduced temperature  $t$  above  $T_c$ , for a variety of amorphous films. The full curve is the Aslamazov-Larkin (AL) theory. (Adapted from Glover[122])



total momentum even after scattering from an impurity potential and continue to be accelerated like they were superconducting pairs. The quasiparticle life is limited, and they decay in several ways, which ultimately include decaying back into a superconducting fluctuation. The calculation of the indirect(Maki-Thompson) contribution can be found in many papers. [56] [57] The MT term explained a larger magnitude and an anomalous temperature dependence of the fluctuation conductivity observed on cleaner superconductor[51].

Measurement of the conductivity requires the application of an electric field, which may affect the measured result. This problem was first posed by Smith *et al.* in 1968, and solved in the high-field limit by Hurault.[44] Experimentally the  $E$  dependence of the conductivity has been studied by Thomas and Parks[45], Klenin and Jensen [46] and other researchers.[47] The effects of the magnetic field on the fluctuation conductivity were also discussed in the late 1960's and early 1970's. A lot of theorists and experimentalists made their contributions, such as H. Schmidt, P. Fulde, K. Maki, R.S. Thompson, B. Serin, R. R. Hake.[51]

The frequency dependence of the fluctuation conductivity  $\sigma'(\omega)$  gives important additional information checking the validity of the time dependent Ginzburg-Landau(TDGL) theory above  $T_c$ . The high-frequency components of the fluctuations fall off above a frequency  $\omega \sim 1/\tau_k = (1 + k^2\xi^2)/\tau_{GL}$ , so that the fall-off of the conductivity with frequency contains direct information about the time dependence of the fluctuations. The frequency dependence of the AL-term was calculated by Schmidt [58] using the time-dependent Ginzburg-Landau equation. And there is also a frequency dependent MT-term, which was calculated by Aslamazov and Varlamov [59].

### 1.3.4 Fluctuations Below $T_c$

Fluctuation effects exist not only above  $T_c$ , but also below  $T_c$ , where fluctuations towards the normal state lead to the appearance of resistance in thin wires and the breakdown of fluxoid quantization in small rings. Well below  $T_c$ , the effects of thermodynamic fluctuations are small. The system departs just a little from the behavior of the ideal superconducting state. Therefore we can describe its behavior starting from the ideal superconducting state, and then consider fluctuations as a kind of perturbation from this ideal behavior. This approach is useful in understanding some phenomena below  $T_c$ . For example, the appearance of resistive behavior below  $T_c$  is caused by fluctuations which lead to individual 'phase-slip' events. This approach forms a natural complement to our understanding of the paraconductivity above  $T_c$  caused by small departures from the ideally normal state. The phase-slip idea was developed before the paraconductivity theories, but its full experimental confirmation came later. Historically, the phase-slip mechanism was proposed by W. A. Little in 1967 [60]. Then Langer and Ambegaokar(LA) developed it and [49] and finally McCumber and Halperin made their contribution in 1970 [50]. Along with the development of the experimental instruments, such as SQUIDs and high precision voltmeters, it was possible to measure fluxoid quantization in superconducting rings and measuring the small resistances directly. In the 1970's, a lot of experimentalists put their efforts here and made things clear. They are Lukens et al, Warburton, Newbower *et al.* and Miller and Pierce.[51]

### 1.3.5 Summary

In this section, we described how thermodynamic fluctuations alter the properties of superconducting materials in the vicinity of the superconducting phase transition in a number of ways for conventional superconductors. Above  $T_c$ , thermodynamic fluctuations lead to the appearance of excess conductivity, diamagnetism, and spe-

cific heat; below  $T_c$  thermodynamic fluctuations lead to the appearance of electrical resistance and the breakdown of flux quantization.

When discussing the thermodynamic fluctuations there is a length scale over which individual fluctuations are important. The length scale is the Ginzburg-Landau coherence length, which determines the dimensionality of a given sample geometry. Generally the fluctuation effects are more important in samples with reduced dimensionality, because the thermal energy  $k_B T$  leads to larger effects in smaller fluctuation volumes ( $k_B T \sim F \xi^D$ , where  $D$  is dimensionality and  $F$  is fluctuation induced free energy density change). A fairly complete picture has been given in this section for the fluctuations effects on the type I superconductors [51].

## 1.4 Fluctuations in High $T_c$ Superconductors

In the previous section thermodynamic fluctuation effects in conventional superconductors in the vicinity of the superconducting phase transition have been described. However, the fluctuation effects in the high temperature superconductor are different. In the high  $T_c$  superconductors, the thermal fluctuation effects are dramatically enhanced due to a combination of factors of higher transition temperatures, shorter coherence length(smaller coherence volume), large magnetic penetration depth and quasi-two dimensionality. It makes the critical regime, in which fluctuations of the order parameter are important, of high temperature superconductors much larger than the conventional superconductors and gives a great opportunity for experimental investigation of fluctuation effects. In this section, I will briefly review the research on fluctuation effects in the HTSC.

### 1.4.1 Universality

In the modern theory of critical phenomena, there are some important things, such as the universality of critical exponents, certain critical amplitude ratios, relations

between the critical exponents and universal scaling functions. Only when we understand these things will we have a clear understanding of phase transitions and critical phenomena. From Wilson's renormalization group, we get a deep understanding of the origin of the universality and the critical power laws.

Continuous phase transitions are characterized by the system undergoing a transition from a symmetric or disordered state to a broken symmetry or ordered state. [52]. As the temperature changes and approaches the continuous phase transition, several remarkable phenomena appear, usually with power laws. They are the so called critical phenomena and the exponents used to characterize those power laws are called critical exponents. There is an important length scale  $\xi$ , which diverges at the critical point. This divergence can be described by a power law:

$$\xi = \xi_0^\pm |t|^{-\nu}, \pm = \text{sign}(t).$$

Here the critical exponent  $\nu$  and the critical amplitude  $\xi_0^\pm$  characterize divergence of the correlation length.  $t$  is the reduced temperature,  $t = \frac{T-T_c}{T_c}$ ,  $\text{sign}(t) = +$  above  $T_c$ ;  $\text{sign}(t) = -$  below  $T_c$ .

In the vicinity of the critical point, dynamical properties also have anomalous behaviors, such as transport coefficients, relaxation rates, and the response to time dependent perturbations. These anomalous properties depend on the equations of motion and are derivable from relaxation time  $\tau$  dependent correlation functions. Similar to the correlation length, this relaxation time diverges as criticality is approached, and there is also a power law dependence on reduced temperatures:

$$\tau_c \propto \xi^z \propto |t|^{-\nu z},$$

where  $z$  is called the dynamic critical exponent and  $\nu$  is the static critical exponent.

One of the important properties here is universality. It turns out that systems which belong to the same universality class have the same complete set of critical exponents. According to the spatial dimensionality  $D$  and number of order parameter degree of freedom  $n$ , the universality classes have three basic cases:

- D,n =3, Heisenberg spins  $S = (S_x, S_y, S_z)$  in D spatial dimensions;
- D,n =2, planar spins  $S = (S_x, S_y, 0)$ (XY-model),superfluids, superconductors in D spatial dimensions;
- D,n =1, Ising spins  $S = (0, 0, S_z)$  in D spatial dimensions.

## 1.4.2 Static Critical Phenomena

It is expected that the normal-superconducting phase transition of HTSC belongs to the universality class of 3DXY, D=3 and n=2, with static critical exponent  $\nu = 2/3$ . Experimentalists have measured thermodynamic properties in zero field, such as penetration depth, magnetic susceptibility, specific heat and thermal expansivity to explore the effects of superconducting fluctuations and to determine the static correlation-length critical exponent  $\nu$ . The following is a brief discussion of the results if these measurement.

### Specific heat and thermal expansivity in zero field

First we consider the critical behavior of the specific heat in zero magnetic field close to optimal doping. Particularly suitable candidates to assess the occurrence of this characteristic 3D-XY critical behavior are  $YBa_2Cu_3O_{7-x}$  and  $DyBa_2Cu_3O_{7-x}$ . The measurements have been done by A. Junod *et al.* [80], A.Kozłowski *et al.* [81], M. B. Salamon *et al.* [67] and N. Overend *et al.* [70].

The capacitance dilatometry method makes it possible to measure the expansivity with high resolution without the necessity to subtract a background. According to thermodynamics, we have relations between expansivity( $\tilde{\alpha}_i$ ), pressure coefficient( $\alpha_{pi}$ ) and specific heat( $C$ ) [85] [86] [87]:

$$\tilde{\alpha}_i^{\pm} = \frac{T_c}{T} \alpha_{pi} C \quad (1.20)$$

$\tilde{\alpha}_i^{\pm}$  is the expansivity along the spatial direction i, and

$$\alpha_{pi} = \frac{1}{T_c} \frac{dT_c}{dp_i} \quad (1.21)$$

denotes the pressure coefficient at  $T_c$ . We obtain a relation between the singular parts of expansivity and specific heat:

$$\tilde{\alpha}_i^\pm = \alpha_{pi}(\frac{A^\pm}{\alpha}|t|^{-\alpha} + B^\pm), \quad \tilde{\alpha}_{b-a} = \alpha_b - \alpha_a \quad (1.22)$$

V. Pasler *et al.* did such an expansibility measurement. Their results, which are given in Fig. 1.9, showed fluctuation-dominated behavior over more than two orders of magnitude of the reduced temperature and are consistent with 3DXY universality.[71] However, due to sample inhomogeneities there is at present no example of a phase transition in solids as clean as the remarkable case of the lambda transition in superfluid helium, for which over more than 7 decades of scaling have been observed.[72]

We also note that as  $t$  gets smaller, which means at temperature close to  $T_c$ , the result starts to deviate from scaling behavior. T. Schneider claimed that this deviation is due to finite size of the sample. He developed a finite size scaling theory that will be discussed later.

### Temperature dependence of the penetration depth

Since the correlation length  $\xi$  diverges close to  $T_c$ , one expects that the penetration depth also diverges and shows critical behavior as:<sup>3</sup>

$$\frac{1}{\lambda_i^2} = \frac{1}{\lambda_{i,0}^2} t^\nu, \quad i = \perp, \parallel. \quad (1.23)$$

Fig. 1.10 gives the experimental data of S. Kamal *et al.*, which clearly showed penetration depth deviations from mean field behavior close to  $T_c$ . The data is also consistent with  $\nu \approx 2/3$ . Data of similar quality have been reported by Buzdin *et al.* [82], Zech *et al.* [75], S. M. Anlage *et al.* [66] and S. Kamal *et al.*[64]. All the measurement showed 3DXY critical behavior around  $T_c$ .

---

<sup>3</sup>In GL theory,  $\lambda \propto n_s^{-1/2}$ ,  $\xi \propto t^{-1/2}$  and  $\lambda \propto t^{-1/2}$ ; close to  $T_c$ ,  $\lambda \propto n_s^{-1/2}$  and  $n_s \propto \xi^{-1}$ , so  $\lambda \propto t^{-\nu/2}$ ; very close to  $T_c$ ,  $\lambda \propto \xi \propto t^{-\nu}$ . [11, 65]

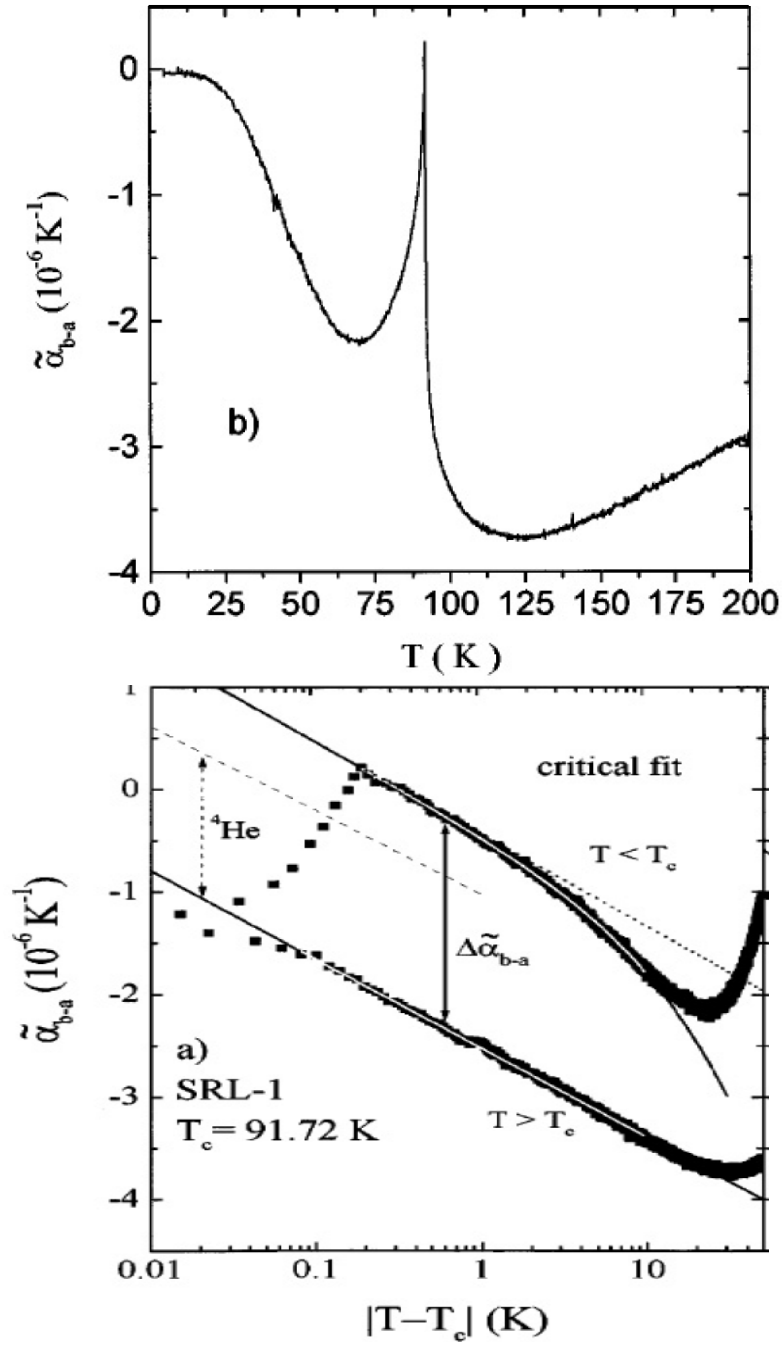


Figure 1.9:  $\tilde{\alpha}_{b-a} = \alpha_b - \alpha_a$  versus temperature  $T$  and reduced temperature  $T - T_c$ , semilog representation. The dashed curves represent a fit yielding  $A^+/A^- = 0.9$  to  $1.1$  and  $|\alpha| \approx 0.018$ . Adapted from [71]

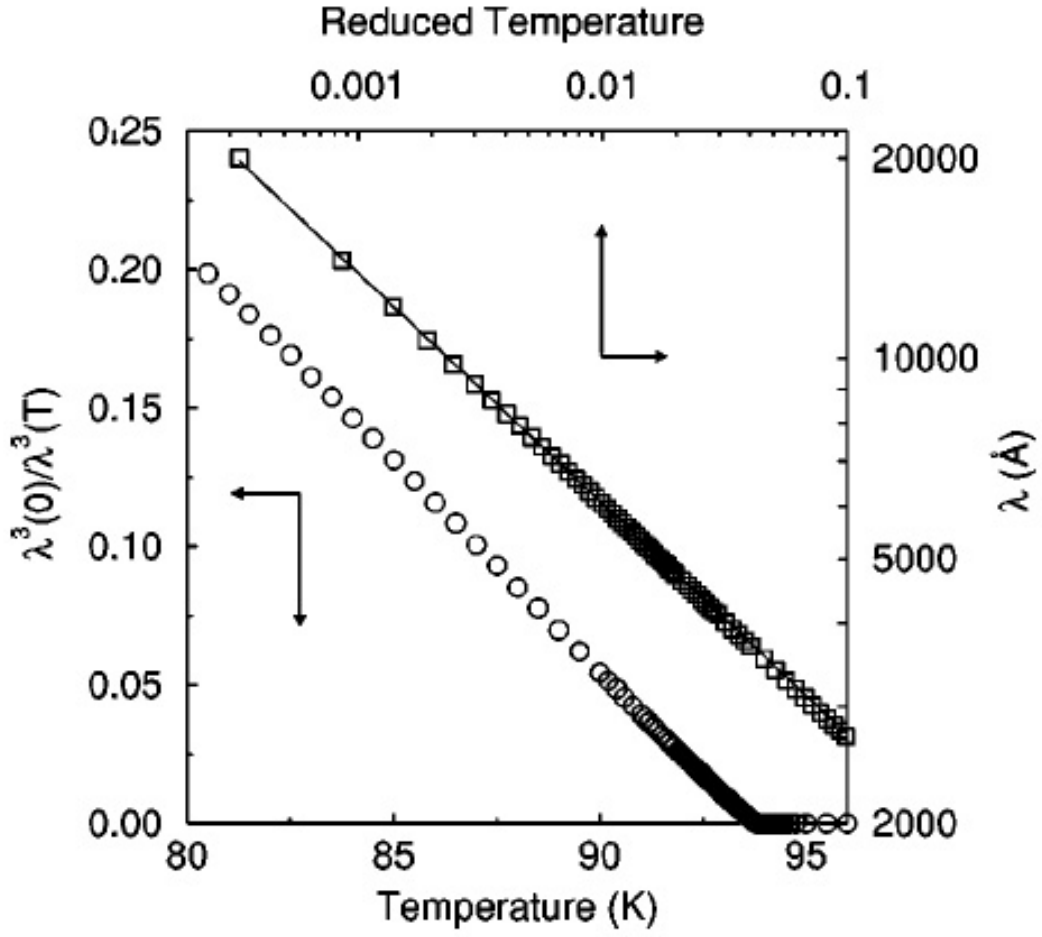


Figure 1.10: 3DXY critical behavior of the superfluid density in the superconducting state of a sample annealed to  $YBa_2Cu_3O_{6.92}$ .  $\lambda^3(T=0)/\lambda^3(T)$  versus  $T$  (○, left and bottom axes) and  $\lambda(t)$  versus reduced temperature  $t = 1 - T/T_c$  on log-log scale (◇, right and top axes). Adapted from [64]



## Temperature dependence of the diamagnetic susceptibility

Similar to the penetration depth, the diamagnetic susceptibility in the zero field limit is altered by critical fluctuations. We have:

$$\chi_z \propto |t|^{-\nu} \quad (1.24)$$

T. Schneider [75] measured the fluctuation contribution to the susceptibility in sintered  $YBa_2Cu_3O_{6.96}$ . In the reduced temperature range  $10^{-4} < t < 10^{-2}$ , he analyzed the data and got  $\nu = 0.66(5)$  and  $T_c = 92.14(4)K$ . The results are consistent with 3D-XY critical behavior. Other groups also reported consistent results, including M. B. Salamon *et al.*, A. Pomar *et al.* and R. Liang.[67, 68, 69]

## Other evidence of 3DXY behavior

Further evidence for critical 3D-XY behavior have been observed in other experiments, such as the magnetization measurement. From the classical scaling theory, which is discussed in Schneider's book [52], the magnetization data should scale and fall onto a single curve. Salamon *et al.* [67] measured magnetization for an untwinned  $YBa_2Cu_3O_{7-x}$  single crystal. With the assumption of  $\nu = 2/3$ , the data collapsed to a single curve very well. Also Roulin *et al.* [83] and Jeandupeux *et al.* [84] got remarkable data collapse from magnetization measurement of  $Bi_2Sr_2CaCu_2O_8$ , which confirmed the agreement of the magnetization data with the 3D-XY scaling behavior.

### 1.4.3 Dynamical scaling

We have shown that a great number of experiments have been done to investigate the static critical phenomena near the normal-superconducting phase transition. Those experimentalists largely agreed that the normal-superconducting phase transition belongs to universality class of 3DXY and static correlation-length critical exponent  $\nu \simeq 0.67$ .

In the vicinity of the critical point, dynamical properties also have scaling behaviors. The dynamical properties, such as transport coefficients, relaxation rates, and the response to time-dependent perturbations, which depends on the nature of the dynamics near  $T_c$ , can determine both the static critical exponent  $\nu$  and dynamical critical exponent  $z$ . Fisher, Fisher and Huse [54] gave a general scaling form to describe the phase transition from the superconducting state to the normal state in transport properties. In zero field  $H = 0$ , the two variables are current density  $J$  and frequency  $\omega$ . This leads to two commonly used methods to investigate the dynamical scaling, DC conductivity measurement and AC conductivity measurement. Now we discuss the two methods separately.

For the DC conductivity measurement, there has been lots of work to investigate fluctuation behavior and to extract critical exponents.[97, 98, 99] The problem is that those measurements have yielded a wide range of values for the critical exponents.

The phase transition in magnetic field, which corresponds to the vortex-glass transition, has been extensively studied using current-voltage(I-V) isotherms and recently a new criterion has been developed to determine whether or not a phase transition has occurred.[95, 96] Although there is a trend to believe that a vortex-glass transition does exist, there is little consensus on the values of the critical exponents  $\nu$  and  $z$ .[97, 98, 99].

In zero magnetic field the existence of an N-S phase transition is not in doubt. Very close to  $T_c$  ( $|T - T_c| \leq 2K$ ),[11] the transition is commonly believed to obey the 3DXY model, with  $\nu = 2/3$ . For a disordered system, the value of  $\nu$  increases.[77, 78, 79] For the universality class of the 3D-XY ( $n=2$ ), the dynamical critical behavior can be model-E or model-A dynamics depending on the conserved quantities. [61] Contrary to the agreement on the value of  $\nu$ , the dynamics of this transition is still under debate and the value of  $z$  is not clear from both theoretical work and experimental results. Tab. 1.1 shows some previous theoretical predictions and numerical simulations on critical exponents in zero field.

Table 1.1: Previous theoretical predictions and numerical simulations on critical exponent  $z$  in zero field

Exponents	$z$	Dynamics	References
theoretical prediction	$z = 2.0$	Model-A	D. S. Fisher <i>et al.</i> [54]
theoretical prediction	$z = 1.5$	Model-E	F. S. Nogueira <i>et al.</i> [73]
numerical simulations	$z = 2.0$	Model-A	V. Aji <i>et al.</i> [74]
numerical simulations	$z = 1.5$	Model-E	J. Lidmar <i>et al.</i> [77]

The experimental results are even more controversial. From voltage current characteristic measurement, J . M. Roberts *et al.* and T. Nojima *et al.* have found vortex-glass-like exponents( $\nu = 1.1$ ,  $z = 8.3$ ) in small fields( $< 10$  mT).[100] Also at low fields, others find 3D-XY-like exponents  $z = 1.25$  and  $\nu = 0.63$  through DC conductivity measurement[101].

In zero field, T. Schneider and H. Keller reported  $z = 2$  and  $\nu = 2/3$  in the reduced temperature range  $6 \times 10^{-3} < t < 10^{-2}$  for sintered  $YBa_2Cu_3O_{6.96}$ . For temperatures close to  $T_c$ , there is a deviation from power-law, which they claim is due to a finite-size effect.[103] More recently, S. H. Han *et al.* reported a 2D to 3D crossover and a critical regime with multiple exponents through DC electrical conductivity measurement of  $Bi_2Sr_2CaCu_2O_{8+\delta}$  single crystals.[104]

AC conductivity measurements are another way to test scaling theory and to obtain the critical exponents. AC measurements determine both the real and imaginary parts of the fluctuation conductivity, providing a stringent test of critical dynamics.[105, 106] Until now, most of the available microwave experimental data have been restricted to fixed frequencies.[107, 105, 108, 109, 113] Measurements over a broad frequency range allow us to probe the dynamical behavior of the system. However these experiments are seldom done, and the available results are inconsistent: Values of  $z$  range from 2 to 5.6. Booth *et al.* systematically investigated the

frequency-dependent microwave conductivity of YBCO films above  $T_c$  and obtained  $z = 2.3$  to  $3$ . [91] Also for a YBCO film, G. Nakielski *et al.* measured frequency-dependent conductivity using a contactless method and obtained  $z \approx 5.6$ . [110] Osborn *et al.* did a similar experiment and discussed the linear and nonlinear scaling of complex conductivity of  $Bi_2Sr_2CaCu_2O_{8+\delta}$  (BSCCO) films below  $T_c$  and obtained  $z \approx 2$ . [111] For an optimally doped  $La_{2-x}Sr_xCuO_4$  (LSCO) film, Kitano *et al.* found that their data were consistent with the 3D-XY model with diffusive dynamics:  $\nu \approx 0.67, z \approx 2$  in a reduced temperature range  $0.008 < t < 0.03$ . [112]

Although lots of work have been done here, there is clearly a lack of consensus on the dynamical fluctuations of the superconducting transition. Further work to extract a reliable value of  $z$  and  $\nu$  is necessary.

## 1.5 Summary

In this chapter, I briefly introduced the background to the normal superconducting phase transition. There have been a lot of work investigating this transition both in magnetic field and zero field. In my work, I concentrate on zero field where the existence of a second-order phase transition is not in doubt. It is hopeful that the zero field result is helpful to clarify the controversial vortex-glass transition.

We use AC measurements over a broad frequency range to probe the dynamical behavior of the YBCO thin film. Our experimental setup, Corbino reflection measurement system, will be introduced in chapter 2. Following that, chapter 3 serves as a theoretical basis for our work on phase transitions.

Then in chapter 4, where the growth and characterization of the sample will be given, the experimental data will be shown and analyzed, and the dynamical critical exponent will be extracted and discussed. In addition, the power dependence measurement will also be mentioned, which is the chapter 5.

AC and DC measurements are two commonly used ways to extract critical ex-

ponents. In chapter 6, I will show the measurement of AC and DC on the same film and compare the results.

The Corbino reflection measurement is a powerful tool, but not only for the high  $T_c$  fluctuation measurement. I also utilize it to measure microwave properties of single walled carbon nanotube films. The results are shown in chapter 7.

Chapter 8 is a summary of the whole thesis.

## Chapter 2

# Corbino Reflection Measurement Technique

The study of the electronic properties of matter has historically provided much important information in the field of condensed matter physics. The investigated materials include not only those commonly used in every-day life like insulators and metals but also more unusual ones, such as superconducting materials that require special conditions to reveal their properties. Depending on the energy scale, or frequency range in another words, that we are interested, the tools used to access these electronic properties are different. In this chapter first a brief overview of the techniques used in different frequency ranges is given and then I focus on our Corbino setup, which is able to measure surface impedance in the frequency range from 10 MHz to 50 GHz.

## 2.1 Overview of the Spectroscopy

The electromagnetic spectrum of interest in condensed matter physics distributes over a very wide frequency range. Presently there is not any single tool which can cover all relevant frequencies. For different energy scales of interest, the tools are different. To cover a very large frequency range, one needs to combine different

tools. Although the tools differ upon the frequency of interest, all spectroscopic systems normally contain four major components: a radiation source, a detector, the sample or device under test, and some mechanism to select, to change, and to measure the frequency of the applied electromagnetic radiation.[119] In this section I will give a brief introduction to spectroscopy including aspects such as sources, detectors and measurement techniques.

Any spectroscopy system needs a source to generate electromagnetic waves. Normally there are four different principles of generating electromagnetic waves: lasers, Electron beam radiation sources, solid state oscillators and thermal radiation sources, as shown in Fig. 2.1. At low frequencies(DC to GHz) normally used sources are solid state oscillators, such as Gunn oscillators or IMPATT diodes. These solid state devices are monochromatic and often tunable over a wide range. Above the GHz range, utilizing the interaction of charge and electric field, the accelerated electron beams can be modulated to create electromagnetic waves.(e.g. klystron, magnetron, backward wave oscillator, gyrotron) Through this method, coherent monochromatic sources can be obtained up to about 2 THz. According to Planck's law, any matter above absolute zero temperature(0 K) emits electromagnetic radiation, which is black-body radiation, also called thermal radiation. Thermal radiation creates a broad spectrum from the far-infrared up to the ultraviolet. However, at both low and high ends of the range the thermal radiation intensity drops off dramatically because their peak intensity is typically in the infrared range. The thermal radiation source can only give incoherent light. In the infrared, visible and ultraviolet spectral ranges, lasers are normally utilized. For some lasers can deliver coherent and also tunable radiation, as well as short pulses. In recent years, the development of new technologies have allowed the spectral range of synchrotron radiation to extend down to the far infrared range.

Generally electromagnetic radiation is detected by its interaction with matter. The principles used for radiation measurement devices includes the photoelectric

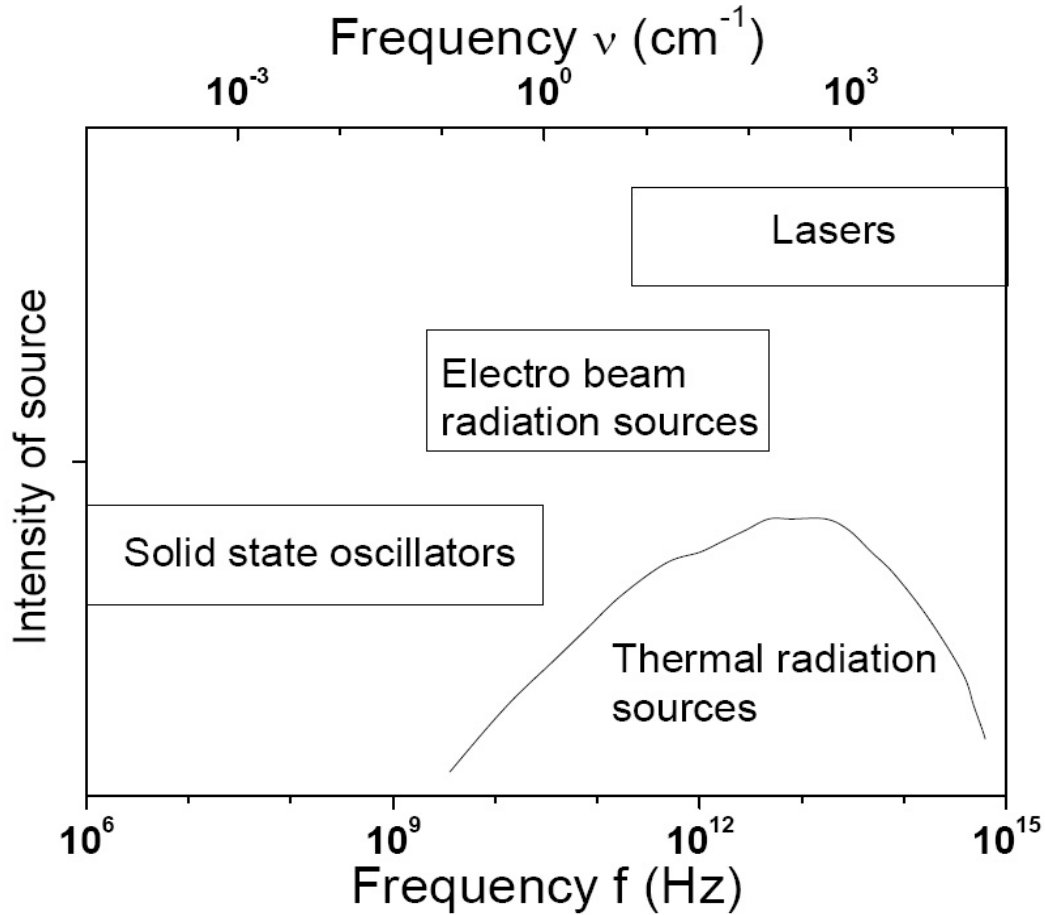


Figure 2.1: Ranges of the electromagnetic spectrum in which the different radiation sources are applicable. Adapted from [119] Page 211.

effect, the thermal effect(heating), luminescence and photochemical reactions. In the low frequency range, from DC to GHz range of frequency, semiconductor devices are used, Schottky diodes for example. For higher frequency ranges, thermal detectors are used, such as Golay cells and bolometers. These thermal detectors can operate up to a few THz. The infrared range is covered by pyroelectric detectors. As for even higher frequencies, in the visible and ultraviolet spectral ranges, photomultipliers are extremely sensitive and widely used detectors. Details of the different detectors, their principles and their advantages can be found in many books.[120] Fig. 2.2



shows the commonly used various detectors and the their roughly covered frequency ranges.

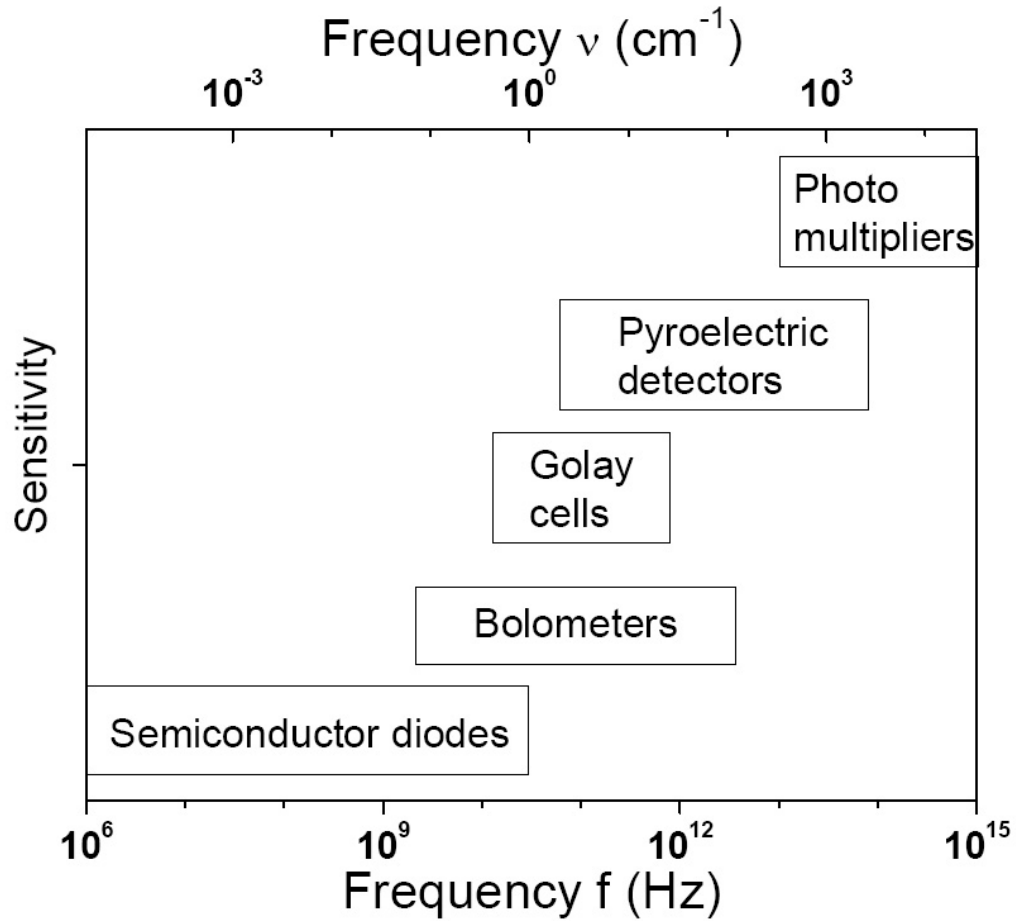


Figure 2.2: Operating frequency ranges of detectors. Adapted from [119] Page 213.

For any measurement system, propagating electromagnetic waves are necessary. For very low frequency, the applied current flows in the conductors and the electromagnetic waves propagate along the conductor, such as wires and cables. In the kHz and MHz range of frequencies, coaxial cables are widely used. The sizes of coaxial cables varies depending on the different application range of frequencies. Recent progress has made coaxial cables available up to 100 GHz. In the microwave and millimeter wave range, striplines and waveguides are generally used to propagate

electromagnetic waves. From the infrared through the visible up to the ultraviolet spectral range, the electromagnetic waves is transmitted like visible light, via free space or in optical fibers.

Although the structures guiding the electromagnetic waves differ very much, the general principles of wave propagation are always the same. As far as wave propagation is concerned, all structures and even free space, can be discussed within the concept of transmission lines. Maxwell's equations can fully describe the propagation of electromagnetic waves in a transmission line. However, it is not necessary to actually solve the wave equations with the boundary conditions each time. The more convenient and commonly used characteristic parameter is the impedance  $\hat{Z}$ . With the impedance  $\hat{Z}$  the wave propagation can normally be discussed in a manner independent of the particular guiding structure.

At different parts of the electromagnetic spectrum, the measurement methods, the hardware and the means of propagation of the electromagnetic radiation are different. One way to classify the different measurement methods is from the interaction of electromagnetic radiation with the material under study. Through this point of view all the different methods can be classified into three categories: single-path method, interferometric techniques and resonant techniques.[119] For each category, the system setup differ depending on the detected frequency.

The name of "Single-path" itself tells us this method light interacts with matter only once and the experiment samples the change of the electromagnetic wave. For example, the light is reflected off the sample surface or transmitted through the sample. Normally some of the radiation is absorbed. Then from the quantity that is absorbed the properties of the material can be determined. This simple method can determine the phase change of the radiation and the attenuation in power due to the interaction. However, only at low frequencies(i.e. at long wavelengths) can the phase change be obtained. For higher frequencies, we can only determine the attenuation in power.

Interferometric techniques compare one part of the radiation, which undergoes interaction with the material(i.e. reflection from or transmission through the material), with a second part of the signal, which serves as a reference.[119] This definition tells that the interferometric technique is a comparative approach. Then the mutual coherence of the two compared radiation beams is crucial. Through this method, the complex response of the sample can be determined since the interference of two beams is sensitive to both the change in amplitude and in phase upon interaction.

Another technique is the resonant technique, which has very high sensitivity. For this technique the electromagnetic waves interact with the material multiple times and the electromagnetic fields are established inside a resonant structure. By observing the two characteristic parameters of the resonance, i.e. the resonance frequency and its quality factor, both the real and imaginary components of the electrodynamic response of the sample can be determined.

All methods mentioned above have advantages and disadvantages. Resonant techniques have very high sensitivity due to the multiple interactions with the sample. The quality  $Q$  can characterize the sensitivity. Normally for a resonant structure of quality  $Q$ , the electromagnetic radiation bounces approximately  $Q$  times from the surface of the sample. So higher  $Q$  brings higher sensitivity. The cost of the high sensitivity is a narrow bandwidth. The resonant techniques is not a broadband technique. Compared to the resonant technique, the single-path and interferometric techniques have lower sensitivity, but they are both broadband techniques, which means they can investigate the properties of samples over a wide frequency range. If there is a significant change in the measured parameters, single-path arrangements are preferred due to its simplicity. Interferometric techniques offer increased sensitivity and precision, but normally are more complex and expensive to produce.

Of course, the different path arrangement can be combined sometimes. This gives rise to a variety of measurement arrangements. Here as a brief summary, I am not able to discuss everything in detail. The relevant knowledge can be found in

many books, such as[119].

## 2.2 Impedance Measurement in the Microwave Frequency Range

Surface impedance measurements at microwave frequencies have provided important information about the fundamental properties of the superconducting state. The microwave penetration depth measurements on single crystals have provided important evidence in the effort to determine the symmetry of the order parameter in high  $T_c$  materials. Microwave measurements also provide a very stringent test of sample quality, and therefore are helpful for improving the quality of these materials, and are important to separate intrinsic and extrinsic effects in these complicated materials. In addition to the fundamental aspects, microwave measurements can also be used to help develop a general phenomenological picture of superconductivity in the absence of a fundamental theory.[93]

Another reason to focus on the microwave properties of superconductors comes from their applications. Since the discovery of HTSC materials, the possibility of obtaining superconductivity in the liquid nitrogen temperature range has excited a series of commercial applications because of their relatively low cooling cost. One significant application of HTSC is in the area of microwave passive components, i.e. resonators and filters. Compared with devices fabricated from normal metals, HTSC devices have lots of advantages, such as lower rf-losses, and smaller denser circuits for a given performance. HTSC material can also form the basis of highly sensitive IR sensors and be used as magnetic shielding.[121] Another application of HTSC is to make high-field magnets. Whereas the  $H_{c2}$  of HTSC is large, current available commercial HTSC magnets generate only  $1T$  of magnetic field. A clear picture of the properties of HTSC near  $T_c$  is required for the application of high field magnets

within the liquid nitrogen temperature range. Microwave surface impedance measurements are important for us to address this issue, to get a deep understanding of the HTSC material, and finally to utilize these materials for applications.

Most of the conventional microwave measurements of the surface impedance use resonance techniques. As we already mentioned, the resonant techniques can provide a very high sensitivity of the surface impedance as a function of parameters such as temperature or magnetic field, but they are not broadband and are limited to at most a few discrete frequency points, and therefore can not provide much information on how the surface impedance varies with frequency. Sometimes the frequency dependent properties are required, for example the behavior of a system at many different frequencies will provide a much more stringent test of a theoretical model.

Broadband measurements take non-resonant techniques and typically measure the transmission or reflection of a microwave signal incident on the sample. The measured quantity is typically a voltage, not a frequency, thus broadband measurements are normally much less sensitive than high-Q resonant measurements. Besides in order to accurately measure both the real and imaginary parts of the response, one must use phase-sensitive measurement techniques, which become increasingly more difficult as the measurement frequency increases and the signal wavelength becomes much smaller than the measurement apparatus.[93] However, since they do not use a resonant mode, there is much more freedom in choosing an operating frequency in these experiments.

The early microwave transmission measurements on superconductors employed the wave guide method, and some of the most important work were carried out by Glover and Tinkham.[122] The measurement system described in my work is different from the waveguide transmission measurements. This technique is called the Corbino reflection technique[92], which can measure the complex reflection coefficient from 10 MHz to 50 GHz of a thin film which forms an electrical short

across a coaxial transmission line.[93] The Corbino reflection technique uses a swept-frequency method and directly measures the full complex resistivity or conductivity of a thin film as a function of frequency. The measurement utilizes coaxial transmission lines, which support the transverse electromagnetic(TEM) mode up to approximately 70 GHz, and all the way down to dc because of the absence of a lower cutoff frequency for the TEM mode. Hence the system covers a very large range of frequency including the radio frequency, microwave and millimeter wave range. The use of the TEM mode also results in a relatively simple field distribution within the thin film sample. Also, for the geometry used here, the measured reflection coefficient is simply related to the complex resistivity of the sample. The detailed introduction of the Corbino technique will be given in the next section.

## 2.3 Experimental Setup of the Corbino Reflection Measurement

### 2.3.1 Advantages of the Corbino Geometry

The measurement employs a network analyzer to measure the complex reflection coefficient  $\hat{S}_{11}$  of a thick film which forms a Corbino geometry at the end of a coaxial cable. Fig. 2.3 shows the scheme of the Corbino geometry. At the top of the coaxial cable, we indicated the high frequency electric field(full arrows) and the magnetic field(dashed circles). At the bottom, the shaded area is the Corbino disk formed on the sample, with the current shown as full arrows.

The measurement takes advantages of the Corbino geometry. Fig. 2.3 shows that in such a Corbino disk the currents in the film flow in the radial direction, so produce magnetic fields only in the azimuthal direction parallel to the surface of the film. Through the Corbino geometry the edge effects of the film are effectively reduced compared to a rectangular or micro-bridge geometry. As for the latter two

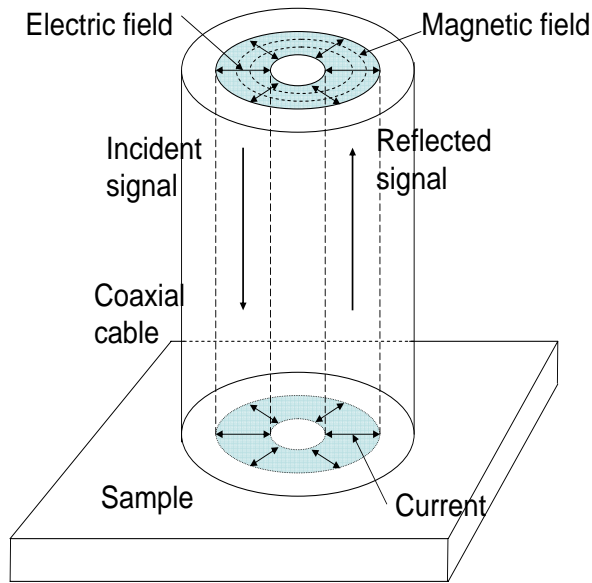


Figure 2.3: Scheme of the Corbino geometry.

geometries, the current will make the self fields perpendicular to the surface, particularly at the edges. The virtue of the Corbino geometry is particularly important when studying the motion of magnetic vortices in the mixed state of superconductors, since without perpendicular self magnetic field, which normally comes from sample edges in other geometries, there is much less contribution to the creation and/or pinning of vortices.[124] An additional advantage of the technique is that it allows for the surface impedance to be determined over a wide range of parameters, including temperature, magnetic field, frequency, rf power and dc bias current.[93]

### 2.3.2 History of the Corbino Technique

The Corbino geometry was historically used for dc transport measurement.[123] The Corbino reflection measurement technique developed out of this virtuous geometry.

N. Bluzer and collaborates built their transient photoimpedance response (TPR) apparatus using the Corbino geometry and measured time-domain picosecond quasiparticle dynamics of superconductors in zero field.[125] Their basic technique has been adapted to the frequency domain. James Booth, a former student of our group, developed the Corbino reflection technique and studied vortex dynamics and fluctuation conductivity in high  $T_c$  superconducting YBCO thin films.[92, 91] With the same setup, Andrew Schwartz, a former post-doc in our group, studied the local magnetic behavior of single-crystal  $La_{0.8}Sr_{0.2}MnO_3$  and investigated the critical behavior of the ferromagnetic phase transition.[126]

Exploiting the relative temperature independence and frequency stability of nichrome thin films M. Stutzman *et al.* at the University of Virginia proposed a calibration method for a long, lossy microwave transmission line with three standards in a cryogenic system, at temperatures down to 100 mK.[128] This procedure requires excellent reproducibility of the cryogenic conditions. Marc Scheffler *et al.* in Germany, compared further calibration schemes based on just a single low-temperature calibration measurement or employing a superconducting sample as a calibration standard for its normal state and applied their spectrometer to study thin films of a heavy-fermion compound.[127] H. Kitano *et al.* in Japan, also investigated the effectiveness of different calibration methods for Corbino setup and with their system, they studied dynamic microwave conductivity near  $T_c$  for  $La_{2-x}Sr_xCuO_4$ (LSCO) thin films with  $x = 0.07$  to  $0.16$ . [112]

Although a lot of work has been done to improve the calibration at cryogenic temperature, there is still no widely accepted calibration standard in this small community. The reason is partially due to the fact that complete reproducibility is very hard to achieve. In addition, these measurement systems are extremely sensitive to outside perturbations. It makes the choice of a calibration method dependent on the particular setup and the research objectives.



### 2.3.3 Our Experimental Setup

#### Schematic of the system

A schematic diagram of our experimental setup is shown in Fig. 2.4. The whole experimental setup includes a cooling system, a control and measurement system and the main part, a cryostat, in which the Corbino probe and the sample are located.

#### Microwave measurement on YBCO thin films

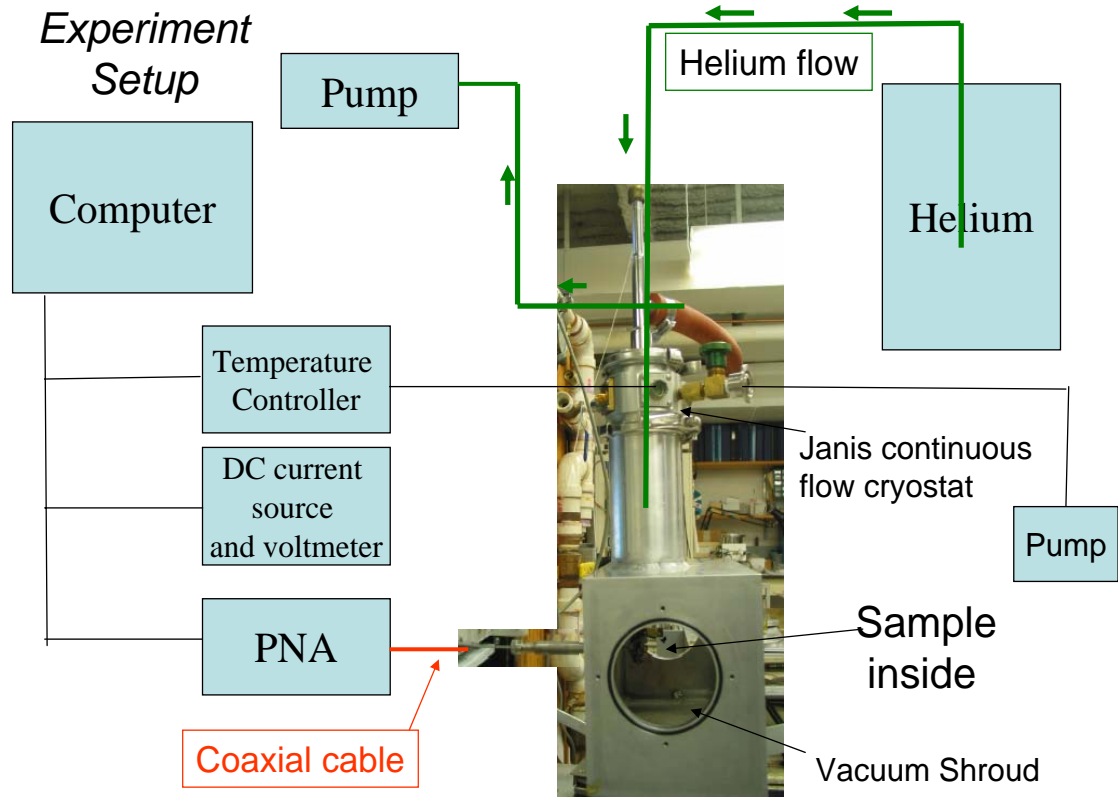


Figure 2.4: Schematic of the Corbino experiment setup on YBCO measurement.

The cryostat can be viewed as two parts. One is the bottom shroud, where the sample is located and measurements are carried out. The other one is a cold finger

extending from the top to the position of the sample, where it is used to cool the sample. The two parts are vacuum insulated from each other.

The shroud has large openings on the front side and two smaller openings on the sides. These openings make it convenient to operate inside the cryostat, such as assemble parts, positioning samples and making calibrations at room temperature. On the backside of the cryostat, our home-made co-axial cable connects the sample and the measurement instrument. For the low temperature measurement, the openings of the cryostat will be covered and the cryostat can be pump down through the valve on the top. The temperature inside the cryostat is controlled by the LakeShore 340 temperature controller.

The cooling system includes a cryoliquid transfer tube and a pump. One end of the cryoliquid tube transfer is put in the Helium dewar, the other end is put in the cold finger of the cryostat. The pump and some valves constitute a pumping station, which can keep a stable pressure (less than 1 atm) in the colder finger of the cryostat. Then a continuous helium flow from the dewar to the cryostat cold finger can be formed. That is how the system is cooled down. Through adjusting the valve of the transfer tube and the pressure, we can control the cooling rate as well as the stable temperature of the system.

A home-made co-axial cable connects the sample with the PNA microwave network analyzer (NWA). A DC current source and a voltmeter are also used here. They are connected through the network analyzer and coaxial cable to the sample and therefore offer a way to measure the resistance of the sample (plus those of the contacts and wires) in a two-point-measurement. GPIB cables connect all the instruments with a computer, so they are easy to control and program for measurement. The control software was written by Labview in Windows operation system. The software automatically monitors the sample temperature and its stability. Our system has pretty good temperature stability, which can stay at the preset temperature with less than 0.005 K offset. Once the sample stables and satisfies the pre-set

condition, the software will control the PNA to the required status, and collect data automatically. The collected data will be organized and processed, then be saved to the assigned files. The above processes can be automatically repeated for different incident microwave powers and temperatures.

### **Coaxial cable sample interface**

A detailed diagram of the coaxial cable/film interface is shown in Fig. 2.5. This is the core part of the whole set up. We employ a vector network analyzer, the Agilent E8354B PNA, to measure the complex reflection coefficient  $\hat{S}_{11}$  of the thin film sample. One end of the coaxial cable is connected to the PNA, the other end is connected with the sample, which is shown in Fig. 2.5.

A direct electrical connection is made between the outer contact of the film and the outer conductor of the connector while the contact between the inner contact of the film and the inner conductor of the connector is made through a spring-loaded small pin which is inserted into the connector center conductor. A pedestal applies pressure to maintain contact through a spring which is assembled with the pedestal. Here we try to minimize the contact resistance between the center conductor and the sample. Actually, stability as a function of temperature is more important, and normally, a small contact resistance comes together with stability. Through this method, the contact resistance can be maintained within the range of  $30\text{ m}\Omega$  (which gives a contact resistivity of approximately  $5 \times 10^{-5} \Omega \text{cm}^2$ ) in the entire temperature range, 70K to 300K.

### **Some improvements made to the Corbino Apparatus**

The Corbino system in our lab was first designed by James Booth, a former student of our group. To make the system fit to my project, I made some modifications and improved the system performance.

One of the most important improvements is that the new Agilent E8364B PNA

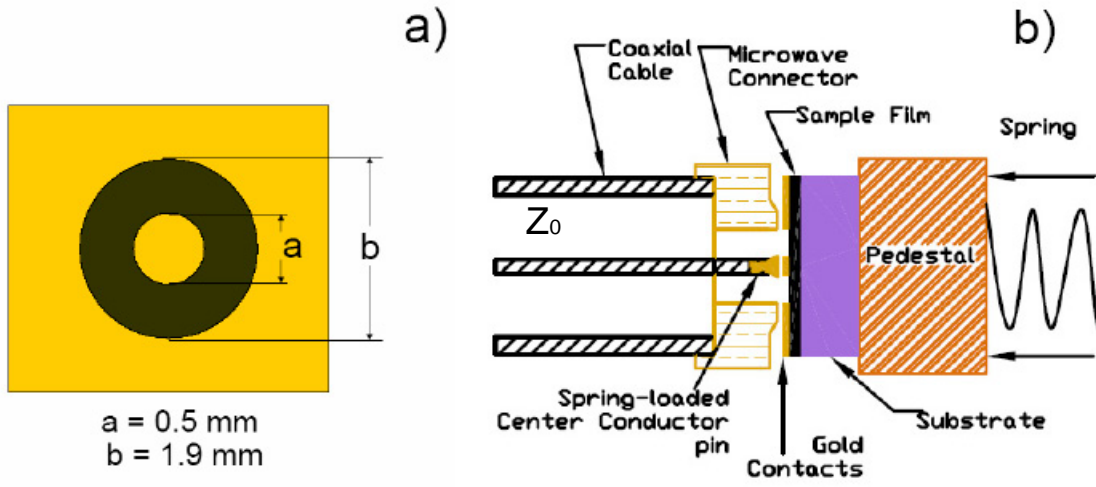


Figure 2.5: (a)Top view of the sample; (b)Cross section view of interface of sample and connector(not to scale). (To show the interface clearly a gap between the sample and microwave connector has been created)

replaced the old HP 8510C NWA. This new PNA offers greater flexibility and convenience for the measurement. The detailed advantages of the PNA over the 8510C NWA can be found from their manuals and the Agilent websites. Here I just mention some crucial ones for our experiment. First, the PNA offers a new electronic calibration method as well as the old mechanical method. Second, the PNA offers a distribution of equally-spaced measurement points in a Log-scale of frequency as well as in a Linear-scale, which gave us more data points at low frequencies for broadband measurement. This is particularly useful for looking at power-law-in-frequency dependence in my data. Third, the PNA offers a convenient instrument state recall function and fast data collection rate, which allowed investigation of properties depending on other parameters, such as microwave power.

Fig. 2.6 shows the electric calibration kit, called Ecal, which can create open, short and load standards electronically. The electronic calibration is superior to mechanical calibration. For example, it requires only one mechanical connection of connectors to finish a calibration. The fewer connecting of the calibration kit helps



Figure 2.6: The Agilent N4693A MW electronic calibration (ECal)

to protect the coaxial cable and extend its life time. Actually one connection can be used for more than one calibration. This reduces the reproducibility problem when we want to investigate properties depending on other parameters, such as different power. Most important, Ecal is more accurate and allows better calibration and better sensitivity for the measurement.

The Ecal module could not be fit inside the original cryostat of the Corbino setup, which is a Janis ST100. So I designed a new shroud which has larger inside space and big openings on the front side. These allows the Ecal module to fit inside and also makes the preparations for the experiment more convenient. In addition

the larger inside space also makes some upgrades possible, such as adding new apparatus. For example, I have designed a magnetic shielding system which can fit inside the shroud. The magnetic shields are specially designed for our Corbino probe and shroud, and are made by the Amuneal company. This magnetic shielding system includes a top-part and a bottom-part, which can be buckled together. There are small holes on the bottom-part, through which the coaxial cable can connect the sample and the PNA. Both top-part and bottom-part include three layers. It effectively decreased the external magnetic field by about 80dB. The magnetic shield also have some EMF shielding effect and reduced the noise of the measurement. In addition. it reduced thermal radiation and improved the thermal stability of the system. The thermal stability is important for our experiment. To improve it, I added some thermal links from the sample stage to the cold finger.

## 2.4 Calibration—Room Temperature

Since the measurement is performed not directly at the location of the sample, in practice the detector is normally connected with the sample through co-axial cables and connectors etc. The experimentally measured reflection coefficients includes the attenuation, multiple reflections and phase shift due to the coaxial cable system. The model, shown in Fig. 2.7 can be used to describe any microwave reflection measurement with any number of error sources according to microwave network theory [129]

In the Fig. 2.7,  $\hat{S}_{11}^{sample}$  is the actual reflection coefficient at the sample (the desired quantity) whereas  $\hat{S}_{11}^{measured}$  is the measured reflection coefficient at the detector. Here  $E_D$ ,  $E_R$  and  $E_S$  are complex error coefficients representing the directivity, the reflection tracking and the source mismatch, respectively. A general expression for the measured reflection coefficient  $\hat{S}_{11}^{measured}$  in terms of the actual reflection

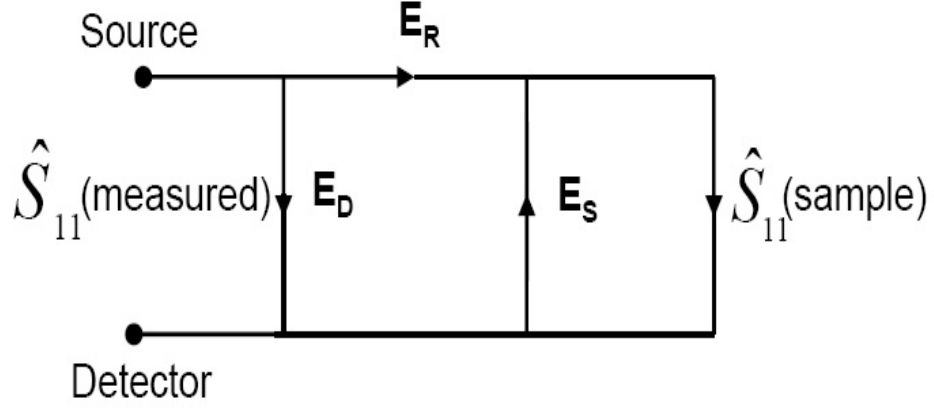


Figure 2.7: General Error model for a microwave reflection measurement

coefficient at the sample  $\hat{S}_{11}^{sample}$  is

$$\hat{S}_{11}^{measured} = E_D + \frac{E_R \hat{S}_{11}^{sample}}{1 - E_S \hat{S}_{11}^{sample}}. \quad (2.1)$$

From Eq. 2.1, the error coefficients can be determined by measuring the  $S_{11}$  of three different known loads. The normally used standards are open, short and matched load.

In our experiment, a room temperature calibration is performed first to determine initial values for the complex  $E_D$ ,  $E_R$  and  $E_S$  as functions of frequency. Our Corbino probe is fabricated from a commercial microwave connector, the Anritsu V101F . At room temperature it can be calibrated with the appropriate commercial calibration standards.

Previously we used the Agilent 85056A 2.4 mm mechanical calibration kit for the room temperature calibration. The 85056A mechanical calibration kit includes a short( $Z \cong 0$ ), an open( $Z \cong \infty$ ), and a matched load( $Z \cong 50\Omega$  corresponding to the characteristic impedance of the coaxial cable). The short and open can be easily realized to high accuracy in the whole frequency range. However, it is much harder for the matched load, particularly for high frequencies. Therefore two different kits

are used as the matched load: for lower frequencies(DC to 4GHz) a broadband load is used and for higher frequencies a sliding load is employed.

With the development of the electronic industry, Agilent developed a new generation of electrical calibration standards, called Ecal. It can simulate different standards open, short and matched load electronically under control of the computer. One need connect only one standard to the connector, then start the calibration with Ecal, the Agilent 8364B will automatically control the Ecal through a USB port, complete the calibration and save the error coefficients. Since every calibration requires only one connection, it decreases the error due to lack of connection reproducibility. The ideal values for  $E_D$ ,  $E_R$  and  $E_S$  are 0, 1 and 0 respectively. Fig. 2.8 gives the magnitude of the three error coefficients,  $E_D$ ,  $E_R$ ,  $E_S$ , obtained from the Ecal at room temperature. It shows that all three error coefficients are close to their ideal values at low frequency and deviate from the ideal value at high frequency.  $E_R$  has some frequency dependence, which decreases as the frequency increases. As for the  $E_D$  and  $E_S$ , they do not have a clear frequency dependence.

The presently performed electrical calibration is superior to mechanical calibrations used in our prior work.[92, 91] After the room temperature calibration, standard open and short connectors are put back to check the calibration quality. In the entire frequency range from 10MHz to 50GHz, after calibration the obtained  $|S_{11}|$  for both standard open and short connectors differ from 1 by less than 0.2dB. In particular for the frequency range from 30MHz to 20GHz,  $|S_{11}|$  measured for standard open and short differ from 1 by less than 0.05dB.

After the calibration, we insert a center pin into the connector and assemble it in a copper housing, inside of which the sample will be placed and measured. To check the calibration, we measured a silver disk after calibration. Fig. 2.9 shows the result of the silver disk measurement. Here the measured  $S_{11}$  should be close to the standard open with  $|S_{11}| = 1$  and  $Phase(S_{11}) = 0$ (also can be seen as  $\pi$ ). From Fig. 2.10, we found that  $|S_{11}|$  only slightly differ from 1. However the  $Phase(S_{11})$



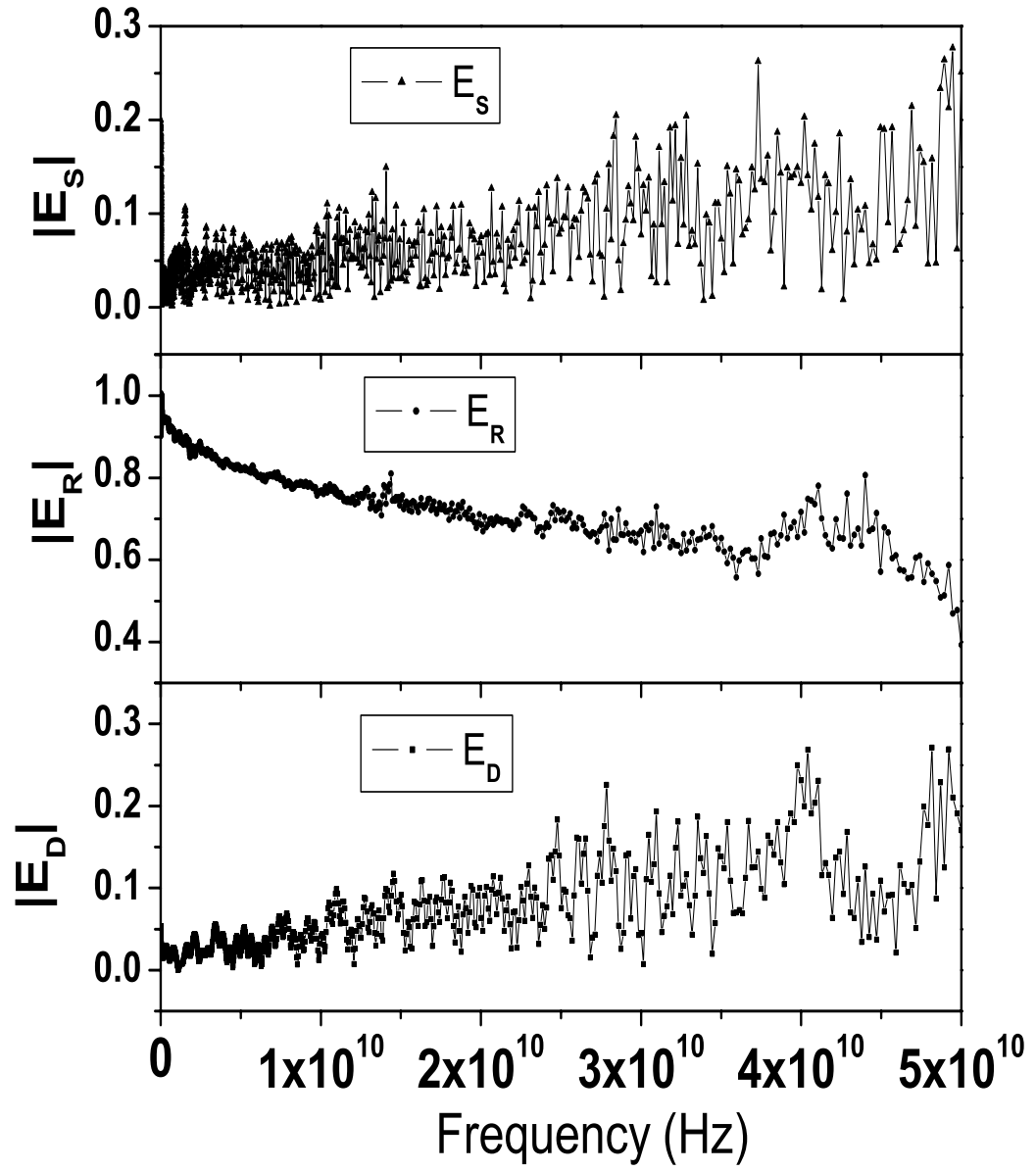


Figure 2.8: Magnitude of the error coefficients vs. frequency.

is different from zero and their difference systematically increase as the frequency increases. This behavior could be due to the fact that during the measurement on samples, a tapered pin is used to make contact between the center conductor of the V101F connector and the sample, (shown in Fig. 2.5) whereas a 2.4 mm male connector is utilized to couple to the modified V101F connector when performing the calibration. The response shown in Fig. 2.9 has been generally seen in a number of different bulk metallic samples. However, we noticed that the reflection coefficient magnitude is close to its expected value in most of the frequency range. Particularly  $|S_{11}| - 1 < 0.005$  from 10 MHz to 20 GHz. There are some peaks at high frequency, which are perhaps due to the higher order mode excitations at the pin.

Fig. 2.10 shows the magnitude and phase of  $S_{11}$  just after we assemble the pin and the housing. Here we see the measured  $S_{11}$  is close to the standard open with  $|S_{11}| = 1$ , but the  $Phase(S_{11}) = 0$  differs from zero and the difference also systematically increase as the frequency increases. This feature comes from the fact that the different connection for performing calibration and the measurement. Note here the magnitude of reflection coefficient is within 2% of its expected value over the entire 3 decades of frequency, in particular  $|S_{11}| - 1 < 0.006$  from 10 MHz to 20 GHz.

## 2.5 Calibration at Cryogenic Temperature – Standards

In many situations, we are interested in sample properties at cryogenic temperature. The previous section explained that the coaxial cable connects the sample and the test instrument PNA, which is always at room temperature. When measuring sample properties at cryogenic temperatures, there is a temperature gradient in the coaxial cable, which changes along with the sample temperature. At least

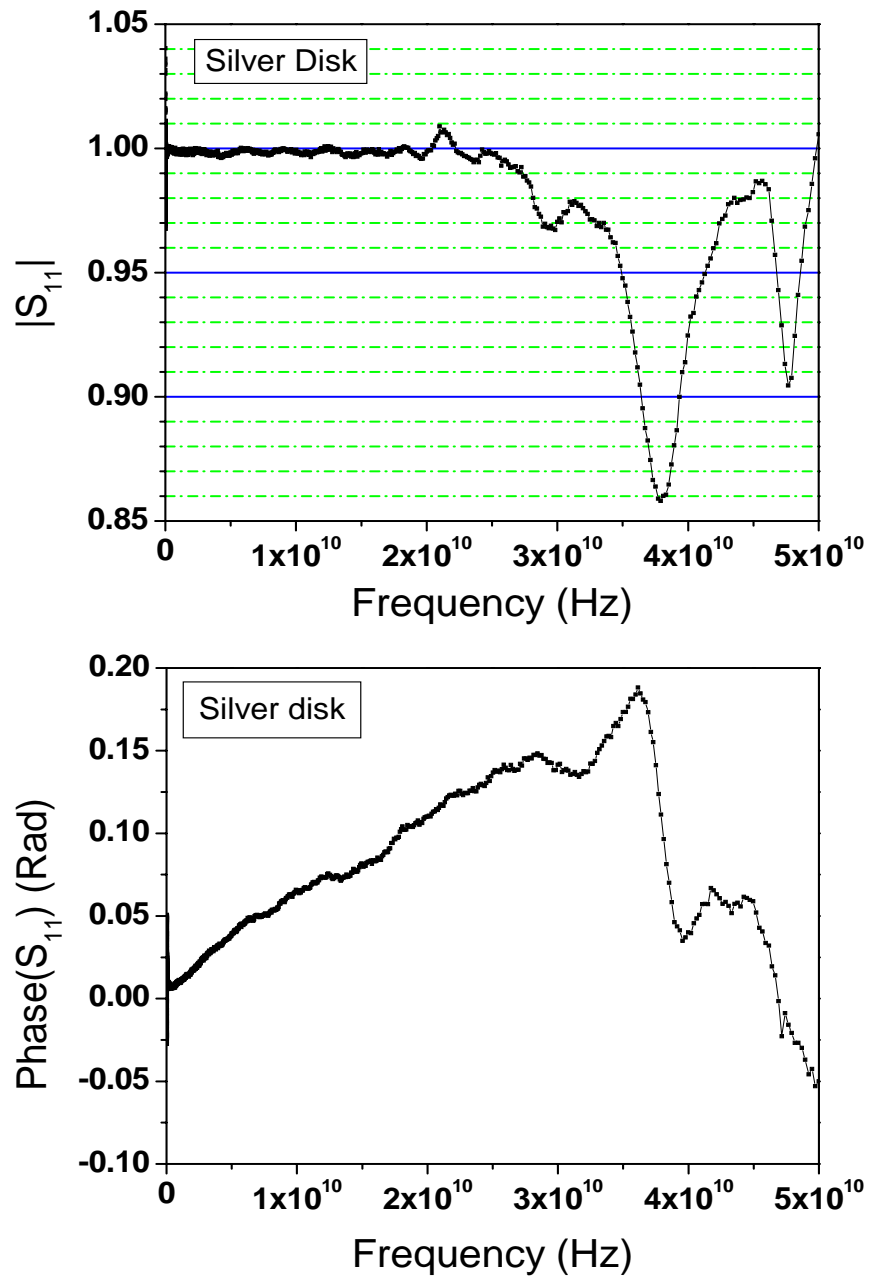


Figure 2.9: Magnitude and phase of  $S_{11}$  vs. frequency for a silver disk after calibration.

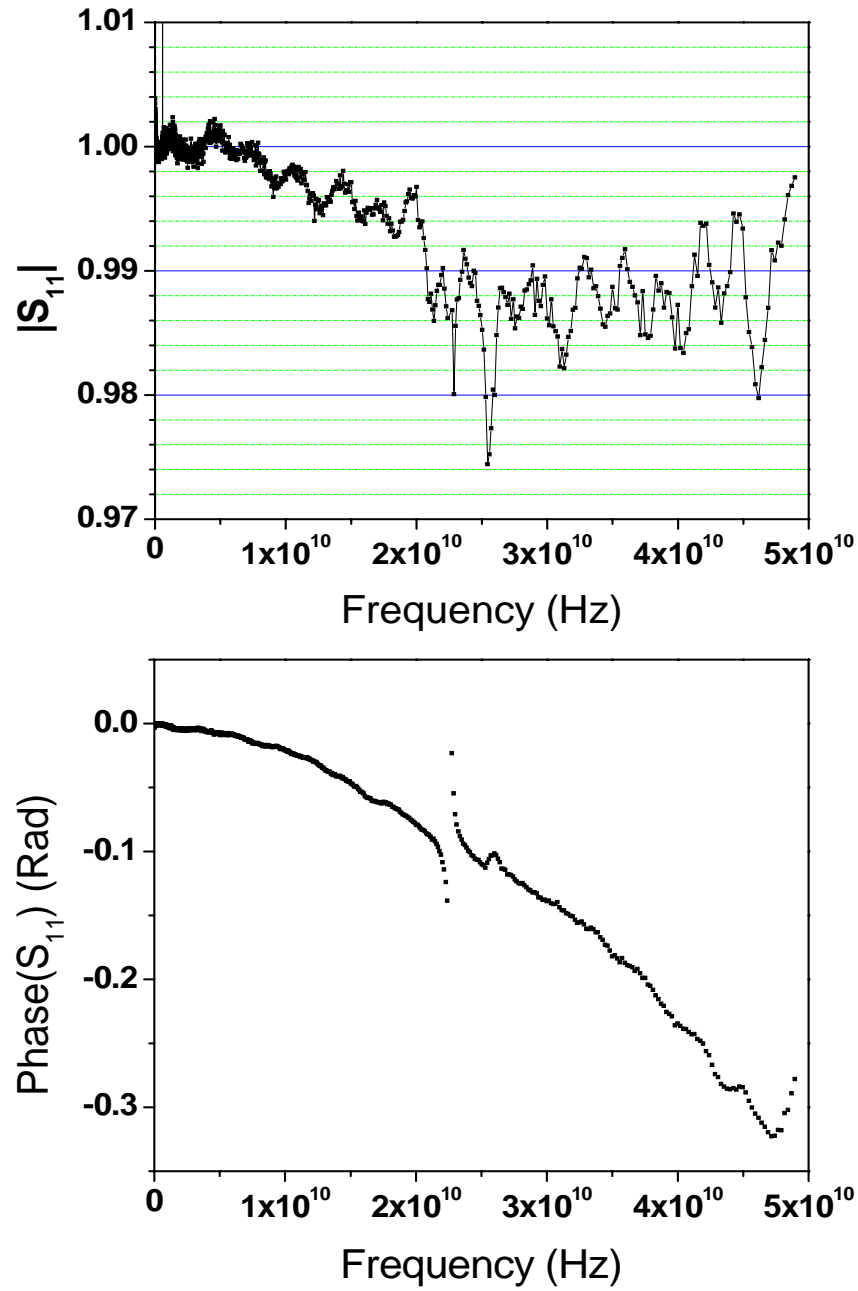


Figure 2.10: Magnitude and phase of  $S_{11}$  vs. frequency when the center pin is inserted and the house is assembled after calibration.

part of the cable is at low temperature, which also changes along with the sample temperature. The temperature change of the transmission line affects its electrical properties and this results in change of attenuation constant  $\alpha$  and phase constant  $\beta$  etc.[130] Because of the temperature dependent electrical properties of the transmission line, the variation of the sample temperature affects the accuracy of the room-temperature calibrations. So a low temperature re-calibration is necessary for the cryogenic temperature measurement.

In principle, the low temperature re-calibration procedure is similar to the above room-temperature calibration. However, both the commercial mechanical standards and the Ecal are designed for use only around room-temperature. In addition the center pin used when measuring sample made another problem for using commercial standards. Thus independent calibration standards have to be used at low temperature.

Basically the low temperature re-calibration is to re-calculate the error coefficients from measured  $\hat{S}_{11}$  with one or more standards that work well at low temperature. Historically there are two calibration methods: short-only and three standards. The short-only standards originated with former students of our group, James Booth, who had developed the Corbino reflection technique.[92, 91] The three standards calibration method was proposed by the Brom group at Leiden University (Leiden Group) and M. Stutzman *et al.* at the University of Virginia (Virginia Group). In spite of the different re-calibration methods, the core ideas are the same, choosing appropriate standards that work well at low temperature. Here I will introduce each low temperature standard first.

### 2.5.1 Low Temperature Standards: Short

The standard short should perfectly reflect all the incident electromagnetic waves. It can be realized by using bulk metals with thickness much larger than the pen-

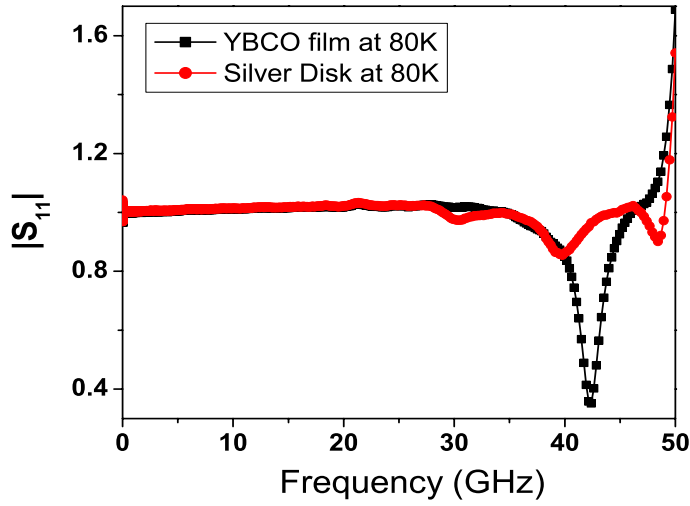


Figure 2.11: Magnitude of the reflection coefficient of a superconducting YBCO film on NGO substrate and silver disk at 80 K

etration depth. Normally high conductivity bulk metal, such as silver, copper and aluminum can be chosen as ideal standard short. Because of their high conductivity, the penetration depth is much smaller than the thickness and the ideal reflection coefficient  $\hat{S}_{11}$  should be  $-1$ . In principle, if the roughness of the surface is much less than the wave length, which always holds for our experiment, it should not make any difference for the reflection coefficient. One concern is that the surface of the standard should be flat and the two surfaces of the standard should be parallel to each other. In our experiment, to reduce the contact resistance, we use a polished silver disk as a standard short.

In our work, we are interested in properties of superconductors. At low temperatures below  $T_C$ , the sample becomes superconducting, which gives another way to perform a short circuit calibration. Superconductors have no resistance at zero frequency. For high frequencies the conductivity become finite and vanishes for frequencies below the energy gap at  $T = 0$ . In many cases the detailed frequency dependence of the microwave conductivity of superconductor is unknown, however,

the two fluid model can give some estimation when  $\omega\tau_n \ll 1$  for temperature below  $T_c$ , where  $\tau_n$  is normal electron relaxation time. From the two-fluid model  $\sigma_1 = t^4/\rho_n(T)$  and  $\sigma_2 = (1 - t^4)/\mu_0\omega\lambda_0^2$ , here  $t = T/T_c$ , the actual  $\hat{S}_{11}$  at a certain temperature can be calculated. We find the calculated  $\hat{S}_{11}$  below  $T_c$  has very little difference from the perfect short  $\hat{S}_{11} = -1$ , so it is safe to use a superconducting film well below  $T_c$  as a perfect short. For maximum accuracy, we also compared the reflection coefficient of a bulk metal and the superconducting film at low temperature. Fig. 2.11 shows the magnitude of  $\hat{S}_{11}$  for a 1500Å thick YBCO film on NGO substrate and a bulk silver disk at 80 K as well. The response of the SC film is nearly identical to that of a bulk disk conductor at 80K from 10 MHz to about 30 GHz and therefore should be appropriate to use as a short standard. At higher frequencies, they do show a difference. However, this difference comes from the irreproducibility of the center pin connection because the  $\hat{S}_{11}$  is very sensitive to the connection at very high frequency. At very high frequency, the  $|\hat{S}_{11}| > 1$ , which is due to resonant and unphysical.

### 2.5.2 Low Temperature Standards: Open

The easiest way to realize an open standard is to measure the probe without any thing attached. However, there is a spring-loaded center pin in our probe, which will protrude from the probe if we do not attach anything. As a result it is hard to tell the microwave characteristics of such a probe. Hence during the calibration measurement of the open standard we have to keep the center pin as close as possible to the place where we measure the sample. To do this a piece of a solid insulator can be used to push the center pin and prevent it from protruding out of the place where we measure the sample. However, this creates a new problem. Fig. 2.12 shows the amplitude of the measured reflection coefficient  $\hat{S}_{11}$  for three states which are: i) the microwave connector only, ii) with center pin inserted and copper housing assembled,

and iii) fused silica sample, respectively. We can see that when the center pin is inserted and the copper housing is assembled, there appear the two peaks around 22 GHz and 37 GHz, which are due to higher order mode excitations. The operating frequency of the coaxial transmission line is below the cutoff of any higher order modes in the coax, so that only the TEM mode (which has no cutoff frequency) can propagate. However, higher order modes can be excited at the location of any discontinuity in the transmission line and can make some contribution to the reflection coefficient in these regions.[93] When the insulating sample is attached, there appear more dips and they move to lower frequencies.

Stutzman *et al.* first proposed using a fused silica disk as a standard open.[128] Following this proposal, I experimentally checked different insulators as standard opens. All samples have higher order mode excitation, which makes them an imperfect open. Fig. 2.13 shows the amplitude of  $\hat{S}_{11}$  for fused silica, sapphire and a teflon disk. For smaller dielectric constant, the first higher-order mode excitation happens at higher frequencies. Hence a teflon disk is used for the standard open because of its small dielectric constant and low loss tangent.

### 2.5.3 Low Temperature Standards: Load

For the third calibration standard, a known load, a NiCr film can be used because of its temperature-independent conductivity. It was first proposed by Stutzman *et al.* of the Virginia Group. They use a NiCr film deposited on fused silica disk substrate as a known load. For a metallic film on an insulating substrate, if the film thickness is much less than the skin depth for the frequencies of interest, then the sheet resistance is governed by the thickness and the conductivity, which can be considered as frequency-independent and real in the microwave frequency range for a normal metal. The used a NiCr alloy of 80% Ni and 20% Cr, which is a well established commercially available material with almost temperature-independent



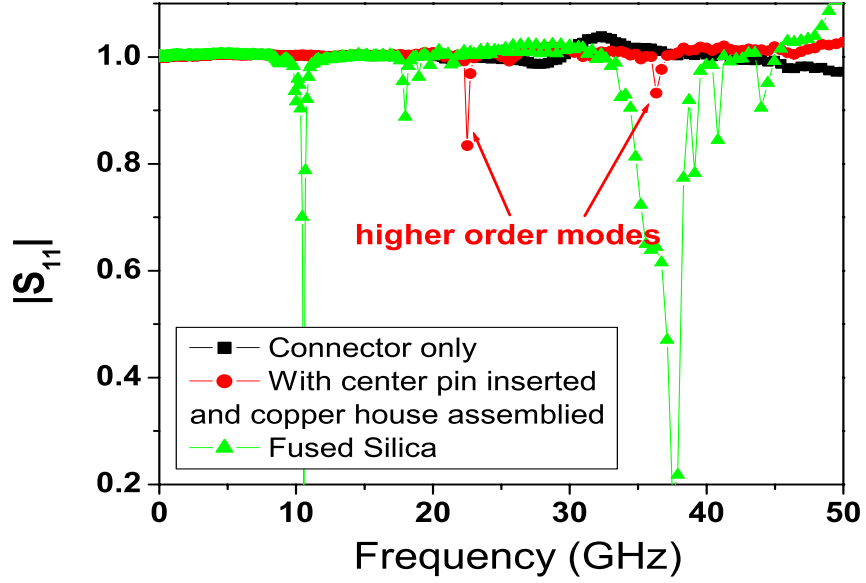


Figure 2.12: Amplitude of measured reflection coefficient for i) microwave connector only, ii) with center pin inserted and copper housing assembled, and iii) fused silica sample, respectively. (The case microwave connector only means the status that there is only the microwave connector and no center pin inserted and no copper housing assembled. See Fig. 2.5. Case ii) means we inserted the center pin and copper house assembled. Case iii) corresponds to the regular measurement, for which the sample stays on a copper pedestal and is pushed tightly with the microwave connector.)

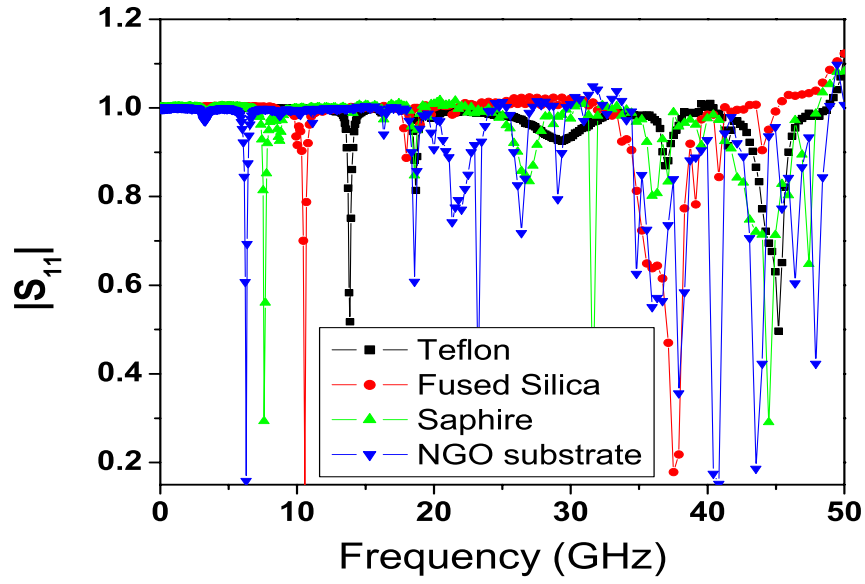


Figure 2.13: Amplitude of measured reflection coefficient at room temperature after calibration for different attached insulators: teflon, fused silica, sapphire and NGO substrate, respectively.

electrical conductivity. The impedance of a normal metal can change by more than 80% when cooled from room temperature to liquid helium temperature. However, the NiCr film will keep its same value of impedance. The NiCr films for my experiment are deposited on fused silica through the normal thermal evaporation method.

A NiCr film is a good choice as a known load. It is necessary to establish the thickness to use for the film. For a general calibration procedure the desired matched load should have an impedance of 50 Ohms. This makes the extraction of error coefficient very easy. However, with the development of computers, the error coefficients can be obtained for only choice of three distinct standards, from Eq. 2.1. In our experiment, we choose relatively thicker films as load standards. There are three reasons for this choice.

Firstly because part of the microwave signal will penetrate the film and enter the substrate, and reflected wave from the substrate can pass the film again and contribute to the measured microwave signal. For most frequencies this will not affect the validity of the calibration scheme presented here. However, there are some dips in  $\hat{S}_{11}(\omega)$  at high frequency, which are due to excited higher order mode contributions. These dips reduce in magnitude as the film thickness increases, because a smaller fraction of the signal can penetrate through the NiCr film.

Secondly it is hard to growth the very thin film uniformly distributed on the substrate. A relatively thick film is more uniform. Besides the very thin film is easily scratched, affecting its impedance.

Thirdly, because we intend to measure surface conductivity of YBCO samples, which have very small surface impedance particularly at low temperature. The surface impedance of the calibration standard close to the sample will increase the accuracy of the measurement.

Since the impedance of the load differs from 50  $\Omega$ , we need to know its actual value. One method to determine the sheet resistance of the NiCr film is to get the resistance in a standard 4-point measurement as a function of temperature and then

calculate its impedance for the Corbino geometry. This is most precise, however, it is rather arduous. The alternative way is to measure the dc resistance of the NiCr film with the Corbino setup. This is a two point measurement and the obtained resistance includes an offset, which comes from the resistance of the coaxial cable and the contact resistance between the connector and the film. I subtracted the offset from the measured dc resistance, then take the resulting value as the true impedance of the film. The disadvantage here is that the offset is poorly defined, can change up to 0.1 Ohm for different measurements and the difference can not be determined through this procedure. In the real measurement, we take the measured dc resistance of the short standard as the offset. Also we noticed that at low frequency (below 100MHz), the calibration has little temperature dependence. Hence we can extract the impedance of the NiCr film from the  $\hat{S}_{11}$  at low frequency, which should be the same as the dc resistance. In the experiment, we usually compare the extracted resistance from the low frequency  $\hat{S}_{11}$ , the resistance coming from the two-point measurement and the calculated resistance from the four point measurement result. They are normally consistent with each other. The average value can then be used as the actual load for the re-calibration.

Except for the normally used NiCr film, other materials can also be used as a known load. For example, the optimally doped superconductor well above  $T_c$  is a conductor just like normal metal, which may be used as known load. However, the substrate contribution makes the impedance complex, and we will discuss this in later sections.

## 2.5.4 Cryogenic Re-calibration Methods

### Three standard re-calibration

In the last section, we introduced the three different standards, short, open and known loads. These standards work effectively at low temperatures and their per-

formance is basically the same as the room temperature ones. From the test results of the three different standards, assuming the actual reflection coefficients of these standards are ideal ones, we can calculate the error coefficient  $E_D$ ,  $E_R$  and  $E_S$  for each frequency at different temperatures. This is the normal three standards re-calibration method, which was first proposed by Stutzman *et al.* The procedure can be found in [128].

The normal three standards re-calibration method have a variation. First perform an Ecal calibration at room temperature. Then measure the response of the three new standards at room temperature. After that, measure the three new standards at low temperature. Now re-calculate the  $E_D$ ,  $E_R$  and  $E_S$  coefficient to make the low temperature response of the three new standards equal to the room temperature response. Hence we can calibrated the error coefficients for the low temperature. This is a modified three standards re-calibration method, which was proposed by the group of Mark Lee at Virginia. For reason of comparison, we tried this varied three standards re-calibration procedure for some of our data. We found that this method is not as good as the the standard three standard re-calibration method.

### **One standard re-calibration – short only**

Using three calibration standards at low temperature is the most general procedure which gives a guideline for the validity of all other calibration methods. We have already seen in the room temperature calibration of Fig. 2.8 the magnitude of  $E_R$  is much larger than that of  $E_D$  and  $E_S$ . The three standards re-calibration shows that  $E_R$  is strongly temperature dependent, whereas  $E_S$  and  $E_D$  have much less temperature dependence. The strong temperature dependence of  $E_R$  can be explained by the changing attenuation of the copper coaxial cable that governs most of the damping of the microwave signals. The strong temperature dependence of  $E_R$  confirms the need for good temperature control and reproducibility.

Compared to  $E_R$ , the other two error coefficient  $E_D$  and  $E_S$  change very little with temperature. Considering the uncertainties of them, their temperature dependence is not significant. The small temperature dependence of  $E_S$  and  $E_D$  makes the short-only re-calibration method possible. In the short-only method, we assume that the temperature dependence effect is due to  $E_R$  alone whereas  $E_S$  and  $E_D$  are temperature independent. So from the measured result of the short standard, the  $E_R$  is re-calculated for low temperature.

### Other re-calibration methods

There are also other calibration methods. For example, if we arbitrary choose two standards, we can assume one error coefficient does not change and re-calibrate the other two. The normally used standards are open and short, which are easier to make and relatively more accurate than the known load. With two standards, we can re-calibrate two error coefficient, usually  $E_R$  and  $E_D$ . Since  $E_S$  is referred to as the source match, which arise due to the re-reflection of a portion of the signal at the measurement port, caused by the slight impedance mismatch between the detectors and the transmission line.[129] Our detector is always in room temperature, hence  $E_S$  can be considered to have very little dependence on temperature.

### Comparison of different re-calibration methods

We have introduced the different re-calibration methods. Among these methods, the normally used one are three standards re-calibration and short-only re-calibration. Marc Scheffler *et al.* compared these two calibration methods in detail.[127] According to their work, if we have a standard short, open and load and perfect reproducibility, the general three standards calibration method is ideal.

However, the existing higher order modes excitations at the high frequency range make the open and load used at low temperature deviate from the standards behavior. Compared to the standard open and load, the standard short is less affected

by the high order modes excitation. This is an advantage of the short-only re-calibration method. The second advantage of short-only re-calibration is that this method decreases the affects of irreproducibility. The short-only calibration method requires only one low-temperature calibration measurement instead of three. In this case the time for the calibration is reduced and the possible irreducibility due to operation is also reduced. In addition, the room-temperature calibration might change along with time. The shorter necessary time between calibration and measurement can reduce this error considerably. The other advantage of short-only re-calibration is its convenience.

Considering these problems, although the three standards re-calibration method is an excellent general calibration method, it is better to be treated as a starting point and serve as a guideline for other calibration methods. Comparing the short-only re-calibration and the three loads re-calibration methods, we found that the results from the two methods usually coincide with each other for low-impedance samples, such as superconductors. Thus for samples with small impedance over the complete frequency range of interest, the short-only re-calibration method is often used due to its convenience.

For our measurement, the YBCO samples have very small impedance in our temperature and frequency range of interest. Hence we used the short-only re-calibration for most of our measurements. In our experiment, we also took measurements on standard open and load at low temperature for reasons of comparison.

## Chapter 3

# Theory of Superconducting Fluctuation Effects

Over the years the basic theoretical understanding of superconductivity has been developed in a series of stages. Our experiment is based on these theoretical foundations. In this chapter, I will present some theory basic for my work. This is not intended to be a deep discussion, but rather to serve as an introduction to the relevant theoretical background.

### 3.1 Ginzburg-Landau Theory

I have briefly introduced the Ginzburg Landau theory in chapter 1. In GL theory, the free energy density is given by[15, 17, 16]

$$f_s(T) = f_n(T) + \alpha|\psi|^2 + \frac{\beta}{2}|\psi|^4 + \frac{\hbar^2}{2m^*}|\left(\frac{\hbar}{i}\nabla - q^*A\right)\psi|^2 + \frac{\mu_0 H^2}{8\pi} \quad (3.1)$$

where  $f_n(T)$  is the normal state free energy density at temperature  $T$  in zero field, and  $\alpha$  and  $\beta$  are material parameters. Near  $T_c$ ,  $\beta$  is a positive constant approximately independent of temperature and  $\alpha$  changes sign at  $T_c$ .  $A$  is the vector potential. The system will be in equilibrium when the free energy is minimized. Using the variational method we find that in zero field the free energy will be a minimum



when[15, 17, 18]

$$-\frac{\hbar^2}{2m^*\alpha_0\frac{T-T_{c0}}{T_{c0}}}\nabla^2\psi + \frac{\beta}{\alpha_0\frac{T-T_{c0}}{T_{c0}}}|\psi|^2\psi + \psi = 0. \quad (3.2)$$

Let us look at simple case first, if there is no spatial variations( $|\nabla\psi| = 0$ ), then

$$f_s(T) - f_n(T) = (\alpha|\psi|^2 + \frac{1}{2}\beta|\psi|^4) \quad (3.3)$$

Above  $T_c$ ,  $\alpha > 0$  and there is a minimum when  $|\psi|^2 = n_s = 0$ . Here  $f_s > f_n$ , which corresponds to the normal state, thus the density of superconducting electrons is zero.

On the other hand, at temperature below  $T_c$ ,  $\alpha < 0$ , then the free energy has a minimum when

$$|\psi|^2 \equiv |\psi_\infty|^2 = -\frac{\alpha}{\beta}. \quad (3.4)$$

This equilibrium value is conventionally called  $\psi_\infty$ . The free energy difference vs. order parameter magnitude is sketched in Fig. 3.1.

So at  $T_{c0}$ ,  $\alpha$  must change sign so that  $|\psi|^2 = n_s$  goes to zero as  $T \rightarrow T_{c0}$ . Here we can take a Taylor expansion for  $\alpha$  around  $T_{c0}$ , to lowest order

$$\alpha(T) = \alpha_0\frac{T - T_{c0}}{T_{c0}}. \quad (3.5)$$

This is strictly true only near  $T_{c0}$ .

Now put back Eq. 3.4 and 3.5 into the Eq. 3.2 and we can obtain the free energy density around  $T_{c0}$ . For  $T < T_{c0}$

$$f_s = f_n - \frac{\alpha_0^2}{2\beta}\left(\frac{T - T_{c0}}{T_{c0}}\right)^2, \quad (3.6)$$

and for  $T \geq T_{c0}$ ,

$$f_s > f_n \quad (3.7)$$

It is clear that the superconducting state has a lower free energy density than the normal state for  $T < T_{c0}$ . The free energy density in the superconducting state can be written as[19]

$$f_s = f_n - \frac{1}{2}\mu_o H_c(T)^2, \quad (3.8)$$

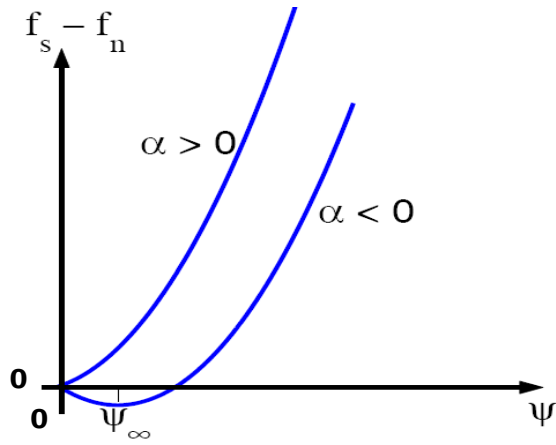


Figure 3.1: The free energy difference when  $\alpha > 0$  and  $\alpha < 0$ . If  $\alpha > 0$ , then the equilibrium value is  $|\psi|^2 = n_s = 0$  (the normal state). For  $\alpha < 0$ ,  $|\psi_\infty|^2 = -\frac{\alpha}{\beta}$  in the superconducting state.

which defines the thermodynamic critical field  $H_c(T)$ .<sup>1</sup> This is the same  $H_c(T)$  as in Sec. 1.2, and thus is directly measurable (at least for type I superconductors). The difference in energy between the normal and superconducting states is called the condensation energy.<sup>2</sup> The condensation energy allows us to make the connection between the parameters  $\alpha_0$ ,  $\beta$ , and  $H_c(T)$ , as

$$\alpha_0^2/\beta = \mu_o H_c^2(0). \quad (3.9)$$

In order to relate both  $\alpha_0$  and  $\beta$  to measurable quantities, another equation is needed.

We go back to zero field, considering an order parameter that varies in space. For

---

<sup>1</sup>Here we use mks units, following Ref. [19] rather than Refs. [15] and [17].

<sup>2</sup>The condensation energy and the source of this energy can be confusing. See Appendix B of Ref. [18] for a valiant attempt to sort out the various thermodynamic free energies, or Refs. [15] and [19].

this case,  $\psi(\mathbf{r})$  will change to minimize the free energy. We can use the variational method and find that the free energy will be a minimum when [15, 17, 18]

$$-\frac{\hbar^2}{2m^*\alpha_0\frac{T-T_{co}}{T_{co}}}\nabla^2\psi + \frac{\beta}{\alpha_0\frac{T-T_{co}}{T_{co}}}|\psi|^2\psi + \psi = 0. \quad (3.10)$$

This reduces to Eq. 3.4 for spatially homogenous order parameters, as expected.

Equation 3.10 predicts that changes in  $\psi$  occur over a characteristic length  $\xi$ . To see this we substitute

$$\psi(\mathbf{r}) = \psi_\infty + \delta\psi(\mathbf{r}) \quad (3.11)$$

into Eq. 3.10 and solve for  $\delta\psi(\mathbf{r})$ . This leads to the following equations for  $\delta\psi$ ;

$$\nabla^2(\delta\psi) = \left(\frac{2m^*\alpha_o|T - T_{co}|}{\hbar^2 T_{co}}\right)(\delta\psi) \quad \text{for } T > T_{co}, \quad (3.12)$$

$$\nabla^2(\delta\psi) = \left(\frac{4m^*\alpha_o|T - T_{co}|}{\hbar^2 T_{co}}\right)(\delta\psi) \quad \text{for } T < T_{co}. \quad (3.13)$$

These equations can be solved for the general solutions in the one-dimensional case

$$\delta\psi \propto e^{\pm x\sqrt{\frac{2m^*\alpha_o|T - T_{co}|}{\hbar^2 T_{co}}}} \quad \text{for } T > T_{co}, \quad (3.14)$$

$$\delta\psi \propto e^{\pm x\sqrt{\frac{4m^*\alpha_o|T - T_{co}|}{\hbar^2 T_{co}}}} \quad \text{for } T < T_{co}. \quad (3.15)$$

Thus, we can assign the following length scales

$$\xi_+ = \sqrt{\frac{\hbar^2 T_{co}}{2m^*\alpha_o|T - T_{co}|}} \quad \text{for } T > T_{co}, \quad (3.16)$$

$$\xi_- = \sqrt{\frac{\hbar^2 T_{co}}{4m^*\alpha_o|T - T_{co}|}} \quad \text{for } T < T_{co}. \quad (3.17)$$

Here we identify the correlation length  $\xi$ . This is the characteristic length over which the order parameter  $\psi$  is uniform. In a pure superconductor far below  $T_c$ ,  $\xi(T) \approx \xi(0)$ , which is the temperature-independent Pippard coherence length; however near  $T_c$ ,  $\xi(T)$  diverges as  $(T_c - T)^{-1/2}$ .

There is another important length in superconductors, called the magnetic *penetration depth*. Superconductors in a magnetic field below  $H_c$  (or  $H_{c1}$  for type II)

expel the field from their bulk. This field does not drop to zero suddenly at the surface, but rather decays exponentially to zero inside the bulk. The decay constant gives the typical length that fields can penetrate inside a superconductor (hence the name). The penetration depth is also related to  $\alpha$  and  $\beta$  via[19]

$$\lambda^2 = -\frac{\beta \mu_o m^*}{\alpha (q^*)^2}, \quad (3.18)$$

where  $q^*$  is the charge of the superconducting particles, and  $m^*$  is their mass.

From the coherence length and the penetration depth, we can define the GL parameter  $\kappa$ [15, 19]

$$\kappa = \frac{\lambda}{\xi}. \quad (3.19)$$

It was Abrikosov who first noted that the GL parameter separates type I and type II superconductors. If  $\kappa \ll 1$ , then the coherence length is much greater than the penetration depth. This is the case for most conventional superconductors, and for all type I superconductors. On the other hand, when  $\kappa \gg 1$ , then the fields penetrate to distances larger than the coherence length. This leads to magnetic field penetrating in flux quanta, and type II superconductivity. The switch from type I to type II occurs at  $\kappa = 1/\sqrt{2}$ .

We can combine Eqs. 3.9, 3.16, and 3.18 to determine  $H_c$  in terms of measurable quantities  $\xi$  and  $\lambda$ [19]

$$H_c = \frac{\Phi_o}{2\sqrt{2}\pi\mu_o\lambda\xi}, \quad (3.20)$$

where we have set  $q^* = 2e$ . For type II superconductors, the above equation is not particularly useful, as nothing occurs at the thermodynamic critical field  $H_c$ . However, we can relate the thermodynamic critical field to the measured upper critical field in type II materials by  $H_{c2} = \sqrt{2}\kappa H_c$ [11, 15]. When combined with Eq. 3.20 this gives

$$H_{c2} = \frac{\Phi_o}{2\pi\mu_o\xi^2}. \quad (3.21)$$

Near  $T_{c0}$  we find that

$$H_{c2}(T) \sim \left| \frac{T - T_{c0}}{T_{c0}} \right|. \quad (3.22)$$

## 3.2 Gaussian Fluctuation

GL theory is a mean field theory, which successfully describes the phenomenology of equilibrium superconductivity. It works well when the order parameter varies slowly or not at all. However, in any material there are always energy fluctuations on the order of  $k_B T$ . For a second-order phase transition, as there is not latent heat, near  $T_c$  the fluctuations can be both large and rapid. The basic GL theory ignores these fluctuations and can not describe such properties of the system, particularly around  $T_c$ .

In Chap. 1, I have introduced the concept of fluctuation and how fluctuations affect the properties of the system around  $T_c$ . To describe these behaviors, fluctuations have been treated as perturbation and incorporated into GL theory. These are called "Gaussian" fluctuations.

In conventional superconductors, the Gaussian fluctuation predictions successfully describe the behavior of physical properties of the superconductor, including diamagnetism, specific heat, and conductivity etc. Here I do not go through the full derivation of the Gaussian fluctuations, but focus on how the gaussian fluctuations affect the conductivity near  $T_c$ , which is the main concern of this thesis.

### 3.2.1 Direct Contribution—Aslamazov-Larkin term

Fluctuations create excess conductivity above  $T_c$ , also called paraconductivity. Firstly we consider the excess conductivity attributable to the direct acceleration of the superconducting pairs created by fluctuations above  $T_c$ . We assume the normal DC conductivity is given by

$$\sigma_n = \frac{ne^2}{m}\tau \quad (3.23)$$

where  $\tau$  is the mean scattering time of the normal electrons in transport properties, and  $n$  is their number density(per unit volume). By analogy, we might expect the

superconducting fluctuations to contribute an additional term

$$\sigma' = (e^{*2}/m^*) \sum_k < |\psi_k|^2 > \tau_k/2 \quad (3.24)$$

Here  $\sum < |\psi_k|^2 >$  correspond to the the number density of the fluctuated superconducting electrons of all spatial frequencies. The sum over wave numbers  $k$  can be converted to an appropriate integration depending on the dimensionality of the sample :

$$\int \frac{d^3k}{(2\pi)^3} \text{ for bulk material(3D)}$$

$$\frac{1}{d} \int \frac{d^2k}{(2\pi)^2} \text{ for thin films(2D) (thickness } d \ll \xi)$$

$$\frac{1}{S} \int \frac{d^k}{(2\pi)} \text{ for filaments(1D) (cross-sectional area } S \ll \xi^2).$$

The results are:

$$\sigma_{3DAL}^{DC} = \frac{1}{32} \frac{e^2}{\hbar \xi(0)} t^{-1/2} \quad (3.25)$$

$$\sigma_{2DAL}^{DC} = \frac{1}{16} \frac{e^2}{\hbar d} t^{-1} \quad (3.26)$$

$$\sigma_{1DAL}^{DC} = \frac{\pi}{16} \frac{e^2 \xi(0)}{\hbar S} t^{-3/2} \quad (3.27)$$

$$(3.28)$$

where  $\xi(0)$  is the coherence length at 0 K, and  $t = |T/T_c - 1|$ . Moreover, for samples of intermediate dimensionality, we can interpolate between the above forms and get the results. For the high- $T_c$  superconductors, because of the layered nature and strong anisotropy, Lawrence and Doniach created the L-D model for the fluctuation contribution to the dc conductivity, which essentially interpolates between the 2D and the 3D forms above.[131]

$$\sigma_{LD}^{fl} = \frac{e^2}{16\hbar dt} \frac{1}{[1 + \frac{1}{t} (\frac{2\xi_c(0)}{d})^2]^{1/2}} \quad (3.29)$$

where here  $\xi_c(0)$  is the c-axis correlation length at zero temperature, and  $d$  is the inter-layer separation. As can be seen from Eq. 3.29, when the c-axis correlation length is much less than the inter-layer spacing ( $\xi_c(0) \ll d$ ), the fluctuation conduc-

tivity reduces to the 2D Gaussian expression Eq. 3.26, while in the opposite limit, when  $\xi_c(0) \gg d$ , Eq. 3.29 reduces to the 3-D form(Eq. 3.25).

The above results were first derived from the microscopic theory by Aslamzov and Larkin [55]. The results can also be calculated within the GL theory through calculation of the dynamical conductivity  $\sigma_\omega$ , and then taking the dc limit. This was done by Abrahams and Woo[41] and Schmid in 1968[42].

In order to calculate the effect of fluctuations of the order parameter on the dynamical conductivity, it is necessary to include a time dependence in the Ginzburg-Landau free energy, since the excess conductivity due to fluctuations will be directly proportional to the lifetime of the fluctuations. The simplest time dependent generalization of GL equation(TDGL) neglecting electromagnetic potentials is given by:

$$\alpha\psi + \beta|\psi|^2\psi - \frac{\hbar^2}{2m^*}\nabla^2\psi = -\gamma\hbar\frac{\partial}{\partial t}\psi \quad (3.30)$$

The linearized TDGL equation is then obtained by neglecting the non-linear term  $\beta|\psi|^2\psi$ , and is given by

$$\frac{\partial}{\partial t}\psi = -\frac{1}{\tau}(1 - \xi^2\nabla^2)\psi \quad (3.31)$$

The temperature-dependent relaxation time of the  $k = 0$  mode is given by

$$\tau_{GL} = \frac{\hbar\gamma}{\alpha} = \frac{\tau_0}{|t|}, \quad (3.32)$$

where  $t = (T - T_c)/T_c$  is the reduced temperature.

From the above formalism, one can calculate the contribution to the conductivity of superconducting fluctuations. Such a calculation has been carried out by Abrahams and Woo[41], Schmid in 1968[42] and later by Dorsey *et al.*[132] The results for the fluctuation conductivity ( $\sigma = \sigma_1 - i\sigma_2$ ) depend upon the dimensionality of the system, and are given in three dimensions by:

$$\sigma_1^{3D} = \sigma_{DC}^{3D} \cdot F_1^\pm(\omega\tau) \quad (3.33)$$

$$\sigma_2^{3D} = \sigma_{DC}^{3D} \cdot F_2^\pm(\omega\tau) \quad (3.34)$$

Here  $F_1^\pm(\omega\tau)$  and  $F_2^\pm(\omega\tau)$  describe the frequency dependence above (+) and below (-)  $T_c$ , and  $\sigma_{DC}$  is the dc fluctuation conductivity given by Eq. 3.25.

In three dimensions, the frequency dependent fluctuations  $F^+$  are given for  $T > T_c$  by

$$F_1^+(\omega\tau) = \frac{8}{3(\omega\tau)^2} [1 - (1 + (\omega\tau)^2)^{3/4} \cdot \cos(\frac{3}{2}\tan^{-1}(\omega\tau))] \quad (3.35)$$

$$F_2^+(\omega\tau) = \frac{8}{3(\omega\tau)^2} [-\frac{3}{2}\omega\tau + (1 + (\omega\tau)^2)^{3/4} \cdot \sin(\frac{3}{2}\tan^{-1}(\omega\tau))] \quad (3.36)$$

The frequency dependent fluctuations  $F^-$  for  $T < T_c$  for three dimensions are given as follow:

$$F_1^-(\omega\tau) = \frac{8}{3(1 + (\omega\tau)^2)} [\sqrt{2} - (1 + (\omega\tau)^2)^{-1/4} \cdot \{(1 - (\omega\tau)^2) \cdot \mathbf{X} + 2\omega\tau\mathbf{Y}\}] \quad (3.37)$$

$$F_2^-(\omega\tau) = \frac{8\omega\tau}{3(1 + (\omega\tau)^2)} [-\sqrt{2} + 2(1 + (\omega\tau)^2)^{-1/4} \cdot \{\mathbf{X} - \frac{(1 - (\omega\tau)^2)}{2\omega\tau} \cdot \mathbf{Y}\}] \quad (3.38)$$

where  $\mathbf{X} = \cos[\frac{1}{2} \cdot \tan^{-1}(\omega\tau)]$ , and  $\mathbf{Y} = \sin[\frac{1}{2} \cdot \tan^{-1}(\omega\tau)]$ . The fluctuation relaxation time  $\tau$  is given by

$$\tau = \frac{\pi\hbar}{16k_B T_c t} \quad (3.39)$$

In two dimensions the result for the fluctuation conductivity are given by the following

$$\sigma_1^{2D} = \sigma_{DC}^{2D} \cdot G_1^\pm(\omega\tau) \quad (3.40)$$

$$\sigma_2^{2D} = \sigma_{DC}^{2D} \cdot G_2^\pm(\omega\tau) \quad (3.41)$$

where once again the function  $G^\pm(\omega\tau)$  describe the frequency dependence, and the two-dimensional dc fluctuation is given by Eq. 3.26, in which  $d$  is the film thickness. The frequency dependent functions  $G^+$  for  $T > T_c$  in two dimensions are

$$G_1^+(\omega\tau) = \frac{1}{\omega\tau} [\pi - 2 \tan^{-1}(\frac{1}{\omega\tau}) - \frac{1}{\omega\tau} \ln(1 + (\omega\tau)^2)] \quad (3.42)$$

$$G_2^+(\omega\tau) = \frac{1}{\omega\tau} [-2 + \frac{\pi}{\omega\tau} - \frac{2\pi}{\omega\tau} \tan^{-1}(\frac{1}{\omega\tau}) + \ln(1 + (\omega\tau)^2)] \quad (3.43)$$



while the corresponding expressions for  $T < T_c$  are

$$G_1^-(\omega\tau) = \frac{\omega\tau}{1 + (\omega\tau)^2} [\pi - 2 \tan^{-1}(\frac{1}{\omega\tau}) - \frac{1}{\omega\tau} \ln(\frac{1 + (\omega\tau)^2}{4})] \quad (3.44)$$

$$G_2^+(\omega\tau) = \frac{\omega\tau}{1 + (\omega\tau)^2} [\pi - 2 \tan^{-1}(\frac{1}{\omega\tau}) + \omega\tau \cdot \ln(\frac{1 + (\omega\tau)^2}{4})] \quad (3.45)$$

The fluctuation relaxation time is the same in two dimensions, still  $\tau = \frac{\pi\hbar}{16k_B T_c t}$ .

### 3.2.2 Indirect Contribution– MT-term

The AL predictions were in good agreement with experiment results on dirty superconductors. However, for cleaner films, the predicted universal behavior failed to appear. Maki and Thompson investigated the difference between the AL prediction and the experimental results. As for the additional conductivity in the cleaner case, they proposed that it comes from the indirect effect of the fluctuations on the quasiparticle conductivity. The direct acceleration of the fluctuation-induced superconducting pairs corresponds to the AL contribution. These superconducting fluctuations then decay into pairs of quasiparticles of nearly opposite momenta. By time-reversal symmetry, the quasiparticles remain in a state of small total momentum even after scattering from an impurity potential, and continue to be accelerated much as they were while they were a superconducting fluctuation. The quasiparticle lifetime is limited, however, in several ways, ultimately including decay back into a superconducting fluctuation, just as the superconducting fluctuation lifetime is limited by decay into quasiparticles.[51]

The calculation of the indirect(Maki-Thompson) contribution can be found in many papers. Here I will not go to the detail and derive it but just give the results as follows [56] [57]:

$$\sigma_{DC}^{3DMT} = \frac{1}{8} \frac{e^2}{\hbar \xi_0} t^{-1/2} \quad (3.46)$$

$$\sigma_{DC}^{2DMT} = \frac{e^2}{8\hbar d} \frac{1}{\epsilon - \delta} \ln(\frac{t}{\delta}) \quad (3.47)$$

$$\sigma_{DC}^{1DMT} = \sigma_{1D}^{AL} 4(t/\delta)[1 + (t/\delta)^{1/2}]^{-1} \quad (3.48)$$

where  $\delta$  is the pair-braking parameter introduced to avoid an un-physical divergence of conductivity at  $T > T_c$  in the 2D and 1D cases. The MT term explained a larger magnitude and an anomalous temperature dependence of the fluctuation conductivity observed in cleaner superconductors[51].

For a clean superconductor, not only does the DC fluctuation conductivity have an indirect MT-term, the frequency dependent conductivity should also have an MT-term, which was calculated by Aslamazov and Varlamov [59]. Starting from a layered superconductor they found, in the 2D and 3D limits, that the contribution of the MT-term should be added to the AL-term. Then the frequency dependent fluctuation contribution should be written as:

$$\sigma^{2DAL+MT}(\omega) = \sigma_{DC}^{2DAL} S^{2DAL+MT}\left(\frac{\pi\hbar\omega}{16k_B T_c t}\right), \quad (3.49)$$

$$\sigma^{3DAL+MT}(\omega) = \sigma_{DC}^{3DAL} S^{3DAL+MT}\left(\frac{\pi\hbar\omega}{16k_B T_c t}\right). \quad (3.50)$$

where

$$ReS^{2DAL+MT}(x) = ReS^{2DAL}(x) + \frac{2\pi x - 2 \ln 2x}{1 + 4x^2}, \quad (3.51)$$

$$ImS^{2DAL+MT}(x) = ImS^{2DAL}(x) + \frac{\pi + 4x \ln 2x}{1 + 4x^2}, \quad (3.52)$$

$$ReS^{3DAL+MT}(x) = ReS^{3DAL}(x) + \frac{4 - 4x^{1/2} + 8x^{3/2}}{1 + 4x^2}, \quad (3.53)$$

$$ImS^{3DAL+MT}(x) = ImS^{3DAL}(x) + \frac{4x^{1/2} - 8x + 8x^{3/2}}{1 + 4x^2}. \quad (3.54)$$

The  $x$  in above equations denotes  $\frac{\pi\hbar\omega}{16k_B T_c t}$ .

### 3.2.3 Ginzburg Criterion

In the last section, Gaussian fluctuations were incorporated into GL theory. The above treatment of the fluctuations is valid as long as the order parameter is small enough so that the non-linear terms in the GL equation can be safely neglected. However, as temperature grows closer to the critical temperature, the fluctuations become larger. Finally in a region very close to the critical temperature, where

the fluctuations can cause the order parameter (and the density of superconducting electrons) vary greatly over small distances and short times, which means  $|\delta\psi|$  is large and comparable to  $|\psi|$ , hence the fluctuations can no longer be treated as perturbations to mean-field theory.

The following argument can help us estimate when the GL theory breaks down. The typical size of a fluctuation,  $\xi$ , will carry an approximate energy  $k_B T_{c0}$ . When this energy density,  $k_B T_{c0}/\frac{4}{3}\pi\xi^3$ , becomes greater than the condensation energy  $\frac{1}{2}\mu_0 H_c^2$ , we can expect the GL theory to break down. From the Eq. 3.16, Eq. 3.21 and Eq. 3.22, we find that GL theory breaks down when

$$|T - T_{c0}| < 72 \frac{\pi\mu_o\kappa^4}{e^2\Phi_o^3 H_{c2}(0)} k_B^2 T_{c0}^3, \quad (3.55)$$

where  $H_{c2} = \sqrt{2}\kappa H_c$ .

A more exact derivation can be obtained from the correlation function  $\Gamma(r)$ , which function tells us how well correlated two regions with a distance  $r$  apart are. Here I will not go to the detailed derivation, but just give the result: [12, 11]

$$|T - T_{c0}| < \frac{\pi\mu_o\kappa^4}{2e^2\Phi_o^3 H_{c2}(0)} k_B^2 T_{c0}^3. \quad (3.56)$$

With the above criterion, we can estimate the size of the critical regime. For conventional superconductors,  $\kappa \approx 1$ ,  $T_{c0} \approx 10$  K, and  $\mu_o H_{c2}(0) \approx 1$  T[11]. Thus, GL theory breaks down only when  $|T - T_{c0}| < 1 \times 10^{-11}$  K, which is impossible to access experimentally. This is why GL theory works well for conventional superconductors.

For the high-temperature superconductors, the situation is very different[11]. Actually due to the anisotropy of these superconductors, the criterion becomes more complicated. The Eq. 3.56 is modified to become[54]

$$|T - T_{c0}| < \frac{1}{\gamma^2} \frac{\pi\mu_o\kappa^4}{2e^2\Phi_o^3 H_{c2}(0)} k_B^2 T_{c0}^3, \quad (3.57)$$

where  $\gamma = \xi_c/\xi_{ab}$ , is the ratio of the coherence lengths along the c and a and b axes. For YBCO,  $\kappa \approx 120$ ,  $\gamma \approx 0.2$ ,  $T_{c0} \approx 90$  K, and  $\mu_o H_{c2}(0) \approx 90$  T[18]. This gives

$|T - T_{c0}| < 0.32$  K. Thus, GL theory fails within a 0.6 K window centered about  $T_{c0}$ , which can be accessed easily experimentally.

### 3.3 Scaling theory

#### 3.3.1 Scaling Theory and Universality

The Ginzburg criterion tells us that in the critical regime, which is very close to critical temperature, the fluctuations are large and the mean field theory breaks down. To describe the system, we need to use scaling theory. In this section, I will focus on the general scaling theory, which utilizes dimensional arguments to obtain a form for the conductivity.

The general scaling theory for the conductivity starts with the assumption that the correlation length  $\xi$  diverges as  $T \rightarrow T_c(t \rightarrow 0)$  as :

$$\xi \sim |t|^{-\nu}, \quad (3.58)$$

where once again  $t \equiv \frac{T-T_c}{T_c}$  is the reduced temperature. Considering a real order parameter with  $\mathbf{n}$  components,  $S = (S_1, \dots, S_q, \dots, S_n)$ , where  $q$  denotes a direction. The basic cases are:  $\mathbf{n}=1$ : Ising spins,  $\mathbf{n}=2$ : planar spins,  $\mathbf{n}=3$ : Heisenberg spins. , the spatial correlations of the order parameter can be described as:

$$\langle S_{iq} S_{jq} \rangle = f((i-j)/\xi), \quad (3.59)$$

where  $i$  and  $j$  label the sites of a D-dimensional hypercubic lattice with M sites. The above equation becomes long-ranged as temperature approaches  $T_c$ . At criticality( $t = 0$ ), since the correlation length diverges, which indicates that the order parameter correlations decay as a power law, which has no intrinsic length scale. Then we can denote the power law by an exponent  $\eta$ :

$$\langle S_{iq} S_{jq} \rangle \propto |(i-j)|^{-D-2+\eta}, \quad (3.60)$$

where  $D$  denotes the spatial dimensionality. There are other important critical exponents. The normally used critical exponents are  $(\alpha, \beta, \gamma, \delta, \nu, \eta)$ , which characterize the critical behavior close to the critical point. The definitions and relations between the critical exponents are carefully discussed in [52, 133]. They are not independent of one another. There hold four relations:

$\alpha + 2\beta + \gamma = 2$ : Rushbrook scaling law

$\gamma = \beta(\delta - 1)$ : Widom scaling law

$\gamma = \nu(2 - \eta)$ : Fisher scaling law

$2 - \alpha = D\nu$ : Josephson scaling law

So we can see that only two exponents are then needed in order to determine all the other exponents except for the case that we know  $\alpha$  and  $\nu$ .

One of the important properties here is Universality. It turns out that systems which belong to the same universality class have the same complete set of critical exponents. Since the correlation length  $\xi$  becomes large upon approaching  $T_c$  and diverges at  $T_c$ , it is believed that details such as the lattice structure do not affect the universal properties. The universality classes have three basic cases:

- $D, n = 3$ , Heisenberg spins  $\vec{S} = (S_x, S_y, S_z)$  in  $D$  spatial dimensions;
- $D, n = 2$ , planar spins  $\vec{S} = (S_x, S_y, 0)$  (XY-model), superfluids, superconductors in  $D$  spatial dimensions;
- $D, n = 1$ , Ising spins  $\vec{S} = (0, 0, S_z)$  in  $D$  spatial dimensions;

In chapter 1 we have shown that the specific heat exhibits a singularity of the form:

$$C = \frac{A^\pm}{\alpha} |t|^{-\alpha}, \quad \text{where } \pm = \text{sign}(t), \quad (3.61)$$

Additionally, the penetration depth and the diamagnetic susceptibility also show critical behavior as:

$$\frac{1}{\lambda_i^2} = \frac{1}{\lambda_{i,0}^2} t^\nu, \quad i = \perp, \parallel, \quad (3.62)$$

$$\chi_z \propto |t|^{-\nu}. \quad (3.63)$$

The theoretical and experimental work on thermal dynamic properties have shown that the zero-field normal-superconducting transition is in the static universality class of the three-dimensional, complex order-parameter (3D XY) model. In the vicinity of the critical point, dynamical properties also have anomalous behaviors, such as transport coefficients, relaxation rates, and the response to time dependent perturbations. These anomalous properties depend on the equations of motion and are derivable from time-dependent correlation functions.

For dynamical properties, the relaxation time  $\tau$  characterizes the relaxation of the system to equilibrium. As with the correlation length, this relaxation time diverges as criticality is approached, and there is also a power law dependence on reduced temperature:

$$\tau_c \propto \xi^z \propto |t|^{-\nu z},$$

where  $z$  is called the dynamic critical exponent. The value of  $z$  depends on the conserved quantities (order parameter, energy, etc). Thus, dynamics introduce one new universal exponent  $z$ . There is considerable evidence that the static critical behavior of the cuprates belongs to the 3D-XY ( $n=2$ ) universality class of the  $\lambda$ -transition in superfluid helium. As for the dynamical properties, the universality of the  $\lambda$  transition in  $^4\text{He}$  is that of an  $n = 2$  order parameter coupled to a conserved density which gives rise to a propagating mode in the ordered state[52]. This is model E dynamics in the notation of Hohenberg and Halperin with  $z = 3/2$  in  $D = 3$  ( $z = D/2$  in  $D$  dimensions)[61]. However, for cuprate superconductors, the dynamics may be very different. There may be no conserved quantities and the dynamics may be dissipative. The dissipative case corresponds to model A dynamics, which has no conserved quantities, with  $z = 2$  [77].

### 3.3.2 DC scaling

In the dynamical properties, the conductivity is an important quantity. Through dimensional analysis, Fisher, Fisher and Huse obtained the scaling relation for the conductivity.

First we assume a superconductor has fluctuation currents  $J$ . The fluctuating currents will lead to a fluctuating magnetic induction  $B$ , which varies in magnitude as the temperature and correlation length change. The fluctuating magnetic induction should be relevant to the number of flux quanta per coherence area,  $\Phi_0 = 2\pi B\xi^2$ . Thus the magnetic induction scales as

$$B \sim \frac{\Phi_0}{\xi^2} \quad (3.64)$$

Since  $B = \nabla \times \mathbf{A}$ , so the scaling dimensionality of the vector potential and electric field are then expressed as:

$$\mathbf{A} \propto \frac{1}{\xi}, \quad \mathbf{E} = \frac{1}{c} \frac{\partial \mathbf{A}}{\partial t} \propto \frac{1}{\xi\tau}, \quad (3.65)$$

in which  $\tau$  is the relaxation time, scaling as  $\tau \propto \xi^z$ . The dimension of the energy density  $f_s = F/V \propto \xi^{-D}$ , so from the definition of the current

$$J = \frac{1}{c} \frac{\partial f}{\partial \mathbf{A}}, \quad (3.66)$$

we obtain the dimension of the current

$$J = \frac{1}{c} \frac{\partial f}{\partial \mathbf{A}} \propto \xi^{-D+1}. \quad (3.67)$$

Since the conductivity  $\sigma = J/E$ , with the above formalism, we can obtain:

$$\sigma = \frac{J}{E} \propto t\xi^{2-D} \propto \tau\xi^{2-D} \propto \xi^{2-D+z}, \quad (3.68)$$

Here we use the scaling dimension of time, which is fixed by  $t \propto \tau \propto \xi^z$ . The relaxation time  $\tau$  describes the rate at which the system relaxes to equilibrium.  $\tau$  diverges at the transition:

$$\tau \propto \xi^z \propto |t|^{-z\nu}, \quad (3.69)$$

in which  $z$  is the dynamical critical exponent.

From Eq. 3.68, the conductivity is ohmic ( $E \propto J$ ). However, we know the superconductor does not respond linearly below  $T_c$  and it has nonlinear effects at high  $J$  above  $T_c$  as well. We need to extend Eq. 3.68 and include non-linear effects in the conductivity as a function of  $J$ :

$$\sigma = \frac{J}{E} \propto \tau \xi^{2-D} \propto \tau \xi^{2-D} G_{\pm}(J \xi^{D-1}) \quad (3.70)$$

where  $G_{\pm}$  is just a dimensionless unknown scaling function. Because  $J \propto \xi^{-D+1}$ , the scaling function dependence on current must be of the dimensionless form  $J \xi^{D-1}$ .

This can be recast into a commonly used form as follows:

$$\frac{E}{J} = \xi^{D-2-z} \chi_{\pm}(J \xi^{D-1}), \quad (3.71)$$

where  $\chi_{\pm}$  are unknown functions,  $+$  means above  $T_c$  and  $-$  means below  $T_c$ .

More formally, we can use the DC scaling equation given by the FFH paper[54]

$$\frac{E}{J} = \xi^{D-2-z} \chi_{\pm}(J \phi_0 \xi^{D-1}/cT). \quad (3.72)$$

where  $c$  is a constant.

## Useful limits

The scaling function  $\chi_{\pm}$  in Eq. 3.71 is an unknown function. However, it has two useful limits. First, above  $T_c$ , the function  $\chi_{+}(x)$  approaches a constant as  $x \rightarrow 0$ . [54] Thus, in the limits of low current density  $J \rightarrow 0$ , Eq. 3.71 becomes

$$\frac{E}{J} \propto \xi^{D-2-z}. \quad (3.73)$$

This limit is only for above  $T_c$  and we can not use the same argument below  $T_c$  since one expects the resistance to vanish as  $J \rightarrow 0$  below  $T_c$ .

The next limit is for  $x \rightarrow \infty$ , which would occur either through  $J \rightarrow \infty$  or  $T \rightarrow T_c$ . [54] In this limit

$$\chi_{+}(x) \approx \chi_{-}(x) \sim x^{(z+2-D)/(D-1)}. \quad (3.74)$$



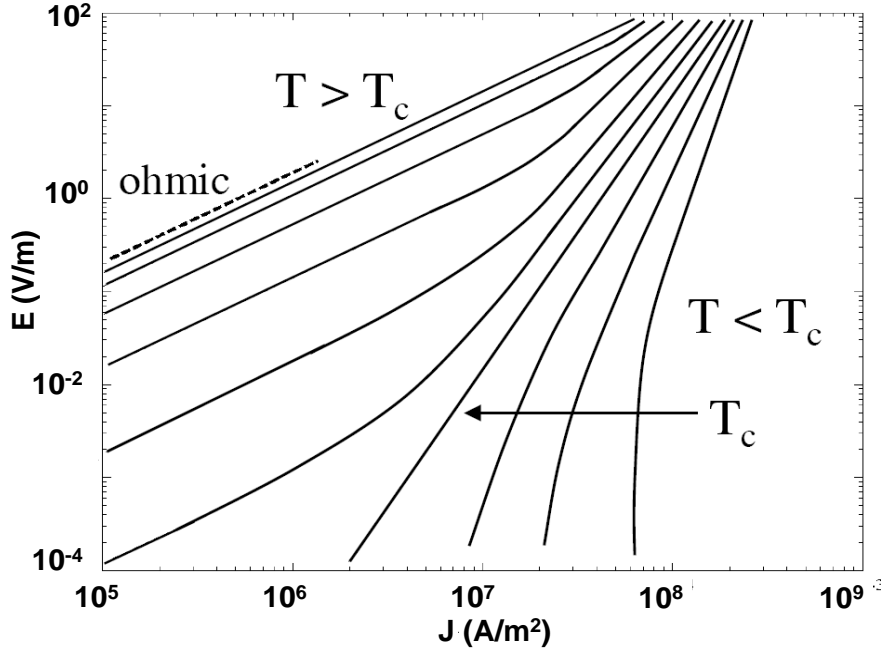


Figure 3.2: Schematic of expected  $E - J$  curves. The dashed line indicates a slope of 1, or ohmic behavior. The isotherm at  $T_c$  is clearly identifiable as a power law (straight line with slope  $\neq 1$  on the log-log plot). Above  $T_c$  for low currents, the isotherms bend towards ohmic behavior. Below  $T_c$ , the isotherms increase in slope as current decreases.

This results in (for  $D=3$ )

$$\frac{E}{J} \sim J^{(z+2-D)/(D-1)} \Rightarrow E \sim J^{(z+1)/(D-1)} \quad (3.75)$$

In a plot of the electric field vs. current density at different temperatures in a log-log scale (E-J plot), we expect to obtain a figure like Fig. 3.2.

One of the major advantages of a log-log plot is the fact that, from Eq. 3.75, we expect the isotherm at  $T_c$  to be a straight line. The slope of the isotherm will then give us  $z$ , as the slope  $= \frac{z+1}{D-1}$ . Isotherms above  $T_c$ , but close enough to  $T_c$  to be affected by fluctuations, are non-linear at high currents and become linear at lower currents, as predicted by Eq. 3.73. Below  $T_c$ , we see the isotherms drop rapidly in

voltage, indicating a transition to a zero voltage state with a finite critical current.

## Derivative Plot

Sometimes it is not easy to determine  $T_c$  from Fig. 3.2, particularly when the data is affected by finite size effects, which will be discussed later in detail. Taking the derivative of  $\log E$  in Eq. 3.72 with respect to  $\ln J$ , one has:

$$\left( \frac{\partial \ln E}{\partial \ln J} \right)_T = G_{\pm}(J\xi^{D-1}), \quad (3.76)$$

Where  $G_{\pm}(J\xi^{D-1}) = \frac{\partial \ln(J\xi^{D-2-z}\chi_{\pm}(J\xi^{D-1}))}{\partial \ln J}$ . At  $T_c$ , taking Eq. 3.74, one find

$$\left( \frac{\partial \ln E}{\partial \ln J} \right)_{T_c} = \frac{z+1}{D-1}. \quad (3.77)$$

So in the derivative plot the  $T = T_c$  isotherm should become a horizontal line whose intercept should give the value for  $z$ . The expected derivative plot is sketched in Fig. 3.3.

Here,  $T_c$  is easily identified as the horizontal isotherm. Moreover, the isotherms above and below the transition temperature  $T_c$  have opposite slopes. This character gives a criterion, called the opposite concavity criterion, which was first proposed by D. R. Strachan.[95]

## Data Collapse

The final prediction is what is called 'data collapse'. We can re-write Eq. 3.72 in the following way:

$$\frac{E}{J} \left| \frac{T - T_c}{T_c} \right|^{\nu(1-z)} = \chi_{\pm} \left( \frac{J}{T} \left| \frac{T - T_c}{T_c} \right|^{-2\nu} \right), \quad (3.78)$$

where  $D = 3$  is used for the dimension. In a plot of the left-hand side of Eq. 3.78 vs. the arguments of the unknown functions  $\chi_{\pm}$  from the right-hand side, the isotherms will fall upon two curves,  $\chi_+$  for above  $T_c$ , and  $\chi_-$  below  $T_c$ . So, for a true phase transition where Eq. 3.78 applies, all of the isotherms from Fig. 3.2 will collapse

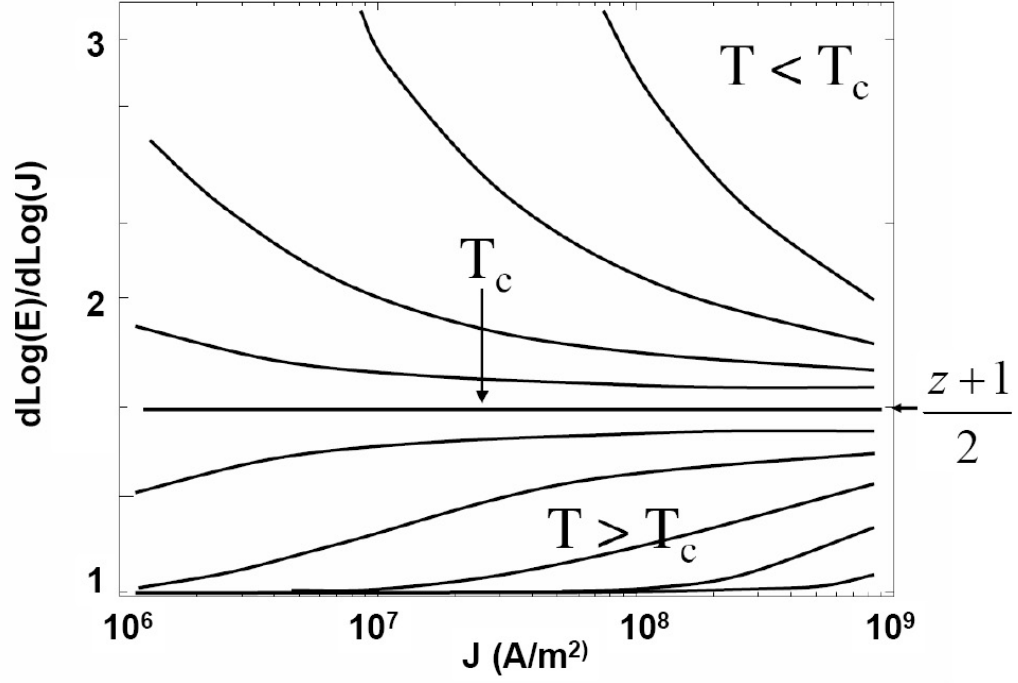


Figure 3.3: Schematic of expected  $\partial \log(E)/\partial \log(J)$ .  $T_c$  is identified as the horizontal isotherm. The intercept is  $(z+1)/2$  with the assumption that  $D=3$ . Isotherms above and below  $T_c$  display opposite concavity about  $T_c$ .  $\partial \log(E)/\partial \log(J) = 1$  indicates ohmic behavior.

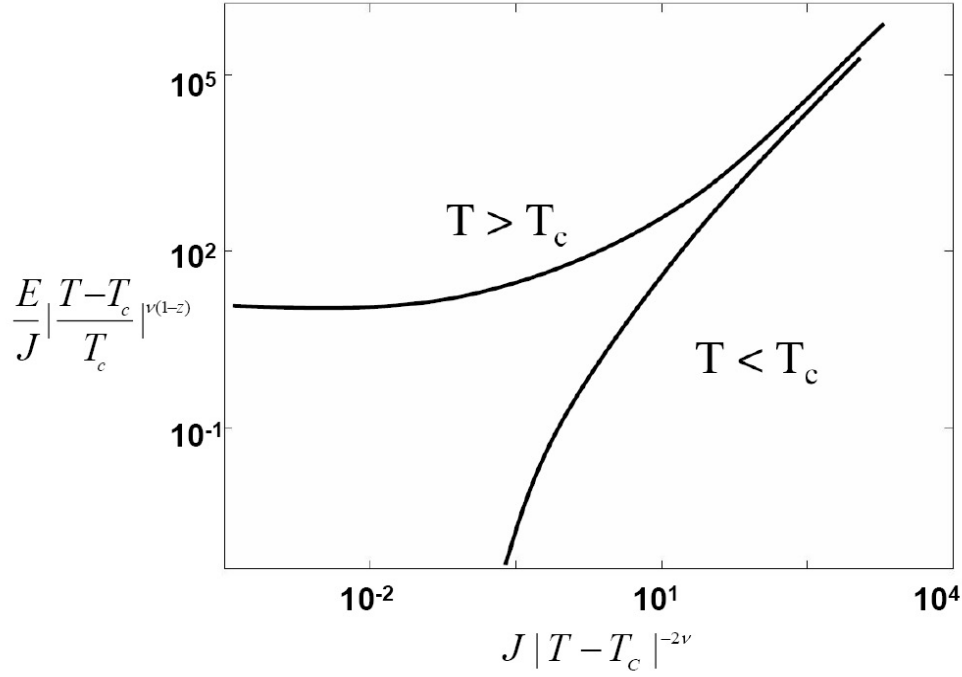


Figure 3.4: Schematic of expected data collapse. The left-hand side of Eq. 3.78 vs. the argument of the unknown functions  $\chi_{\pm}$ . All the isotherms from Fig. 3.2 fall on one of two curves for above and below  $T_c$ . A good data collapse is viewed as strong evidence for a phase transition as well as confirmation of the correct choices for  $T_c$ ,  $z$ , and  $\nu$ .

onto two distinct curves. A data collapse is sketched in Fig. 3.4. It depends on the values for  $T_c$ ,  $z$ , and  $\nu$ . A good data collapse is evidence of the correct choices for these critical parameters.

### 3.3.3 AC Conductivity Fluctuations

The form of the fluctuation conductivity at finite frequencies can also be determined by dimensional arguments. For  $T < T_c$  and low frequency, the complex conductivity has the form

$$\sigma(\omega) \approx \frac{\rho_s}{-i\omega + \epsilon} \quad (3.79)$$

where  $\epsilon \rightarrow 0+$ , the real part thus having a  $\delta$  function at zero frequency. Here  $\rho_s$  is the superfluid density, and we know that  $\rho_s \sim \xi^{2-D}$  [62] and that the characteristic relaxation time scales as  $\tau \sim \xi^z$ . This indicates that the low frequency linear conductivity should scale as:[54]

$$\sigma = \xi^{z+2-D} S_{\pm}(\omega \xi^z), \quad (3.80)$$

where the scaling functions  $S_{\pm}$  apply above (+) and below (-)  $T_c$ . This scaling function may be also obtained by following the scaling analysis method for the DC case. Actually from Eq. 3.70, we have known  $\sigma \propto \xi^{z+2-D}$ . Since we want to find the frequency dependent linear conductivity, function that includes  $\omega$  should be put in.  $\omega\tau$  can be used as the variable so that the function itself and the variable are both dimensionless. Then we obtained Eq. 3.80

For the AC scaling, there are also some limits. Firstly for  $x \rightarrow 0$ , the scaling function behaves as  $S_+(x) \rightarrow \text{real constant}$  above  $T_c$  and  $S_-(x) \sim 1/(-ix)$  below  $T_c$ , reflecting the low-frequency behaviors.

The other limit is for  $x \rightarrow \infty$ , representing  $T \rightarrow T_c$ . We have

$$S_+(x) \approx S_-(x) \approx \tilde{c} x^{(D-2)/(z-1)} \quad (3.81)$$

with  $\tilde{c}$  a complex constant.[54] Hence, at  $T_c$ , both the real and imaginary parts of  $\sigma$  diverge for  $\omega \rightarrow 0$  as

$$\sigma(\omega) \sim \omega^{-(z+2-D)/z} \quad (3.82)$$

The complex AC conductivity can be write as  $\hat{\sigma} = |\sigma|e^{i\phi}$ , so we have

$$|\sigma| = \xi^{z+2-D} |S_{\pm}(\omega \xi^z)|, \quad (3.83)$$

$$\phi = \Phi_{\pm}(\omega \xi^z). \quad (3.84)$$

A scaling argument yields the power-law relation at  $T_c$ .

$$|\sigma| \sim \omega^{-(z+2-D)/z}, \quad (3.85)$$

And also for the phase we have:

$$\phi = \frac{\pi}{2}(z + 2 - D)/z, \quad (3.86)$$

Similar to DC fluctuation, we also have the corresponding AC derivative scaling relation:

$$-\left(\frac{\partial \ln |\sigma|}{\partial \ln \omega}\right)_T = F_{\pm}(\omega \xi^z). \quad (3.87)$$

At  $T_c$ , this becomes

$$-\left(\frac{\partial \ln |\sigma|}{\partial \ln \omega}\right)_{T_c} = (z - 1)/z. \quad (3.88)$$

However, because AC measurement of conductance vs. frequency is noisy compared to DC measurement of voltage vs current, it is difficult to take derivatives to analyze the data.

### Wickham-Dorsey Scaling function

Alan Dorsey considered the effects of critical superconducting fluctuations on the scaling of the linear ac conductivity  $\sigma(\omega)$ , of a bulk superconductor slightly above  $T_c$  in zero applied magnetic field. He applied the dynamic renormalization group method to the relaxational time-dependent Ginzburg-Landau model of superconductivity. He found the critical dynamics are governed by the relaxational XY-model renormalization-group fixed point and also he verified the scaling hypothesis  $\sigma(\omega) \sim \xi^{z+2-D} S_{\pm}(\omega \xi^z)$  proposed by Fisher, Fisher, and Huse.[54] Most important, the universal scaling function  $S(y)$  is computed above  $T_c$  [106]:

$$S_+(y, D, z) = \frac{2z^2}{(D - 2 - z)(D - 2)} \frac{1}{y^2} \left[ 1 - \frac{D - 2 - z}{z} i y - (1 - i y)^{(D-2+z)/z} \right], \quad (3.89)$$

where  $y = \omega \tau \sim \omega \xi^z$ .

Fig. 3.5 shows the phase and magnitude of the above scaling function  $S_+(y)$  for different values of dimensionality  $D$  and critical exponent  $z$ . The figure also shows that the phase of  $S_+(y)$  increases and the magnitude of  $S_+(y)$  decreases as  $y$  increases. From the figure, we find at large  $y$ , which means close to  $T_c$ , the  $S_+(y)$

is sensitive to the dimensionality  $D$  and critical exponent  $z$ . However, for small  $y$ , which means far above  $T_c$ , the  $S_+(y)$  is essentially independent of dimension  $D$  and  $z$ . This is natural since the fluctuation contribution is small when far above  $T_c$ .

It is instructive to compare the universal function  $S_+(y)$  for the critical theory with the experiment result. Robert A. Wickham and Alan T. Dorsey compared the critical theory with measurements of the microwave conductivity of a thin-film sample of  $YBa_2Cu_3O_{7-\delta}$  in the range of 45 MHz-45 GHz near  $T_c$ . They found the critical theory fits the experimental scaling curve very well over almost four decades in scaled frequency  $y$ , but deviates from the experimental data taken nearest to  $T_c$ . [106] However, there are still some unresolved questions from this analysis. First is that the reported value of  $z \approx 2.6$  can not be explained in the frame of 3D-XY. R. A. Wickham *et al.* claimed that this is might be due to the uncertainties in the experimental determination of  $T_c$  and more ac conductivity measurements with higher temperature resolution near  $T_c$  may resolve this issue, and allow a more accurate determination of  $z$ . It is also possible that the films under study contain strong disorder, which could affect the scaling near  $T_c$ . [106]

The universal function  $S_+(y)$  above  $T_c$  is useful. If we could have also the  $S_-(y)$  below  $T_c$ , it would be more important for us to investigate the critical behavior around  $T_c$ . However, it is a pity that the R. A. Wickham *et al.* did not compute the  $S_-(y)$  below  $T_c$ . Right now there is still no universal function below  $T_c$ , which incorporates critical theory.

We checked that Wickham-Dorsey Scaling function reduces to the 3D Gaussian predictions. When choosing the dimension  $D = 3$  and  $z = 2$ , taking real and imaginary parts of  $S_+(y)$ , we obtained  $F_1^+$  and  $F_2^+$  in Eq. 3.35 and Eq. 3.36 respectively. As another check, one can show that Eq. 3.89 reduces to the 2D Gaussian predictions when choosing  $D = 2$  and  $z = 2$ . (Note that one needs to carefully take the limit  $d \rightarrow 2$ )

Here starting from the above  $S_+(y)$ , and also the form of the Gaussian fluctu-

ations, we can construct a universal function  $S_-(y)$  below  $T_c$ , which satisfies some known constraints, which are that  $S_-(y)$  reduces to 3D Gaussian predictions when choosing  $D = 3$  and  $z = 2$ , and 2D Gaussian predictions when choosing  $D = 2$  and  $z = 2$ . According to these limiting constraints, we constructed a proposed scaling function  $S_-(y)$  below  $T_c$ , which is

$$S_-(y, D, z) = \frac{2z}{\frac{D-2+z}{z}(D-2)} \frac{1}{1+y^2} (\sqrt{D-1}(1-iy) - \frac{1}{1+y^2} (1-iy)^{(D-1+z)/z} \sqrt{1+iy}). \quad (3.90)$$

The above proposed form of the scaling function has the correct 3D limit and almost the correct 2D limit. We are still working on this and trying to construct a scaling function with both correct 3D and 2D limits. Of course this  $S_-(y)$  is a constructed function instead of a result derived from basic theory. However, it does give us some information about the critical behavior below  $T_c$ .

### 3.4 Finite Size Effect

Previously we have mentioned the finite size effect on fluctuations. Due to inhomogeneities, a solid is always homogeneous only over a finite length  $L$ . In this case, the actual correlation length  $\xi(t) \propto |t|^{-\nu}$  can not grow beyond  $L$  as  $t \rightarrow 0$ , and the transition will become rounded. This finite size effect has been investigated for a long time. We also notice that the DC scaling should exist only with  $\xi \sim \left| \frac{T-T_c}{T_c} \right|^{-\nu}$  where  $\xi$  is correlation length. When  $T$  is close enough to  $T_c$ ,  $\xi$  might be very large and close to the thickness of the film. So there comes another so-called finite size effect. This finite size effect in the DC case was discussed by Matt Sullivan [94]. How does the finite size affect the AC fluctuation conductivity? This question has not been solved yet. In Chap. 5, we will start from the experimental data and discuss the finite size effect on the AC fluctuation conductivity.



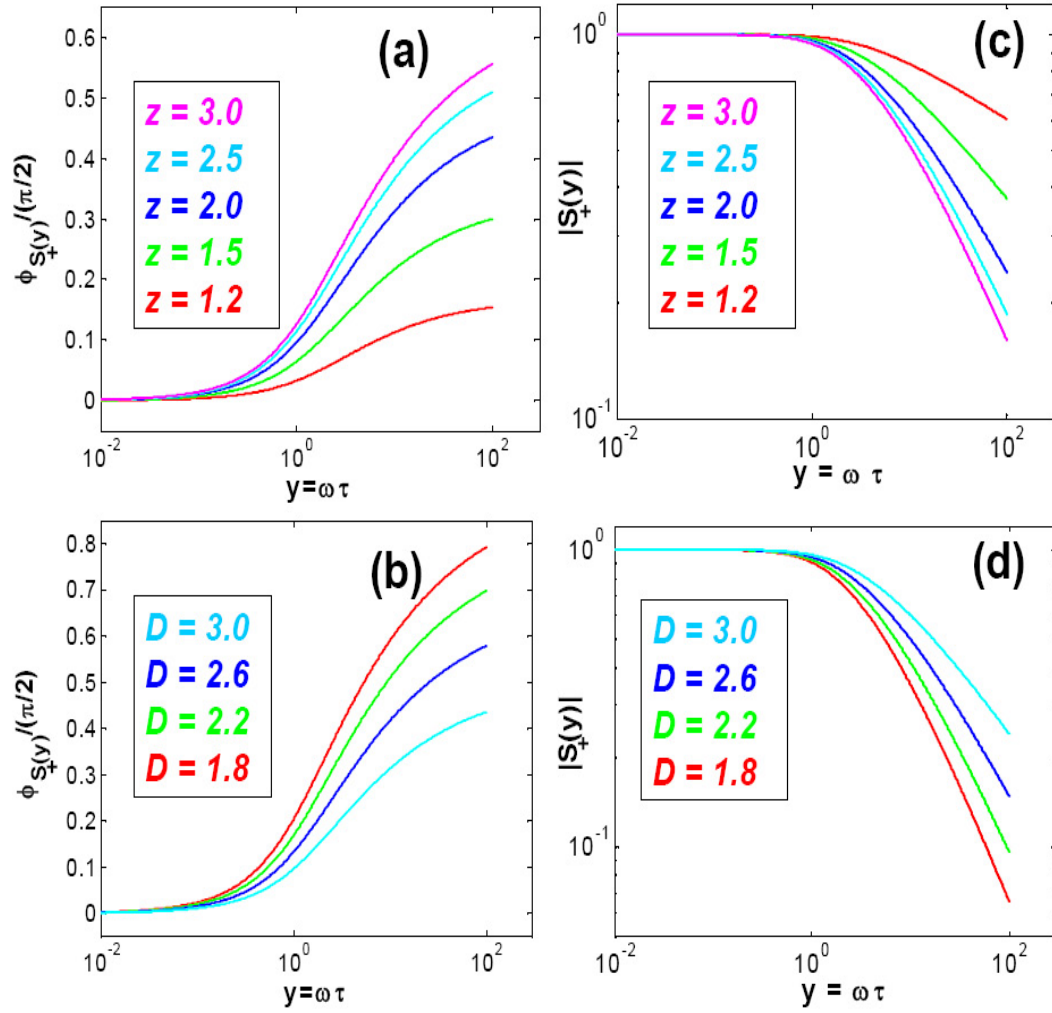


Figure 3.5: Phase and Magnitude of Dorsey's scaling function  $S(y)$  above  $T_c$  for different  $D$  and  $z$ . (a) Phase part of  $S(y)$  for  $D=3$  and different value of  $z$ . (b) Phase part of  $S(y)$  for  $z=2$  and different dimensions. (c)  $|S(y)|$  for  $D=3$  and different value of  $z$ . (d)  $|S(y)|$  for  $z=2$  and different dimensions.

## Chapter 4

# AC Experiment And Data Discussion

## 4.1 Sample Preparation And Characterization

### 4.1.1 The Material: YBCO Thin Film

In our experiments, the samples are  $YBa_2Cu_3O_{7-\delta}$  (YBCO) thin films, which was discovered in 1987 and was the first superconducting material in the liquid nitrogen temperature range.[8, 9, 10]. YBCO is a typical high temperature superconductor with a layered structure. This is very different from the conventional superconductors, which are normally elements (e.g. mercury, tin) or simple compounds (e.g. NbN, Nb<sub>3</sub>Ge). A unit cell of YBCO is shown in Fig. 4.1. The unit cell of YBCO is orthorhombic, with  $a = 3.83\text{\AA}$ ,  $b = 3.89\text{\AA}$ ,  $c = 11.66\text{\AA}$ . However, since  $a \approx b$ , it is often reasonable to assume  $c \approx 3a \approx 3b$  and consider the unit cell to be tetragonal. <sup>1</sup> Fig. 4.1 shows the copper-oxygen planes, which are an important feature of HTSCs. Superconductivity occurs in these planes. Normally with the layered structure, HTSCs tend to be anisotropic. Compared with other HTSCs, YBCO is relatively isotropic, and has a small anisotropy parameter  $\gamma \equiv \frac{\xi_{ab}}{\xi_c} \sim 2$  to 8.

YBCO is a hole-doped superconductor, for which the carrier concentration is determined by the oxygen vacancies. The oxygen vacancies are important in YBCO.

---

<sup>1</sup>Information on crystal structures and properties taken from Ref. [134].

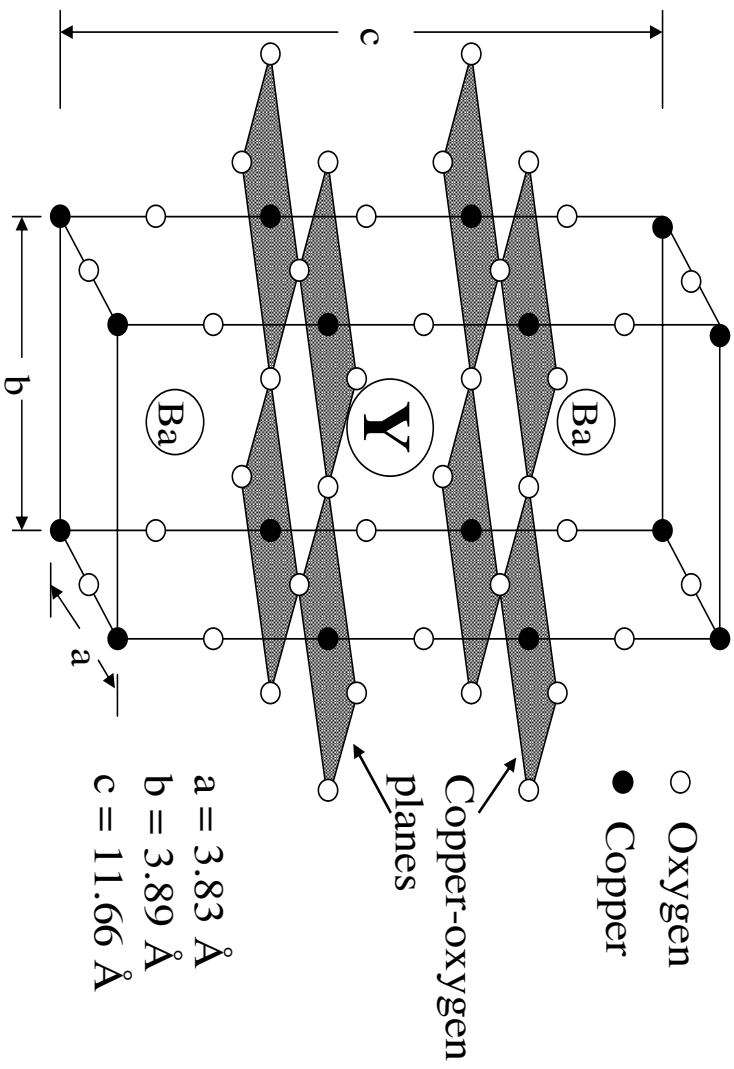


Figure 4.1: The unit cell of YBCO. The additional oxygen atoms indicate the copper-oxygen planes, where superconductivity occurs in this material. The lengths of the unit cell axes  $a$ ,  $b$ , and  $c$  are given. Graph is adapted from Ref. [89]

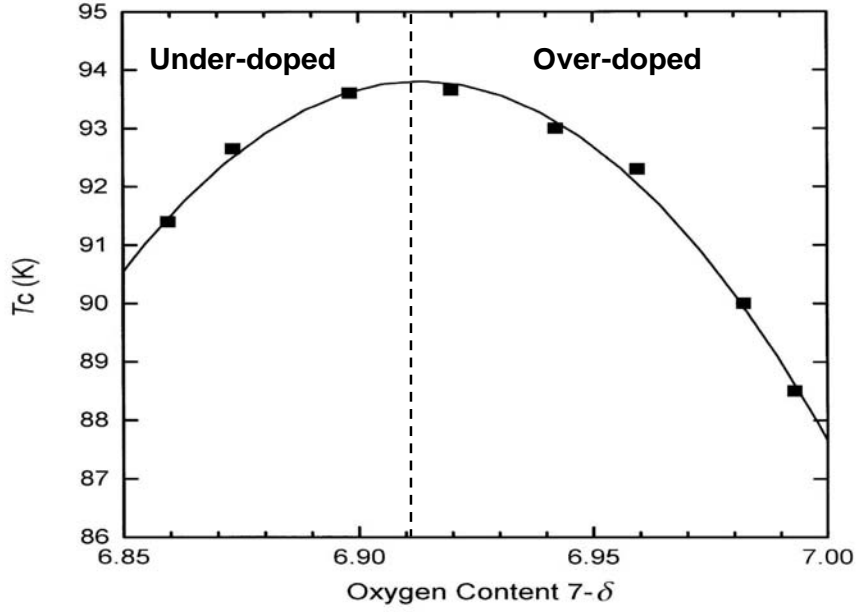


Figure 4.2: Transition temperature vs. doping in YBCO. Graph is adapted from [63].

For example, the transition temperature of YBCO varies strongly with oxygen doping, as shown in Fig. 4.2. YBCO has its highest  $T_c$  at optimal doping where small changes in doping have less affect on  $T_c$  than they do for over- and under-doped samples. So in our work, we investigate optimally-doped YBCO films.

#### 4.1.2 Film Growth via Pulsed Laser Deposition

There are several different methods for YBCO film growth, such as sputtering, molecular beam epitaxy, and pulsed laser deposition (PLD). PLD is an economic, time efficient and relatively easy method of grow YBCO films. Basically when using the PLD method to grow films, a high energy laser pulse is fired at a target and a plasma is ejected from the target, which deposits on a substrate with appropriate conditions. The schematic of the system is shown in Fig. 4.3.

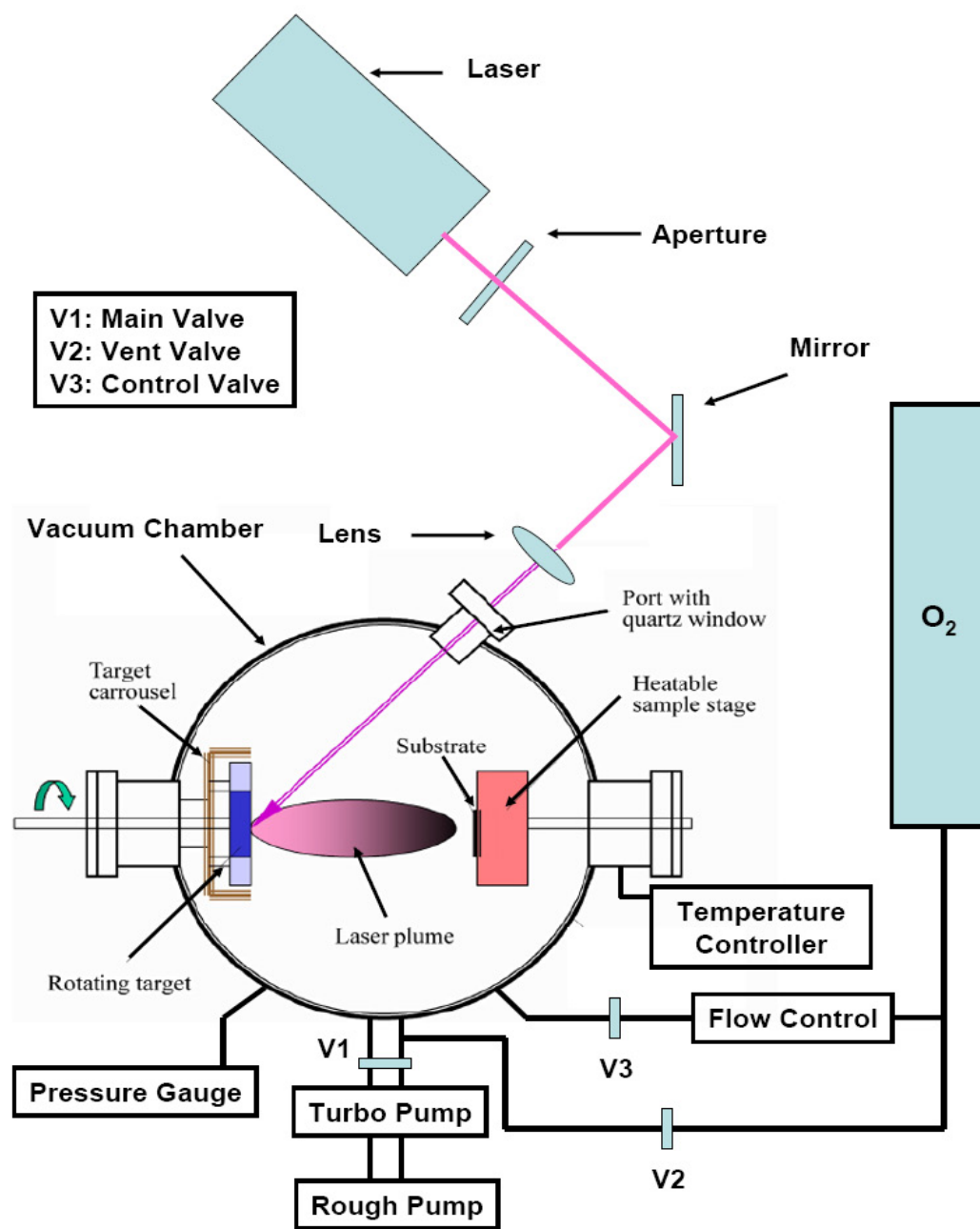


Figure 4.3: Schematic of PLD setup, showing laser, vacuum chamber, target and heater. (not to scale)

The core part of the PLD system is a vacuum chamber, normally called the PLD chamber. As shown in Fig. 4.3, there is a target carousel and heatable sample stage inside the chamber. When using a PLD chamber to grow a film, a high-energy laser pulse is fired into a vacuum chamber onto a rotating target. The energy density on the surface of the target is important, and can be controlled by adjusting the laser's high voltage setting, the aperture size, position and the lens distance from the target. The high energy laser pulse makes the surface layers of the target form a plasma plume, which is ejected from the target to the substrate on the heater. This plasma combines with the oxygen in the chamber and is deposited on the heater and substrate. Under appropriate conditions, heater temperature and oxygen pressure, an epitaxial crystalline film will grow on top of the substrate. When the deposition is finished, an annealing process is performed. To do this, we close the main valve and insulate the chamber from the outside environment. Then we fill the chamber with a certain pressure of oxygen through the vent valve and gradually cool the sample down to room temperature. After this annealing, we will obtain the superconducting thin film on the substrate.

High-quality YBCO films require that copper-oxygen planes must align, oxygen content must be uniform, etc. In order to make high-quality films, some parameters have to be carefully controlled, including aperture size, lens distance from the target, target distance from the heater, heater temperature, thermal link from the substrate to the heater, laser energy, oxygen pressure during deposition, annealing conditions, and more. Doug Strachan, a former student in our group, listed a table with detailed parameters of growth condition for YBCO film, and more importantly gave a step-by-step description of PLD film growth in Appendix A of Ref. [18]. I will not repeat these again. Here I just point out that the deposition conditions, energy density and temperature would depend on the target. However, generally our films were grown with an ultra-violet Kr-F laser ( $\lambda = 248$  nm), at a heater temperature of  $\approx 850^\circ\text{C}$ , in a 150 mTorr  $\text{O}_2$  environment, with an energy density of  $\approx 1$  J/cm<sup>2</sup>, and a pulse

rate of 5 Hz to 10 Hz.

For YBCO film growth, a lot of substrates can be used, including  $\text{LaAlO}_3$  (LAO),  $\text{SrTiO}_3$  (STO),  $\text{NdGaO}_3$  (NGO), MgO and yttria-stabilized zirconia(YSZ). LAO, STO and NGO are normally used by researchers. LAO substrates have the disadvantage that they have significant twinning and warping upon heating and cooling, which causes structural damage in the YBCO films. STO substrates do not have a structure change with temperature, and also have better lattice match to YBCO. One other advantage of STO substrates is that it is relatively easy to obtain high quality YBCO films on this substrate. These advantages make the STO substrate popular. However STO has a high dielectric constant at room temperature( $\approx 300$ ), which also changes with temperature, thus is not a good choice for high-frequency measurements. NGO has a relatively small dielectric constant ( $\approx 20$ ), and even a smaller lattice mismatch with YBCO than STO, and is actually an ideal candidate for film growth. However, we found it is difficult to grow high quality films on NGO. It is very sensitive to the deposition parameters, in particular the substrate temperature and laser energy. After carefully adjusting the parameters, we successfully grew high quality YBCO samples on NGO substrates for our AC experiment.

### 4.1.3 Film Characterization

Optimization of the sample growth conditions and obtaining a good film is not so easy. In order to obtain high quality films, it is necessary to test the quality of the film by different characterization methods, such as AC susceptibility, x-ray diffraction etc.

#### AC susceptibility

The AC susceptibility measurement is a fast and convenient method to determine  $T_c$  and inhomogeneities. With AC susceptibility we do not need to pattern the film

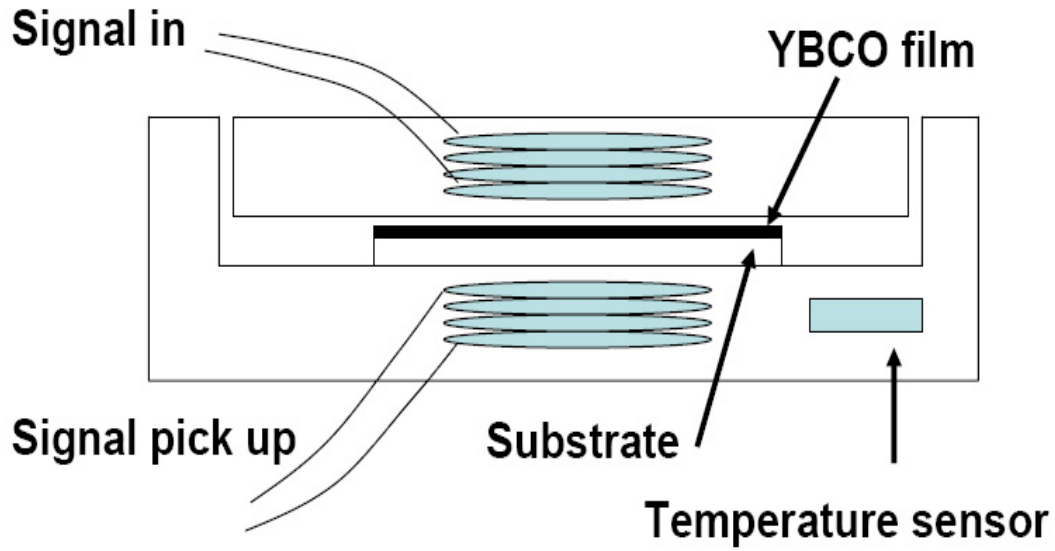


Figure 4.4: Schematic of the AC susceptibility measurement, showing sample, coils and temperature sensor. (not to scale) An AC signal is applied to the top coil and picked up on the other side of the film. As the film becomes superconducting, it screens the magnetic field and changes the mutual inductance of the coils, reducing the signal at the pickup.

and make electric connections on the sample. So it is a damage-free method to test the sample. What we need to do is just place the sample in-between two coils, as shown in Fig. 4.4. A small signal is applied to the top coil and picked up on the other side of the film. It is actually a measurement of the mutual inductance of the coils.

Superconductors are perfect diamagnets and expel magnetic field below  $T_c$ . Thus, as the temperature of the film goes below  $T_c$ , the film becomes superconducting and screens the magnetic field, and changes the mutual inductance between the two coils. The amount of magnetic flux reaching the pickup will be reduced.



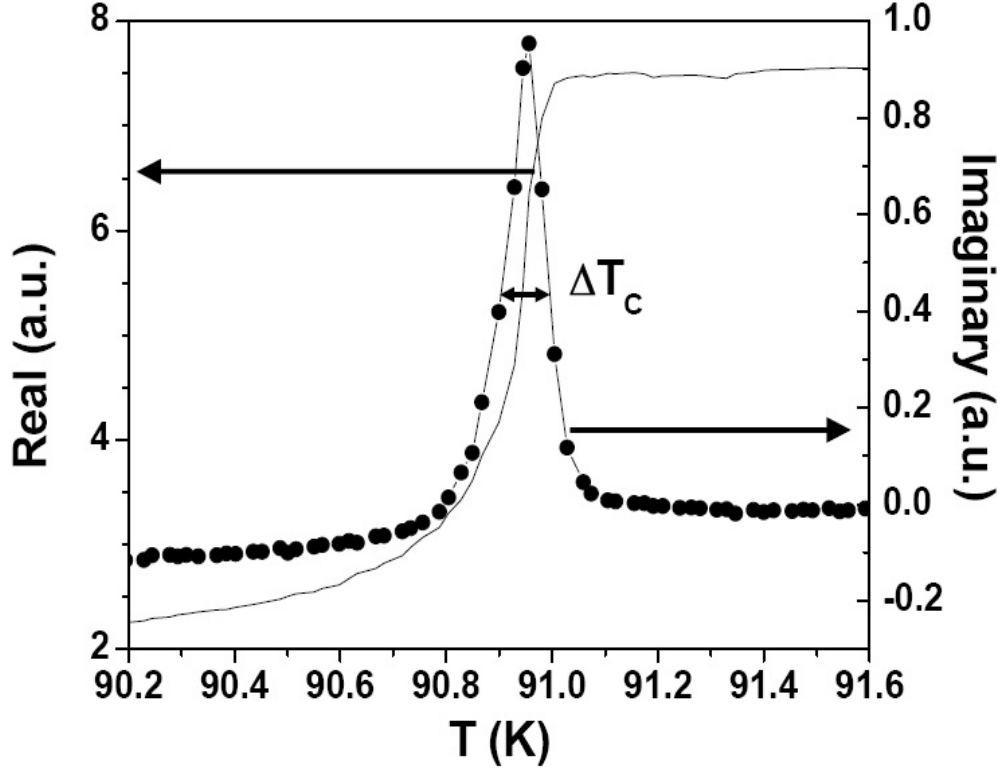


Figure 4.5: Both real and imaginary parts of the AC susceptibility versus temperature for a good sample (xuh132). Here  $T_c \approx 90.9K$  and  $\Delta T_c \approx 0.1K$ .

So according to the AC susceptibility we can determine the  $T_c$  of the sample. Also because the flux goes through the bulk of the film, AC susceptibility can give us inhomogeneity information about the film.

Fig. 4.4 shows the schematic of the AC susceptibility measurement apparatus. The applied AC signal is typically 200 kHz. On the other side of the film, the voltage created in the pickup coil is detected by a lock-in amplifier. The signal measured here has both real and imaginary parts, since  $\chi = \chi' + i\chi''$ . As the sample temperature decreases through  $T_c$ , the real part goes down because of less flux through the film. For a paramagnetic material, the magnetization will be in phase and for a diamagnetic material, the magnetization will be out of phase. The

imaginary part  $\chi''$  is nearly zero both above and below  $T_c$ . Around  $T_c$ , due to the fluctuations, the magnetization will be neither perfectly in phase or out of phase, so  $\chi'' \neq 0$ . Normally we take the peak in  $\chi''(T)$  as  $T_c$ . The width of the peak tells us homogeneity information about the sample. We take the full-width at half maximum as  $\Delta T_c$ . High  $T_c$  and small  $\Delta T_c$  means a good film. Fig. 4.5 shows an example of an AC susceptibility plot of sample xuh132. The imaginary peak gives  $T_c \approx 91.9$  K, and the width gives  $\Delta T_c \approx 0.1$  K.

Susceptibility measurements not only tell us which films are of high quality, but also help us to identify some common problems in films. In Fig. 4.6, we show four different AC susceptibility measurements. Fig. 4.6(a) is the same as Fig. 4.5, and is one of our best films. Fig. 4.6(b) shows a film with two transitions. However, sometimes when the substrate is poorly glued to the heater, the temperature may vary substantially over the substrate, which causes different oxygen concentrations in the film. The other possibility is there are also some a-axis grains in the film, which also results in the double transition. This kind of film is exactly what we must avoid. Fig. 4.6(c) exhibits a film with a shoulder below the main transition. Although it still indicates different oxygen concentrations in the film, in this kind of film, these different concentrations normally come from the edge of the film. We have found that the silver paint used to glue the substrate usually covers the sides of the substrate, which makes the edges of the substrate have a slightly different temperature from the middle. This gives the edges of the film a slightly different  $T_c$  than the center. For this kind of film, the shoulder will disappear if we cut off the edges of the film and measure it again. Since the center of the film is still uniform, it is still possible to use these films for subsequent measurements. The film in the last panel, Fig. 4.6(d), has a wide transition and a low transition temperature. This film is not useful for our measurements.

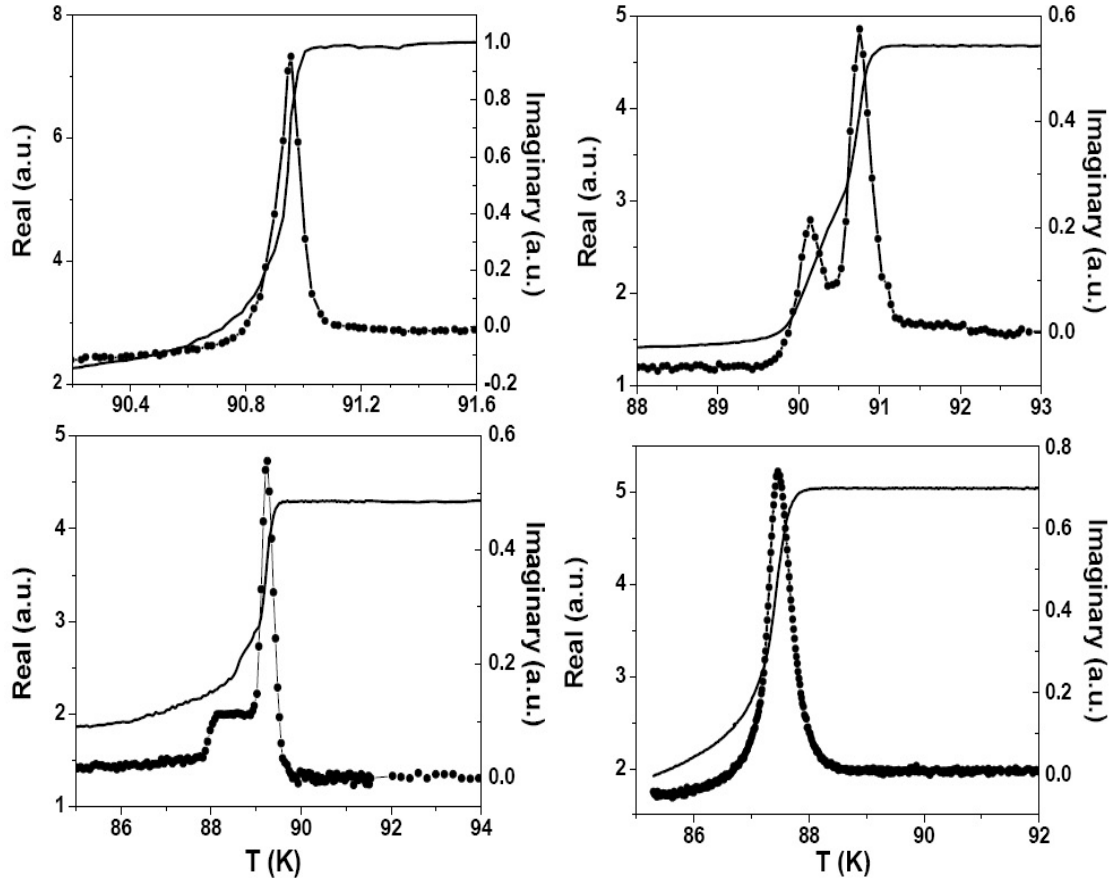


Figure 4.6: The AC susceptibility graphs of four different samples are shown: a) xuh132, b) xuh080, c) xuh078, and d) xuh005. Solid lines are the real part, lines with dots are the imaginary part. Panel (a) shows a good film, (b) a film with two transitions, (c) a film with a "shoulder", and (d) a generally poor film with a low  $T_c$  and wide transition.

## X-ray diffraction

If a YBCO film has the c-axis perpendicular to the surface of the substrate and the copper-oxygen planes stacked on top of each other, parallel to the surface of the substrate, it is called c-axis oriented. For a-axis and b-axis films, the copper-oxygen planes are perpendicular to the surface of the substrate. In our experiment, we want to investigate properties of c-axis oriented YBCO. Thus we hope to avoid a- and b-axis grains.

X-ray diffraction (XRD) is a simple and fast, yet powerful method of analyzing crystalline phases in a material. With this technique, high angular resolution and accurate structure data of the sample can be obtained, which makes XRD one of the most common techniques for material analysis. In our experiment, we use X-ray diffraction to look at the crystallinity of our films and to determine whether they are c-axis films.

An x-ray diffractometer shines x-rays of a certain wavelength at our sample at a given angle  $\theta$ , measured between the source and the sample. These x-rays reflect off the surface of the film and also off the lattice planes inside the film. The Bragg equation sets the condition for constructive interference of the X-rays scattered from atomic planes of the material

$$2d \sin \theta = n\lambda \quad (4.1)$$

where  $\lambda$  is the X-ray wavelength,  $n$  is an integer,  $\theta$  is the scattering angle and  $d$  is the lattice spacing.[134] With the Bragg equation and the linewidths of the diffracted peaks, we can determine the crystalline orientation of the planes, internal stresses and strains in the film, and the irregularities in the structure of atoms (i.e. lattice defects).[135]

The XRD data is usually plotted as counts vs.  $2\theta$ , where the counts is proportional to the number of photons reaching the detector. From the position of the peaks and the wavelength of the incident photons, we can determine the lattice

spacing that created that peak. The expected lattice spacings,  $2\theta_1$ , and  $2\theta_2$  values for YBCO, NGO, and some common impurity phases can be found in Ref. [136] using the Miller indices (hkl) in the reciprocal lattice of the crystallographic planes.

One of the major problems in c-axis YBCO films is a-axis grain growth, which can be identified with an x-ray diffractometer. Because  $c \approx 3a$ , a substrate matched to the  $a$  and  $b$  axes of YBCO can still grow a-axis films. In fact, very thick films ( $d \gtrsim 4000$  Å) are a mixture of c- and a-axis. In addition, films thinner than  $1000$  Å generally have a lower  $T_c$ . Hence, most films tend to be in the range  $1000$  Å  $< d < 4000$  Å. But even films in this optimum thickness range can grow a-axis grains. In particular, during annealing, a-axis grains form as an outgrowth on the surface of the c-axis films. Again, because  $c \approx 3a$ , these outgrowths form rectangular structures at  $90^\circ$  to one another on top of the c-axis structures.[89]

Unfortunately the a-axis peaks occur close to the substrate peaks, so small amounts of a-axis can be drowned out by the substrate.[136] The a-axis peak easiest to see is the YBCO (200) peak, which appears just to the right of the STO (200) and YBCO (006) peaks. In Fig. 4.7, sample mcs89 (solid) shows no a-axis, whereas sample mcs141 (dashed) shows a small a-axis peak at  $2\theta = 48^\circ$ .<sup>2</sup> [89]

## Surface analysis

If there are a-axis outgrowths on the surface of the film, they can be seen using an atomic force microscope (AFM). More readily it can be seen using a scanning electron microscope (SEM) since the c- and a-axis direction have very different conductivities. Fig. 4.8 shows SEM pictures of the surfaces of two films. Fig. 4.8.a is a film with a-axis growths on the surface and Fig. 4.8.b is pure c-axis oriented. We can see that there are rectangular structures at  $90^\circ$  to one another in Fig. 4.8.a.

---

<sup>2</sup>The peaks do not occur at exactly the values predicted in Ref. [136]. The diffractometer has a slight offset which changes as a function of  $\theta$ , and our lattice spacings never match exactly those found in references.

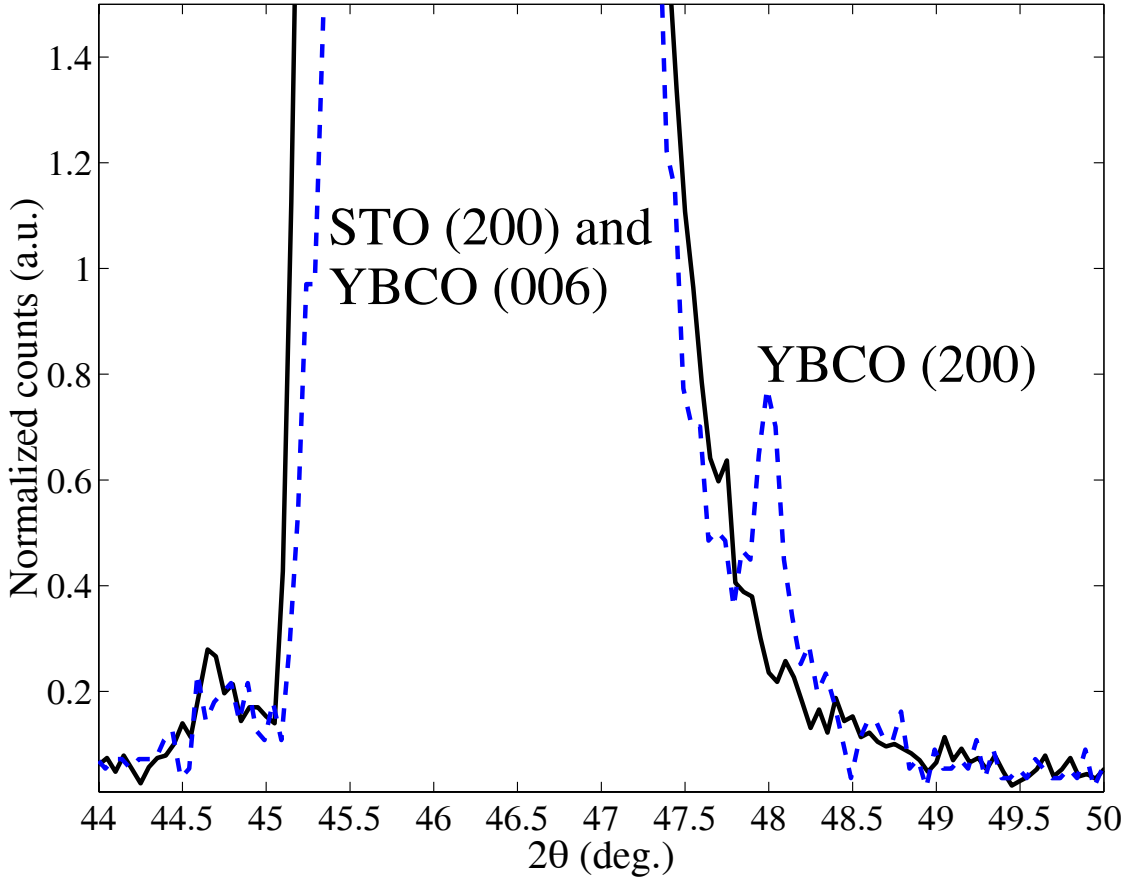


Figure 4.7: X-ray diffraction pattern for mcs89 (solid) and mcs141 (dashed). The large peak is STO (200) and YBCO (006). At  $2\theta = 48^\circ$ , mcs141 has a small a-axis peak (YBCO (200)). Adapted from Ref. [89]

These rectangular structures are the signature of the a-axis impurity. In these rectangular structures, the c-axis points parallel to the long side of the rectangle. Away from the rectangular structures, the c-axis points out of the page. Fig. 4.8.b is a pure c-axis oriented film where there are no rectangular structures.

Another important piece of information that can be obtained from the SEM and AFM images is the roughness of the film, which is

$$R_a = \frac{1}{N} \sum_{i=1}^N |Z_i - \bar{Z}|, \quad (4.2)$$

where  $Z_i$  is the height of each of  $N$  points in the image and  $\bar{Z}$  the average height. A good film normally has a roughness somewhere between 50 Å and 100 Å, which is about 3-5% of the typical thickness. Taking an AFM picture is more time efficient than taking an SEM picture. So AFM is normally used for the surface roughness analysis.

A typical AFM picture of a YBCO film is shown in Fig. 4.9. This film has a roughness of 130 Å. We noticed that there are some big peaks of height  $> 100$  nm. These peaks are common in our films, which might be dust and can be removed by cleaning the film. Measuring roughness in an area which does not include a peak, we find a roughness  $\approx 70$  Å.

The AFM have also been used to study the degradation of the film's surface as a function of time by previous students in our group. Their results showed that there is no real change in roughness from 15 minutes to 75 days, and also no change after cleaning the film with acetone. Thus, the roughness measure can be done at any point in a film's lifetime.[89]

## Other analysis

There are also other methods to characterize YBCO films, such as critical current density measurement, resistance measurement and Rutherford back scattering(RBS). I have also used these methods to analyze the quality of films.

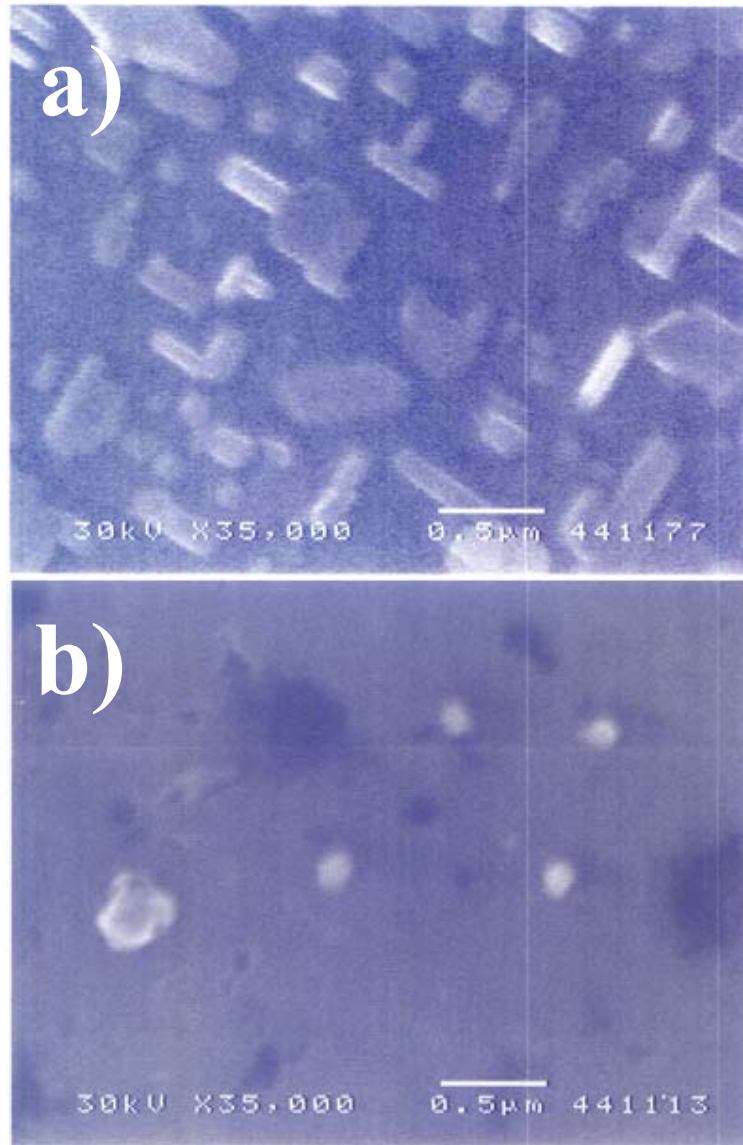


Figure 4.8: a) SEM image for a film with a-axis outgrowth on the surface of the film. b) SEM image for a pure c-axis oriented film. Films imaged by M. Lilly and D. Tobias. Adapted from Ref. [89]



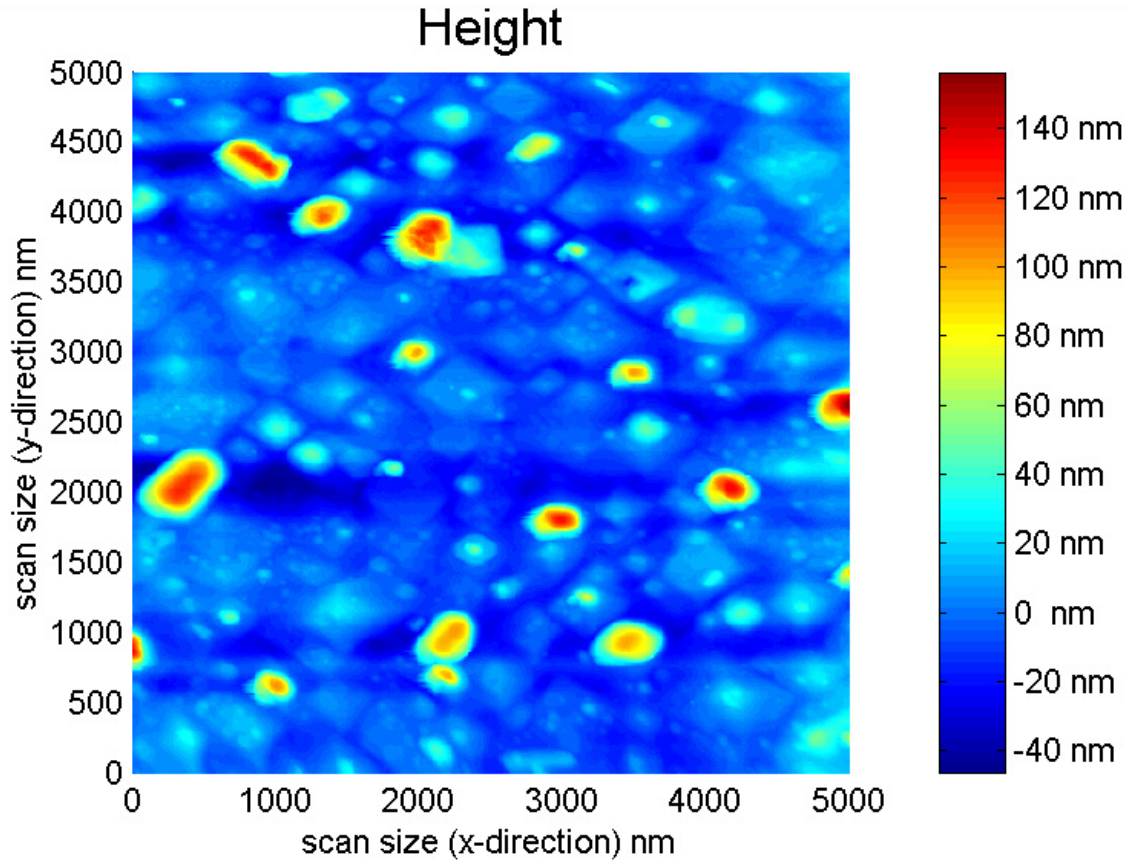


Figure 4.9: AFM image of a typical film (mcs172), with  $R_a = 130 \text{ \AA}$ . The large peaks (height  $> 100 \text{ nm}$ ) are a recurring feature in our films, but break off easily. Film imaged by M. Lilly. Adapted from Ref. [89]

#### 4.1.4 Sample Preparation and Measurement

According to the above characterization method, we optimized the film growth conditions. After a good film was made, we deposited gold contacts on its surface immediately by thermal evaporation. Here the "good film" definition is that the  $YBa_2Cu_3O_{7-\delta}$  films are of predominant c-axis orientation, which are verified by X-ray diffraction; the transition widths(10% to 90%) are less than 0.5 K and  $T_c$  is around 90 K, which are measured by AC susceptibility.

Through a washer-shaped shadow mask, we made the gold contact in the form of a Corbino disk, which has been shown in chapter 2. The sample was used to terminate a coaxial transmission line where the complex reflection coefficient  $\hat{S}_{11}$  can be measured. To insure that the power incident at the sample was independent of frequency, a power-flattening calibration is performed at the sample plane.

The experimentally measured reflection coefficients include the attenuation, multiple reflection and phase shift due to the coaxial cable system. A general expression for the measured reflection coefficient  $\hat{S}_{11}^{measured}$  in terms of the actual reflection coefficient at the film  $\hat{S}_{11}^{film}$  is

$$\hat{S}_{11}^{measured} = E_D + \frac{E_R \hat{S}_{11}^{film}}{1 - E_S \hat{S}_{11}^{film}}. \quad (4.3)$$

Here  $E_D$ ,  $E_R$  and  $E_S$  are complex error coefficients representing the directivity, the reflection tracking and the source mismatch, respectively. From Eq. (4.3), the error coefficients can be determined by measuring the  $S_{11}$  of three different known loads. A room temperature calibration is performed first to determine initial values for the complex  $E_D$ ,  $E_R$  and  $E_S$  as functions of frequency.

The present experiment is performed with an electrical calibration that is superior to mechanical calibrations used in our prior work. [92, 91] After the room temperature calibration, standard open and short connectors are put back to check the calibration quality. In the entire frequency range from 10MHz to 50GHz, after calibration the obtained  $|S_{11}|$  for both standard open and short connectors dif-

fer from 1 by less than 0.2dB. In particular for the frequency range from 30MHz to 20GHz,  $|S_{11}|$  measured for standard open and short differ from 1 by less than 0.05dB.

As temperature is decreased, the error coefficients of the system can change. Then through the calibration and analysis procedures that have been discussed in chapter 2, we performed a re-calibration and obtained the correct reflection coefficient of the films around  $T_c$ . To do this, the YBCO sample is assumed to be an ideal short ( $Z_L(f) = 0\Omega$ ) in the superconducting state (well below the transition temperature), and an ideal resistive load at temperatures in the normal state (well above the transition temperature). A silver disk and a teflon disk are measured in the same temperature range as well for reference. Analyzing the measured  $\hat{S}_{11}$  of 2 references and  $\hat{S}_{11}$  of samples in the superconducting and normal states, corrected error coefficients valid for the system at low temperature are derived. Using these new error coefficients the surface impedance can be extracted as [92]

$$Z_s(\omega) = Z_0 \frac{2\pi}{\ln \frac{b}{a}} \cdot \frac{1 + \hat{S}_{11}(\omega)}{1 - \hat{S}_{11}(\omega)}, \quad (4.4)$$

where  $Z_0 = 50\Omega$  is the characteristic impedance of the coaxial transmission line and **a** and **b** are dimensions shown in Fig. 2.5.

The surface impedance  $Z_s(\omega)$  here includes contributions from the YBCO sample, the substrate and the sample holder. Above and close to  $T_c$ , the film thickness  $t_0$  and the complex propagation constant  $k$  in the film satisfy  $t_0|k| \ll 1$ , so:

$$\frac{1}{Z_s(\omega)} \cong \frac{1}{Z_s^{YBCO}} + \frac{1}{Z_s^{sub}(\omega)} \quad (4.5)$$

where  $Z_s^{sub}(\omega)$  is the total contribution of the substrate and the sample holder and  $Z_s^{YBCO}$  is the desired surface impedance of the YBCO film sample. Far above  $T_c$ , the YBCO sample is in the normal state and  $Z_s^{YBCO} = \rho(\omega)/t_0$  is a constant as a function of frequency. From the DC resistivity of the sample that is measured above  $T_c$ , the substrate and the sample holder contribution  $Z_s^{sub}(\omega)$  can be calculated

according to Eq. (4.5). Since the substrate and the sample holder contribution have little temperature dependence,  $Z_s^{sub}(\omega)$  is used to obtain  $Z_s^{YBCO}$  at all temperatures.

## 4.2 The Complex Resistivity Near $T_c$ in YBCO Films

The main advantage of the Corbino reflection measurement is the ability to measure the complex resistivity  $\rho = \rho_1 + i\rho_2$  over a wide range of frequencies, including dc. Fig. 4.10(a) shows the temperature dependence of  $\rho_1$  at a number of different frequencies for a typical YBCO thin film, xuh139. The dc resistivity of the sample is also shown in Fig. 4.10(a) as a solid thick line. The main feature of the temperature-dependent data is the fact that the transition broadens considerably as the measurement frequency increases. At higher temperature where the sample is in the normal state the data at different frequencies (including dc) overlap each other, because the normal state scattering rate  $1/\tau_n$  is much greater than the measurement frequency over the entire frequency range.

Fig. 4.10(b) shows the  $\rho_2$  dependence on temperature around  $T_c$ . From the plots, we can see  $\rho_2$  has a peak close to the transition temperature and the temperature at which the peak occurs depends on frequency and moves systematically lower for higher frequencies. The measured  $\hat{S}_{11}$  has noise, which is less than  $0.2dB$  in the entire frequency range and is much smaller for frequency less than  $20GHz(< 0.05dB)$ . The measurement resolution of  $\Delta\hat{S}_{11}$  is about  $0.01dB$  for the frequencies in Fig. 4.10(b). This translates to a resolution limit about  $0.25 \times 10^{-7}(\Omega m)$  for resistivity or  $4 \times 10^7(1/\Omega m)$  for conductivity. Above  $T_c$ , the imaginary part of the resistivity has larger noise due to the process of removing the substrate contribution through Eq. 4.5, adding resistivity noise on the order of  $0.5 \times 10^{-7}(\Omega m)$ .

Fig. 4.10(c) and Fig. 4.10(d) show the frequency dependence of  $\rho_1$  and  $\rho_2$  at

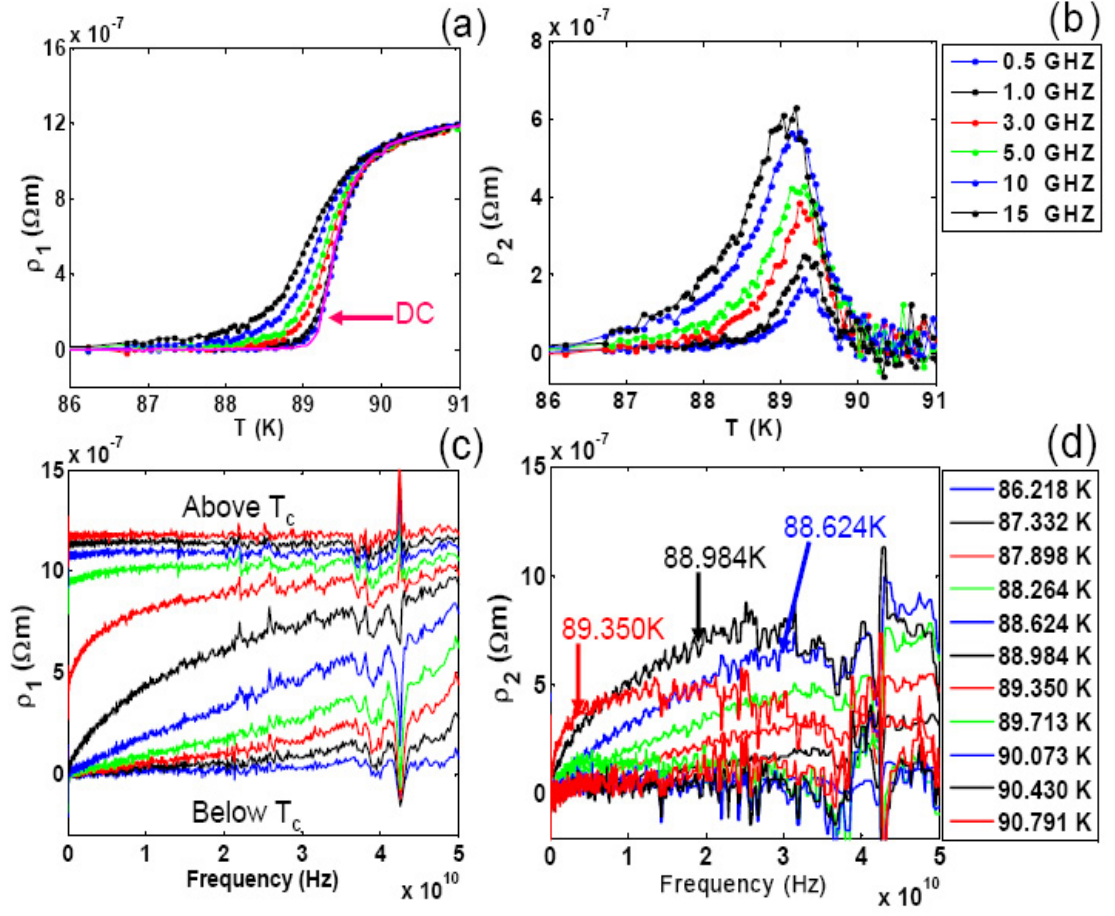


Figure 4.10: Complex resistivity of YBCO film xh139 around  $T_c$ . (a) Temperature dependence of the real part of the resistivity at different frequencies; (b) and imaginary part of the resistivity; (c) frequency dependence of the real part of the resistivity around  $T_c$ ; (d) and imaginary part of the resistivity around  $T_c$ .

different temperatures. In Fig. 4.10(c), it is clear that  $\rho_1$  is frequency independent above and below  $T_c$  and strongly depends on frequency in the vicinity of  $T_c$ . Fig. 4.10(d) shows that above  $T_c$ ,  $\rho_2$  is roughly zero and frequency independent, which is consistent with a normal state resistivity that is completely real. Below  $T_c$ ,  $\rho_2$  is approximately linear in frequency, since  $\rho_2 \approx \mu_0 \omega \lambda^2(T)$  for  $T < T_c$ . Close to  $T_c$   $\rho_2$  is large and depends on frequency in a non-linear manner. From Fig. 4.10 we have a rough idea that  $T_c$  is  $89.20 \pm 0.30 K$ .

### 4.3 The Fluctuation Conductivity Near $T_c$

We are interested in the dynamic fluctuation conductivity of the sample. To extract the frequency-dependent fluctuation conductivity, we convert the measured complex resistivity to conductivity and then remove the mean-field contribution as determined from the dc resistivity which is measured from room temperature down to the lowest temperature in the same experiment. Fig. 4.11 shows the magnitude  $|\sigma_{fl}|$  and phase  $\phi_\sigma$  of the resulting fluctuation conductivity vs. frequency at different temperatures. In this figure, both the magnitude  $|\sigma_{fl}|$  and phase  $\phi_\sigma$  become noisy at low frequency for some lower temperatures where they are close to the sensitivity limit of the experiment. Particularly, it is hard to determine the phase when measuring a very large conductivity because we are in the limit of  $\hat{S}_{11} \rightarrow -1$  in Eq. 4.4 and noise dominates the determination of  $Z_s$ . Although the magnitude of the conductivity is large, its phase information is lost in the impedance step of the data analysis. When doing analysis, we have to be more cautious with data at low frequency especially for temperatures below  $T_c$ .

Fisher, Fisher and Huse(FFH)[54] have argued that near the second order phase transition, dynamic scaling holds

$$\frac{E}{J} = \xi^{D-2-z} \chi_\pm(J\xi^{D-1}, \omega\xi^z, H\xi^2, \dots), \quad (4.6)$$

which has been discussed in detail previously in Chap. 3. In zero magnetic field

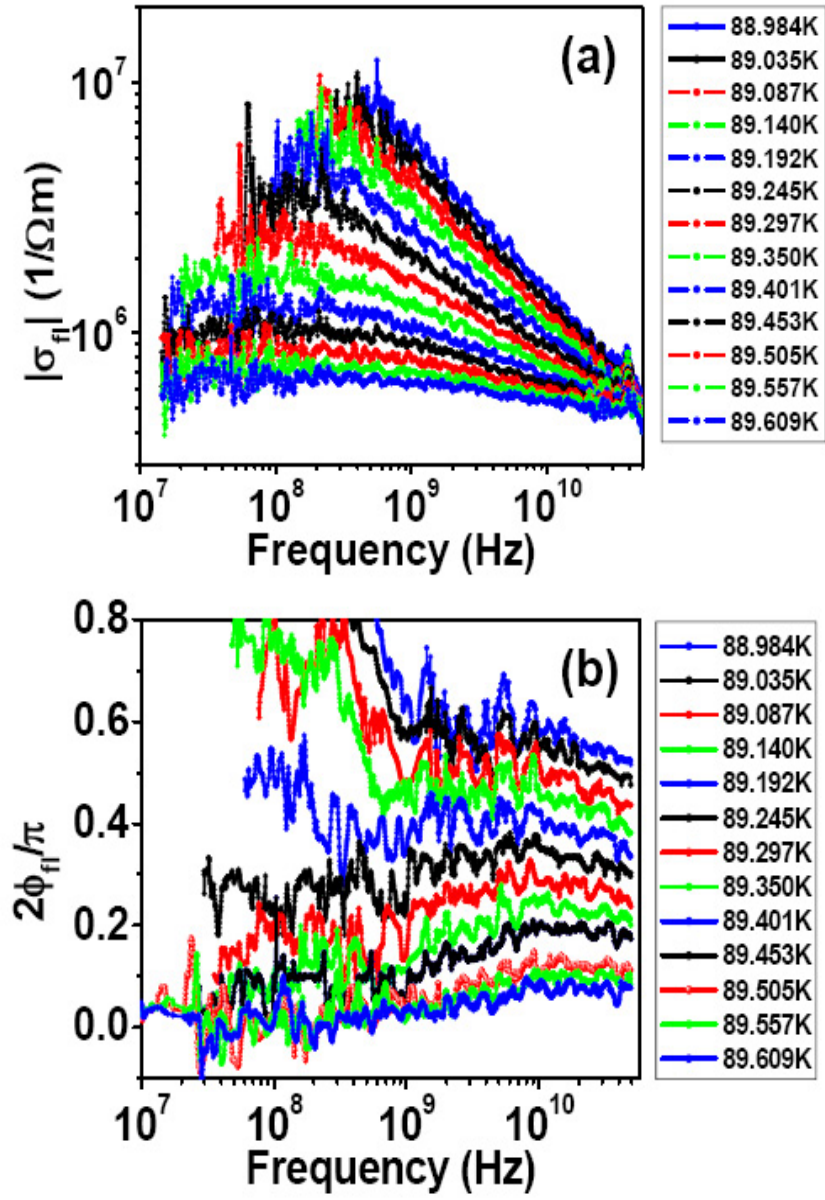


Figure 4.11: Measured magnitude  $|\sigma_{fl}|$  and phase  $\phi_\sigma$  of fluctuation conductivity vs. frequency at different temperatures near  $T_c$  for sample xuh139.

when the current density is small the complex AC fluctuation conductivity should scale as

$$\sigma_{fl}(T, \omega) \approx \xi^{z+2-D} S_{\pm}(\omega\tau_{fl}). \quad (4.7)$$

In this chapter, in order to determine the correct critical exponents the applied microwave power is -46dBm, which is very small and but also still gives relatively good sensitivity. Detailed discussion about the applied microwave power will be given in the next chapter. In this chapter, we applied -46dBm microwave power for the measurement and extract the critical exponent from the results.

In Eq. 4.7,  $\xi$  is the correlation length and  $\tau_{fl}$  is the fluctuation lifetime. The function  $S_{\pm}$  is a universal scaling function above (below)  $T_c$ , which should be the same for all members of a given universality class. As temperature approaches  $T_c$ , both  $\xi$  and  $\tau_{fl}$  will diverge:  $\xi = \xi_0|t|^{-\nu}$ ,  $\tau_{fl} = \tau_0|t|^{-\nu z}$  with  $t = (T - T_c)/T_c$ . The scaling functions behave as  $S_+(y) \rightarrow \text{real constant}$  and  $S_-(y) \rightarrow 1/(-iy)$  for  $y \rightarrow 0$ , reflecting the low frequency behavior above and below  $T_c$  respectively. As  $y \rightarrow \infty$ , representing  $T \rightarrow T_c$ ,  $S_+(y) \approx S_-(y) \approx \tilde{c}y^{(D-2)/(z-1)}$  with  $\tilde{c}$  a complex constant and  $D$  is the dimensionality of the system. The complex fluctuation conductivity can be written as  $\sigma_{fl} \approx |\sigma_{fl}|e^{i\phi_{\sigma}}$ , so both the magnitude and phase are predicted to scale:  $|\sigma_{fl}| \approx \xi^{z+2-D}|S_{\pm}(\omega\xi^z)|$ ,  $\phi_{\sigma} = \Phi_{\pm}(\omega\xi^z)$  where  $\Phi_{\pm}$  is the phase of the scaling function  $S_{\pm}$ . At  $T_c$ , one expects:  $|\sigma_{fl}| \sim \omega^{-(z+2-D)/z}$ ,  $\phi_{\sigma} = \frac{\pi}{2}(z+2-D)/z$ . [106]

## 4.4 The Conventional Analysis Method and its Improvement

Examining experimental data with the above scaling formula Eq. 4.7 and Eqs. 3.85 3.86 in previous chapter, one can search for the temperature at which the conductivity magnitude best fits to the power law and has a constant value of  $\phi_{\sigma}$ . This then determines  $T_c$  and the dynamical critical exponent  $z$ . Proceeding this way,



since  $\xi = \xi_0|t|^{-\nu}$ ,  $\tau_{fl} = \tau_0|t|^{-\nu z}$ , Eq. 4.7 can be re-written as

$$\tilde{A}\sigma_{fl}t^{\nu(z+2-D)} \approx S_{\pm}(\omega\tau_0t^{-\nu z}) \quad (4.8)$$

where  $\tilde{A}$  is a complex constant. If we plot the magnitude of the left-hand side of Eq. 4.8 vs. the argument of the scaling function  $S_{\pm}$ , then the isotherms should fall upon two curves, which we call "data collapse". Such a collapse has been widely used to determine the critical exponent  $\nu$  and verify the presence of a phase transition. This is the conventional analysis method. In this method the choice of  $T_c$  is crucial because it directly determines the value of  $z$ . If  $T_c$  and  $z$  are only known approximately, an accurate value of  $\nu$  can not be obtained through data collapse.

To illustrate this point, Fig. 4.12 shows data collapse results for our measured frequency dependent microwave conductivity around  $T_c$  with 4 different sets of parameters (Fig. 4.12(a),  $\nu = 2.30, z = 2.71, T_c = 88.68$  K; Fig. 4.12 (b),  $\nu = 1.50, z = 3.71, T_c = 88.88$  K; Fig. 4.12 (c),  $\nu = 1.35, z = 2.05, T_c = 89.10$  K; Fig. 4.12 (d),  $\nu = 1.45, z = 1.53, T_c = 89.25$  K). The red lines in the figure are a theoretical fit of Wickham and Dorsey's scaling function  $S_+$ [106] to the critical behavior above  $T_c$ , which will be discussed later. Fig. 4.12 shows that good data collapses on the same data set can be obtained for a large range of parameters, and all of them are consistent with the theoretical prediction for the scaling function above  $T_c$ . Hence to get reliable critical exponents, a precise determination of  $T_c$  and  $z$  has to be done first, then data collapse can be used to obtain the value of  $\nu$ . In this chapter, we concentrate on the determination of  $T_c$  and  $z$ .

From the experimental data in Fig. 4.11, it is clear that the AC fluctuation conductivity at all temperatures deviates from a power law at low frequency. This is because the scaling function  $S_+(y) \approx S_-(y) \approx \tilde{c}y^{(D-2)/(z-1)}$  shows power-law behavior only as  $y = \omega\tau_{fl} \rightarrow \infty$ . For low frequency or for temperatures far away from  $T_c$ ,  $y$  is not in this asymptotic limit and the scaling function deviates from a power law. In addition, we found the fluctuation conductivity at low frequency

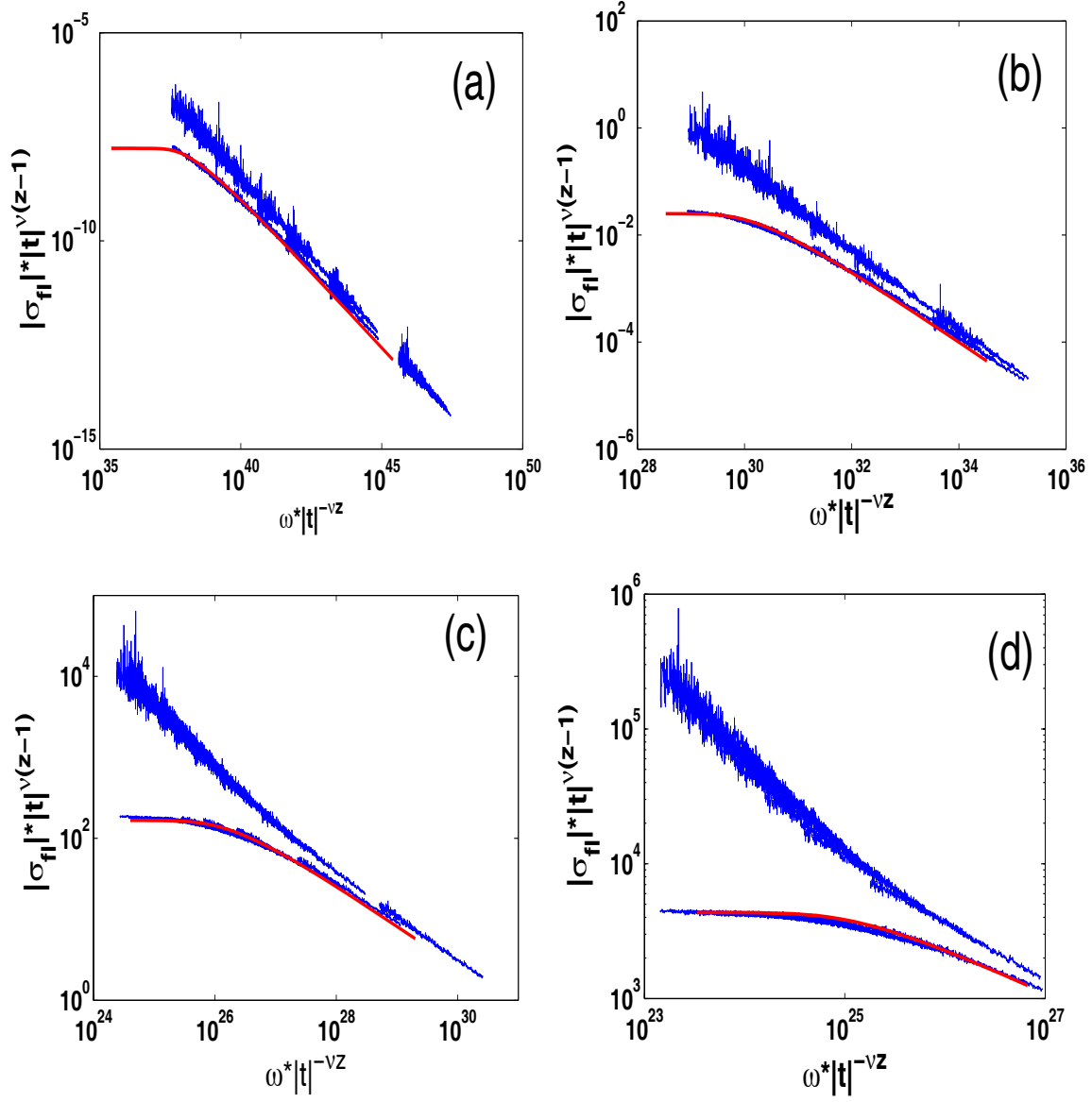


Figure 4.12: Data Collapse of magnitude of microwave conductivity vs. frequency for one data set and different sets of parameters. (a)  $\nu = 2.30, z = 2.71, T_c = 88.68K$ ; (b)  $\nu = 1.50, z = 3.71, T_c = 88.88K$ ; (c)  $\nu = 1.35, z = 2.05, T_c = 89.10K$ ; (d)  $\nu = 1.45, z = 1.53, T_c = 89.25K$ . Red lines are a theoretical prediction calculated from the scaling function  $S_+(y)$ [106]

systematically depends on the applied microwave power, which may arise from a finite size effect. We will discuss this low frequency power dependence in detail in chapter 5. Because of these issues, we are forced to use a higher frequency range to obtain the critical exponents. At very high frequency, the calibration degrades and the process of removing the normal channel contribution makes  $\sigma_{fl}$  vs. frequency show upward curvature. Hence a frequency range from 0.4GHz to 10GHz is chosen to analyze the data. In this frequency range, the calibration is good, the normal channel subtraction has less effect and the finite size effect has less effect on the fluctuation conductivity, and the fluctuation conductivities are independent of incident microwave power, which will be shown later.

Fig. 4.11 shows a log-log plot of the magnitude  $|\sigma_{fl}|$  and the semi-log plot of the phase  $\phi_\sigma$  of the resulting fluctuation conductivity vs. frequency at different temperatures. The power-law behavior  $|\sigma_{fl}| \sim \omega^{-(z+2-D)/z}$  corresponds to a straight line in the log-log plot of  $|\sigma_{fl}|$  vs. frequency. To choose the straightest line in Fig. 4.11(a) to determine  $T_c$ , a quadratic fit method is used. From the scaling theory  $\log |\sigma_{fl}(f)|$  vs.  $\log f$  is known to be a convex function below  $T_c$  and a concave function above  $T_c$ . Unlike the DC I-V curve where Strachan *et al.* used an opposite concavity criterion to determine  $T_c$  in a  $dI/dV$  plot,[95] it is hard to take the frequency derivative of  $|\sigma_{fl}(f)|$  because of noise. An alternative approach is to do a quadratic fit to the data on a log-log plot. Below  $T_c$ , the curve bends up with a positive coefficient of  $(\log f)^2$  and above  $T_c$ , the curve bends down with a negative coefficient of  $(\log f)^2$ . Table 4.1 shows that the coefficient of the  $(\log f)^2$  term changes sign between temperatures 89.192K and 89.245K, bracketing  $T_c$  for sample xuh139. See Appendix B for more details about this fit procedure.

The scaling theory also predicts a constant phase angle  $\phi_\sigma(\omega)$  at  $T_c$ .  $\phi_\sigma(\omega)$  vs.  $\log f$  is known to be a decreasing function below  $T_c$  and an increasing function above  $T_c$ . A linear fit of  $\phi_\sigma(\omega)$  vs.  $\log f$  also has been done and the result shows it to have a negative slope at 89.192K and a positive slope at 89.245K, which is consistent

Table 4.1: Quadratic fit result of  $\log(|\sigma_{fl}|)$  vs.  $\log(f)$  and linear fit result of  $\phi_{fl}$  vs.  $\log(f)$  for sample xuh139 in the frequency range 0.4 to 10GHz

Temperature(K)	Quadratic fit for magnitude	Linear fit for phase
89.087	$+0.0052 \log(f)^2 - 0.631 \log(f) + 11.9$	$-0.0458 \log(f) + 0.937$
89.014	$+0.0068 \log(f)^2 - 0.617 \log(f) + 11.5$	$-0.0305 \log(f) + 0.743$
89.192	$+0.0103 \log(f)^2 - 0.615 \log(f) + 11.1$	$-0.0068 \log(f) + 0.462$
89.245	$-0.0097 \log(f)^2 - 0.190 \log(f) + 8.81$	$+0.0123 \log(f) + 0.221$
89.297	$-0.0195 \log(f)^2 - 0.061 \log(f) + 7.24$	$+0.0408 \log(f) + 0.110$
89.350	$-0.0025 \log(f)^2 - 0.228 \log(f) + 6.09$	$+0.0630 \log(f) + 0.376$

with the quadratic fit result of  $\log|\sigma_{fl}(f)|$  vs.  $\log f$ . (see Tab. 4.1) See Appendix B for more details about this fit procedure.

The next step is to do a linear fit for  $\log|\sigma_{fl}(f)|$  verses  $\log(f)$  to get the slope of  $\log|\sigma_{fl}(f)|$  at  $T_c$ . The slope is almost independent of the frequency range used to do the linear fit, and it mainly depends on the temperature. The slope and the corresponding values of  $z$  are shown in Table 4.2. The average of the  $\phi_\sigma(\omega)$  at  $T_c$  also gives an estimate of  $z$ . There is some difference between  $z$  values obtained from the slope of magnitude and from the average of phase. Due to the difficulty of high frequency calibration, the phase develops a downward curvature at high frequency. The magnitude is not as sensitive to calibration as the phase part. That is why the  $z$  value that comes from the slope of the magnitude is a little larger than that coming from the average of the phase. Since the temperatures 89.192K and 89.245K are bracketing  $T_c$ , we can take their average as  $T_c = 89.22K$  and interpolate between them to get value of  $z$ , which is  $z = 1.62$ .

Adjusting the frequency range used to do the fits, the determined  $T_c$  can change by up to 50mK. The discussion in detail can be found in Appendix B. After carefully

Table 4.2: Linear fit slope of  $\log |\sigma_{fl}|$  vs.  $\log(f)$  and average of  $\phi_{fl}$  for sample xuh139 from 0.4 to 10GHz and corresponding value of  $z$

T(K)	89.087	89.140	89.192	89.245	89.297	89.350
slope of $\log  \sigma_{fl} $	-0.534	-0.481	-0.423	-0.370	-0.302	-0.239
Value of "z" from $\log  \sigma_{fl} $	2.15	1.93	1.73	1.58	1.43	1.31
average of $\phi_{\sigma_{fl}}$	0.510	0.460	0.399	0.335	0.269	0.210
Value of "z" from $\phi_{\sigma_{fl}}$	2.04	1.85	1.67	1.50	1.37	1.27

checking different frequency range results we conclude that  $T_c = 89.22 \pm 0.05K$ . It is clear that value of  $z$  from this analysis is very sensitive to the determined  $T_c$ , with  $dz/dT_c \approx 4K^{-1}$ . The 0.05 K uncertainty of  $T_c$  brings an uncertainty of about 0.20 to the value of  $z$ , so  $z = 1.62 \pm 0.20$ . At this point we can use the determined  $T_c$  and  $z$  to estimate a value of  $\nu$  by data collapse.[91] However, there is a large uncertainty for value of  $\nu$ , roughly  $\nu = 1.50 \pm 0.50$ .

So finally from this method we get the critical temperature and the critical exponents  $z$  for sample xuh139

$$T_c = 89.22 \pm 0.05K, z = 1.62 \pm 0.20.$$

There is also an estimation of value of  $\nu$ ,

$$\nu = 1.50 \pm 0.50.$$

## 4.5 New Data Analysis Method

Wickham and Dorsey verified that the AC conductivity satisfies the FFH scaling hypothesis and proposal a scaling function above  $T_c$ :[106]

$$S_+(y) = \frac{2z^2[1 - \frac{D-2-z}{z}iy - (1-iy)^{(D-2+z)/z}]}{y^2(D-2-z)(D-2)}, \quad (4.9)$$

where  $y = \omega\tau_{fl} \propto \omega\xi^z$ . We find at small  $y$ , corresponding to temperatures far above  $T_c$ , the function  $S_+(y)$  is essentially independent of dimensionality  $D$  and  $z$  because the fluctuation contribution is small far above  $T_c$ . According to Eq. 4.7, one can write  $\sigma_{fl}(T, \omega) = \sigma_0(T)S(\omega/\omega_0)$ . Both the phase  $\phi_\sigma (\equiv \tan^{-1}[\sigma_2^{fl}/\sigma_1^{fl}])$  of  $\sigma_{fl}$  and the magnitude  $|\sigma_{fl}|/\sigma_0$  can be treated as scaled quantities with two temperature-dependent scaling parameters  $\omega_0(T)$  and  $\sigma_0(T)$ . This suggests a new data collapse method, pioneered by Kitano *et al.*[112] They pointed out that the advantage of this new collapse method is the independence of the two scaling parameters  $\omega_0(T)$  and  $\sigma_0(T)$ . In this new method, the parameters  $\omega_0(T)$  and  $\sigma_0(T)$  are chosen at each temperature to collapse  $\phi_\sigma(T)$  vs.  $\omega/\omega_0$  and  $|\sigma_{fl}|/\sigma_0(T)$  vs.  $\omega/\omega_0$  to smooth and continuous curves, without *a priori* determination of  $T_c$  or critical exponents.

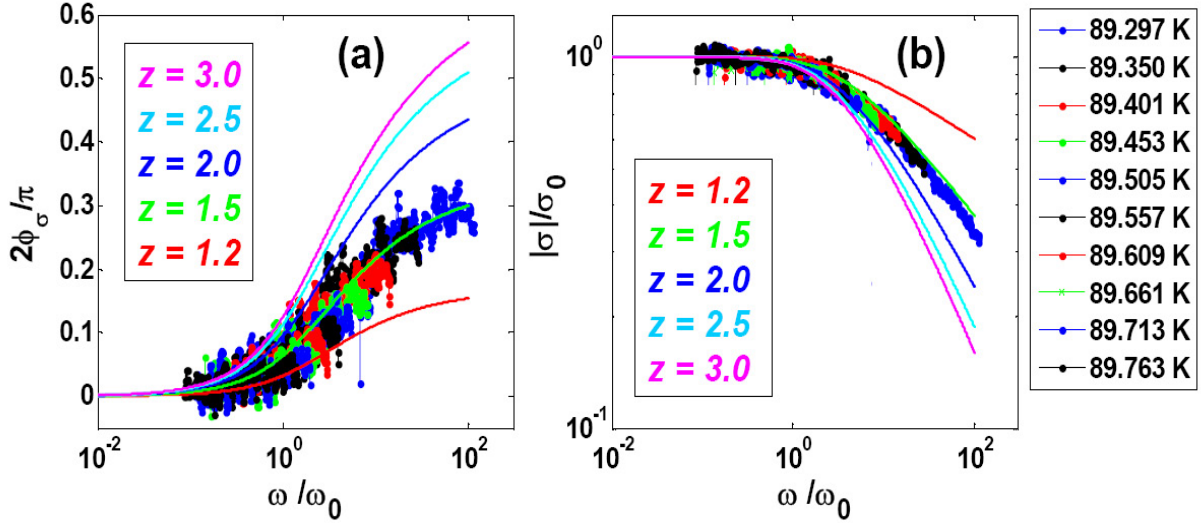


Figure 4.13: Scaling of phase and magnitude of fluctuation conductivity to determine  $\omega_0(T)$  and  $\sigma_0(T)$ . (a)  $\phi_\sigma$  vs.  $\omega/\omega_0(T)$ ; (b)  $|\sigma_{fl}|/\sigma_0(T)$  vs.  $\omega/\omega_0(T)$ . Solid lines are theoretical calculation from Eq. 4.9 for different values of  $z$ , assuming  $D = 3$ .

First  $\omega_0(T)$  is determined through a collapse plot of  $\phi_\sigma$  vs.  $\omega/\omega_0(T)$  from high temperature to low temperature. Using the feature that  $S_+(y)$  is not sensitive to

dimensionality  $D$  and  $z$  far above  $T_c$ , for temperature points far above  $T_c$ , the appropriate  $\omega_0(T)$  is chosen to make the measured  $\phi_\sigma(\omega/\omega_0(T))$  overlap with the theoretical prediction from the known scaling function  $\phi(S_+(y))$ . Then at temperatures closer to  $T_c$  where  $S_+(y)$  starts to depend on  $D$  and  $z$ ,  $\omega_0(T)$  for each temperature is chosen to connect smoothly to the existing curve of  $\phi_\sigma(\omega/\omega_0(T))$  and to make all the temperature curves collapse into one smooth and continuous curve. This process continues in the direction of lower temperature until a certain temperature where  $\phi_\sigma(\omega/\omega_0(T))$  can not be connected smoothly to the existing curve. In this way,  $\omega_0(T)$  for temperature points above  $T_c$  can be determined.

To scale the conductivity magnitude, we start with the determined  $\omega_0(T)$  for each temperature, then plot  $|\sigma_{fl}|/\sigma_0(T)$  vs.  $\omega/\omega_0(T)$ , where  $\sigma_0(T)$ , similarly to  $\omega_0(T)$ , is determined for each temperature to make a smooth and continuous curve of  $|\sigma_{fl}|/\sigma_0(T)$  vs.  $\omega/\omega_0(T)$ .

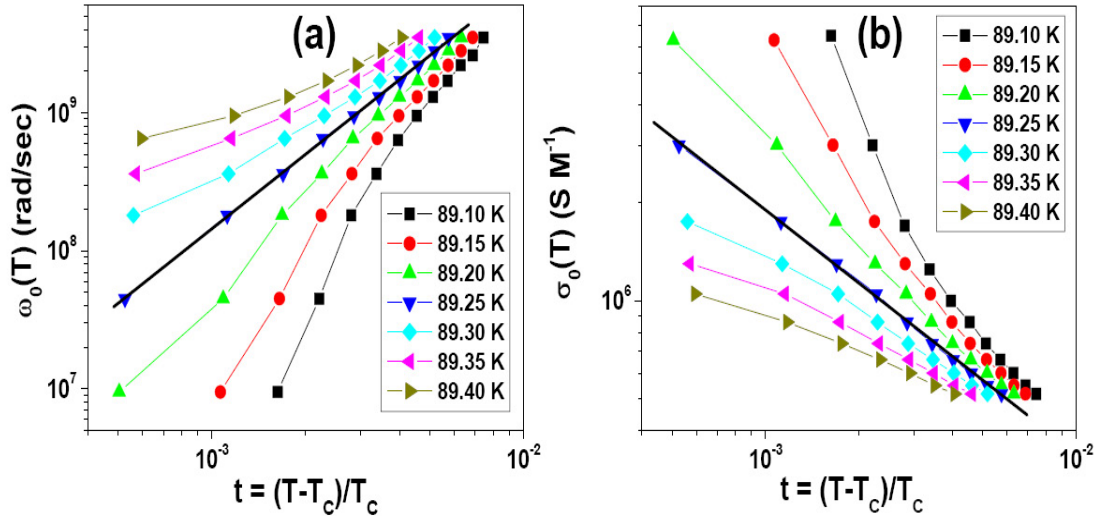


Figure 4.14:  $\omega_0(T)$  vs.  $t$  and  $\sigma_0(T)$  vs.  $t$  for different assumed  $T_c$ ,  $t = |(T - T_c)/T_c|$ , for sample xuh139 and temperature from 89.297K to 89.763K. The error bars of  $\omega_0(T)$  and  $\sigma_0(T)$  are about the size of points.

Fig. 4.13 shows the resulting scaling plots of  $\phi_\sigma$  vs.  $\omega/\omega_0(T)$  and  $|\sigma_{fl}|/\sigma_0(T)$  vs.  $\omega/\omega_0(T)$  with the determined  $\omega_0(T)$  and  $\sigma_0(T)$ . The solid lines are theoretical calculations from Eq. 4.9 for different values of  $z$  assuming  $D = 3$ . In Fig. 4.13(a), theoretical curves with larger values of  $z$  are at the top and curves with smaller values of  $z$  are at the bottom. In Fig. 4.13(b), the theoretical curves with larger values of  $z$  have larger slope and are at the bottom. Roughly the experimental data agrees with the green theoretical curve, which is  $z = 1.5$ .

From the determined  $\omega_0(T)$  and  $\sigma_0(T)$  further useful information can be obtained. With the assumption  $\xi = \xi_0|t|^{-\nu}$ ,  $\tau_{fl} = \tau_0|t|^{-\nu z}$  in the critical regime, which is about  $0.3K$  to  $2K$  wide for YBCO,[11, 114] the following dependencies should be expected:

$$\omega_0(T) \propto 1/\tau_{fl} \propto \xi^{-z} \propto |t|^{\nu z} \quad (4.10)$$

$$\sigma_0(T) \propto \xi^{z+2-D} \propto |t|^{-\nu(z+2-D)} \quad (4.11)$$

where  $t = (T - T_c)/T_c$  is the reduced temperature. An assumption is made here that for the correct  $T_c$ ,  $\omega_0(T)$  versus  $t$  will be a straight line in a log-log plot of slope  $\nu z$  and  $\log(\sigma_0)$  vs.  $\log(t)$  is a straight line of slope  $-\nu(z - 1)$ .

Using this power-law assumption,  $T_c$  can be determined. Fig. 4.14 shows  $\omega_0(T)$  vs.  $t$  and  $\sigma_0(T)$  vs.  $t$  for different assumed values of  $T_c$ . The correct  $T_c$  can be determined from the line showing a pure power-law. Fig. 4.14(a) shows that the blue line which corresponds to an assumed  $T_c = 89.25K$  is straightest. Fig. 4.14(b) also shows that the blue line is straightest. From these two figures,  $T_c$  is consistently determined to be

$$T_c = 89.25 \pm 0.03K.$$

According to Eq. 4.10, from the slope at  $T_c = 89.25K$  in the log-log plot, the critical exponents can also be determined. From Fig. 4.14 we find  $\nu z = 1.78 \pm 0.10$  and  $-\nu(z - 1) = -0.70 \pm 0.10$ , yielding

$$z = 1.64 \pm 0.20, \nu = 1.08 \pm 0.20.$$



This method offers an independent way to determine  $T_c$  and to extract the critical exponents  $z$  and  $\nu$ . The error of this method mainly comes from the choice of  $\omega_0(T)$  and  $\sigma_0(T)$ . Deciding which assumed  $T_c$  is correct in Fig. 4.14 does not bring much error. More data points for  $\omega_0(T)$  and  $\sigma_0(T)$  in the critical region can reduce the error of determine  $T_c$  and critical exponents.

## 4.6 Discussion

In the section, we have used two methods to extract  $z$  and  $\nu$  from experimental fluctuation conductivity data. The first one, an improved conventional method, is based on the assumption that  $|\sigma_{fl}| \approx \omega^{-(z+2-D)/z}$ ,  $\phi_\sigma = \frac{\pi}{2}(z+2-D)/z$  at  $T_c$ . In this method, determination of  $T_c$  is very crucial and the extracted  $z$  is sensitive to the determined  $T_c$ . The error in this method mainly comes from the determination of  $T_c$ . In the second method, which is newly developed in this thesis, we scaled the data and assumed the pure power-law behavior of  $\omega_0(T)$  and  $\sigma_0(T)$  on reduced temperature  $t$ . The assumption is only true for a certain temperature range near  $T_c$ . For sample xuh139, we find a good power law in the temperature range from  $T_c$  to  $T_c + 0.5K$ . From this, we have an estimation of the critical regime above  $T_c$ , which is about 0.5K wide. This estimation is consistent with that reported in the literature.[11, 91, 114] In this method, the error mainly comes from the determination of  $\omega_0(T)$  and  $\sigma_0(T)$ , through collapse. Although the directly extracted  $z$  and  $\nu$  from this method have large error, it is still useful because of its advantage of more precisely determining  $T_c$ .

The improved conventional method is good at determining the value of  $z$  for a given  $T_c$ . We can combine the advantages of the two methods together for better determination of critical exponents. Using the determined  $T_c$  from the new method to extract a value of  $z$  by doing temperature interpolation through Table 4.2, we get

$$z = 1.55 \pm 0.12.$$

According to the obtained slopes from Fig. 4.14,  $\nu$  can be determined

$$\nu = 1.15 \pm 0.2.$$

Here the value of  $z$  is better determined than the value of  $\nu$ . The determination of  $\nu$  uses the obtained value of  $z$  and slopes from Fig. 4.14. Both of them have error and make the value of  $\nu$  less well determined.

Comparing the results of the two methods we find that the determined  $T_c$  and dynamical critical exponents  $z$  are consistent. A combination of the two methods makes the result more stringent. Smaller temperature steps and more precise measurement of  $\hat{S}_{11}$  help to reduce errors and determine the critical exponents accurately.

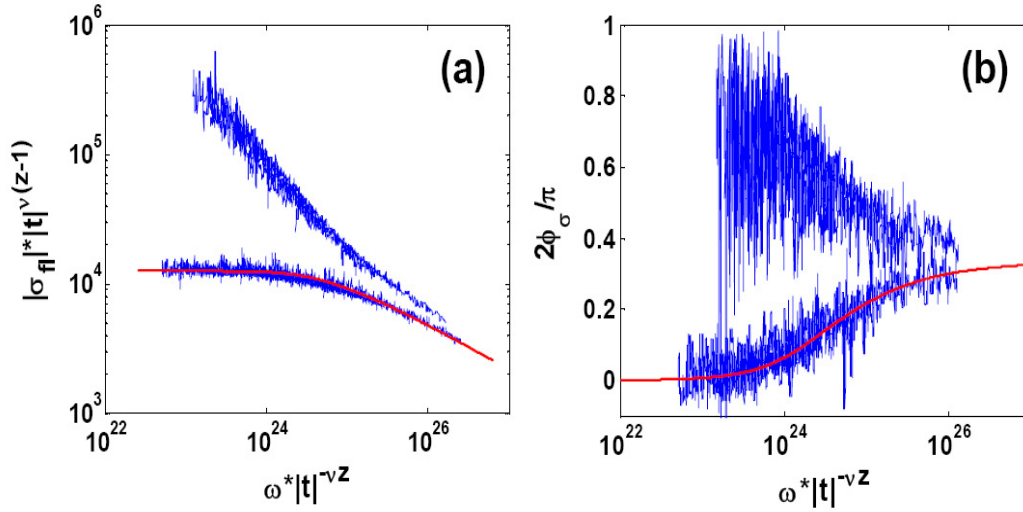


Figure 4.15: Data collapse as a check for  $T_c$ , critical exponent  $z$  and  $\nu$  for xuh139. The relatively good data collapse was obtained for  $T_c = 89.25K, z = 1.55, \nu = 1.15$ . Both magnitude and phase parts are consistent with the calculated result of the scaling function Eq.4.9, which are shown as red lines in the figure.

Finally data collapse can be used to verify the existence of a second-order phase transition. Fig. 4.15 shows that data collapse plots with the determined  $T_c$ ,  $z$  and  $\nu$

Table 4.3: critical temperature  $T_c \pm \Delta T_c$  and exponents determined for different YBCO film samples

<i>Sample</i>	Substrate	$T_c(K)$	$\Delta T_c(K)$	$z$	$\Delta z$	$\nu$	$\Delta \nu$
<i>xuh117</i>	NGO	88.90	0.05	1.60	0.15	1.40	0.30
<i>xuh130</i>	NGO	88.23	0.08	1.60	0.20	1.30	0.30
<i>xuh139</i>	NGO	89.25	0.03	1.55	0.12	1.15	0.20
<i>xuh142</i>	NGO	89.62	0.10	1.55	0.25	1.50	0.40
<i>xuh153</i>	NGO	89.97	0.05	1.50	0.15	1.20	0.30
<i>xuh156</i>	STO	89.66	0.10	1.70	0.30	1.30	0.40

look good. The scaled data above  $T_c$  is in excellent agreement with the Wickham-Dorsey scaling function  $S_+(\omega\tau_{fl})$  shown in red. By combining the two methods the critical temperature and exponents for this sample were determined:

$$T_c = 89.25 \pm 0.03K, z = 1.55 \pm 0.12, \nu = 1.15 \pm 0.20.$$

The critical exponents should be independent of sample. To check the results, I not only repeated measurement on the same sample, but also repeated my experiment on different samples. Films of different thickness were also examined, and the obtained values of  $z$  are independent of the thickness. Table 4.3 shows results on different samples. These samples are grown under nominally the same conditions and their properties are similar, so they could improve the statistics for the critical exponents.

From the table, we get critical exponents:

$$z = 1.56 \pm 0.10, \nu = 1.28 \pm 0.20.$$

We see the values of  $z$  for different samples are very consistent. The value of  $\nu$  is less precisely determined by this experiment and it has a larger error bar.

The dynamical critical exponent  $z$  is consistent with model-E dynamics of the 3D-XY universality class, which predict  $z \approx 1.5$  in 3D. Our recent DC conductivity measurements also gives  $z = 1.60 \pm 0.15$ , which will be discussed in chapter 7.

The static exponent  $\nu$  is bigger than the 3DXY prediction, although measurements on thermodynamic properties agree that  $\nu \approx 0.67$ . The large value of  $\nu$  is found by many transport measurements.[115] For example, Booth *et al.* obtained  $\nu = 1.2$ ;<sup>[91]</sup> Strachan *et al.* obtained  $\nu = 1.5$ .<sup>[95]</sup> It is also predicted by some theorists: Lidmar *et al.* predicted  $\nu \approx 1.3$  and Olson *et al.* obtained  $\nu = 1.39 \pm 0.20$  for a sample in a magnetic field.<sup>[79][116]</sup> Peligrad *et al.* claimed that  $\nu = 1$  close to  $T_c$  and crosses over to  $\nu = 2/3$  at the higher temperature range  $0.05 < t < 0.12$  for YBCO.<sup>[105]</sup> In this chapter we investigated microwave conductivity at temperatures very close to  $T_c$ , so that  $\nu$  is determined in the temperature range  $t < 0.004$ . In a temperature range very close to  $T_c$ , sample disorder may affect the value of  $\nu$ , which makes the value obtained here larger than what is expected. However, the dynamical critical exponent  $z$  obtained by AC measurement should not be affected by the disorder.<sup>[117]</sup>

In this chapter, we investigated fluctuation effects in  $\text{YBa}_2\text{Cu}_3\text{O}_{7-\delta}$  thin films around  $T_c$  by taking frequency-dependent microwave conductivity measurements. We proved that the determination of  $T_c$  is crucial for the conventional data analysis method. With an improved setup, we took measurements at a smaller temperature increments than ever before. Through an improved conventional data analysis method and a newly developed analysis method, the critical temperature can be determined precisely. We obtained a critical exponent  $z = 1.56 \pm 0.10$ , which is consistent with model-E dynamics of the 3D-XY universality class. Finally the scaling behavior of the fluctuation conductivity was also shown both above and below the critical temperature.

## Chapter 5

# Power Dependence of the Microwave Fluctuation Conductivity

Microwave conductivity measurements as a method to test scaling theory and to obtain the critical exponents has been discussed in chapter 4. When measuring AC conductivity, one needs to apply a certain current. In chapter 4, I determined the  $T_c$  and obtained the critical exponents with very small applied microwave power, -46dBm. One natural question is whether a -46dBm microwave power is small enough to measure the linear response fluctuation conductivity. The other question is how the different applied microwave current density affects the conductivity and the extraction of the critical exponents. I will address these two questions in this chapter.

### 5.1 Power Dependent Measurements

High power incident microwaves, corresponding to high current density in the sample, will cause pair breaking of the fluctuating Cooper pairs, decreasing the fluctuation conductivity. The breaking of Cooper pairs by high power microwaves is an interesting topic, which is being investigated by another student in our group, Dragos Mircea. In my experiment, I also observed a decrease of fluctuation con-

ductivity due to high incident microwave power. In addition, for lower power, there is a linear region, in which the microwave conductivity is independent of incident power. In the study of DC fluctuation conductivity, Sullivan *et al.* discussed low current density behavior and the existence of a current-induced length scale.[94]. This brings up the question of whether and how the current-induced length scale affects the microwave conductivity. As sketched in Fig. 5.1, I want to investigate the microwave conductivity at very low current density. This investigation, combined with the research of others, is not only helpful to clarify theoretical questions about the critical exponents, but also important in applications for HTS materials.

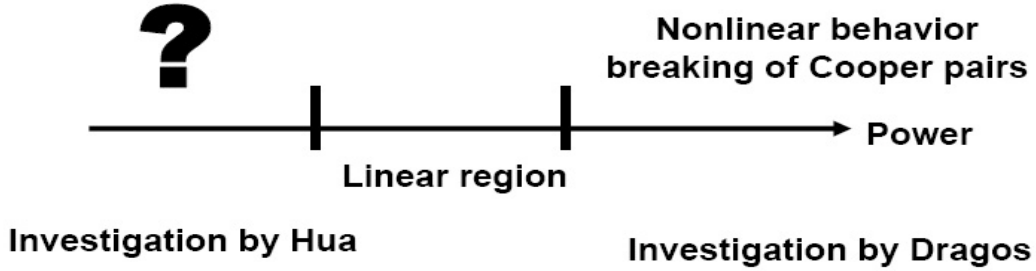


Figure 5.1: Sketch of the power region for frequency dependent fluctuation conductivity.

Although lots of experimental and theoretical work has been done to investigate fluctuation effects, there has been no unified framework that describes the phase transition of the superconducting state to the normal state in HTSC up to now. The possibility of obtaining superconducting properties by cooling down HTSC materials with liquid nitrogen at low cost has fueled a series of commercial applications. One of the applications of HTSC is to make high-field magnets. Whereas the  $H_{c2}$  of HTSC is large, researchers have only achieved 1T field with HTSC magnets at 77 K. A clear picture of the properties of HTSC near  $T_c$  is needed to build high

field magnets within the liquid nitrogen temperature range. The other significant application of HTSC is in the area of microwave passive components (resonators and filters). Compared with devices fabricated from normal metals, HTSC devices have lots of advantages. However, a serious issue in the operation of HTSC microwave passive components arises when the surface impedance becomes power-dependent and undesirable nonlinear effects can ultimately compromise the benefits of using HTSC components. To minimize the nonlinear response of HTSC microwave components, it is necessary first to understand the nonlinear response of the HTSC material. To address this issue, there has been much recent work examining the nonlinear (rf power dependent) surface impedance.[118] However, most of the work concentrates on the large power end and there are few measurements investigating nonlinear surface impedance for the small power end.

In this chapter, I will discuss the microwave conductivity of  $\text{YBa}_2\text{Cu}_3\text{O}_{7-\delta}$  thin films around  $T_c$  for different input microwave powers. I will focus on how the microwave fluctuation conductivity deviates from simple scaling theory and how the deviations systematically depend on the input microwave power at low frequency.

For the power dependent measurement, we still use the Corbino setup to investigate YBCO films deposited via pulsed laser deposition on NGO(110) substrates. To investigate the power dependence property of the conductivity, frequency-independent constant applied power is necessary for the measurement. Power-flattening calibrations are carried out at the sample plane for different incident power ranges from 0dBm to -50dBm. After the power-flattening calibrations, the room temperature calibration is performed for every different incident power. After this, the YBCO sample is put in and the system is cooled down. At each temperature around  $T_c$ , microwaves with different power were incident on the sample, and reflection coefficients depending on frequency were measured. Similar to the procedure in Chap. 4, we obtained the conductivity vs. frequency for different incident microwave power around  $T_c$ .

## 5.2 Power Dependent Fluctuation Conductivity Phenomena

### 5.2.1 Nonlinearity Effects of Microwave Fluctuation Conductivity $\sigma_{fl}$ –High Power End

To see how nonlinearity affects microwave fluctuation conductivity, we plotted the fluctuation conductivity vs. frequency for various temperatures at different incident microwave power in Fig. 5.2. The blue lines were measured with -22dBm of power while the red lines were measured with -2dBm at the same temperature.

Fig. 5.2 clearly shows that the applied microwave power affects the measured fluctuation conductivity, particularly at low frequencies. As the applied power increases, the current density also increases and it decreases the magnitude of the fluctuation conductivity, which is shown in Fig. 5.2(a). Fig. 5.2(b) shows that the phase part of the fluctuation conductivity is also affected by the applied current density. Larger current density tends to decrease the phase. Particularly at low frequency, larger current density makes the phase part tend to zero, which corresponds to ohmic response. The reason is that the critical point is located in the limit of zero  $H$ ,  $J$ , and  $\omega$  and the increased applied current should drive the system away from the transition and thus into the ohmic regime. This is in fact seen in the red line deviations of Fig. 5.2(b).

Although at low frequency the current density clearly affects the fluctuation conductivity, it has less effect at higher frequencies. To explain this, let us review the Fisher, Fisher and Huse(FFH)[54] dynamic scaling function first:

$$\frac{E}{J} = \xi^{D-2-z} \chi_{\pm}(J\xi^{D-1}, \omega\xi^z, H\xi^2, \dots). \quad (5.1)$$

In our measurement, the magnetic field  $H$  is small and the scaling dependence on  $H\xi^2$  can be ignored. Then there are two terms left in the scaling function  $J\xi^{D-1}$



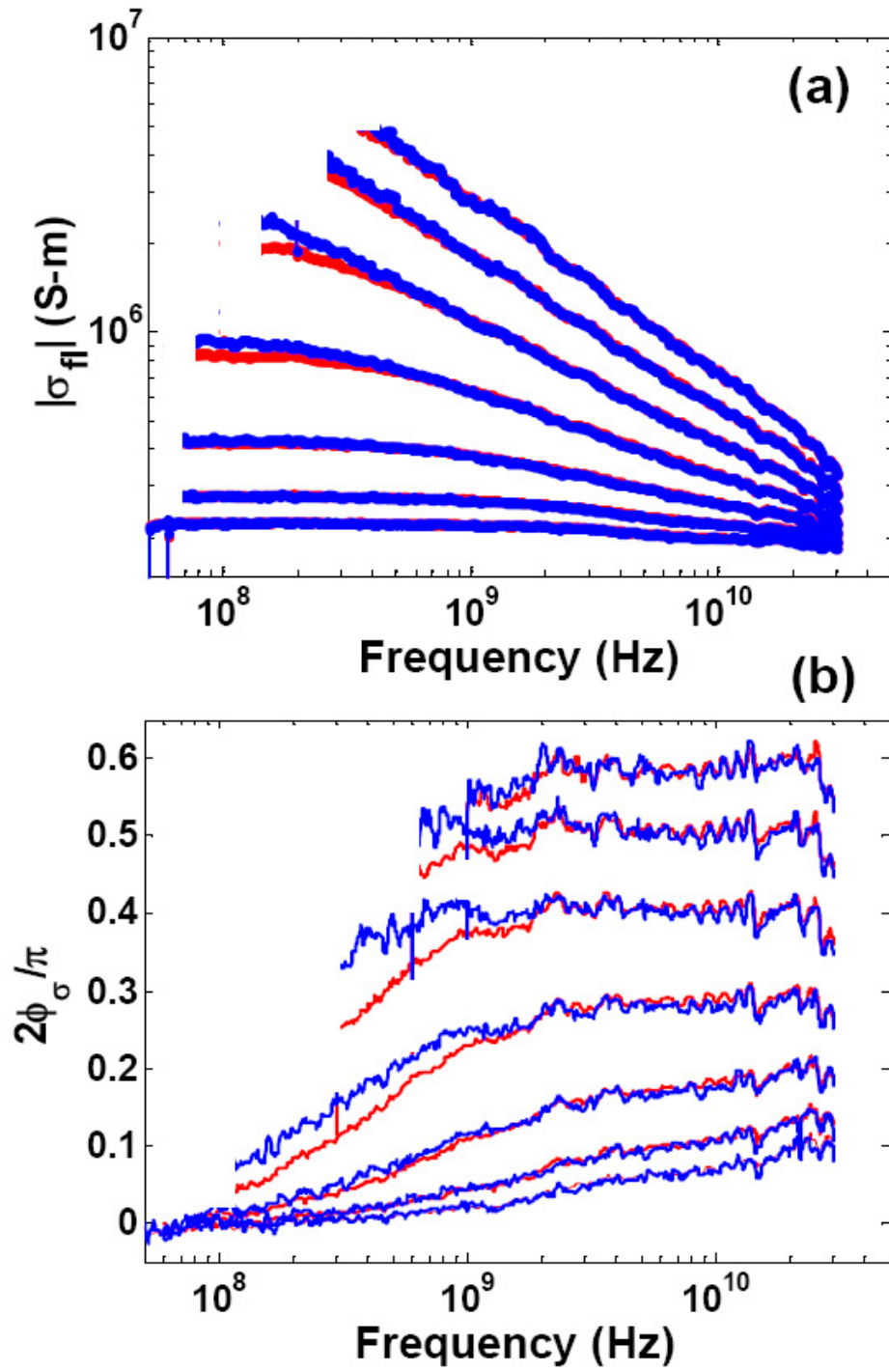


Figure 5.2: Magnitude  $|\sigma_{fl}|$  and phase  $\phi_{\sigma}$  vs. frequency for various temperatures. The blue lines were measured with -22dBm of power while the red lines were measured with -2dBm at the same temperature.

and  $\omega\xi^z$ . For higher frequency, the later term  $\omega\xi^z$  is much larger than  $J\xi^{D-1}$ , so the current density has less effect at high frequency. At low frequency,  $\omega\xi^z$  is small, so the current density, corresponding to the term  $J\xi^{D-1}$ , has more of an effect on the fluctuation conductivity.

In order to determine the correct critical exponents we need to reduce the  $J\xi^{D-1}$  term, so we performed the AC measurements at an incident microwave power of -46 dBm, corresponding to current density  $2.2 \times 10^5 A/m^2$  at the inside edge of the Corbino ring, which is very small and also still gives relatively good sensitivity. One question here is whether -46 dBm is small enough. This will be discussed later by combining both AC and DC experiments on the same sample. Before we move to that, we will focus on the AC measurements first, since there are still some interesting phenomena to reveal.

### 5.2.2 Low Frequency Downward Curvature of Fluctuation Conductivity $|\sigma_{fl}(\omega)|$

In the last chapter, using -46 dBm data the critical temperature  $T_c = 89.25 \pm 0.03$  K was determined for sample xuh139. Fig. 5.3(a) shows that the data agree with scaling theory at high frequency. Very close to  $T_c$ , the  $|\sigma_{fl}|$  vs. frequency is a straight line which means a power law behavior. However, at low frequency,  $|\sigma_{fl}(\omega)|$  starts to deviate from scaling behavior and has a down turn. In the previous section we found that the larger applied current density affects the fluctuation conductivity at low frequency. Here we examine how the low frequency deviation and the down turn behavior depend on the applied current density.

Fig. 5.3(b) shows the  $|\sigma_{fl}|$  vs. frequency for different incident microwave power at a fixed temperature. At high frequency, all five curves would overlap with each other if they had not been displaced vertically. The fluctuation conductivity is almost independent of incident microwave power at high frequency. Quantitatively,

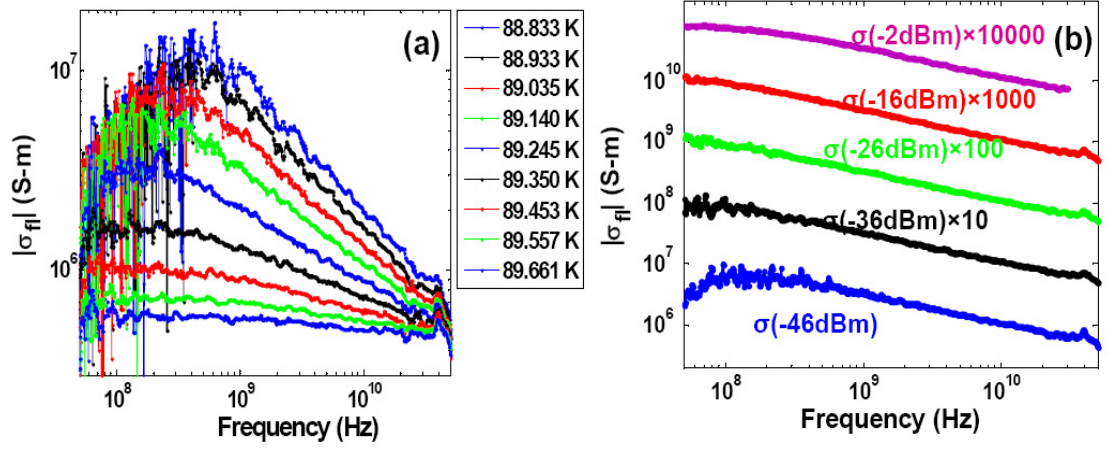


Figure 5.3: (a)  $|\sigma_{fl}|$  vs. frequency at different temperature for input power -46dBm; (b)  $|\sigma_{fl}|$  vs. frequency at a fixed temperature ( $T=89.140$  K) for different power. To show the differences at low frequency clearly, the curves are offset vertically.

the fit slopes of  $\log |\sigma_{fl}|$  vs.  $\log(f)$  of different powers are the same for frequencies larger than  $0.4\text{GHz}$ .

### 5.2.3 Confidence Check of the Downturn Behavior

The observed power dependent downturn behavior above has not been reported before. There are also no theoretical predictions for this. So before we do some analysis and detailed discussion about this phenomenon, we want to make sure that it is real and not coming from some systematic errors.

To check the reliability, I did several things. At first, I repeated the measurement on other samples. Similar behavior is observed on different YBCO samples and also on samples with various thicknesses.

Secondly, I checked the calibration procedure. The re-calibration method that I use here is the short-only one assuming that the superconducting film far below  $T_c$  is

a perfect conductor. Here firstly I compared the reflection coefficient  $\hat{S}_{11}$  of a YBCO film at 10 K below  $T_c$  and the  $S_{11}$  of a bulk silver disk at the same temperature. I found that both real and imaginary parts of  $S_{11}$  of them are almost the same, particularly at low frequency. The difference between them is less than 0.05dB from 10MHz to 25GHz. There are larger differences at very high frequency. These differences are due to the ir-reproducibility of the connection, because the  $\hat{S}_{11}$  is very sensitive to the connection at very high frequency.

I also tried different calibration methods. For example, using bulk silver as a perfect short, and a teflon disk as a perfect open, I did a 2-standards re-calibration. Adding another perfect load (using the difference of the YBCO sample at two temperatures above  $T_c$ ), we also did a 3-standards full re-calibration. The different calibration methods only affect the high frequency data, normally above 10 GHz. However, the low temperature downturn behaviors remain for all the different calibration methods.

Finally, we systematically checked our data processing programs. Professor An-lage used GL theory with Gaussian fluctuations and calculated the conductance for a given thickness YBCO film around  $T_c$  from 10 MHz to 50 GHz. Then he simulated the reflection coefficient based on the conductance data. He also applied error coefficients to the  $\hat{S}_{11}$ . With this 'calculated data file' and the error coefficients, I recovered the conductivity of the YBCO film with my data processing programs successfully. The recovered data is exactly the same as calculated from the model.

According to the above confidence check procedures, I believe that our observed downturn behaviors at low frequency are real, despite the fact that they had not been predicted.

### 5.2.4 Power Dependent Fluctuation Conductivity at Low Frequency

$|\sigma_{fl}|$  vs. incident microwave power at different frequencies are plotted in Fig. 5.4. It is clear that the power dependence behavior of  $|\sigma_{fl}|$  varies with frequency. At lower frequency  $|\sigma_{fl}|$  depends on incident microwave power more than at higher frequency. Fig. 5.4 also shows that at higher frequencies (1 GHz, 5 GHz)  $|\sigma_{fl}|$  has almost no power dependence. As frequency decreases, the incident microwave power starts to affect the  $|\sigma_{fl}|$  and the power dependence becomes stronger. At low frequencies (20MHz, 30MHz and 40MHz),  $|\sigma_{fl}|$  strongly depends on the incident power. For these frequencies,  $|\sigma_{fl}|$  vs. incident power increases first as applied power increases. At some incident power,  $|\sigma_{fl}|$  saturates and becomes power independent. However, at very high power, the  $|\sigma_{fl}|$  decreases again.

### 5.2.5 Applied Current Amplitude

The applied power is directly related to the current density appearing in the sample. By calculating the time averaged power flowing down the coaxial cable, we can approximately calculate the applied AC current density.

In general, TEM modes have transmission line signals which behave as

$$V = F_+(t - x/s) + F_-(t + x/s) \quad (5.2)$$

$$I = \frac{1}{Z_0} [F_+(t - x/s) - F_-(t + x/s)], \quad (5.3)$$

where  $t$  is time,  $x$  is distance along the coax line, and  $s$  is the velocity of the signal. The above voltage  $V$  refers to the voltage differences between the inner and outer conductors of the coax cable at same position  $x$  and  $I$  refers to the longitudinal current following in the inner conductor.

In the Corbino disk geometry the rf currents flow in the radial direction, and the rf current density in the film is proportional to  $1/r$ , where  $r$  is the distance from the

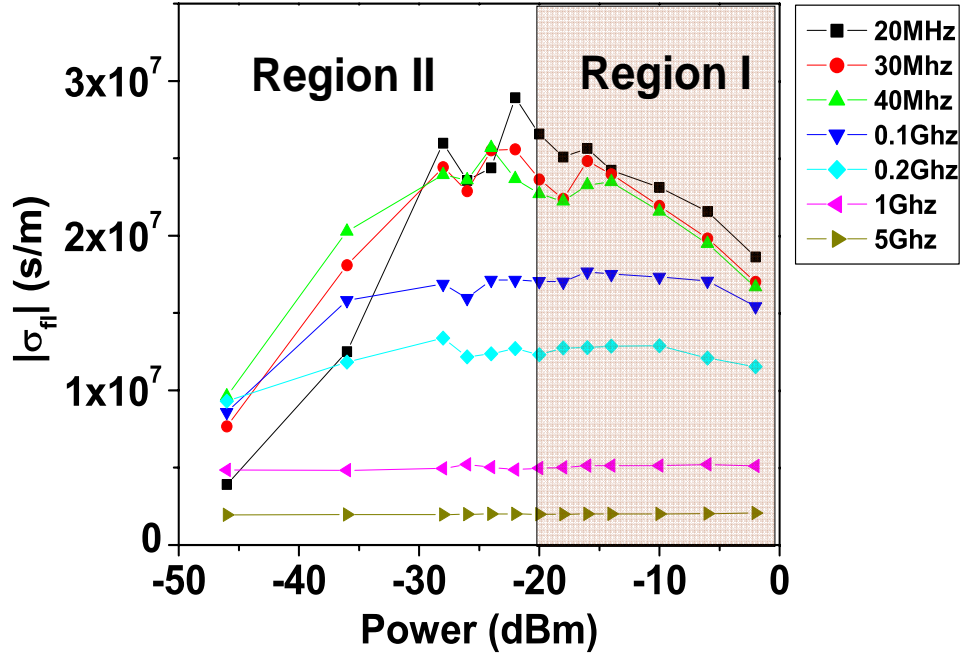


Figure 5.4:  $|\sigma_{fl}|$  vs. incident microwave power at different frequencies at a fixed temperature of 89.087 K for sample xuh139.

center of the Corbino disk. The rf current density also depends on the film thickness and the rf power supplied by the source. If the sample is much thinner than the appropriate skin depth, the current density will be uniform in the film thickness. Integrating the current density  $J(r)$  over the volume of the Corbino disk, we should obtain the applied current  $I$ , which gives

$$J(r) = I/2\pi t_0 r, \quad (5.4)$$

where  $t_0$  is the film thickness.

The incident power  $P$  transferred along the transmission line is given by the Poynting vector  $P = (E \times H)$  integrated over the cross section of the transmission

line, which gives simply  $P = I \cdot V$ . The incident power is usually given as the time averaged power  $\langle P \rangle$

$$\langle P \rangle = \frac{1}{2} I_{max} V_{max} = \frac{1}{2} \frac{V_{max}^2}{Z_0}. \quad (5.5)$$

In the following discussion, I will use average  $V_{ave}$  and  $I_{ave}$  ( $V_{ave} = V_{max}/\sqrt{2}$  and  $I_{ave} = I_{max}/\sqrt{2}$ ). For convenience, the subscript 'ave' will be omitted.

According to Eq. 5.2

$$V_0^+ = \sqrt{P * Z_0}, \quad (5.6)$$

$$V_0^- = V_0^+ \frac{Z_L - Z_0}{Z_L + Z_0} = V_0^+ S_{11} \quad (5.7)$$

where  $Z_0$  is the characteristic impedance of the coaxial cable and  $Z_L$  is the lumped impedance of the sample. The current traveling through the sample is

$$I = (V_0^+ - V_0^-)/Z_0 = (1 - \hat{S}_{11})\sqrt{P Z_0} \quad (5.8)$$

$$J(r) = (1 - S_{11}) \frac{\sqrt{P/Z_0}}{2\pi r t_0} \quad (5.9)$$

Here  $J(r)$  is the time averaged current density at the distance  $r$  from the center of the Corbino disk.

In Fig. 5.5, I show the corresponding current density for different incident microwave powers for a film thickness of  $1300 \text{ \AA}$ . The black solid line denotes the current density at the inside edge the Corbino disk where the current density is larger than what is at the outside edge. The red dotted line gives the current density at the outside edge of the Corbino disk.

In a typical DC I-V curve measurements on films of comparable thickness, we found that when the current density is below  $1 \times 10^6 A/m^2$ , it is in the pure ohmic regime. When the current density is above  $2 \times 10^7 A/m^2$ , the sample shows power-law V-I behavior around  $T_c$ . The current density from  $1 \times 10^6 A/m^2$  to  $2 \times 10^7 A/m^2$  is a transition regime.

For -46 dBm incident power, the time averaged current density at the inside edge of the Corbino disk around  $T_c$  is  $J \approx 2.2 \times 10^5 A/m^2$ . This current density

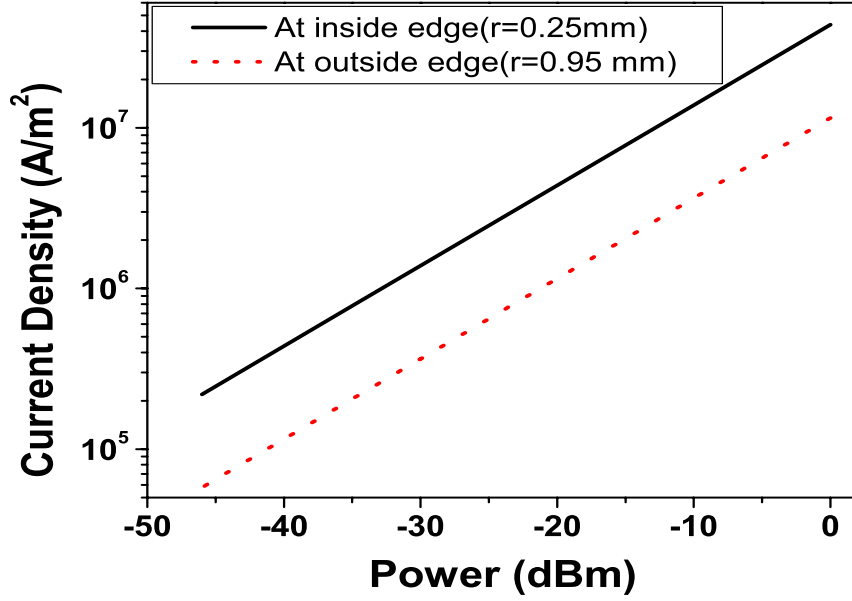


Figure 5.5: Corresponding current density vs. incident microwave power for a film thickness  $1300 \text{ \AA}$  in the Corbino geometry with  $\hat{S}_{11} \approx -1$ .

is very small and corresponds to the pure ohmic regime in DC I-V measurements. Therefore nonlinearities due to breaking of the fluctuating Cooper pairs by current density can be ignored for this applied microwave power.

For the incident microwave power of  $-2 \text{ dBm}$ , the corresponding current density at the inside edge of the Corbino ring is  $3.4 \times 10^7 \text{ A/m}^2$  around  $T_c$ . From the mentioned DC measurements discussed above, we know this current density is large enough to show clear nonlinearity in the V-I curves. Hence it is not surprising to see clearly a conductivity decrease, particularly at low frequency. Hence the AC and DC measurements are consistent with respect to current density nonlinearities.



### 5.3 Analysis and possible explanation

After Fisher, Fisher and Huse[54] discussed dynamic scaling for the ac fluctuation conductivity, Wickham and Dorsey did a theoretical calculation and gave the form of the scaling function  $S_+(y)$  above  $T_c$  [106]. Peligrad *et al.* investigated the short-wave length cutoff effects of the AC fluctuation conductivity of superconductors and discussed the limitation of the scaling theory[105]. The high frequency behavior, which is the power-independent part, is consistent with these theoretical works. However, the power dependence behavior at low frequency showed by Figs. 5.3 and 5.4 can not be explained by these theories.

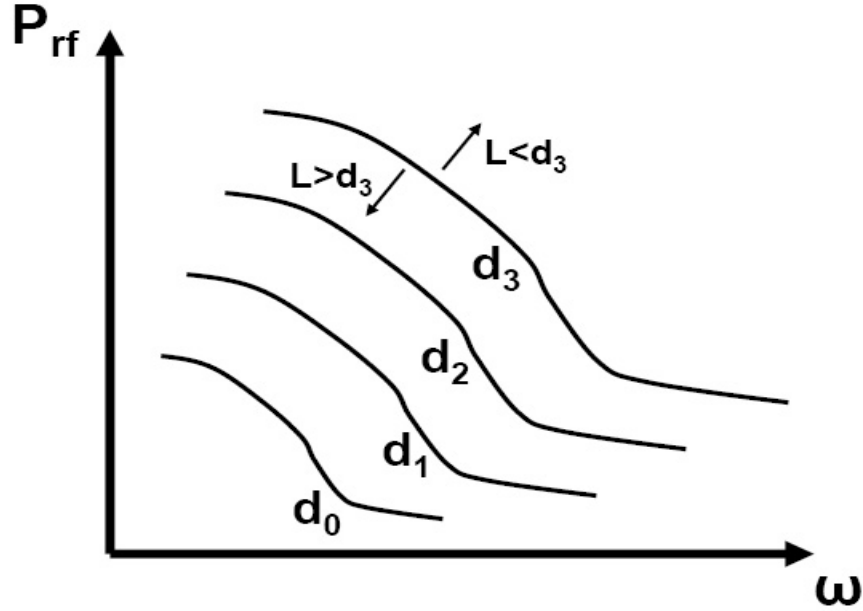


Figure 5.6: Sketch of the power, frequency and thickness relation in frequency dependent fluctuation conductivity.  $d_0, d_1, d_2, d_3$  correspond to different thickness and  $d_0 > d_1 > d_2 > d_3$ . The lines denote the locus of  $(P_{rf}, \omega)$  points where the probed length scale  $L$  is equal to the thickness of the film. The probed length scale  $L$  is shorter than thickness  $d$  outside the line, and longer than the thickness inside the line.

Since the applied power is directly related to the current density, it makes us consider the effect of current density first. In a simple physical model, fluctuations can be assumed as closed circular vortex loops of radius  $\mathbf{r}$ . In an infinite superconductor with no applied current, vortex loops of different size occur with different probabilities as thermal fluctuations. When a current with density  $J$  is applied, some vortex loops (with large  $\mathbf{r}$ ) will blow out to infinite size; this process leads to dissipation. Some vortex loops (with small  $\mathbf{r}$ ) shrink and annihilate; this process leads to no dissipation. The current density induced length scale separates vortex loops into two categories, depending on their ultimate fate. The shrinking of a vortex takes time. The shrinking time depends on the size of the vortex. Smaller vortices shrink faster than larger vortices and this corresponds to smaller time scales. So this makes the size of a vortex related to a time scale. In AC measurements, small frequency means large length scale, so one investigates large size vortex loops. For the real measurement, the samples have finite size. The size of the sample will limit the size of the vortex. The above thoughts are a qualitative discussion about the possible length scales in AC measurement.

The effect of a current-induced length scale has been discussed by Sullivan *et al.* for the normal state to superconducting state phase transition in zero field[94]. From their work, an applied current density  $J$  probes fluctuations of typical size  $L_J = (ck_B T / \Phi_0 J)^{1/2}$ , where  $\Phi_0$  is the magnetic flux quantum and  $c$  is a constant. Hence as power decreases,  $J$  decreases and  $L_J$  increases. The similarity of dynamical scaling of the ac fluctuation  $\sigma_{fl}(T, \omega) \approx \xi^{z+2-D} S_{\pm}(\omega \tau_{fl})$  and the dc scaling  $E/J \approx \xi^{D-2-z} F_{\pm}(J \xi^{D-1})$  makes us consider the possibility of a typical frequency probed length scale of the microwave measurement,  $L_{\omega}$ . Low frequency probes larger sizes and high frequency probes smaller sizes. At low frequency and small power, both  $L_J$  and  $L_{\omega}$  increase. The probed length scale may be affected by both  $L_J$  and  $L_{\omega}$ , and may also be limited by the thickness of the sample. This then may cause the unusual power dependence behavior. This is rough thinking at the moment and a

schematic diagram of the relation between power, frequency and thickness is shown in Fig. 5.6.

### 5.3.1 Current-induced Length Scale

To understand the dissipation process near the phase transition, I discuss in detail the current-induced length scale and its physical meanings in Appendix A. Here I will just give a brief introduction to this length scale. Basically, assuming  $\varepsilon(r)$  is the energy per unit length of the vortex loop of radius  $r$ , then the energy of such a loop can be written as

$$U_{loop} = 2\pi r \varepsilon(r) \quad (5.10)$$

Plausibly we can assume that the typical total energy of a planar vortex loop of size  $r_{thermal}$  is equal to  $k_B T$ . Then simply we have

$$r_{thermal} = \frac{k_B T}{2\pi \varepsilon}. \quad (5.11)$$

Next consider that a current per unit area  $J$  is applied to a plane perpendicular to the area of the loop. The total Lorentz force on the loop is

$$F_{ext} = 2\pi r J \Phi_0. \quad (5.12)$$

Taking minus one times the derivative of Eq. 5.10 gives the force that the loop exerts on itself. Summing the forces and finding the point where the force is equal to zero leads to a critical loop size

$$r_{blowout} = \frac{\varepsilon}{\Phi_0 J}, \quad (5.13)$$

where, for simplicity,  $\varepsilon(r)$  is assumed to be independent of  $\mathbf{r}$ .

Physically, if a vortex loop has  $r > r_{blowout}$ , the external current "blows out" the loop to infinite size; this process leads to dissipation. If  $r < r_{blowout}$ , the vortex loop shrinks and annihilates.

Here is the physical significance of comparing the lengths,  $r_{blowout}$  and  $r_{thermal}$  to each other. If  $r_{thermal} \ll r_{blowout}$ , the current is probing a length scale where there are very few vortices. The current thus acts as a very small perturbation on the system. If  $r_{thermal} \gg r_{blowout}$ , the current is probing a very short length scale, and a large portion of the intrinsic vortex population is being disrupted by the current. The point where  $r_{thermal} = r_{blowout}$  thus marks a crossover in the behavior from current acting as a small perturbation to current acting as a large perturbation.

What is the physical significance of comparing the various lengths,  $r_{blowout}$  and  $r_{thermal}$ , Eqs. A.8 and A.10, to the film thickness  $d$ ? It is plausible to say  $r_{thermal} \ll d$  is the three-dimensional limit, while  $r_{thermal} \gg d$  is the two-dimensional limit, since in the second case most of the vortex loops are interrupted by the film thickness, while in the first case they are not. This is true as far as it goes, but it misses the key point that an applied current probes physics at the scale of  $r_{blowout}$  and larger, as discussed above. Thus, even in the limit  $r_{thermal} \gg d$ , if  $r_{blowout}$  is small enough, it will probe physics on length scales smaller than  $d$ , and thus the measurement will not be affected by the finite thickness of the film. *What is required is that the current probes a significant fraction of the loop population and also probes lengths on the scale of the film thickness.* For this to be true, it is reasonable to require that

$$r_{blowout} = r_{thermal} \equiv L_J \quad (5.14)$$

Combining Eqs. A.8, A.10 and A.11 gives

$$L_J = \left( \frac{kT}{2\pi\Phi_0 J} \right)^{\frac{1}{2}} \quad (5.15)$$

This suggests the following physical description for  $L_J$ : For any  $J$  there is a length scale  $L_J$ , given by Eq. A.12, such that roughly half the equilibrium (zero current) vortex population is blown out by  $J$ , and the other half are not. This is the length that one should compare to the film thickness for seeing whether or not the measurements are in the two or three dimensional limit. The requirements are that there

be a significant fraction of the loops that feel the film thickness, and, in addition, that the current is probing the same length scale.

### 5.3.2 Frequency-induced Length Scale

In this section, we will discuss the frequency-induced length scale. First, we start from the time dependent Ginzburg Landau(TDGL) theory to deduce the frequency-induced length scale.

#### Frequency induced length scale from TDGL theory

The coherence length near  $T_c$  can be written in the following form according to Eq. 4.24 of Tinkham's book ([15])

$$\xi(T) = 0.74 \frac{\xi_0}{(1-t)^{1/2}}, \text{pure} \quad (5.16)$$

$$\xi(T) = 0.855 \frac{(\xi_0 l)^{1/2}}{(1-t)^{1/2}}, \text{dirty} \quad (5.17)$$

where  $\xi_0 = a \frac{\hbar V_F}{k_B T_c}$  and  $a = 0.18$  for BCS theory. When discussing the time dependence of fluctuations, Tinkham also gave a relaxation time for fluctuations of wave number  $k$ :

$$\tau_k = \frac{\tau_0}{1 + k^2 \xi^2} \quad (5.18)$$

$$\tau_0 = \frac{\pi \hbar}{8 k_B (T - T_c)}. \quad (5.19)$$

Now let us make Eq. 5.18 look like a scaling relation. To do this, we rewrite Eq. 5.16 as

$$\xi(T) = \frac{\xi(0)}{(1-t)^{1/2}} \quad (5.20)$$

Note that  $\xi(0) \neq \xi_0$ . Then  $1-t = [\frac{\xi(0)}{\xi(T)}]^2$ , plug this into Eq. 5.18, which can be written

$$\tau_0 = \frac{\pi \hbar}{8 k_B T_c} \frac{1}{|1-t|} \quad (5.21)$$

To get

$$\tau_0 = \frac{\pi\hbar}{8k_B T_c} \left[ \frac{\xi(T)}{\xi(0)} \right]^2 \quad (5.22)$$

Multiply both sides of the above equation by  $\omega$ :

$$\omega\tau_0 = \omega \frac{\pi\hbar}{8k_B T_c} \left[ \frac{\xi(T)}{\xi(0)} \right]^2 \quad (5.23)$$

This suggests defining an  $L_\omega$  such that

$$\omega L_\omega^2 \frac{\pi\hbar}{8k_B T_c} \frac{1}{\xi(0)^2} \equiv C, \quad (5.24)$$

where  $C \sim 1$ , then

$$L_\omega = \left[ \frac{8C}{2\pi^2} \frac{k_B T_c}{\hbar} \frac{1}{f} \right]^{1/2} \xi(0). \quad (5.25)$$

Taking  $T \sim 90K$ ,  $k_B = 1.38 \times 10^{-23} J/K$  and  $\hbar = 1.05 \times 10^{-34} J \cdot s$ , we get

$$L_\omega = 2.19 \times 10^6 \left[ \frac{C}{f} \right]^{1/2} \xi(0), \quad (5.26)$$

where  $f$  is in Hz. This is quite interesting, and suggests that a cross over frequency (where  $L_\omega =$  film thickness) may play a role at the lower end of our frequency range.

The next thing to do is to generalize to the case where  $z \neq 2$ . Starting with Eq. 5.22, write

$$\tau_0 = \frac{\hbar}{k_B T_c} \left[ \frac{\xi(T)}{\xi(0)} \right]^z \quad (5.27)$$

An analog of Eq. 5.25 can be obtained

$$L_\omega = \left[ \frac{8C}{2\pi^2} \frac{k_B T_c}{\hbar f} \right]^{1/z} \xi(0) \quad (5.28)$$

Here  $L_\omega \sim f^{-1/z}$  obeys the scaling ansatz. Numerically

$$L_\omega = \left[ \frac{4.79 \times 10^{12} C}{f} \right]^{1/z} \xi(0) \quad (5.29)$$

## Frequency-induced length scale from other models

Petter Minnhagen gave a systematic review of the two-dimensional Coulomb gas model and its connection to vortex fluctuations in two-dimensional superfluids.[186] In his paper, he discussed the frequency-dependent screening and gave the following dynamical length scale

$$L_\omega = \sqrt{\frac{14D}{\omega}} \quad (5.30)$$

where  $D$  is called the dissipation constant, which can be written as  $k_B T \cdot \tilde{\mu}$ ,  $\tilde{\mu}$  is vortex mobility

$$\tilde{\mu} = \frac{(\xi e^*)^2}{2\hbar^2 \pi \sigma_N}, \quad (5.31)$$

where  $\sigma_N$  is the 2D conductivity, and can be approximated as  $\sigma_{3D} \cdot \xi$  ( $\xi \sim 10\text{\AA}$ ).

The  $L_\omega$  deduced from the two different methods above have some differences. However, both of them have similar frequency dependent behavior. In addition, for the same frequency, the calculated  $L_\omega$  from the two methods are close. In the following discussion, we will use a frequency-induced length scale from Minnhagen's paper, which is

$$L_\omega = \sqrt{\frac{14D}{\omega}} \quad (5.32)$$

### 5.3.3 Power and Frequency Dependent Fluctuation Conductivity

Now we have estimates of the current-induced length scale and frequency-induced length scales. As the current density  $J$  decreases, the current-induced length scale  $L_J$  increases. As the frequency  $\omega$  decreases, the frequency-induced length scale  $L_\omega$  also increases. From the experimental data in Figs. 5.2 and 5.3, we know there is less power dependence in the high frequency range, in which the  $L_\omega$  is small. When

$L_\omega$  is large, which means at low frequency, there is large power dependence. Let us review the dynamical scaling of the frequency and current density:

$$\sigma = \xi^{z+2-D} S_\pm(\omega \xi^2, J \xi^{z-1}) \quad (5.33)$$

When  $\omega$  is small, then the second term  $J \xi^{z-1}$  can have a larger effect. Using the language of length scales, we can claim that the smaller length scale will dominate the behavior of the scaling function. In order to understand these length scales and also use them to explain our data, we compare these two length scales first. When they are equal,

$$L_\omega = L_J \Rightarrow \sqrt{\frac{14D}{\omega}} = \sqrt{\frac{k_B T}{\Phi_0 J}} \quad (5.34)$$

So

$$J = \frac{k_B T}{14 \Phi_0 D} \omega \equiv X_{para} \omega \quad (5.35)$$

Here we defined  $\frac{k_B T}{14 \Phi_0 D}$  as an X-parameter,  $X_{para}$ . Taking  $T \sim 90K$ ,  $\sigma \sim 5 \times 10^5 S/m$  and GL constant  $\xi_{GL} \sim 1nm$ ,  $X_{para} = 0.074 A \cdot sec / Rad \cdot m^2$ . Fig. 5.7 compares the domains where the current-induced and frequency-induced length scales dominate.

As for the behavior in region II of Fig. 5.4, it can not be simply explained by these two length scales. We need to consider another length scale, which is the thickness of the film. For DC VI characteristic measurement, the current-induced length scale  $L_J$  has been compared to the film thickness  $d$ . For any  $J$  there is a length scale  $L_J$ , given by Eq. A.12, such that roughly half the equilibrium (zero current) vortex population is blown out by  $J$ , and the other half are not. This is the length that one should compare to the film thickness for seeing whether or not the measurements are in the two or three dimensional limit. Only if there is a significant fraction of the loops that feel the film thickness, and, in addition, the current is probing on the same length scale, then the measurements are in the two dimensional limit. For AC measurement, there is also a frequency-induced length



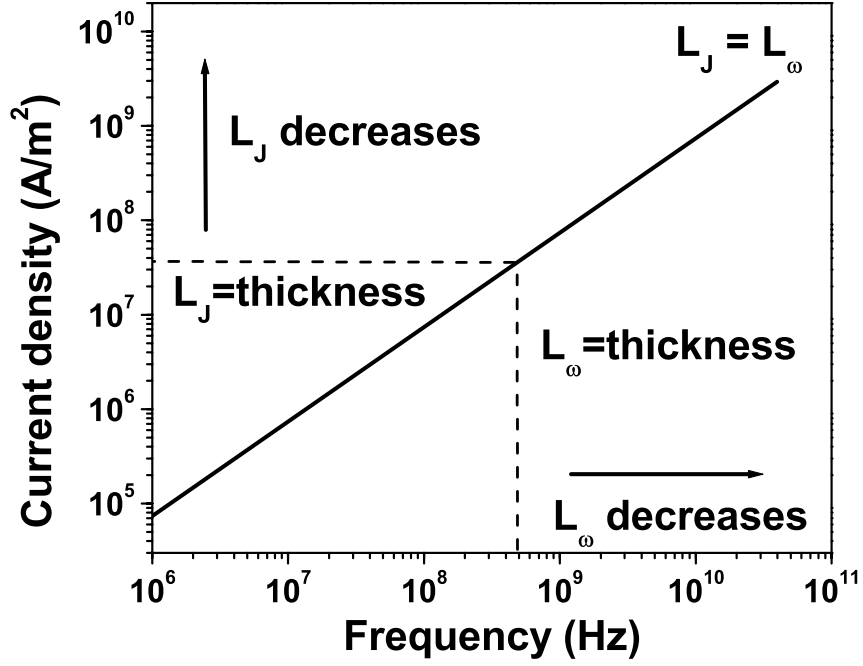


Figure 5.7: Plot of current density and frequency at which the current-induced and frequency-induced length scales are equal. The solid line in the figure gives the boundary  $L_J = L_\omega$ . On the right side,  $L_\omega < L_J$ , so the frequency induced-length scale dominates. We expect to observe more frequency dependent behavior. On the left side of the line,  $L_\omega > L_J$ , and more current induced nonlinear effects will be observed. The horizontal and vertical dashed lines shows when  $L_J = d$  and  $L_\omega = d$ , respectively, for film thickness  $d = 130nm$ .

scale. The probed length scale and the fluctuation conductivity will both be affected by frequency and current density. Here a plausible expression for the probed length scale for AC measurement can be written as

$$\frac{1}{L_{AC}} = \frac{1}{L_J} + \frac{1}{L_\omega}. \quad (5.36)$$

This formula is proposed because it has the correct limits:  $L_{AC} = L_J$  when  $L_J \ll L_\omega$  and  $L_{AC} = L_\omega$  when  $L_J \gg L_\omega$ . It also interpolates smoothly between the two limits. Theoretical work to conform or correct Eq. 5.36 would be very useful. When  $L_{AC}$  approaches the thickness of the film, there comes the finite size effect and the fluctuation conductivity will show deviations from the scaling theory.

Fig. 5.8 summarizes the length scales in an AC measurement in terms of experimental quantities. The dotted line in the figure gives the boundary  $L_J = L_\omega$ . On the right side of the dotted line, when  $L_\omega \ll L_J$ , the frequency induced length scale dominate the fluctuation conductivity. We observe mainly frequency dependent behavior of the fluctuation conductivity. On the left side of the dotted line, when  $L_\omega \gg L_J$ , current-induced nonlinear effects will dominate the behavior. This explains the features shown in Fig. 5.2 and Fig. 5.4, where the current density has less effect on the fluctuation conductivity at high frequency and larger effect at low frequency.

At low frequency and small current density, the probed length scale  $L_{AC}$  may approach the thickness of the sample. When  $L_{AC}$  is close to the thickness of the sample, the thickness of the film will finally limit the probed size of the fluctuation. Hence deviations from the general scaling theory will happen. This is the reason for the downturn behavior at low frequency of  $|\sigma(\omega)|$  in Fig. 5.3. From Fig. 5.8, we know that for higher incident power, the length  $L_{AC}$  approaches the thickness of the sample at lower frequency, and for lower incident microwave power, the  $L_{AC}$  approaches the thickness of the sample at higher frequency. This explains the feature seen in Fig. 5.3.(b) that the fluctuation conductivity measured at lower incident power

deviates from scaling theory at higher frequency and the fluctuation conductivity measured at higher incident power deviates from scaling theory at lower frequency.

In AC measurements, we want to probe the frequency dependent fluctuation conductivity. Hence we choose to stay at low  $J$  but high  $\omega$ . In this region we can find the true critical behavior without getting into finite-size effect difficulties. However, at low current density  $J$  and low frequency  $\omega$ ,  $L_{AC} > d$ , the critical behavior will be destroyed by finite-size effects. In this region, we can not observe the phase transition. So the observed fluctuation conductivity at low frequency can not be explained by scaling theory.

If we stay at low  $\omega$  but high  $J$ , we will mainly probe the current density dependent conductivity. Particularly for  $\omega = 0$ , which corresponds to the DC conductivity measurements. I will discuss this question in the next chapter.

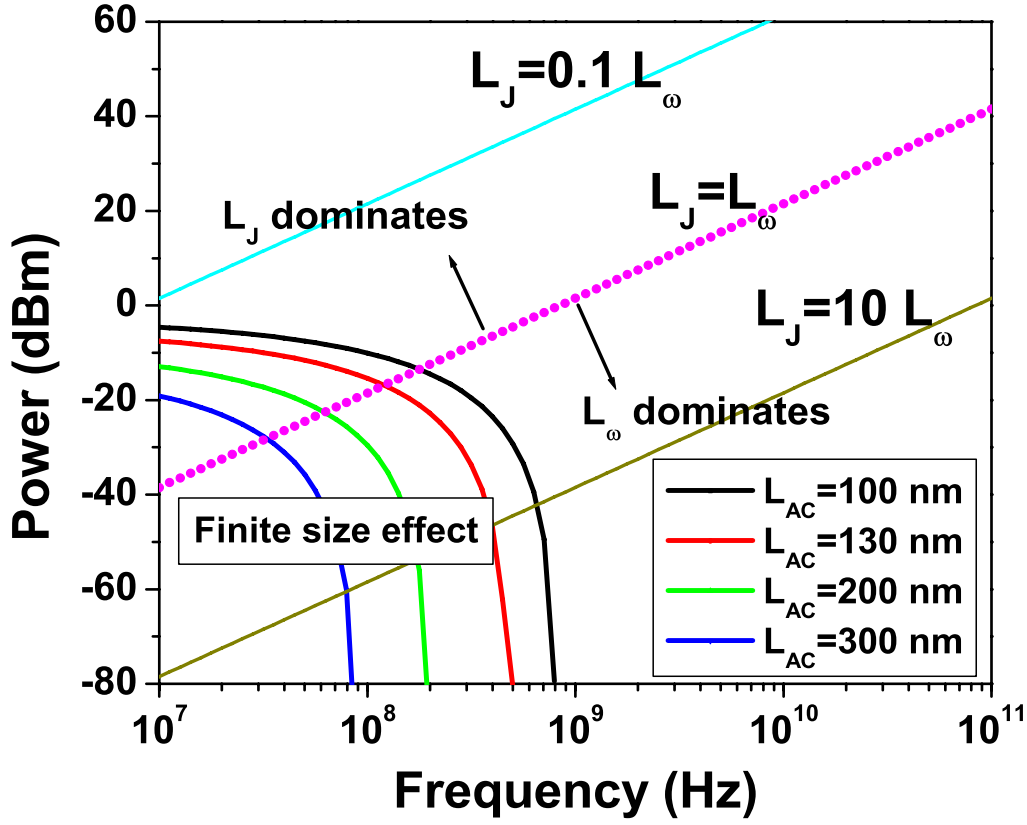


Figure 5.8: Summary of length scales and finite size effects in AC measurements of fluctuation conductivity. The dotted line in the figure gives the boundary  $L_J = L_{\omega}$ . On the right side, when  $L_{\omega} \ll L_J$ , the frequency-induced length scale dominates. We observe mainly frequency-dependent behavior of fluctuation conductivity. On the left side, when  $L_{\omega} \gg L_J$ , current induced nonlinear effects will dominate the behavior of fluctuation conductivity. At low frequency and small current density, the probed length scale  $L_{AC}$  approaches the thickness of the sample. The four curves correspond to  $L_{AC} = 100$ nm, 130nm, 200nm and 300nm, respectively.

## Chapter 6

# DC and AC Conductivity Measurements on the Same Sample

In the previous chapters we investigated the normal to superconducting phase transition through microwave conductivity measurements. We studied the length scales in AC measurements and found that a small applied power data should be used to determine the  $T_c$  and critical exponents. With -46dBm of applied microwave power we determined the  $T_c$  and critical exponents for  $\text{YBa}_2\text{Cu}_3\text{O}_{7-\delta}$  thin films. In this chapter, we will combine the DC and AC measurements on the same film to verify that the -46dBm applied power is small enough for determination of the critical exponents. The DC VI characteristic measurement is another way to probe fluctuations and determine critical exponents. For DC measurements, we use a specially-designed low-field (measured to be less than 0.3 mGauss) low-noise probe. If we are able to obtain consistent results by the two methods, the results will be more reliable than if obtained in only one experiment. If the results are inconsistent, having independent experiments provides diagnostic information to help resolve the disagreement.

## 6.1 DC scaling

DC scaling was discussed in Chap. 3. The DC scaling equation is given in the FFH paper[54]

$$\frac{E}{J} = \xi^{D-2-z} \chi_{\pm}(J\phi_0\xi^{D-1}/cT). \quad (6.1)$$

The above scaling function  $\chi_{\pm}$  has two useful limits. First, above  $T_c$ , the function  $\chi_+(x)$  approaches a constant as  $x \rightarrow 0$ . Thus, in the limit of low current density  $J \rightarrow 0$ , the Eq. 6.1 becomes

$$\frac{E}{J} \propto \xi^{D-2-z} \propto (T - T_c)^{\nu(z+2-D)}. \quad (6.2)$$

This limit is only valid above  $T_c$  and we can not use the same argument below  $T_c$  since one expect the resistance to vanish as  $J \rightarrow 0$  below  $T_c$ .

The next limit is for  $x \rightarrow \infty$ , which would occur either through  $J \rightarrow \infty$  or  $T \rightarrow T_c$ . In this limit,  $E/J$  must be finite, which requires that

$$\chi_+(x) \approx \chi_-(x) \sim x^{(z+2-D)/(D-1)}. \quad (6.3)$$

This results in

$$E \sim J^{(z+2-D)/(D-1)} \quad (6.4)$$

The conventional method suggests that one choose the critical isotherm – the first isotherm without an ohmic tail – as  $T_c$ . Douglas R. Strachan and Matthew C. Sullivan showed that the conventional data analysis and its accompanying data collapse can not uniquely determine the critical parameters.[18, 89]. To resolve this, they proposed the opposite concavity criterion in a derivative plot of the data. This criterion is easiest to see on a plot of  $d \log(E)/d \log(J)$  vs.  $J$ . Taking the derivative of Eq. 6.1 we have

$$\left( \frac{\partial \ln E}{\partial \ln J} \right)_T = G_{\pm}(J\xi^{D-1}), \quad (6.5)$$

At  $T_c$ , with the assumption of  $D=3$ , we obtain

$$\left( \frac{\partial \ln E}{\partial \ln J} \right)_{T_c} = (z + 1)/2. \quad (6.6)$$

So in a derivative plot there should be a horizontal line at  $T = T_c$  whose intercept should give us a value for  $z$ . The expected derivative plot is sketched in Fig. 3.3.

For a simple geometry system, if  $E \propto V$  and  $J \propto I$ , then the geometrical factors can be absorbed into the unknown functions  $\chi_{\pm}$  and written as[53, 54]:

$$\frac{V}{I} = \xi^{D-2-z} F_{\pm}(I\xi^{D-1}) \quad (6.7)$$

The two limits above can also be applied here. So by taking data of voltage vs. current ( $V - I$ ) at different temperatures over many decades of current and voltage, we can probe the fluctuation conductivity and determine the critical exponents.

## 6.2 Experimental Procedure

### 6.2.1 Introduction to the DC Experiment

The AC experimental technique has been introduced in the previous chapters. Here I want to do both AC and DC measurement on the same film. On the surface, the DC experiment is simple: apply a current and then measure a voltage. However, the measurement is taken close to  $T_c$  and the measured voltage is normally very small. For these reasons, excellent temperature control, a low noise environment and a sensitive voltmeter and current source are needed.

A current is applied through a patterned bridge. Bridges of different dimensions were used. Bridges are specified by  $w \times l$ , where  $l$  is the length of the bridge and  $w$  is the width. The current through the bridge can be written as  $I = J \times wd$ , where  $d$  is the thickness of the film and  $J$  is the current density in the bridge. A typical bridge is  $8 \times 40\mu m$ , and such a bridge is shown in Fig. 6.1 Current flows from  $I+$  to  $I-$  and the voltage is measured between  $V+$  and  $V-$ , which is a typical 4-probe measurement. There are 4 larger gold contact pads( $1.5mm \times 1.5mm$  each) connected to each lead. They are not shown in this figure.

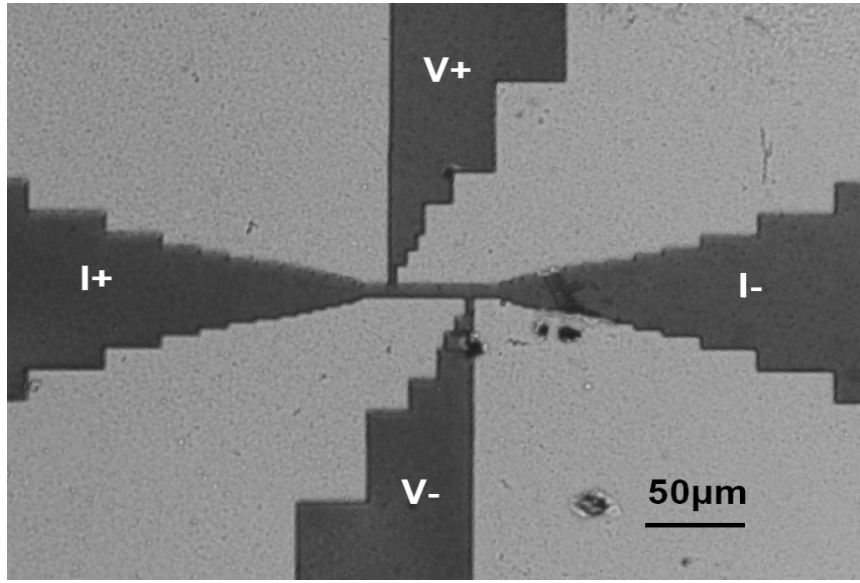


Figure 6.1: YBCO bridge pattern ( $8\mu\text{m} \times 40\mu\text{m}$ ) for sample xuh112. YBCO is black and the substrate is grey.

The voltage leads are directly connected to the bridge and measure the voltage drop across the bridge. In the experiment, the voltage leads are connected to the voltmeter from the top of the probe through various stages of wiring, solder joints, copper wires and gold wires. The connections between different metals cause thermal emfs, which are around  $V_{th} \sim 1\mu\text{V}$ . [89] To remove these emfs, we reverse the direction of current and measure the voltage one more time. The thermal emfs in the leads will not switch sign. By taking the difference of the voltage measured while switching the polarity of the current, the voltage drop on the sample can be obtained as,

$$V = \frac{V(I+) - V(I-)}{2} = \frac{(V(I+) + V_{th}) - (-V(I-) + V_{th})}{2} \quad (6.8)$$

The time for a reverse-polarity measurement is short, usually less than 0.5 s. The thermal voltage are expected to not change on that time scale.

To obtain high precision results,  $V$  is measured many times and the average,  $\bar{V}$ , is calculated. In this process the standard deviation,  $\sigma_{\bar{V}}$ , is also calculated. For



each temperature, the measurement continues until a pre-set limit is achieved, which is normally  $\bar{V}/\sigma_{\bar{V}} > 1000$  or  $\sigma_{\bar{V}} < 1nV$ . The later criterion normally happens when the voltage is near the resolution of the volt meter ( $\approx 1nV$ ).

The experimental and the DC transport probe have been discussed in detail in [89], and is not repeated here.

### 6.2.2 Procedure of Combined AC and DC Experiments

The DC experiment requires patterning the YBCO film into a small bridge, making it impossible to perform AC measurement on the film again. So for both AC and DC experiments on the same film, the AC measurement is taken first and then the DC measurement.

The AC measurement is the same as we introduced in chapter 4. After measuring the microwave conductivity, I prepare the film for a DC experiment. To do so, the standard photolithography method is used. The photoresist used is Shipley S-1813 resist. It was spun on the samples at 5000 rpm for 45 s, giving about  $1\text{ }\mu\text{m}$  thickness of photoresist. Afterwards the films were baked for 1 minute at  $90\text{ }^{\circ}\text{C}$ . Then part of the film is exposed to UV light ( $\lambda = 365\text{ nm}$ ) at  $8\text{ mW}/\text{cm}^2$  for 12.5 s. The exposed photoresist is removed by Shipley developer, a 1:1 ratio of water and CD-30. The develop time is about 20 seconds. Through the above method, bridges of  $2\text{ }\mu\text{m}$  width and larger can be made.

In the above process, the mask used is the normal one for DC measurement. However, due to the previous AC measurement, part of the sample surface is covered by gold. In this case the mask has to be placed in an appropriate position and direction. Fig. 6.2 shows how to put the mask in place on the Corbino disk. The mask place is adjusted in order that the bridge stays on the Corbino ring and also four leads stay on the sample. If appropriately adjusted, the gold contact on the sample for Corbino measurement can still be used as contact leads for DC

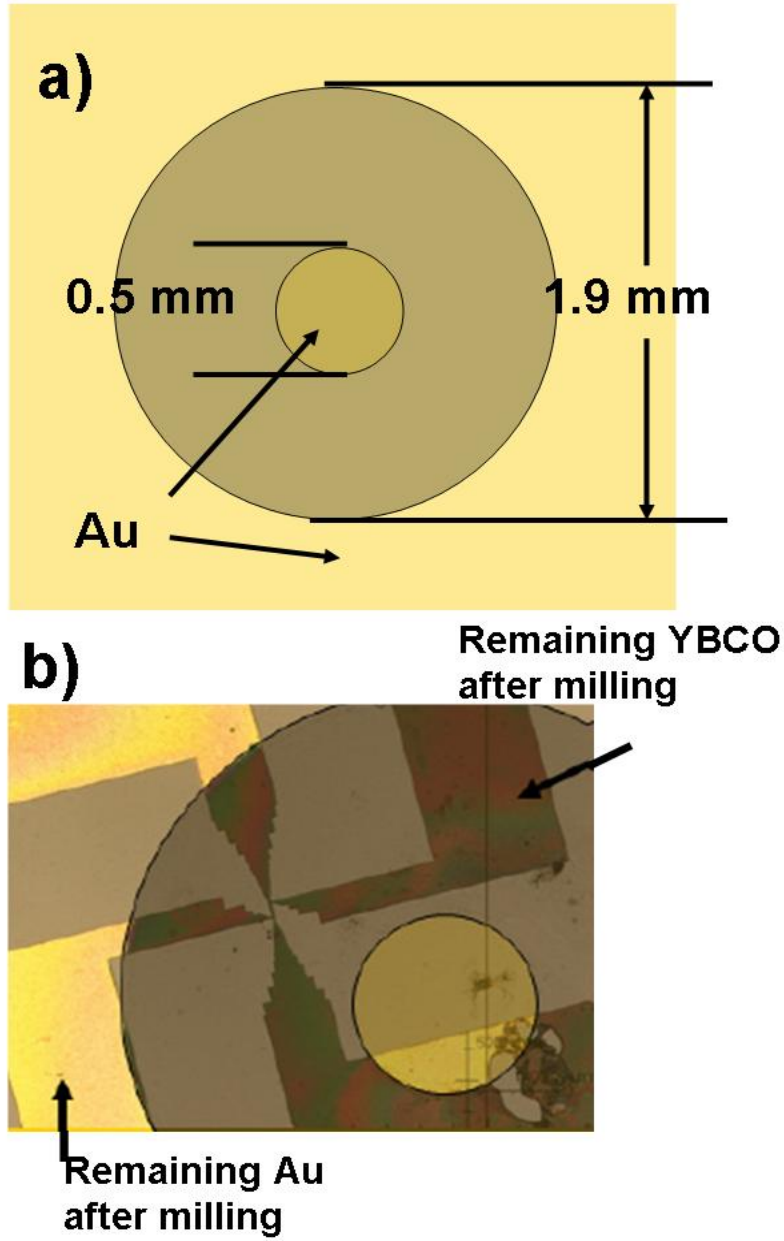


Figure 6.2: Schematic of the patterned bridge for DC measurement on samples after AC measurement. (a) YBCO samples after AC measurement. Part of the surface is covered with gold. (b) YBCO samples processed for DC I-V measurements after AC measurement. The bridge is adjusted on the Corbino ring. The picture showed only part of the processed sample, and the leads do not short out.

measurement.

After the bridge pattern is made on top of the film, the extra YBCO and gold must be removed. However, when etching gold, the gold etchant will damage the YBCO sample. I tried wet etches many times, but never successfully obtained even one good YBCO bridge. An alternative etching process had to be developed.

In an ion mill, argon atoms are stripped of their electrons and accelerated towards the sample. Before impact, they are neutralized with an electron beam. The argon atoms hit the sample with such force that atoms on the sample are knocked free. The photoresist is much thicker than the sample ( $1\text{ }\mu\text{m}$  compared to  $2000\text{ }\text{\AA}$ ), and its mill rate is slower (typically half that of YBCO), so the exposed YBCO will be removed before the photoresist, leaving the YBCO underneath the pattern of photoresist untouched.[89]

The ion mill can make very exact patterns and avoids any over-etching, which is very good. However, the disadvantage is that when the atoms hit the sample at high speeds the sample can be heated. This heat may drive oxygen from the sample and change its superconducting properties since the sample is put in vacuum when doing milling. To avoid this disadvantage, I use a relatively small milling rate and also try to keep good thermal contact between sample substrate and the mill stage, which is water-cooled to avoid heating.

After removing the extra YBCO and gold, the sample is glued to the DC stage by GE varnish and wires are attached to the sample. The remaining steps are just the standard DC experiment procedures, which have been discussed in [89] by M. S. Sullivan.

## 6.3 Experimental Results and Discussion

### 6.3.1 DC experimental results

In Fig. 6.3, we present an E-J plot of sample xuh139 in a large temperature range. We have measured the microwave conductivity of this sample and the results have been discussed in previous chapters. The isotherms in Fig. 6.3 differ by 0.05 K from 90.050 K to 92.000 K. In order to analyze the DC experiment data, D. R. Strachan proposed the opposite concavity criterion to determine  $T_c$  and the critical exponent  $z$ . [18, 95]. However from this E-J plot, I can not find a single straight line that separates the isotherms into two groups which are concave and convex exclusively. Some curves have negative curvature at high current density and positive curvature at low current density, and exhibit ohmic behavior at even lower current density. This is due to finite size effects, which produce ohmic response even below the transition temperature  $T_c$  for very small current density. Because of finite size effects, the conventional analysis that chooses  $T_c$  as the first isotherm that separates the isotherms with low current ohmic tail from ones without should not apply. So we should use the  $d \log E / d \log J$  vs.  $J$  plot, derivative plot, to determine  $T_c$ .

Fig. 6.4 shows a derivative plot of sample xuh139. The isotherms differ by 0.02 K from 91.38 K to 90.98 K. Because of the finite size effect, there is no isotherm that is horizontal over the entire range of current density. All the isotherms tend towards  $d \log E / d \log J = 1$  at low current density, which corresponds to ohmic behavior. This is true even for isotherms that are clearly below  $T_c$ . Hence we should use the higher current density data to determine  $T_c$  and the critical exponent. Fig. 6.3 shows that the isotherm at 91.220 K is horizontal at high current density. Below 91.220 K, the isotherms bend up corresponding to a convex E-J curve. Above 91.220 K, the isotherms bend down corresponding to a concave E-J curve. So from Fig. 6.3, the critical temperature is about 91.220 K and the critical exponent  $z$  is about  $1.75 \pm 0.1$ . The error bar of  $T_c$  is set by the temperature step of the measurement,

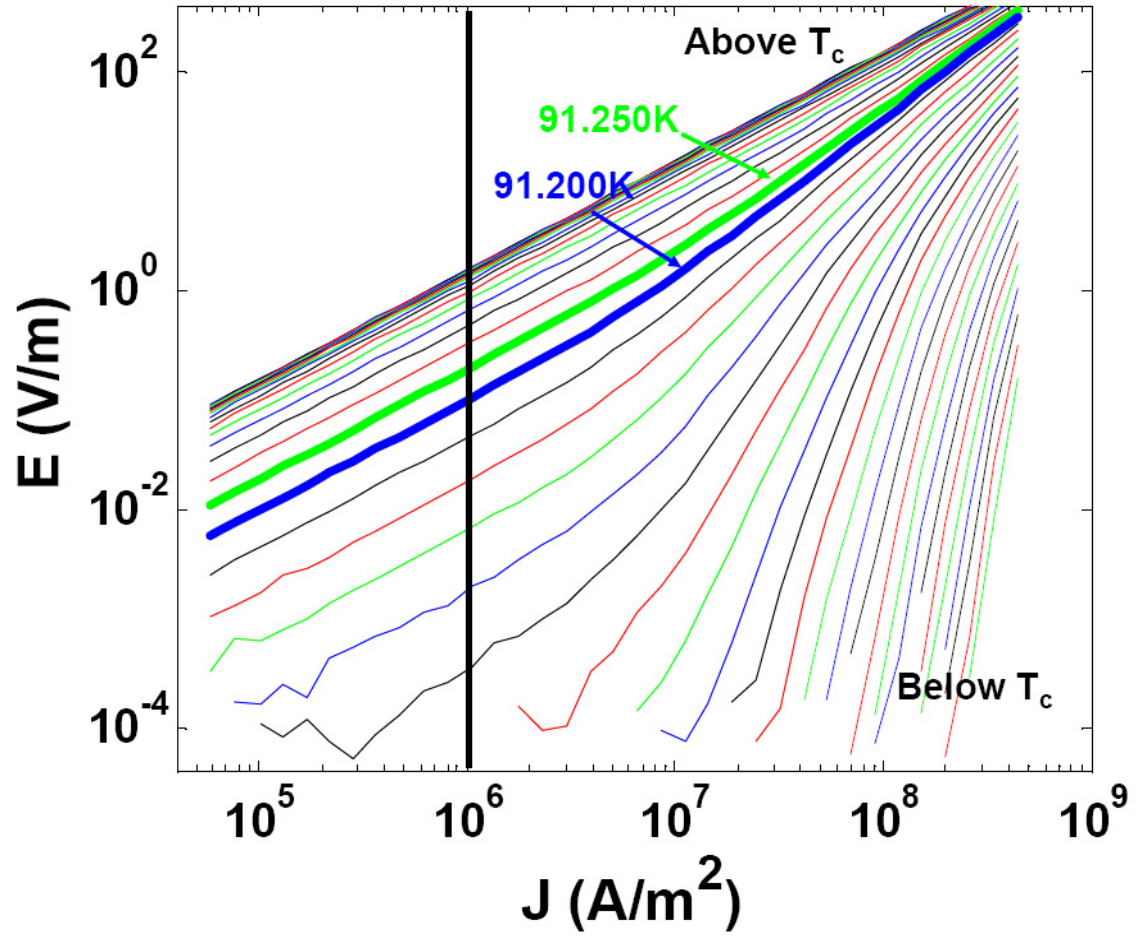


Figure 6.3: E-J isotherms for sample xuh139, performed after the AC experiment.

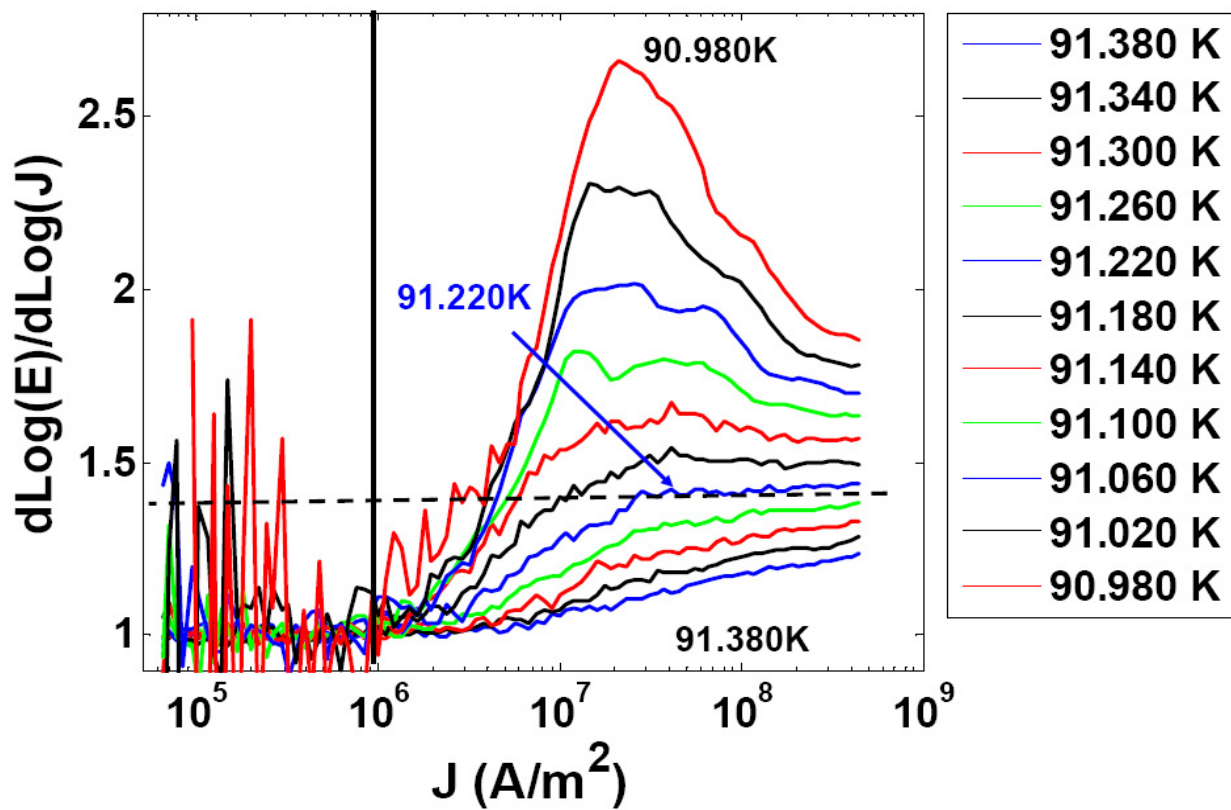


Figure 6.4: Derivative plot for xuh139 in zero magnetic field.

0.02K.

Fig. 6.3 shows an E-J plot of this sample over a larger temperature range. The thicker isotherms span the  $T_c$ . In this E-J plot all the measurable isotherms have slope 1 for current density below  $1 \times 10^6 A/m^2$  around  $T_c$ . In derivative plot, we see  $d \log E / d \log J \approx 1$  for current density below  $1 \times 10^6 A/m^2$ . From this we know that the current density below  $1 \times 10^6 A/m^2$  will have only ohmic response around  $T_c$ .

In microwave conductivity measurement, we used -46dBm applied power to extract the critical exponent in chapter 4. For -46 dBm incident power and  $T \cong T_c$ , the time averaged current density at the inner edge of the Corbino disk  $J \approx 2.2 \times 10^5 A/m^2$ . Fig. 6.3 and 6.4 show there is only ohmic response on around  $T_c$  for the current density below  $1 \times 10^6 A/m^2$ . This means for -46 dBm incident power the fluctuation conductivity is not affected by the current density ( $J\xi^2$  argument in the conductivity scaling function), but depends only on frequency. So it is appropriate to determine  $T_c$  and critical exponents with -46dBm microwave power and the high frequency part of the data. A summary of the length scales and finite size effects in AC measurements has been given in Fig. 5.8 of chapter 5.

### 6.3.2 Comparison with the AC Experimental Results

We have performed both AC and DC experiments on this sample. Now let us compare the results from both methods. First consider  $T_c$  and  $z$ . From AC measurement we obtained:  $T_c = 89.25 \pm 0.03K$ ,  $z = 1.55 \pm 0.12$ . Here the above DC measurement  $T_c = 91.22 \pm 0.02K$ ,  $z = 1.75 \pm 0.10$ .

The difference of the  $T_c$  is due to the different thermal lag of the two systems. Although the thermometers are placed as close as possible to the sample, there is some distance to the sample in both experimental setups. The existing thermal gradient between the thermometer and the sample makes for a certain temperature difference between the thermometer and the sample, which I call thermal lag. The

thermal lags for different probes are different. In the DC experiment, special techniques have been utilized to keep the thermal stability and decrease the temperature gradient. In this case I believe the thermal lag is very small( 20 mK). However in the AC experiment, the sample is in direct contact with the coaxial cable, which is directly connected to a room temperature instrument. Also the thermometer is located between the sample and the liquid He coolant, and the thermal lag is relatively large. The resistance vs. temperature(R vs. T) plots from the AC and DC experiment have a 2 K temperature offset, which is exactly the difference of the determined  $T_c$  from these two methods. Hence the determined  $T_c$  from both the AC and DC experiments are consistent.

The value of  $z$  determined from DC measurement is a little larger than  $z$  obtained from the AC measurement although we expect them to be the same. We need to carefully examine diagnostic information from two experiments to resolve the disagreement.

First we tried to repeat the experiment(both DC and AC measurement on the same sample) for different samples. This is difficult, and I have only successfully performed both experiments on 6 samples in three years. The samples name are xuh083, xuh111, xuh112, xuh139, xuh142 and xuh156. The microwave conductivity measurements were carried out only at -22 dBm for the first three samples, which made the their AC experimental results are less reliable. So we will concentrate on the last three samples. Here xuh139 and xuh142 are YBCO on NGO substrate, and xuh156 is YBCO on STO substrate.

For both samples xuh139 and xuh142, the  $z$  value from DC measurement is larger than  $z$  obtained from AC measurement. Also from the previous AC work, Tab. 4.3 shows that the AC results are pretty consistent, and the value of  $z = 1.56 \pm 0.10$  for NGO samples. The AC result of xuh156(YBCO on STO substrate) is not as reliable as NGO substrate results because the large dielectric constant of STO substrate makes for only a narrow band of the frequency data useful for AC data analysis.



Table 6.1: Comparison of results for both AC and DC experimental measurements on the same films

Measurement method		AC		DC	
Sample	Substrate	$T_c \pm \Delta T_c(\text{K})$	$z \pm \Delta z$	$T_c \pm \Delta T_c(\text{K})$	$z \pm \Delta z$
xuh139	NGO	$89.25 \pm 0.03$	$1.55 \pm 0.12$	$91.22 \pm 0.02$	$1.75 \pm 0.10$
xuh142	NGO	$89.62 \pm 0.10$	$1.55 \pm 0.25$	$91.60 \pm 0.04$	$1.7 \pm 0.15$
xuh156	STO	$89.66 \pm 0.10$	$1.70 \pm 0.30$	$91.66 \pm 0.02$	$1.60 \pm 0.10$

The interesting result here is that the DC measurement on STO substrate gives  $z \approx 1.60$ , which is quite close to the AC measurement results on NGO substrate.

### 6.3.3 Other DC Experimental Results

To clarify these issues, we repeated the DC experiment on different samples including both STO and NGO substrates. First a summary of my work on NGO substrates is shown in Tab. 6.2. I see the value of  $z$  ranges from 1.54 to 2.06 with relatively large error bar. The mean value is  $z = 1.78 \pm 0.18$ . This is a strange value, just between 1.5, which corresponds to Model-E dynamics of 3D-XY and 2, which corresponds to Model-A dynamics of 3D-XY.

We carefully analyzed the effect of  $T_c$ , resistivity and thickness of the sample on the determined critical exponent  $z$ . We found some systematic relation between  $T_c$  and the obtained value of  $z$ , as shown in Fig. 6.5. We see that as the sample  $T_c$  increases it tends to give a smaller value of  $z$  for these YBCO samples on NGO substrate. A sample with higher  $T_c$  is normally more homogeneous (with sharper transitions temperature), has less disorder, and corresponds to higher quality sample. The effect of inhomogeneity and disorder on the static critical exponents  $\nu$  has been discussed [79][116][105]. However, there is less discussion about these effect on the dynamical critical exponents  $z$ . It is tend to believe that the determined  $z$

Table 6.2: Results of DC measurement on NGO substrate, the bridge sizes are all  $8\mu m \times 40\mu m$ . The \* marks the sample finished both AC and DC experiments.

Sample	$T_c$ (K)	$\Delta T_c$ (K)	$z$	$\Delta z$
xuh111	90.72	0.02	2.06	0.06
xuh112	90.36	0.02	2.00	0.06
xuh131	91.23	0.04	1.66	0.15
xuh138	91.56	0.02	1.62	0.15
xuh139*	91.22	0.02	1.75	0.10
xuh142*	91.42	0.02	1.74	0.15
xuh150	90.64	0.02	1.94	0.15
xuh151	90.8	0.02	1.92	0.15
xuh165	91.66	0.03	1.66	0.15
xuh166	91.68	0.04	1.54	0.15

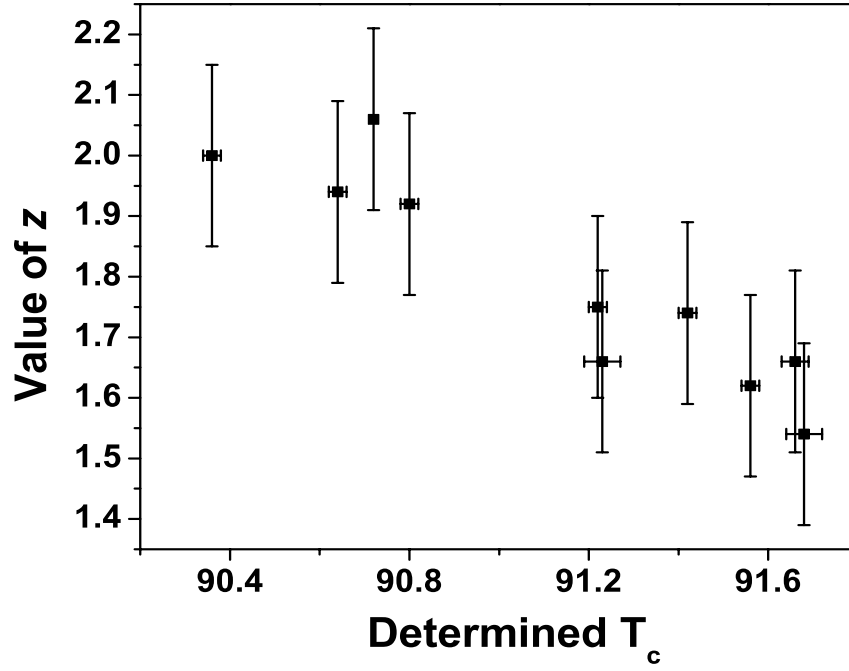


Figure 6.5: Obtained value of  $z$  vs.  $T_c$  for different YBCO samples on NGO substrates. the bridge sizes are all  $8 \times 40 \mu m$ .

value from the higher quality sample is more close to the intrinsic value of  $z$ . Tab. 6.2 gives the  $z = 1.54 \pm 0.12$  for sample xuh166 with highest  $T_c$ . From this point of view, DC and AC measurement results are consistent with each other.

The proposed argument above need to be tested. There are two questions here need to be clarified. One is that how and why the obtained values of  $z$  are dependent on the  $T_c$  of the sample. To systematically answer this question more theoretical and theoretical works are required. I will only give some qualitative discussion in this thesis. The other question is whether the highest  $T_c$  sample shown in Fig. 6.5 is homogeneous enough and has low enough disorder to give us intrinsic value of  $z$ . We did some experiments to clarify the second question.

The STO substrate normally gives films with higher  $T_c$ , sharper transition and

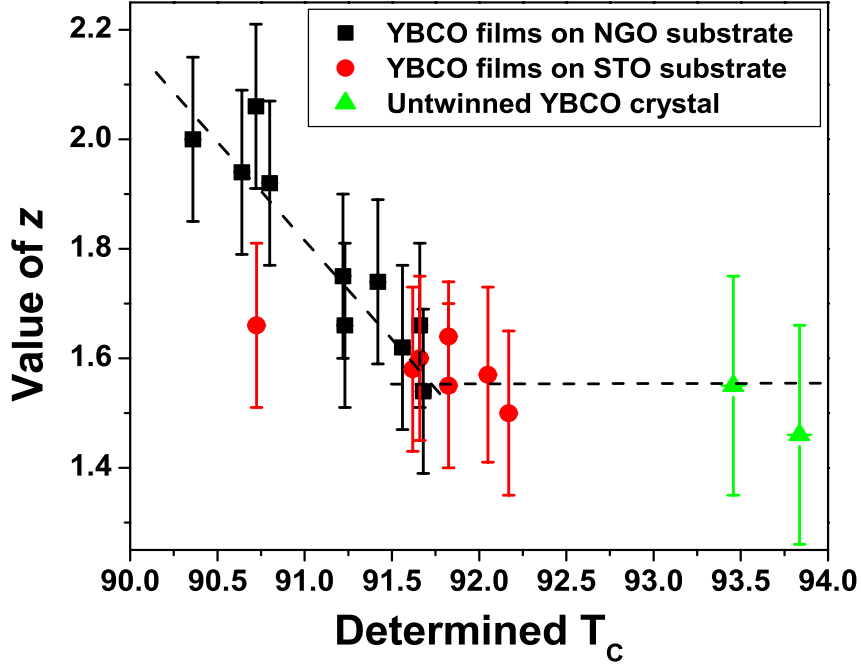


Figure 6.6: Obtained value of  $z$  vs.  $T_c$  for different YBCO samples. The bridge sizes are all  $8 \times 40\mu m$  for films.

smaller resistivity than NGO substrate. So I also performed DC measurements on YBCO films grown on some STO substrates. Some of my results, and those of others, are shown in the Table. 6.3. In addition, measurements on high quality YBCO untwinned crystals, which have less disorder and more homogeneous than any known films, have been performed by Su Li.[139] The results are also shown in Table. 6.3.

The values of  $z$  for different samples are very consistent, particularly for small bridge sizes  $8 \times 40\mu m$ . Taking an average of  $z$  for the 7 samples of bridge sizes  $8 \times 40\mu m$ , I obtained  $z = 1.57 \pm 0.08$ . Averaging over all 12 samples, I obtained  $z = 1.56 \pm 0.14$ . These results are consistent with  $z$  value obtained from the highest  $T_c$  YBCO samples on NGO substrates. The discussion about the bridge size has

Table 6.3: Results of DC measurement on YBCO samples on STO substrate and YBCO crystals. The first 7 samples from xuh156 to MCS136 are measured with the bridge sizes  $8 \times 40\mu m$ . The next 5 samples are with bridge  $20 \times 100\mu m$ , and the last two samples are YBCO crystals.

<i>Sample</i>	$T_c$ (K)	$\Delta T_c$ (K)	$z$	$\Delta z$	bridge size
Xuh156	91.66	0.02	1.60	0.15	$8 \times 40\mu m$
Su113	91.825	0.02	1.55	0.15	$8 \times 40\mu m$
Zhengli14	90.725	0.02	1.66	0.15	$8 \times 40\mu m$
Zhengli26	92.17	0.02	1.44	0.15	$8 \times 40\mu m$
MCS120	92.05	0.05	1.57	0.15	$8 \times 40\mu m$
MCS124	91.62	0.04	1.58	0.15	$8 \times 40\mu m$
MCS136	91.825	0.04	1.64	0.15	$8 \times 40\mu m$
MCS138	91.925	0.02	1.84	0.15	$20 \times 100\mu m$
MCS139	91.66	0.03	1.46	0.15	$20 \times 100\mu m$
MCS145	91.68	0.05	1.42	0.15	$20 \times 100\mu m$
MCS146	91.46	0.04	1.66	0.15	$20 \times 100\mu m$
MCS160	92.64	0.04	1.34	0.15	$20 \times 100\mu m$
CrystalI	93.457	0.005	1.55	0.20	crystal
CrystalII	93.836	0.005	1.46	0.20	crystal

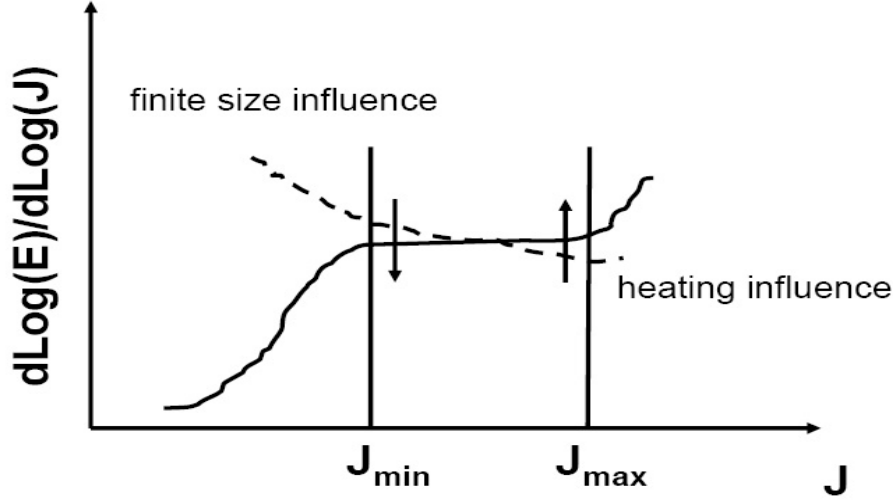


Figure 6.7: Schematic of heating and the finite size effect influence on derivative E-J plot. The solid line denotes the measured  $d\text{Log}(E)/d\text{Log}(J)$  vs.  $J$  that is chosen as  $T_c$ . The dashed line denotes what the  $d\text{Log}(E)/d\text{Log}(J)$  vs.  $J$  curve might be if the finite size effect and heating influence could be removed for this temperature.

been presented in Su Li's thesis.[139] Basically samples with small bridge size are more appropriate to determine  $T_c$  and the value of  $z$ . I will not repeat the arguments again, but just use small bridge data as result.

Fig. 6.6 shows the obtained value of  $z$  vs.  $T_c$  for different YBCO samples. The plot shows that the obtained values of  $z$  are dependent on the  $T_c$  for samples with lower  $T_c$  (less than 91.60 K) and independent of the  $T_c$  for higher  $T_c$  samples (higher than 91.60 K). Combined with the results of the high quality untwinned crystals, we believe that samples with higher  $T_c$  give intrinsic value of  $z$ . So finally I take an average of the results for crystals and films with higher  $T_c$  and obtain  $z = 1.57 \pm 0.08$ . This result is consistent with the AC measurement result.

Now let us look at the question that how and why the obtained values of  $z$  are dependent on the  $T_c$  for samples with lower  $T_c$ . I examined the process of

determination of  $T_c$  and critical exponent  $z$  from an E-J derivative plot. In the DC experiment, heating can be a big problem. At low enough applied current, the heating effect is negligible. However, at high applied current, the sample will be heated and the heating of the sample at high current density can create extra nonlinear behavior and distort the shape of the I-V curves.[139] In addition to that, another problem in DC experiments is the influence of finite size effects, which distorts the low current density data.

To avoid these problems, we use  $d\text{Log}(E)/d\text{Log}(J)$  vs.  $J$  in the middle range of current density to determine  $T_c$  and critical exponent  $z$ , in which range the curves are thought to be less distorted. Fig. 6.7 shows how finite size effects and heating possibly change the  $d\text{Log}(E)/d\text{Log}(J)$  vs.  $J$  curve. When  $J_{min}$  and  $J_{max}$  are far away from each other and  $d\text{Log}(E)/d\text{Log}(J)$  vs.  $J$  curve is flat in a large current density range at  $T_c$ , the determined  $T_c$  and critical exponent  $z$  should be correct.

Samples with lower transition temperature are normally less homogeneous, with more disorder and larger resistivity. The larger resistivity increases the influence of heating, which means  $J_{max}$  will be smaller. The inhomogeneities may also introduce another length scale inside the sample. If this length scale is less than the thickness of the film, it will increase the finite size effects, which means  $J_{min}$  will be larger. Due to stronger finite size effects and the influence of heating, we tend to systematically choose a lower temperature isotherm as  $T_c$  and then obtain a larger value of  $z$ .

A similar phenomena is that thinner samples tend to give larger values of  $z$  and the larger bridge size samples also tend to give larger values of  $z$ . The latter case has been discussed in Su Li's thesis.[139]

From the above discussion, the  $T_c$  dependence of the value  $z$  from DC measurement might be due to another length scale related with sample quality or due to the heating influence in the measurement that is correlated with  $T_c$ . To systematically clarify this question, more experimental and theoretical work are needed.

To summarize, I performed DC measurements on YBCO films grown on both

NGO and STO substrates. The obtained value of  $z$  from DC measurement depends on  $T_c$  of the sample. This dependence might be due to another length scale related with sample quality or due to some systematic error in the measurement that is correlated with  $T_c$ . To clarify this question, both experimental and theoretical work are needed. However, for films with high  $T_c$ , sharper transition and small resistivity, I obtained value of  $z = 1.56 \pm 0.08$ , which is consistent with previous AC result  $z = 1.55 \pm 0.15$ . In addition, the latest DC measurement on high-quality crystals also gave  $z \approx 1.5$ . [139] These results tell that the superconducting to normal phase transition is consistent with the model-E dynamics of the 3D-XY universality class, which predicts  $z \approx 1.5$ .



## Chapter 7

# Electronic Transport Properties of Single-walled Carbon Nanotube Films

### 7.1 Introduction

Networks with randomly distributed single-walled carbon nanotubes (SWCNTs) are emerging as novel materials for various applications. [140, 162, 163] Sub-monolayer networks close to the percolation threshold have shown potential as thin film transistors with higher mobility than organic semiconductors.[164, 165, 166] Thin SWCNT networks with thickness in the range of 10 to 100 nm have high sheet conductance while maintaining high optical transparency. [156, 160, 161, 176] These films can be used as transparent electrodes, which have already been demonstrated to be excellent anodes particularly in organic solar cells and light emitting diodes.[167, 168, 169, 170, 171] Thick SWCNT networks with thickness on the order of micrometers have potential application as electrodes for fuel cells due to their highly porous surface structure and large surface area.[172, 173]

For the sake of applications of SWCNT networks, a comprehensive understanding of the electrical transport properties of such networks is important. For example, when using SWCNT networks to construct high speed transistors, knowledge of their frequency dependent electric transport properties are required. Also use of

SWCNT networks as inter-connects in circuits requires knowledge of their electric field-dependent properties. It has been established that the overall resistance of the films is determined by the junction resistance between different tubes.[141, 142, 174]

To fully explore the potential applications of NT films as a type of electrical and photonic material, it is important to map out the conductivity in a wide frequency range. AC conductance measurements of a percolating NT network up to 1 MHz have shown a universal power law in frequency, which is commonly observed in systems with randomly distributed barriers. [143] In the THz range, the effective Maxwell-Garnet (M-G) model has been introduced where both the metallic and semiconducting NTs were embedded in a dielectric host.[144] Optical conductance in the far-infrared and visible range has been obtained by measuring the reflectance of NT films and a Kramers-Kronig transformation.[145, 146, 147] Study of conductance in the microwave frequency range is important for high speed NT thin film field effect transistors (FET). Microwave conductivity of individual SWCNT and operation as a transistor at 2.6 GHz have been measured by Burke *et al.*[148] They also gave an RF circuit model for carbon nanotubes.[149] However there is a paucity of conductivity measurements on SWCNT films in this frequency range. So far, a few groups have measured with a cavity setup, which can only lead to conductivity values at a few discrete frequencies.[150, 151]

In addition, the frequency dependent and electric field dependent conductivity have been investigated for certain density SWCNT networks. For example, the AC conductance of carbon nanotube polymer composites close to the percolation threshold are found to be increasing with frequency up to several MHz, exhibiting a universal power law in frequency, which is commonly observed in systems with randomly distributed barriers to transport.[143, 175] For thicker films with thickness in the range of tens of micrometers, P. Peit *et al.* found that conductivities at DC and 10 GHz are almost the same.[151] M. Fuhrer *et al.* observed the nonlinearity of the electric field-dependent conductivity of relatively thick nanotube networks and

they claimed that the charge carriers can be localized by disorder of SWCNTs with an approximate localization length scale  $L$  of  $1.65 \mu\text{m}$ . [177, 178] However there is a lack of frequency and electric field dependent conductivity investigation for various network densities, and also there is no correlation study between the onset frequency  $\omega_0$  and localization length scale  $L$ .

In this chapter, I first studied the microwave shielding effect of transparent and conducting SWCNT networks with 30 nm thickness at different temperatures, I found that SWCNT films are promising for the application of transparent EMI shielding. Then I investigated the frequency and electric field-dependent conductivity for SWCNT networks with systematically varying densities. I find that the onset frequency  $\omega_0$  extracted from the frequency dependence measurement increases as the film thickness increases while the length scale extracted from the electric field dependent measurement decreases at the same time. Using the measured  $\omega_0$  and localization length scale  $L$  for different films, I developed an empirical formula and established a relation between the two measurement methods, which is important not only for the understanding of transport properties but also the application of this novel material system.

## 7.2 Microwave Shielding of Transparent and Conducting Single-walled Carbon Nanotube Films

Electromagnetic radiation at radio and microwave frequencies, such as those emanated from cell phones, tend to interfere with electronic devices. The electromagnetic interference (EMI) leakage from radio frequency to microwave is still a serious problem for our society. The primary mechanism of EMI shielding is usually reflection. Thin metal foil and metal grids are commonly used for this purpose. Recently light-weight, flexible and highly effective shielding can be achieved by means of a

conducting polymer coating,[154] although degradation is an intrinsic problem. A matrix containing conductive fillers is an attractive alternative for shielding.[154] Composites incorporating NTs have extremely low percolation threshold(volume fraction around  $10^{-4}$ ) due to the high ratio of length to diameter.[152] Highly conducting SWCNTs and multiwalled carbon nanotubes(MWNT)[153] have been incorporated into composites for EMI shielding purposes and 49 dB shielding effectiveness at 10 MHz has been achieved for 15% NT loading of a polymer composite.[155]

In many situations visibly transparent EMI shielding is required and indium tin oxide (ITO) is the current material of choice. NT films have shown potential as the replacement for ITO for transparent electrodes in devices.[140] Up to now, there is no systematic investigation on EMI shielding effects of NT films, especially for the microwave frequency range where the EMI leakage is mostly concentrated. In this chapter, by measuring the microwave conductivity of NT films from 10 MHz to 30 GHz at different temperatures, we found that SWCNT films are promising for the application of transparent EMI shielding.

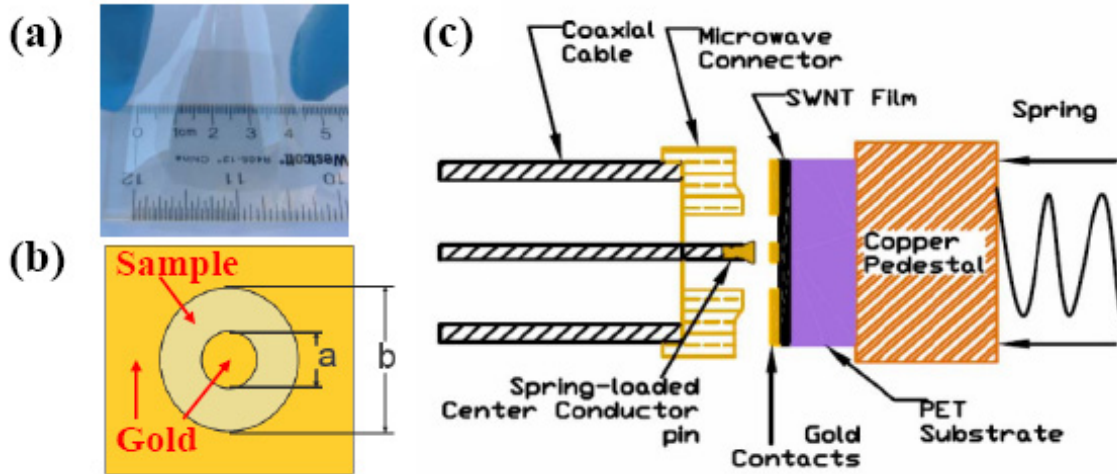


Figure 7.1: (a) A photograph of SWCNT films on PET substrate; (b) Top view of the gold corbino contact to the sample( $a=0.5\text{mm}$  and  $b=1.9\text{mm}$ ); (c) interface of microwave connector to the sample(not to scale)

SWCNT films on polyethylene terephthalate (PET) substrates are fabricated by the transfer printing method[156]. A typical test film has 30 nm thickness and 80% optical transmittance, shown in Fig. 7.1.(a). A gold contact was deposited to form a Corbino disk on the sample surface, as shown in Fig. 7.1(b). Fig. 7.1(c) shows the coaxial cable/film interface. With this setup, we are able to measure the complex reflection coefficient  $\hat{S}_{11}$  of the film continuously over the frequency range from 10 MHz to 30 GHz using an Agilent E8364B PNA.[91, 92] The surface impedance of the sample can be extracted from  $\hat{S}_{11}$ :

$$Z_s(\omega) = Z_0 \frac{2\pi}{\ln \frac{b}{a}} \cdot \frac{1 + \hat{S}_{11}(\omega)}{1 - \hat{S}_{11}(\omega)}, \quad (7.1)$$

where  $Z_0 = 50\Omega$  is the characteristic impedance of the coaxial transmission line and "a" and "b" are the inner and outer diameters of the sample contact, respectively. The obtained surface impedance  $Z_s(\omega)$  includes a contribution from the NT film  $Z_s^{NT}$  and a contribution from the substrate and the sample holder  $Z_s^{sub}$ . To extract the surface impedance of the NT film alone we also measured  $\hat{S}_{11}$  of the pure dielectric PET substrate on the same sample holder. In our measurement, the film thickness  $t_0$  and the complex propagation constant  $k_{NT}$  in the NT film satisfy  $t_0|k_{NT}| \ll 1$  and measurements are made below the frequency of the lowest propagating waveguide mode in the sample/substrate so  $\frac{1}{Z_s(\omega)} \cong \frac{1}{Z_s^{NT}} + \frac{1}{Z_s^{sub}(\omega)}$ . The surface impedance  $Z_s^{NT}$  of the NT film is obtained by subtraction and the conductivity is obtained as  $\sigma(\omega) = 1/Z_s^{NT}t_0$ .

Real and imaginary parts of the conductivity vs frequency are plotted in Fig. 7.2(a) and (b). For all the different temperatures, the conductivities keep their dc value up to about 100 MHz and start to increase at higher frequency. Both the real and imaginary parts of the conductivity start to increase dramatically approximately from 10 GHz and no saturation is observed in the measurement range. The real part increases by a factor of around 2 from 1 GHz to 30 GHz. P. Peit *et al.* found that conductivities at DC and 10 GHz are almost the same.[151] The discrepancy between

our data and theirs might be due to the difference of NT sources and purities, which could change the frequency onset of the increase. In many disordered materials the extended pair approximation model  $\sigma(\omega) = \sigma_0(1 + k(\omega/\omega_0)^s)$ ,  $s < 1$ , is used to describe the frequency dependence of the conductivity.[143] Using this model to fit the data, we found good agreement with  $k = 0.134$  and  $s \approx 0.55$  for frequencies below 10 GHz. At higher frequency, the data begin to deviate from this model as also reported by Kilbride *et al.*[143] The extended pair approximation model is too simple to fully describe the complete behavior of such a system and a more sophisticated model is needed.[143]

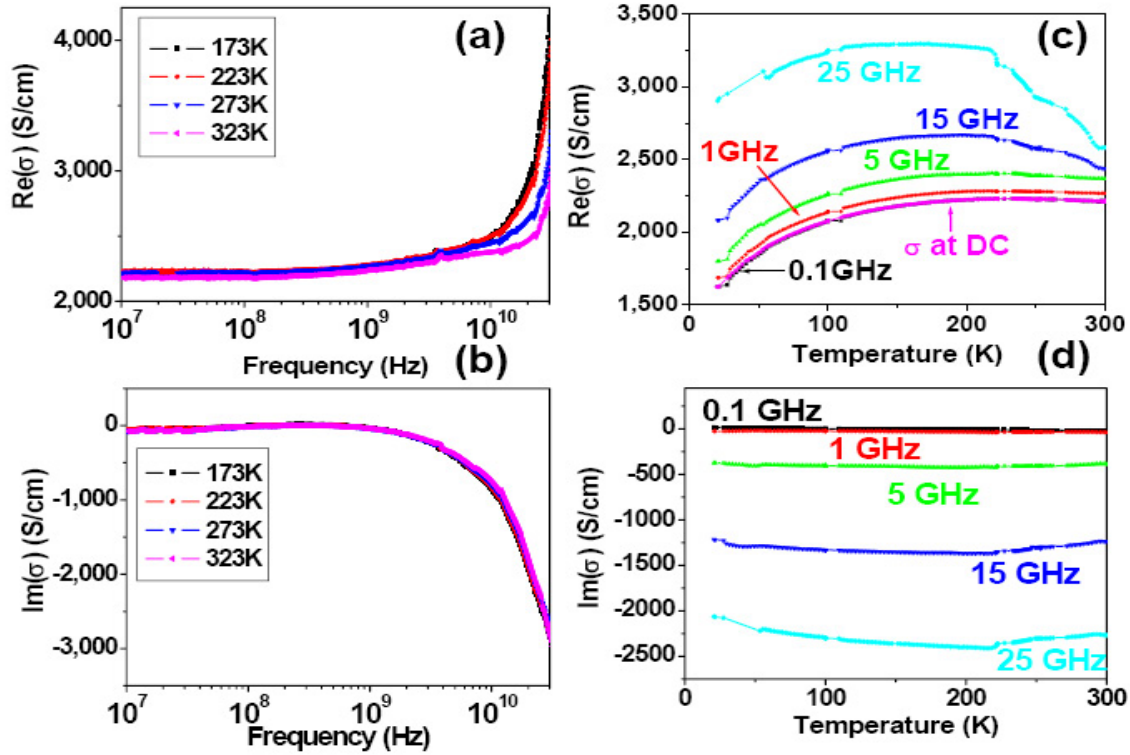


Figure 7.2: (a) and (b) are real and imaginary parts of conductivity vs microwave frequency at different temperatures; (c) and (d) are real and imaginary parts of conductivity vs temperature at various frequencies, respectively.

We measured the conductivity of the sample from 173 K to 323 K, where shielding materials are normally used. The temperature dependence of  $Re(\sigma)$  is small and

$Re(\sigma)$  gets slightly larger at high frequency, while the temperature dependence of  $Im(\sigma)$  remains small, demonstrating that the shielding effectiveness is not temperature sensitive.

Fig. 7.2(c) shows the DC conductivity and the real part of AC conductivity vs. temperature at various fixed frequencies. The real part of conductivity increases with temperature and displays a shallow maximum at  $T^* \approx 225K$ . This non-metallic to metallic crossover phenomena was investigated by Fischer *et al.*[157] The difference in  $T^*$  between this report and others is a result of high intertubular coupling, which was discussed by Bekyarova *et al.*[158] The DC resistivity fits very well to the tunneling model

$$\rho_T = Ae^{-\frac{T_m}{T}} + Be^{\frac{T_b}{T_s+T}} \quad (7.2)$$

with  $T_m = 775.2K, T_b = 30.5K, T_s = 45.9K$ , where  $Ae^{-\frac{T_m}{T}}$  is the metallic contribution and  $Be^{\frac{T_b}{T_s+T}}$  is semiconducting part contribution. The first term in Eq. 7.2 accounts for the quasi-1-D metallic conduction with a characteristic energy  $k_B T_m$  to account for the backscattering of the charge carriers, and the second term corresponds to fluctuation-induced tunneling between metallic regions that are separated by small barriers; A and B are geometrical factors,  $k_B T_b$  is the energy required for charge carrier tunneling through the barriers, and  $T_s/T_b$  is the quantum-induced tunneling in the absence of fluctuations and accounts for the suppression of the conductivity at low temperature.[158] The good fitting suggests that the carrier transport in the SWCNT films is governed by tunneling through barriers between conducting NTs. The imaginary part of AC conductivity does not change significantly with temperature, as plotted in Fig. 7.2(d).

The dielectric constants  $\varepsilon = \varepsilon_1 + i\varepsilon_2$  of SWCNT films are calculated using:  $\varepsilon_1 = 1 + \frac{Im(\sigma)}{\omega\varepsilon_0}, \varepsilon_2 = \frac{Re(\sigma)}{\omega\varepsilon_0}$ . As plotted in Fig. 7.3(a), the real part increases from around  $-10^7$  at 10 MHz to around  $-10^{-5}$  at 10 GHz. The negative value of  $\varepsilon_1$  indicates that the charge transport is dominated by delocalized-carriers(metallic).[150] The

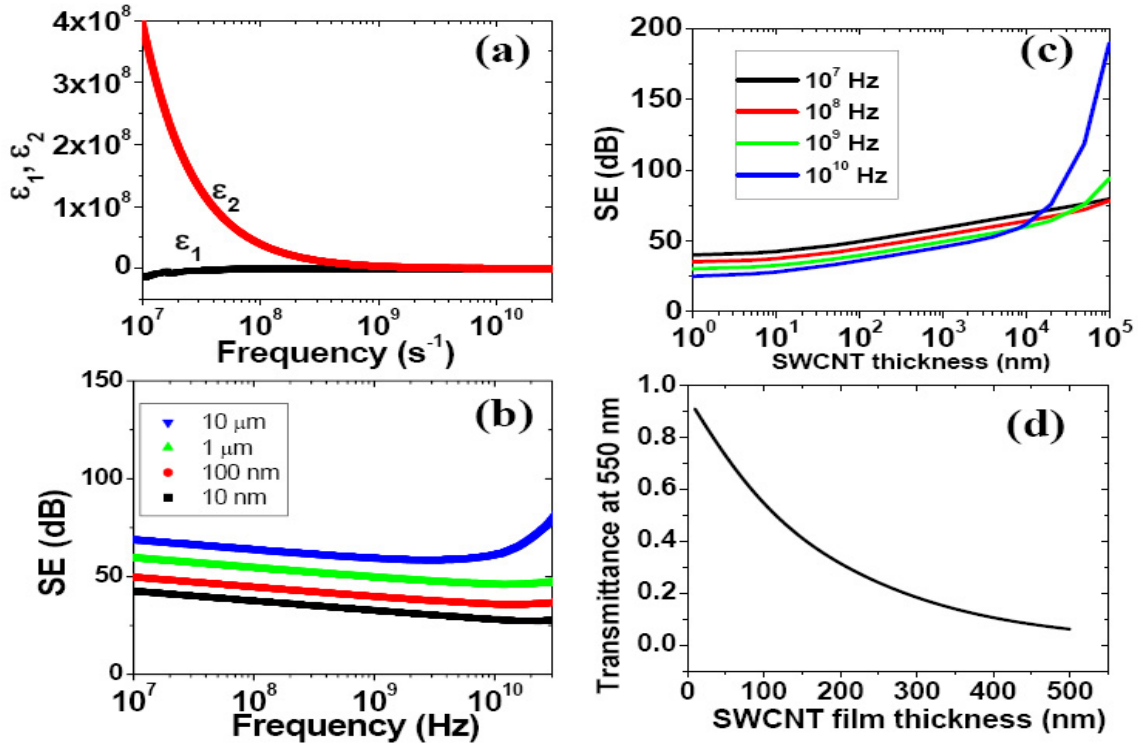


Figure 7.3: Shielding effectiveness and transmittance of SWCNT films. (a)  $\epsilon_1$  and  $\epsilon_2$  vs frequency; (b) microwave shielding effectiveness (SE) vs frequency; (c) Microwave shielding effectiveness vs thickness; (d) Calculated SWCNT optical transmittance vs thickness.

imaginary part decreases significantly from around  $4 \times 10^8$  in the MHz range to  $10^5$  in the GHz range.

The shielding effectiveness (SE) as a function of frequency for different film thickness is calculated through the formula [119]:

$$SE_{total} = -10 \log T, \quad (7.3)$$

where  $T$  is the electromagnetic radiation transmittance, which depends on the complex index of reflection  $n + ik$  and the bulk reflectivity  $R$ . This formula is applicable when the film thickness is much less than the wavelength. Calculated values of  $SE$  deduced from data are plotted in Fig. 7.3(b). The shielding effectiveness decreases as frequency increases (approximately  $SE \propto \log(1/f)$ ), except for the  $10 \mu\text{m}$  thickness



film for which a sharp increase occurs at about 1 GHz due to internal interference in the film. For the 10 nm film, the shielding effectiveness varies from 43 dB to 28 dB in the range of 10 MHz to 30 GHz. For the 10  $\mu\text{m}$  film the shielding effectiveness is 70 dB at 10 MHz and 78 dB at 30 GHz, which meets the military shielding requirement.[159] The data for shielding effectiveness vs film thickness at different frequencies are plotted in Fig. 7.3(c). At all frequencies, the shielding effectiveness increases with thickness (approximately  $SE \propto \log(d)$ ) except for the sharp jump at 10  $\mu\text{m}$  for 1 GHz and 10 GHz.

SWCNT films are widely studied for transparent electrodes due to the high transmittance in the visible and infrared range.[160] For the sake of transparent shielding applications, we calculate the visible transmittance(at a wavelength of 550nm) vs. film thickness using the formula in Ref.[119] with index of refraction  $N = 1$  for air and  $N = 1.06 + 0.24i$  for the NT film.[147] In Fig. 7.3(d), the transmittance of SWCNT films is 90% for 10 nm thickness and 60% for 80 nm thickness. For the 30 nm thickness film, the optical transmittance is about 80% and shielding effectiveness is 33 dB at 10 GHz, 36 dB at 1 GHz and 46 dB at 10 MHz. The widely used transparent shielding material, Indium tin oxide (ITO) with sheet resistance  $100\Omega/\square$ , has 30 dB shielding effectiveness at 1 GHz for 80% transmittance with 1  $\mu\text{m}$  thickness, which is lower than that of SWCNT films.

The conductivity of NT films has been measured by others in different frequency ranges. The frequency dependent conductivity follows the plasma behavior similar to that in metals with a plasma frequency between 0.1 THz and 1 THz.[150] At higher frequency it was found that the conductivity has two peaks. One peak is near 10-20 meV corresponding to the secondary bandgap which may be caused by rolling up graphene to create the NT.[145] The location of this peak varies substantially from sample to sample dues to the different SWCNT sources. The other peak is the optical bandgap around 1 eV. The conductivity at the optical bandgap edge slightly depends on chemical doping and NT purity, whereas that of the secondary bandgap

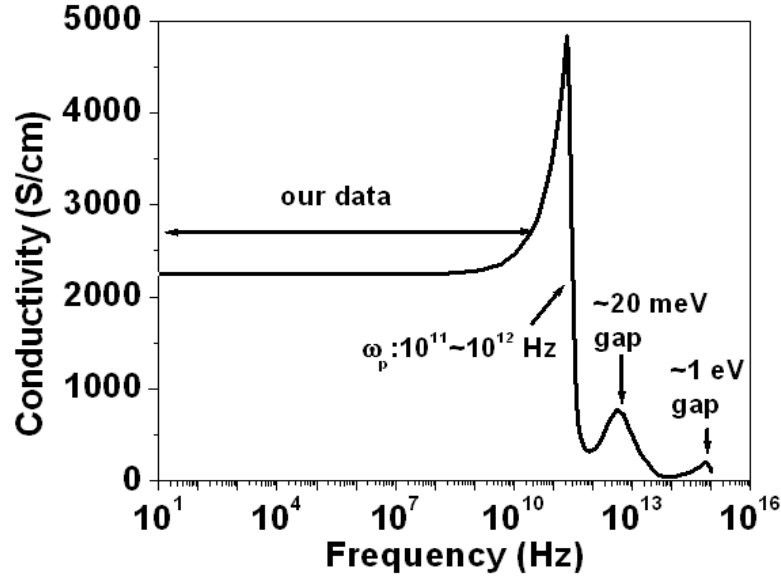


Figure 7.4: Sketch of conductivity of SWCNT film in a broad frequency range: from DC to visible.

largely depends on doping and purity.[147] Combined with our measurement, a master sketch of conductivity is made in a broad frequency range(DC to  $10^{16}Hz$ ), as shown in Fig. 7.4. For different NT sources, purities and chemical doping levels, the position and height of the peak corresponding to the 20 meV gap as well as the plasma frequency will change. Meanwhile, the peak at the optical band gap remains the same.

We found the shielding effectiveness of SWCNT films satisfies requirements for some commercial applications (e.g. cell phones require approximately 20dB shielding effect). For some extremely high shielding requirements, such as for magnetic resonant imaging window where 60 dB shielding effectiveness is required, the current transparent NT films still needs to be improved. This can be done by using optimized chemical doping, longer tubes or solely-metallic NTs, which will increase the shielding effectiveness without sacrificing the optical transmittance.[161] Along with

more development of commercial NT sources, larger scale and cheaper fabrication methods, SWCNT films are promising for transparent EMI shielding applications. The master sketch of conductivity provides guidance for exploring the potential applications of NT films as a type of electrical and photonic material.

### **7.3 Frequency and electric field dependent conductivity of single walled carbon nanotube networks of varying density**

In this section, we focus on the frequency and electric field dependent conductivity of single walled carbon nanotube networks of various densities. The ac conductivity as a function of frequency follows the extended pair approximation model and increases with frequency above an onset frequency  $\omega_0$  which varies over seven decades with a range of film thickness from sub-monolayer to 200 nm. The nonlinear electric field-dependent conductivity shows strong dependence on film thickness as well. Measurement of the electric field dependence of the resistance  $\mathbf{R}(\mathbf{E})$  allows for the determination of the length scale  $\mathbf{L}$  of localized states, which is found to systematically decrease with increasing film thickness. The onset frequency  $\omega_0$  of ac conductivity and the localization length scale  $\mathbf{L}$  of SWCNT networks are found to be related and an empirical formula has been constructed. Such studies will help the understanding of transport properties and broaden the applications of this novel material system.

SWCNT networks on polyethylene terephthalate (PET) are prepared by the spraying method.[179] Nanotube powder from Carbon Solution Inc. was dispersed in water with Sodium dodecyl sulphate (SDS) surfactants. After the nanotubes were sprayed on the substrate, the samples were rinsed in water thoroughly to wash away the surfactant. The network density was controlled by the solution concentration

and the spraying time. The nanotubes formed bundles with size of 4-7 nm.[179] The thickness of the films range from submonolayer to 200 nm corresponding to sheet conductance ranging from  $10^{-6}$  to  $10^{-2}$  S. Fig. 7.5 shows SEM pictures of two films with different densities.

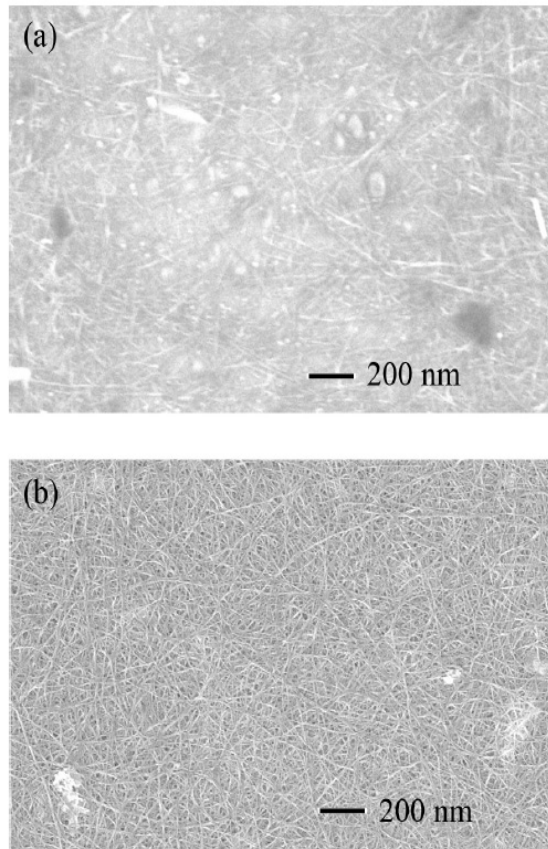


Figure 7.5: SEM of two samples with different densities. (a) sub-monolayer nanotube film; (b) nanotube film with thickness about 20 nm.

Here we still use the the Corbino reflectometry setup to investigate the conductivity of the SWCNT networks. In order to measure the conductivity in as broad a frequency range as possible, two test instruments are used, the Agilent E8364B network analyzer (covering 10 MHz to 50 GHz) and the Agilent 4396B network

analyzer (covering 100 kHz to 1.8 GHz).

### 7.3.1 Frequency dependent conductivity for various film thicknesses

The data of conductance vs. frequency are shown in Fig. 7.6(a). For all the films, the real parts of the conductance keep their dc value up to a characteristic frequency and start to increase at higher frequency. This kind of behavior has been widely observed for disordered systems.[180, 181] Similar behavior has been found for carbon nanotube polymer composites close to the percolation threshold, in which the extended pair approximation model was applied to describe the observed phenomena.[143, 175] The carbon nanotube networks in Fig. 7.6(a) have density well above the percolation threshold. However, since the junction resistance between different tubes are much larger than the resistance of the tubes themselves,[141, 142, 174] SWCNT networks above the percolation threshold can still be seen as systems with randomly distributed barriers for electrical transport. In this case the extended pair approximation model can be used to describe the ac conductance:

$$\sigma = \sigma_0(1 + k(\omega/\omega_0)^s) \quad (7.4)$$

where  $s \leq 1.0$ ,  $k$  is a constant and  $\omega_0$  is the onset frequency.[181]

Our obtained frequency dependent conductivities fit well to the extended pair approximation model. Fig. 7.6 shows the relation between the fit film onset frequency and the dc sheet conductance. The onset frequency changes from  $2 \times 10^6$  to  $1 \times 10^{10}$  Rad/sec as the sheet conductance increases from the  $10^{-6}$  to  $10^{-2}$  S. The onset frequency of the ac conductance increases as the dc conductance increases. The solid line in the figure has slope one, implying a linear relation between the onset frequency and their dc sheet conductance, or  $\omega_0 \sim \sigma_0$ .

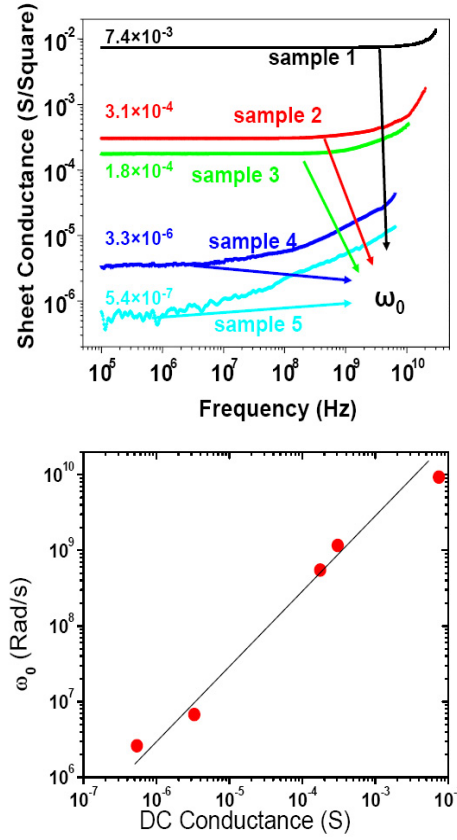


Figure 7.6: (a) Real parts of the ac conductance for samples with different densities; (b) Fit onset frequencies vs dc conductance of nanotube networks. The solid line has slope 1.

The universality of ac conduction is common in many disordered materials.[180, 181] For the polymer-nanotube composite thin films, the scaling behavior of conductivity and frequency have also been shown. [143] Similar to Kilbride *et al.*'s work, taking the dc conductivity  $\sigma_0$  and the onset frequency  $\omega_0$  as scaling parameters, we plotted the ac conductivity data for different samples in Fig. 7.7. They display a scaling behavior with all data sets falling on the same master curve.

We also measured the frequency-dependent conductance of ultra thin sub-monolayer nanotube networks, which are fabricated via the filtration method.[183] We choose Chloroform as the solvent instead of water to avoid the washing steps which can

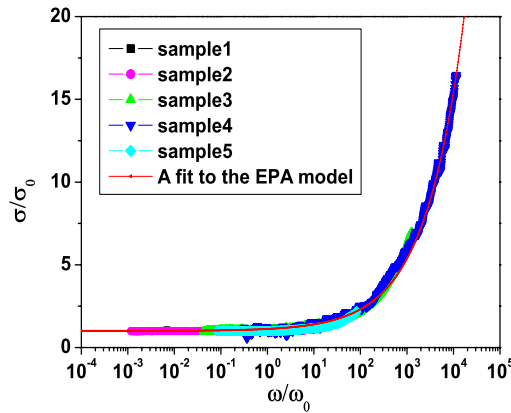


Figure 7.7: Master scaling curve showing the ac conductivity for samples with different densities. The red line is a fit to the extended pair approximation model.

easily destroy the sub-monolayer film structure. The network density is controlled by the concentration and volume of the solvent used.[183] The conductance of these films are measured by an impedance meter covering the frequency range from 20 Hz to 1 MHz. For these films just above the percolation threshold, their frequency dependent conductivities also fit well to the extended pair approximation model. In Fig. 7.8, we plot the onset frequency versus their dc sheet conductance. For comparison, we also used results in Kilbride *et al.*,[143] and plotted the onset frequency vs. conductance for Polymer-nanotube composites. The three solid lines in Fig. 7.8 all have slope one ( $rad/sec \cdot S$ ). Here an interesting result is that although the intercepts are very different, the slopes of the three different samples are essentially the same. The difference in intercept is due to the different sources. Different carbon nanotube sources have different bundle sizes, which causes the conductivity difference. The polymer-CNT composite has much smaller DC conductance than the other two, which is due to the separation of SWCNTs by polymer that leads to charge transfer barriers.

In order to explain the observed onset frequency change with the SWCNT volume

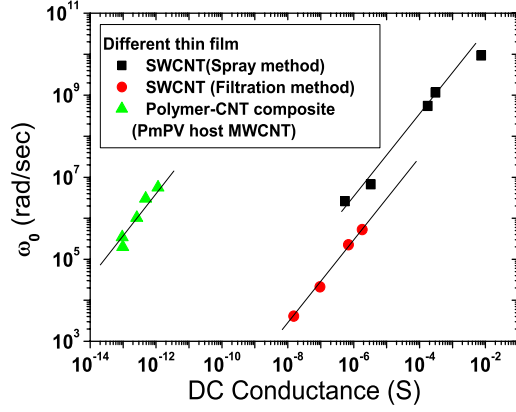


Figure 7.8: The onset frequency vs. dc conductance for different nanotube networks. The three solid lines all have slope one.

fraction for polymer-nanotube composites close to percolation threshold, Kilbride *et al.* defined a characteristic length scale, the correlation length  $\xi$ . [143] For our samples which are well above the percolation threshold, we can similarly define the correlation length  $\xi$  as the distance between connections in the sample, i.e., the distance between junctions of the multiply-connected SWCNT network. When one measures the frequency dependent conductivity for a given frequency, there is a typical probed length scale. At low frequencies (corresponding to long time scales), the carriers travel long distances in one-half ac cycle and the experiment investigates longer length scales. At high frequencies, the carriers travel short distances in one half ac-cycle and the probed length scale is shorter. In the absence of an applied DC electric field, the probed length scale  $L_\omega \propto \omega^{-1/2}$ . [143]

For low frequency,  $L_\omega > \xi$ , the probed length scale spans multiple junctions of the SWCNT network. The junction resistances between different tubes are much larger than the resistances of the tubes themselves. [141, 142, 174] Hence the conductance is small and equal to the dc conductance. As the frequency increases,  $L_\omega$  becomes smaller than  $\xi$ ,  $L_\omega < \xi$ , and the junction resistances have less contribu-



tion to the total resistance. The intrinsic properties of the SWCNT then dominate the measurement. Therefore the observed conductance increases as the frequency increases. The transition frequency is expected to be that where carriers scan an average distance of order of the correlation length. [143]

The SWCNT film can be treated as a random walk network, in which the probed length scale at a given frequency goes as  $L_\omega \propto \omega^{-1/2}$ . Then with the onset frequency  $\omega_0$  of samples we are able to estimate their correlation length  $\xi \propto L_{\omega_0} \propto \sqrt{\frac{1}{\omega_0}}$ . As the density of the SWCNT networks increases, there are more junctions and the average distance between connections, the correlation length  $\xi$ , becomes smaller and thus the onset frequency  $\omega_0$  increases. This is the behavior shown in Fig. 7.6.

### 7.3.2 Electric field dependent conductivity for various film thicknesses

From the observed frequency dependent conductivity, we observed that the correlation length  $\xi$  varies as the thickness of the film increases. Due to the large resistance of junctions between different tubes, the carriers in the SWCNT networks are easier to move on small length scales than on larger length scales. This phenomenon inspires us to investigate the localization properties of such a system. According to the works of M. S. Fuhrer *et al.* and A. B. Kaiser *et al.*, the localization behavior of SWCNT network can be studied by measuring the electric field dependent non-linearity of the conductivity. [151, 177] Generally increasing both the temperature and the electric field reduces the effects of localization. So a system of localized charge typically displays a characteristic electric field at which nonlinear conductivity begins to appear. Through measurement of the characteristic field  $E_c$  one can determine a length scale of the localized system:

$$L = \frac{k_B T}{e E_c} \quad (7.5)$$

where  $L$  corresponds to the size of the regions with good conductivity. For our SWCNT films  $L$  depends on the average distance between connections,[184]  $eEL$  is the energy gained by a carrier in one conducting region on average. In the case that the localization of carriers results from strong disorder,  $L$  is a measure of the Bohr radius  $a$  of a localized state.[185] For relatively thick films with low sheet resistance, Fuhrer *et al.* found the temperature-independent localization length scale  $L$  is approximately  $1.65\mu\text{m}$  in a SWCNT film.[177, 178]

Here we investigated the electric field-dependent conductivity for different films, and we found that the nonlinear behavior strongly depends on the thickness of the film. At low temperature, all the samples show nonlinear behavior of resistance on electric field, and the critical field  $E_C$  is larger for thicker samples and smaller for thin samples. At room temperature, all the other samples are purely ohmic(linear) in electric fields up to  $100\text{ V/cm}$ , except for the thinnest sample, sample 5, which showed electric field-dependent conductivity at all temperatures.

Here the probe used to perform the measurement was specially designed to reduce the heating effect. The heating effect and the possible induced temperature rise on sample when performing voltage current characteristic measurement in this probe have been addressed in Su Li's thesis.[139] According to his discussion, the possible temperature rise on SWCNT films should be less than  $1\text{ K}$  in our measurement range.

The resistance vs. electric field of a very thin film(sample 5) at different temperatures is shown in Fig. 7.9(a). We can see clearly that there is nonlinear behavior even at room temperature. As sketched in Fig. 7.9(a), we extracted  $E_c$  for each temperature, which is the characteristic electric field at which nonlinear conductivity begins to appear.[177] Fig. 7.9(b) shows the extracted  $E_c$  vs temperature for this sample. As temperature increases,  $E_c$  also increases. Roughly  $E_c$  and temperature have a linear relationship and satisfy the equation  $E_c = k_B T / eL$ , with  $L \approx 50\mu\text{m}$ .

The observed localization length scale  $L \approx 50\mu\text{m}$  in this very thin film is much

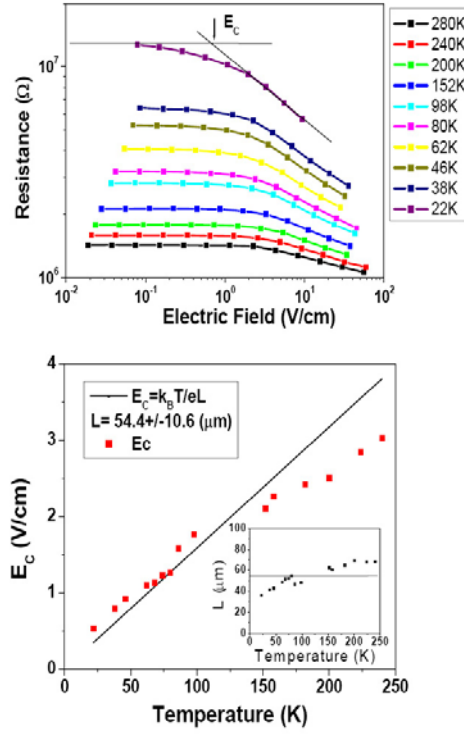


Figure 7.9: (a) Resistance vs electric field for a very thin film (sample 5) at different temperatures. (b)  $E_c$  vs temperature and extracted localization length scale for this sample.

larger than what was reported by M. S. Fuhrer *et al.*[177, 178] For this very thin film, the localization length scale was dramatically increased compared to the thick film. To investigate the dependence of the localization length scale on the film thickness, we measured the electric field-dependent conductivity for samples with various thicknesses and extracted their localization length scale. The localization length scale for different density films are shown in Fig. 7.10 as round-dot. Clearly the localization length scale  $L$  depends on the density of the SWCNT networks. For the thicker film with larger SWCNT density, which has larger sheet conductance, the localization length scale is smaller. Combined with the frequency dependent conductivity, we believe that the poor inter-bundle junctions affected the localization

length scale. The lower density with larger average distance between the junctions has larger localization length scale. The higher density film, which has smaller average distance between the junctions, has smaller localization length scale.

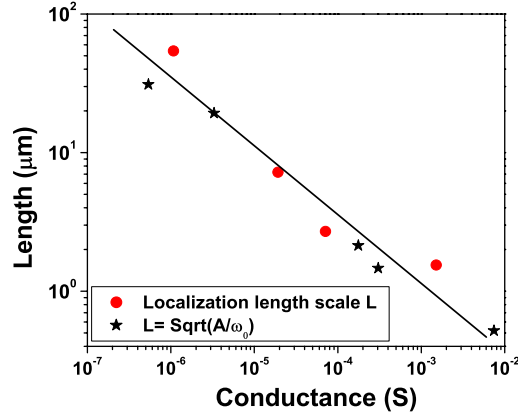


Figure 7.10: Comparison of the localization length scale obtained from electric field depend conductivity data (red dot) and the estimated localization length scale from frequency dependent conductivity measurement (black star). The line has slope  $-1/2$  in the above log-log plot.

Although the localization behavior may be affected by the individual SWCNT [177, 178], the above result shows that the localization behavior is also a consequence of poor electric conduction between inter-bundle junctions. For very thin films, the inter-bundle connections even dominate the localization behavior. As the thickness and density increase, there are more and more connections, which decreases the localization length scale, as shown in Fig. 7.10.

When the film thickness increases to a large value, the density of the SWCNTs and connections of the film will finally saturate and stop increasing. For those very thick SWCNT films (also called mats), their correlation length  $\xi$  will be independent of the thickness. The localization length scale and the onset frequency are determined by the distribution of nanotubes and the properties of individual bundles,

which include both the disorder of the individual nanotube and also the geometry of the bundles. These properties affect the junction resistance and also the density. Hence the difference of SWCNT sources and purities can change the onset frequency. We believe this is the reason that our previous work found that the ac conductivity follows the extended pair approximation model with an onset frequency  $\omega_0$  about 10 GHz, but Peit *et al.* found that SWCNT networks have the same conductivities at DC and 10 GHz for SWCNT networks with thickness in the range of tens of micrometers.[176, 151]

### 7.3.3 Discussion of the frequency and electric field dependent conductivity

The frequency dependent conductivity shows that the onset frequency  $\omega_0$  increases with the sample thickness and gives an estimation of the correlation length  $\xi$  of the sample,  $\xi \propto L_{\omega_0} \propto \sqrt{\frac{1}{\omega_0}}$ .  $\xi$  and  $L_{\omega_0}$  decrease as the sample thickness increases. The DC conductivity measurement shows the localization length scale  $\mathbf{L}$  of the samples also decreases with the sample thickness. Qualitatively  $L_{\omega_0}$  and  $\mathbf{L}$  have the same dependence on the sample thickness. Because both  $L_{\omega_0}$  and  $\mathbf{L}$  depend on the  $\xi$ , we propose a linear relation between  $\mathbf{L}$  and  $L_{\omega_0}$ :

$$L = C_f L_{\omega_0} \quad (7.6)$$

Here  $L_{\omega_0}$  is the typical probed length scale at the onset frequency  $\omega_0$  and  $C_f$  should be a constant on the order of one. With the assumption  $C_f = 1$ , we can assume  $L_{\omega} \propto \sqrt{\frac{A}{\omega}}$ , where  $A$  is fitting parameter. We can obtain this fitting parameter  $A$  from our experiment data,  $A \sim 2.5 \times 10^{-3} m^2/s$ . With this parameter, the onset frequency  $\omega_0$  can be translated to the localization length scale  $\mathbf{L}$ . Fig. 7.10 shows the comparison of the localization length scale  $\mathbf{L}$  measured directly through electric-field dependent conductivity measurements(round-dot) and the translated  $\mathbf{L}$  from the frequency dependent measurement(black-square). They are consistent with each other. In

this way we obtained an empirical formula to relate the frequency dependent and the electric field dependent conductivity. In the above discussion, we take  $A$  as a constant, which may depend on the diffusion properties of the SWCNT films.[186] To get deep physical understanding of this constant, more investigation and theoretical work are needed.

The combination of the frequency dependent and electric field dependent conductivity measurements confirmed the localization behavior is not only due to the individual SWCNTs, but also a consequence of conduction across poor interbundle connections. For thinner films, the localization length scale is larger and the interbundle resistance contributed more to the resistivity, which we have tested by performing temperature dependent conductivity measurements for different density films.

To conclude, we systematically studied the frequency and electric field dependent conductivity of SWCNT films with various thicknesses. We found the poor interbundle junctions affect the localization behavior of the carriers in the SWCNT films, which causes strong thickness dependence of the localization length scale. A thinner film has larger correlation length  $\xi$  and localization length scale  $\mathbf{L}$ , so it has smaller onset frequency  $\omega_0$ , whereas a thicker film with smaller correlation length  $\xi$  and localization length scale  $\mathbf{L}$ , has larger onset frequency  $\omega_0$ . The approximate empirical formula of the onset frequency  $\omega_0$  and localization length scale relates the frequency and the electric field dependent conductivity, which helps us to understand the electric transport properties of the SWCNT films.

## Chapter 8

# Conclusion and future work

### 8.1 Results and Conclusions

I have successfully developed a unique broadband frequency measurement system for surface electrical conductivity measurement (100 kHz to 50 GHz) from room temperature to cryogenic temperatures. We conducted research on the fluctuations at the superconductor to normal phase transition and electric transport properties of single walled carbon nanotube networks with the developed system.

I studied microwave conductivity of  $\text{YBa}_2\text{Cu}_3\text{O}_{7-\delta}$  thin films around  $T_c$  for different incident microwave power. The length scales in AC measurement have been systematically discussed. At low current density  $J$  but high  $\omega$ , the critical behavior can be examined without getting into finite-size effects. However, at low current density  $J$  and low frequency  $\omega$ ,  $L_{AC} > d$ , the critical behavior will be destroyed by finite-size effect. In this region, we can not observe the phase transition.

With very small applied microwave power, which is -46dBm, and using the high frequency part of the data, I investigated fluctuation effects in  $\text{YBa}_2\text{Cu}_3\text{O}_{7-\delta}$  thin films around  $T_c$  by taking frequency-dependent microwave conductivity measurements. We proved that the determination of  $T_c$  is crucial for the conventional data analysis method. With an improved setup, I took measurements at a smaller temperature increment. Through an improved conventional data analysis method and

a newly developed analysis method, the critical temperature can be determined precisely. I obtained a critical exponent  $z = 1.55 \pm 0.15$ , which is consistent with model-E dynamics of the 3D-XY universality class. Finally the scaling behavior of the fluctuation conductivity was also shown both above and below the critical temperature.

Frequency-dependent microwave conductivity measurements and dc current-voltage characteristics have also been combined together to investigate fluctuation effects of  $YBa_2Cu_3O_{7-\delta}$  on the same film. The dc measurement verified that the applied microwave power of -46dBm in our ac measurement is small enough for the correct determination of  $T_c$  and critical exponents. I found that the dc measurement could be affected by disorder. For higher  $T_c$  YBCO films and crystals, the critical exponent  $z$  is also around 1.5, which is consistent with the ac measurement.

Finally, using our broadband experimental technique and DC VI measurement system, I measured the transport properties of single-walled carbon nanotube films. A shielding effectiveness of 43 dB at 10 MHz and 28 dB at 10 GHz is found for films with 90% optical transmittance, which suggests that SWNT films are promising as a type of transparent microwave shielding material.

I also systematically studied the frequency and electric field dependent conductivity of SWCNT films with various thicknesses. I found that the poor interbundle junctions affect the localization behavior of the carriers in the SWCNT films, which causes strong thickness dependence of the localization length scale. A thinner film has larger correlation length  $\xi$  and localization length scale  $\mathbf{L}$ , and has smaller onset frequency  $\omega_0$  whereas a thicker film with smaller correlation length  $\xi$  and localization length scale  $\mathbf{L}$ , has larger onset frequency  $\omega_0$ . The approximate empirical formula of the onset frequency  $\omega_0$  and localization length scale relates the frequency dependent and the electric field dependent conductivity together and helps us to understand the electric transport properties of the SWCNT films.



## 8.2 Future Work

Although we could finish here with all we have accomplished, I feel it is better to list some interesting things that have not been done.

One extension of this work here is to study the power dependent properties at even lower frequency. By utilizing additional instruments we can measure the surface conductivity at lower frequencies. We may be able to observe the clearer crossover of frequency dominant fluctuation conductivity to current density dominant fluctuation conductivity. Taking this kind of experiment on different thickness of films and also crystals with different applied power, we will be able to establish a quantitative relation between probed length scale  $L_{AC}$  and current density and frequency.

Another extension of the work is to study fluctuation effects in magnetic fields. It would be interesting to see how the critical exponents and scaling functions in zero field are modified by applied magnetic field. It would also be interesting to compare the dc results in magnetic field with the ac result in magnetic field. Although it is an interesting topic, there are lots of challenges here. There would be three variables, frequency  $\omega$ , current density  $J$  and magnetic  $H$ , as well as sample thickness. They might all have induced length scales, and interact with each other, which would make this question difficult, but interesting.

In this work, we studied the optimal-doped  $YBa_2Cu_3O_{7-\delta}$  film and investigated the universality of the scaling behavior of the fluctuation conductivity in the high  $T_c$  superconductors. So one natural question is how about other samples? A systematic experimental investigation of different high  $T_c$  superconducting materials would be very helpful for studying the universality of the scaling behaviors.  $YBa_2Cu_3O_{7-\delta}$  is a hole-doped HTSC material. It would be interesting to investigate some electron-doped HTSC materials, for example, PCCO film, which can be easily fabricated in our Center. For this experiment, we only need to add some extra thermal shielding layers in the system so that the sample can be cooled to lower temperature.

The other interesting thing to do is to investigate under-doped YBCO films. I have successfully developed a method of fabrication of different doping YBCO samples. Using our broadband measurement system, we can investigate the frequency dependent conductivity of under-doped YBCO samples, particularly above  $T_c$ , and the pseudogap properties.

Finally, since the broadband measurement technique is powerful, we may also apply it to other fields outside the superconductivity, such as investigate frequency dependent properties of carbon nanotube films, and study dielectric critical phenomena. I believe this will give us lots of opportunities. An open mind will lead us forward.

## Appendix A

# Current-Induced Length Scale (Notes Due to Prof. C. J. Lobb)

### A.1 Initial considerations

Consider a simple model for fluctuations in superconductors, where we assume that the only fluctuations are circular vortex loops of radius  $\mathbf{r}$ . The energy of such a loop can be written as

$$U_{loop} = 2\pi r \epsilon(r) \tag{A.1}$$

where  $\epsilon(r)$  is the energy per unit length of the vortex loop of radius  $r$ . For a straight vortex, the energy was given in Eq. 5.17 by Tinkham in Gaussian unit [15],

$$\epsilon(r = \infty) = \left(\frac{\Phi_0}{4\pi\lambda}\right)^2 \ln\left(\frac{\lambda}{\xi}\right). \tag{A.2}$$

In general, curvature will increase the energy per unit length.

In an infinite superconductor with no applied current, vortex loops of different sizes occur with different probabilities as thermal fluctuations. Formally, the probability of finding a loop of size  $\mathbf{r}$  in a range  $d\mathbf{r}$  is given by

$$P(r)dr = \frac{e^{-\frac{2\pi\epsilon(r)}{kT}} dr}{\int_{\xi}^{\infty} e^{-\frac{2\pi\epsilon(r)}{kT}} dr}. \tag{A.3}$$

Note that here vortex loops of all sizes occur.

Suppose we wanted to find the size of a typical vortex loop. One way to do this is to integrate Eq. A.3 from this typical size, which we call  $r_{thermal}$ , to  $\infty$ , and require that the fraction of loops  $F$  with  $r > r_{thermal}$  be equal to  $\frac{1}{2}$ ,

$$F = \frac{\int_{r_{thermal}}^{\infty} e^{-\frac{2\pi\epsilon(r)}{kT}} dr}{\int_{\xi}^{\infty} e^{-\frac{2\pi\epsilon(r)}{kT}} dr} \equiv \frac{1}{2}. \quad (\text{A.4})$$

In Eq. A.4, I used the approximation that  $\epsilon(r)$  is independent of  $\mathbf{r}$ . Eq. A.4 leads to

$$r_{thermal} = \xi + \frac{kT}{2\pi\epsilon} \ln 2. \quad (\text{A.5})$$

If the second term on the right hand side of Eq. A.5 dominates, this gives

$$r_{thermal} = \xi + \frac{kT}{2\pi\epsilon} \ln 2 \rightarrow \epsilon = \frac{kT}{2\pi r_{thermal}} \ln 2. \quad (\text{A.6})$$

Eq. A.6 states that, within a factor of  $\ln 2$ , the total energy of a vortex loop of size  $r_{thermal}$  is equal to  $kT$ , which is a plausible result.

To check whether the second term on the right side of Eq. A.5 is the dominant one, combine Eqs. A.2 and A.5. Using  $\kappa \equiv \lambda/\xi$ , this leads to

$$r_{thermal} = \xi \left[ 1 + \frac{\xi}{\left(\frac{16\pi^2 kT}{\Phi_0^2}\right)} \frac{\kappa^2 \ln 2}{2\pi \ln \kappa} \right] = \xi \left[ 1 + \frac{\xi}{\Lambda_T} \frac{\kappa^2 \ln 2}{2\pi \ln \kappa} \right] \quad (\text{A.7})$$

where  $\Lambda_T$  is defined in Eq.1.1 of the Fisher, Fisher, and Huse paper.[54] The second term in Eqs. A.5 and A.7 dominate in the critical regime because  $\xi$  diverges while  $\Lambda_T$  is fixed. For simplicity, we drop the  $\ln 2$  in Eq. A.5, and use

$$r_{thermal} = \frac{kT}{2\pi\epsilon}. \quad (\text{A.8})$$

Next consider that a current per unit area  $J$  is applied to a plane perpendicular to the area of the loop. The total Lorentz force on the loop is

$$F_{ext} = 2\pi r J \Phi_0. \quad (\text{A.9})$$

Taking the minus one times the derivative of Eq. A.1 gives the force that the loop exerts on itself. Summing the forces and finding the point where the force is equal to zero leads to a critical loop size

$$r_{\text{blowout}} = \frac{\xi}{\Phi_0 J}, \quad (\text{A.10})$$

where, for simplicity,  $\xi(r)$  is again assumed to be independent of  $\mathbf{r}$ .

Physically, if a vortex loop has  $r > r_{\text{blowout}}$ , the external current "blows out" the loop to infinite size; this process leads to dissipation. If  $r < r_{\text{blowout}}$ , the vortex loop shrinks and annihilates.

The above equation can be also interpreted in different ways. The presence of a current density  $J$  significantly alters the population of vortex loops with  $r > r_{\text{blowout}}$ , and has less effect on the vortex loops with  $r < r_{\text{blowout}}$ . In this sense, a current  $J$  probes the physics on length scales of order  $r_{\text{blowout}}$  and larger. This is the type of language that has been used to describe  $L_J$ . As I'll show below, it is probably not correct to describe  $L_J$  in this manner.

What is the physical significance of comparing the various lengths,  $r_{\text{blowout}}$  and  $r_{\text{thermal}}$ , Eqs. A.8 and A.10, to each other? If  $r_{\text{thermal}} \ll r_{\text{blowout}}$ , the current is probing a length scale where there are very few vortices. The current thus acts as a very small perturbation on the system. If  $r_{\text{thermal}} \gg r_{\text{blowout}}$ , the current is probing a very short length scale, and a large portion of the intrinsic vortex population is being disrupted by the current. The point where  $r_{\text{thermal}} = r_{\text{blowout}}$  thus marks a crossover in the behavior from current acting as a small perturbation to current acting as a large perturbation.

What is the physical significance of comparing the various lengths,  $r_{\text{blowout}}$  and  $r_{\text{thermal}}$ , Eqs. A.8 and A.10, to the film thickness  $d$ ? It is plausible to say  $r_{\text{thermal}} \ll d$  is the three-dimensional limit, while  $r_{\text{thermal}} \gg d$  is the two-dimensional limit, since in the second case most of the vortex loops are interrupted by the film thickness, while in the first case they are not. This is true as far as it goes, but it misses the

key point that an applied current probes physics at the scale of  $r_{blowout}$  and larger, as discussed above. Thus, even in the limit  $r_{thermal} \gg d$ , if  $r_{blowout}$  is small enough, it will probe physics on length scales smaller than  $d$ , and thus the measurement will not be affected by the finite thickness of the film. What is required is that the current probes a significant fraction of the loop population and also probes lengths on the scale of the film thickness. For this to be true, it is reasonable to require that

$$r_{blowout} = r_{thermal} \equiv L_J \quad (\text{A.11})$$

Combining Eqs. A.8,A.10 and A.11 gives

$$L_J = \left( \frac{kT}{2\pi\Phi_0 J} \right)^{\frac{1}{2}} \quad (\text{A.12})$$

This suggests the following physical description for  $L_J$ : For any  $J$  there is a length scale  $L_J$ , given by Eq. A.12, such that roughly half the equilibrium (zero current) vortex population is blown out by  $J$ , and the other half are not. This is the length that one should compare to the film thickness for seeing whether or not the measurements are in the two or three dimensional limit. The requirements are that there be a significant fraction of the loops that feel the film thickness, and, in addition, that the current is probing on the same length scale.

## A.2 A More Realistic Model for $\epsilon(r)$

In this section, we use the analogy between a vortex loop and wire loop to calculate  $\epsilon(r)$ . For convenience, the SI units are used. We start with an analogy between a long straight wire carrying a current  $I_1$ . This current creates a magnetic field  $B_1$  given by

$$B_1 = \frac{\mu_0 I_1}{2\pi r} \quad (\text{A.13})$$

A parallel wire carrying a current  $I_2$  feels a force per unit length given by

$$f = B_1 I_2 \quad (\text{A.14})$$

and the energy per unit volume associated with a field B is given by

$$\frac{E}{V} = \frac{B^2}{2\mu_0} \quad (\text{A.15})$$

Next, consider a straight vortex. Outside the core but inside the penetration depth, for  $\xi \ll r \ll \lambda$ , there is a circumferential velocity given by

$$v_1 = \frac{n_1 h}{2\pi m^* r} \quad (\text{A.16})$$

Where  $n_1$  is an integer,  $h$  is Planck's constant, and  $m^*$  is the Cooper pair mass. ( $n_1$  is included to make comparisons clearer, the usual case is  $n_1 = 1$ ). If there is a second parallel vortex with vorticity  $n_2$ , the force per unit volume exerted by the first vortex on the second is given by

$$f = j_1 n_2 \Phi_0 \quad (\text{A.17})$$

Where  $j_1$  is the current per area created by the first vortex, so that  $j = n^* q^* v$ , where  $n^*$  is the Cooper pair density,  $q^* = 2e$ , and  $v$  is the superfluid velocity.

Finally, the energy per unit volume associated with a superfluid velocity is just the kinetic energy,

$$\frac{E}{V} = \frac{1}{2} n^* m^* v^2 \quad (\text{A.18})$$

Eqs. A.13-A.15 are analogous to A.16-A.18, and the physics is the same. In both cases, there is a  $1/r$  field (B or v) with an energy that is quadratic in the field. You can use the analogy to map well-understood problems involving currents and inductances onto problems involving vortices.

To do this, the following translation table has been made, See Tab. A.1. By substituting quantities in the first column into results from circuit theory, you get analogous results for vortices. For example, substituting the appropriate second-column quantities into Eq. A.13 leads to Eq. A.16.

This is particularly valuable to calculate energies of systems. This is done using the inductive energy formula

$$E = \frac{1}{2} L I^2. \quad (\text{A.19})$$

Table A.1: Analogy between wire loop and vortex loop

Currents	Vortices
$\mu_0$	$\frac{1}{m^*n^*}$
$I$	$hm^*n^*$
$B$	$v$

Ramo, Whinnery, and Van Duzer's book gives the formula for the inductance of a wire loop with a radius  $\mathbf{a}$  bending into a loop radius  $\mathbf{r}$ , which is the distance from the center of the loop to the center of the wire.[137] The formula is

$$L = \mu_0(2r - a)[(1 - \frac{k^2}{2})K(k) - E(k)] \quad (\text{A.20})$$

Where  $E(k)$  and  $K(k)$  are complete elliptic integrals of the first and second kind,

$$E(k) = \int_0^{\pi/2} \sqrt{1 - k^2 \sin^2 \phi} d\phi, K(k) = \int_0^{\pi/2} \frac{1}{\sqrt{1 - k^2 \sin^2 \phi}} d\phi \quad (\text{A.21})$$

and

$$k^2 = \frac{4r(r - a)}{(2r - a)^2}. \quad (\text{A.22})$$

Using the translation table A.1 and Eqs. A.19 to A.22, we can get the energy of a vortex loop of radius  $r$  and thus the energy per unit length  $\epsilon(r)$ . Note that the analogy requires that the superfluid velocity varies as  $1/r$ , so that  $\xi \ll r \ll \lambda$ .

As an example, I'll look at Eq. A.20 in the limit  $a \ll r$ , ie, the loop is much larger than the coherence length. In this limit,  $E(k) \approx 1$  and  $K(k) \approx \ln(\frac{4}{\sqrt{1-k^2}})$ , which leads to

$$L = \mu_0 r [\ln(\frac{8r}{a}) - 2]. \quad (\text{A.23})$$

Using table A.1 and Eqs. A.19 and replacing  $\mathbf{a}$  by  $\xi$ , this leads to the energy per unit length of a vortex loop with radius  $r$  of

$$\epsilon = \pi \frac{\hbar^2}{m^*} n^* [\ln(\frac{r}{\xi}) + \ln 8 - 2] \approx \pi \frac{\hbar^2}{m^*} n^* [\ln(\frac{r}{\xi})] \quad (\text{A.24})$$



It is interesting to note that the last form matches Eq. A.2 at  $r = \lambda$ , even though it was derived assuming that  $r \ll \lambda$ . Thus it is probably a good approximation to use

$$\epsilon(r) \approx \left(\frac{\Phi_0}{4\pi\lambda}\right)^2 \left[\ln\left(\frac{r}{\xi}\right)\right], \text{ for } \xi \ll \leq \lambda \quad (\text{A.25})$$

$$\epsilon(r) \approx \left(\frac{\Phi_0}{4\pi\lambda}\right)^2 \left[\ln\left(\frac{\lambda}{\xi}\right)\right], \text{ for } r \gg \lambda \quad (\text{A.26})$$

## Appendix B

# Fitting of microwave conductivity for sample xuh139 in different frequency ranges

In the chapter 4, I determined  $T_c$  through an improved conventional data analysis method by doing quadratic fits of  $\log(|\sigma_{fl}|)$  vs.  $\log(f)$  and linear fits of  $\phi_{fl}$  vs.  $\log(f)$  in the frequency range 0.4 to 10 GHz. In this appendix, I show in more detail the fitting results in different frequency ranges.

The positive sign of the second order coefficient of the quadratic fit of  $\log |\sigma_{fl}|$  vs.  $\log(f)$  means the curves bend up in a log-log plot and a negative sign means they bend down. So the determined  $T_c$  should be between the two isotherms where their signs change. Similarly, signs of the slope of  $\phi_{\sigma}(\omega)$  vs.  $\log f$  also tell where  $T_c$  should be.

Here the Table B.1 and B.1 show that the determined  $T_c$  can change upon adjustment of the frequency range used to do the fits. This brings some error in the determination of  $T_c$ . After carefully checking Table B.1 and B.2, we determine  $T_c = 89.22 \pm 0.05$  K.

Table B.1: Sign of the coefficient of  $(\log f)^2$  of quadratic fit for  $\log |\sigma_{fl}|$  vs.  $\log(f)$  in different frequency ranges for different temperatures for sample xuh139.

Frequency range (GHz)	89.087	89.140	89.192	89.245	89.297	89.350
0.2 to 10	+	+	+	+	-	-
0.3 to 10	+	+	+	-	-	-
0.4 to 10	+	+	+	-	-	-
0.5 to 10	+	+	-	-	-	-
0.7 to 10	+	+	+	+	-	-
0.9 to 10	+	+	+	+	-	-
0.3 to 4	+	+	+	-	-	-
0.3 to 6	+	+	+	-	-	-
0.3 to 8	+	+	+	-	-	-
0.3 to 12	+	+	+	+	-	-
0.4 to 4	+	+	+	-	-	-
0.4 to 6	+	+	+	-	-	-
0.4 to 8	+	+	+	-	-	-
0.4 to 12	+	+	+	+	-	-
0.5 to 8	+	+	-	-	-	-
0.5 to 12	+	+	+	+	-	-
0.6 to 8	+	+	+	-	-	-
0.6 to 12	+	+	+	+	-	-
0.7 to 8	+	-	-	-	-	-
0.7 to 12	+	+	+	+	-	-
0.8 to 8	+	+	-	-	-	-
0.8 to 12	+	+	+	+	-	-

Table B.2: Sign of the slope of linear fits to  $\phi_\sigma(\omega)$  vs.  $\log f$  for different frequency ranges for different temperatures for sample xuh139.

Frequency range (GHz)	89.087	89.140	89.192	89.245	89.297	89.350
0.2 to 10	-	-	-	+	+	+
0.3 to 10	-	-	+	+	+	+
0.4 to 10	-	-	-	+	+	+
0.5 to 10	-	-	-	+	+	+
0.7 to 10	-	-	-	-	+	+
0.9 to 10	-	-	-	-	+	+
0.3 to 4	-	-	+	+	+	+
0.3 to 6	-	-	+	+	+	+
0.3 to 8	-	-	+	+	+	+
0.3 to 12	-	-	+	+	+	+
0.4 to 4	-	-	+	+	+	+
0.4 to 6	-	-	+	+	+	+
0.4 to 8	-	-	+	+	+	+
0.4 to 12	-	-	-	+	+	+
0.5 to 8	-	-	-	+	+	+
0.5 to 12	-	-	-	+	+	+
0.6 to 8	-	-	-	+	+	+
0.6 to 12	-	-	-	+	+	+
0.7 to 8	-	-	-	+	+	+
0.7 to 12	-	-	-	-	+	+
0.8 to 8	-	-	-	+	+	+
0.8 to 12	-	-	-	-	+	+

# Bibliography

- [1] H. Kamerlingh Onnes, *Leiden Comm.* **120b**, **122b**, **124c** (1911).
- [2] W. Meissner and R. Ochsenfeld, *Naturwissenschaften* **21**, 787 (1933).
- [3] F. London and H. London, *Proc. Roy. Soc.(London)* **A149**, 71 (1935).
- [4] V. L. Ginzburg and L. D. Landau *Zh. Eksp. Teor. Fiz.* **20**, 1064-82 (1950).
- [5] J. Bardeen, L. N. Cooper and J. R. Schrieffer *Phys. Rev.* **108**, 1175-204 (1957).
- [6] L. P. Gor'kov *Zh. Eksp. Teor. Fiz.* **36**, 1918-23 (1959).
- [7] G. Bednorz and K. L. Muller *Zeit. Phys. B* **64**, 189-193 (1986).
- [8] M. K. Wu and J. R. Ashburn and C. J. Torng and P. H. Hor and R. L. Meng and L. Gao and Z. J. Huang and Y. Q. Wang and C. W. Chu *Phys. Rev. Lett* **58**, 908-910 (1987).
- [9] S. Hikami and T. Hirai and S. Kagoshima *Jpn. J. Appl. Physics* **26**, L314 (1987).
- [10] Z. X. Zhao and L. Q. Chen and Q. S. Yang and Y.H. Huang and G.H. Chen and R. M. Tang and G.R. Liu and C. G. Cui and L. Chen and L. H. Wang and S. Q. Guo and S. L. Li and J. Q. Bi *Kexue Tongbao* **33**, 661 (1987).
- [11] C. J. Lobb, *Phys. Rev. B* **36**, 3930 (1987).
- [12] V. L. Ginzburg, *Fiz. Tverd. Tela* **2**, 2031 (1960).

- [13] M. B. Salamon *et al.*, Phys. Rev. B **38**, 885 (1988); S. E. Inderhees *et al.* Phys. Rev. Lett **66**, 232 (1991); S. E. Regan *et al.*, J. Phys. Condens. Matter **3** 9245 (1991).
- [14] Koch *et al.*, Phys. Rev. Lett. **63**, 1511 (1989); Koch *et al.* Phys. Rev. Lett. **64**, 2586 (1990); Y. Ando *et al.* Phys. Rev. Lett. **69**, 2851 (1992); B. Brown *et al.* Phys. Rev. B **55**, R8713 (1997); C. Dekker *et al.* Phys. Rev. Lett. **68**, 3347 (1992); M. Charalambous *et al.* Phys. Rev. B **58**, 9510 (1997); Z. Sefrioui *et al.* Phys. Rev. B **60**, 15423 (1999); P. Voss-deHaan *et al.* Phys. Rev. B **60**, 12443 (1999); Z. L. Xiao *et al.* Sol. State Comm. **95**, 53 (1995); C. Wengel *et al.* Phys. Rev. B **54**, R6869 (1996); H. Kawamura *et al.* J. Phys. Soc. Jpn. **69**,29(2000).
- [15] M. Tinkham, *Introduction to Superconductivity* (McGraw-Hill, New York, 1996).
- [16] James F. Annett, *Superconductivity, Superfluids and Condensates* (Oxford Univeristy Press, Oxford New York, (2004).
- [17] D. L. Goodstein, *States of Matter* (Prentice-Hall, Inc., Englewood Cliffs, New Jersey, 1975).
- [18] D. R. Strachan, *The Superconducting Transition of YBCO*, Ph. D. thesis, Univeristy of Maryland, 2002.
- [19] T. P. Orlando and K. A. Delin, *Foundations of Applied Superconductivity*, (Addison-Wesley, 1991).
- [20] P. W. Anderson and Y. B. Kim, *Rev. Mod. Phys.* **36**, 39 (1964).
- [21] A. I. Larkin, *Sov. Phys. JETP* **31**, 784 (1970).
- [22] A. I. Larkin and Yu. V. Ovchinnikov, *J. Low Temp. Phys.* **34**, 409 (1979).

- [23] R. A. Buhrman and W. P. Halperin, *Phys. Rev. Lett.* **30**, 692-5 (1973).
- [24] J. B. Parkinson *J. Phys. F: Metal Phys.* **2**, 966-71 (1972).
- [25] B. Muhlschlegel, D. J. Scalapino and R. Denton *Phys. Rev. B* **6**, 1976-77 (1972).
- [26] V. V. Shmidt *Zh. Exp. Teor. Phys. Pis Red.* **3**, 141-5 (1966), *Engl. trans. JETP Lett.* **3**, 89-91 (1966).
- [27] V. V. Shmidt *Proc. 10th Int. Conf. on Low Temperature Physics* **vol IIb, pp205-9** (ed. M P Malkov, 1967)
- [28] A. Schmid *Phys. Rev.* **180**, 527-9 (1969).
- [29] J. P. Gollub, M. R. Beasley, R. S. Newbower and M. Tinkham, *Phys. Rev. Lett.* **22**, 1288-91 (1969); J. P. Gollub, M. R. Beasley, R. S. Newbower and M. Tinkham, *Physica* **55**, 303-5 (1971).
- [30] R. E. Prange, *Phys. Rev. B* **1**, 2349-50 (1970).
- [31] B. R. Pattpn, V. Ambegaokar and J. W. Wilkins, *Solid St. Commun.* **7**, 1287-90 (1969).
- [32] J. P. Gollub, M. R. Beasley and M. Tinkham, *Phys. Rev. Lett.* **25**, 1646-9 (1970); J. P. Gollub, M. R. Beasley and M. Tinkham, *Proc. 12th Int. Conf. on Low Temperature Physics, Kyoto* pp271-2 (1970).
- [33] R. A. Ferrell *J. of Low Temp. Phys.* **1** 241-271 (1969).
- [34] P. A. Lee and M. G. Payne, *Phys. Rev. Lett.* **26**, 1537-41 (1971); P. A. Lee and M. G. Payne, *Phys. Rev. B* **5**, 923-31 (1972).
- [35] J. Kurkijarvi, V. Ambegaokar and G. Eilenberger, *Phys. Rev. B* **5**, 868-79 (1972).

- [36] K. Maki *Phys. Rev. Lett.* **30**, 648-52 (1973).
- [37] G. D. Zally and J. M. Mochel, *Phys. Rev. Lett.* **27**, 1710-2 (1971); G. D. Zally and J. M. Mochel, *Phys. Rev. B* **6**, 4142-50 (1972).
- [38] L. Gunther and L. W. Gruenberg, *Solid St. Commun.* **10**, 567-70 (1972).
- [39] R. E. Glover, *Phys. Lett.* **25A**, 542 (1968).
- [40] S. Grossmann, P. H. Richter and C. Wissel, *Solid St. Commun.* **11**, 443-6 (1972).
- [41] E. Abrahams and J. W. F. Woo *Phys. Lett.* **27A**, 117-8 (1968).
- [42] A. Schmid *Z. Phys.* **215**, 210-2 (1968).
- [43] R. O. Smith, B. Serin and E. Abrahams, *Phys. Lett.* **28A**, 224-5 (1968).
- [44] J. P. Hurault *Phys. Rev.* **179**, 494-6 (1969).
- [45] G. A. Thomas and R. D. Parks, *Physica* **55**, 215-23 (1971).
- [46] M. A. Klenin and M. A. Jensen, *Physica* **55**, 279-87 (1971).
- [47] K. Kajimura and N. Mikoshiba *Solid st. Communi.* **8**, 1617-9 (1970); K. Kajimura, N. Mikoshiba and K. Yamaji *Phys. Rev. B* **4**, 209-16 (1971).
- [48] W. A. Little *Proc. 10th Int. Conf. on Low Temperature Physics, Moscow*, ed M. P. Malkov, pp115-8 (1967); W. A. Little *Phys. Rev.* **156**, 396-403 (1967).
- [49] J. S. Langer and V. Ambegaokar, *Phys. Rev.* **164**, 498-510 (1967).
- [50] D. E. McCumber and B. I. Halperin *Phys. Rev. B* **1**, 1054-70 (1970).
- [51] W. J. Skocpol and M. Tinkham, *Rep. Prog. Phys.* **38**, 1049-1097 (1975).



- [52] T. Schneider and J.M. Singer, *Phase transition approach to high temperature superconductivity universal properties of cuprate superconductors* Imperial College Press.
- [53] D. S. Fisher, M. P. A. Fisher, and D. A. Huse, *Phys. Rev. Lett.* **62**, 1415 (1989).
- [54] D. S. Fisher, M. P. A. Fisher, and D. A. Huse, *Phys. Rev. B* **43**, 130 (1991);  
D. A. Huse, D. S. Fisher, and M. P. A. Fisher, *Nature* **358**, 553 (1992).
- [55] L. G. Aslamazov and A. I. Larkin, *Phys. Lett.* **26A**, 238 (1968).
- [56] K. Maki, *Progr. Theoret. Phys.(Kyoto)* **39**, 897 (1968).
- [57] R. S. Thompson, *Phys. Rev. B* **1**, 327 (1970).
- [58] H. Schmidt, *Z. Phys.* **216**, 336 (1968).
- [59] L. G. Aslamazov and A. A. Varlamov, *J. Low Temp. Phys.* **38**, 223 (1980).
- [60] W. A. Little, *Proc. 10th Int. Conf. on Low Temperature Physics*, *Phys. Rev.* **156**, 396-403 1967.
- [61] P. C. Hohenberg and B. I. Halperin, *Rev. Mod. Phys.* **49**, 435, (1977).
- [62] M. E. Fisher, M. N. Barber and D. Jasnow, *Phys. Rev. A* **8**, 1111 (1973).
- [63] R. Liang, D.A. Bonn, and W.N. Hardy, *Physica C* **304**, 105 (1998).
- [64] S. Kamal, D.A. Bonn, N. Goldenfeld, P.J. Hirschfeld, R. Liang, and W.N. Hardy, *Phys. Rev. Lett.* **73**, 1845 (1994).
- [65] T. C. Lubensky, Private communication with C. J. Lobb.
- [66] S.M. Anlage, J. Mao, J.C. Booth, D.H. Wu, and J.L. Peng, *Phys. Rev. B* **53**, 2792 (1996).

- [67] M.B. Salamon, J. Shi, N. Overend, and M.A. Howson, *Phys. Rev. B* **47**, 5520 (1993); M.B. Salamon, W. Lee, K. Ghiron, J. Shi, N. Overend, and M.A. Howson, *Physica A* **200**, 365 (1993).
- [68] A. Pomar, A. Diaz, M.V. Ramallo, C. Torron and J.A. Veira, *Physica C*, **218** 257 (1993)
- [69] R. Liang, D.A. Bonn, and W.N. Hardy, *Phys. Rev. Lett.* **76**, 835 (1996).
- [70] N. Overend, M.A. Howson, and I.D. Lawrie, *Phys. Rev. Lett.* **72**, 3238 (1994).
- [71] V. Pasler, P. Schweiss, C. Meingast, B. Obst, H. Wuhl, A.I. Rykov, and S. Tajima, *Phys. Rev. Lett.* **81**, 1094 (1998).
- [72] J. A. Lipa *et al.* *Phys. Rev. Lett.*, **76**, 944(1996).
- [73] F. S. Nogueira and Dirk Manske, *Phys. Rev. B* **72**, 014541 (2005)
- [74] V. Aji and N. Goldenfeld, *Phys. Rev. Lett.* **87**, 197003 (2001)
- [75] T. Schneider abd H. Keller *Int. J. Mod. Phys. B* **8**, 487 (1993).
- [76] M. B. Salamon *et al.* *Phys. Rev. B*, **47**,5520 (1993).
- [77] Jack Lidmar, Mats Wallinef *et al.* *Phys. Rev. B*, **58**, 2827 (1998).
- [78] Jack Lidmar *et al.* *Phys. Rev. B*, **67**, 092501 (2003).
- [79] Jack Lidmar *Phys. Rev. Lett*, **91**, 097001 (2003).
- [80] A. Junod *et al.* *Physica C*, **229**, 209 (1994).
- [81] A. Kozlowski *et al.* *Physica C*, **184**, 113 (1991).
- [82] A. Buzdin and D. Feinberg *Physica C*, **220**, 74 (1993).
- [83] M. Roulin *et al.* *Physica C*, **296**, 137 (1998).

- [84] O. Jeandupeux *et al.* *Phys. Rev. B*, **53** 12475 (1996).
- [85] K. Huang *Statistical Mechanics* J. Wiley and Sons, New York (1987).
- [86] C. Meingast *et al.* *Phys. Rev.* **67**, 1634 (1991).
- [87] A. B. Pippard. *The elements of classical thermodynamics*. Cambridge University Press, Cambridge, (1966).
- [88] D.R. Strachan, M.C. Sullivan, P. Fournier, S. P. Pai, T. Venkatesan and C.J. Lobb, *Phys. Rev. Lett.* **87**, 067007 (2001).
- [89] Matt Sullivan, *The normal-superconducting phase transition in zero magnetic field*, Ph. D. thesis, Univeristy of Maryland, 2004.
- [90] Robert A. Wickham and Alan T. Dorsey *Phys. Rev. B*, **61**, 6945 (2000)
- [91] J.C. Booth, D.H. Wu and S.M. Anlage, *Phys. Rev. Lett*, **77**, 4438 (1996).
- [92] J. C. Booth *et al.* *Rev. Sci. Instrum.* **65**, 2082 (1994).
- [93] J. C. Booth, *Novel measurements of the frequency dependent surface impedance of cuprate thin film superconductors*, Ph. D. thesis, Univeristy of Maryland, 1996.
- [94] M. C. Sullivan, D. R. Strachan and C. J. Lobb *Phys. Rev. B*, **69**, 214524 (2004)
- [95] D. R. Strachan, M. C. Sullivan, P. Fournier, S. P. Pai, T. Venkatesan, and C. J. Lobb, *Phys. Rev. Lett.* **87**, 067007 (2001).
- [96] D. R. Strachan, M. C. Sullivan, and C. J. Lobb, *Proc. SPIE* **65**, 4811 (2002).
- [97] R. H. Koch *et al.*, *Phys. Rev. Lett.* **63**, 1511 (1989); R. H. Koch, V. Foglietti, and M. P. A. Fisher, *Phys. Rev. Lett.* **64**, 2586 (1990).

- [98] Y. Ando, H. Kubota, and S. Tanaka, Phys. Rev. Lett. **69**, 2851 (1992); B. Brown, J. M. Roberts, J. Tate, and J. W. Farmer, Phys. Rev. B **55**, R8713 (1997); P. J. M. Wöltgens, C. Dekker, J. Swüste, and H. W. de Wijn, Phys. Rev. B **48**, 16826 (1993); C. Dekker, W. Eidelloth, and R. H. Koch, Phys. Rev. Lett. **68**, 3347 (1992); T. K. Worthington *et al.*, Phys. Rev. B **43**, 10538 (1991);
- [99] M. Charalambous *et al.*, Phys. Rev. Lett. **75**, 2578 (1995); M. Charalambous, R. Koch, A. D. Kent, and W. T. Masselink, Phys. Rev. B **58**, 9510 (1997); M. Friesen, J. Deak, L. Hou, and M. McElfresh, Phys. Rev. B **54**, 3525 (1996); A. Sawa *et al.*, Phys. Rev. B **58**, 2868 (1998); H. Yamasaki *et al.*, Phys. Rev. B **50**, 12959 (1994); C. Dekker *et al.*, Phys. Rev. Lett. **69**, 2717 (1992); L. Hou, J. Deak, P. Metcalf, and M. McElfresh, Phys. Rev. B **50**, 7226 (1994); Z. Sefrioui *et al.*, Phys. Rev. B **60**, 15423 (1999); P. Voss-deHaan, G. Jakob, and H. Adrian, Phys. Rev. B **60**, 12443 (1999).
- [100] J.M. Roberts *et al.*, Phys. Rev. B **49**, 6890 (1994); Tsutomu Nojima *et al.*, Czech. Jour. Phys. **46** Suppl. S3, 1713 (1996).
- [101] Katerina Moloni *et al.*, Phys. Rev. Lett. **78**, 3173 (1997).
- [102] N.-C. Yeh *et al.*, Phys. Rev. B **47**, 6146 (1992); N.-C. Yeh *et al.*, Phys. Rev. B **45**, 5654 (1992).
- [103] T. Schneider and H. Keller. Int. J. Mod. Phys. B, 8:487, (1993).
- [104] S. H. Han, Yu. Eltsev, and O. Rapp, Phys. Rev. B, **57**, 7510 (1998); S. H. Han, Yu. Eltsev, and O. Rapp, Phys. Rev. B, **61**, 11776 (2000).
- [105] D. N. Peligrad *et al.*, Phys. Rev. B **69**, 144516 (2004).
- [106] R. A. Wickham and A. T. Dorsey Phys. Rev. B **61**, 6945 (2000)

- [107] S. Okuma *et al.*, Phys. Rev. B **56**, 14138 (1997).
- [108] S. L. Liu *et al.*, Phys. Lett. A **339**, 408-413 (2005).
- [109] H. J. Fink *et al.*, Phys. Rev. B **61**, 6346 (2000).
- [110] G. Nakielski *et al.* Phys. Rev. B **55**, 6077 (1997).
- [111] K. D. Osborn *et al.*, Phys. Rev. B **68**, 144516 (2003).
- [112] H. Kitano *et al.* Phys. Rev. B **73**, 092504 (2006).
- [113] S. M. Anlage *et al.* Phys. Rev. B, **53**, 2792 (1996).
- [114] S. E. Inderhees *et al.* Phys. Rev. Lett. **60**, 1178 (1988); M. B. Salamon *et al.* Phys. Rev. B **38**, 885 (1988); M. P. Kathleen *et al.* Phys. Rev. B, **59**, 6545 (1999).
- [115] J. M. Roberts *et al.* Phys. Rev. B **49**, 6890; R. H. Koch *et al.* Phys. Rev. Lett. **63**, 1511(1989); K. Moloni *et al.* Phys. Rev. B **56**, 14784(1997); T. Klein *et al.* Phys. Rev. B. **58**, 12411(1998); A. M. Petrean *et al.* Phys. Rev. Lett. **84**, 5852(2000).
- [116] T. Olson *et al.* Phys. Rev. B **61**, 12467(2000).
- [117] Private communication with C. Kallin A. J. Berlinsky.
- [118] R. Pinto *et al.* Solid Sta. Comm. **84**, 1107,(1992); A. Velichko *et al.* Physica C **277**, 101 (1997); J. Mateu *et al.* Appl. Phys. Lett. **90**, 012512 (2007); J. C. Booth *et al.* IEEE Tran. on Appl. Superconductivity **15**, 1000 (2005); J. C. Booth *et al.* IEEE Tran. on Appl. Superconductivity **13**, 3590 (2003).
- [119] Martin Dressel and George Gruner, *Electrodynamics of Solids* (Cambridge University Press, Cambridge, United Kingdom, 2002).

- [120] P.N.J. Dennis, *Photodetectors* (Plenum Press, New York, 1986); E.L. Dereniak and D.G. Crowe, *Optical Radiation Detectors* (J. Wiley, New York, 1984); *Detection of Optical and Infraed Radiation*, edited by R.H. Kingston, Springer Series in Optical Sciences **10**(Springer-Verlag, Berlin, 1978); *Optical and Detectors*, edited by R. J. Keyes, 2nd edition, Topics in Applied Physics, **19** (Springer-Verlag, Berlin, 1980); A. Rogalski, *Infrared Detectors* (Gordon and Breach, Amsterdam, 2000); *Semiconductors and Semimetals*, **5**, edited by R.K. Willardson and A.C. Beer (Academic Press, New York, 1970).
- [121] H. Rietschael *Physica Scripta*, **T49**, 24-27 (1993)
- [122] R. E. Glover, III, and M. Tinkham, *Phys. Rev.* **108**, 243 (1957).
- [123] O. M. Corbino *Nuovo Cimento* **1** (1911); R. P. Heubner, *Magnetic Flux structures in superconductors*, (Springer, Berlin, 1979, Page 128).
- [124] M. P. Shaw and P.R. Solomon, *Phys. Rev.* **164**, 535 (1967).
- [125] N. Bluzer, D. K. Fork, T. H. Geballe, M. R. Beasley, M. Y. Reiser, S. R. Greenfield, J. J. Stankus, and M. Fayer, *IEEE Trans. Magn.* **27**, 1519 (1991); N. Bluzer, *J. Appl. Phys.* **71**, 1336 (1992).
- [126] Andrew Schwartz, Marc Scheffler, and Steven M. Anlage *Phys. Rev. B* **61** R870 (2000).
- [127] Marc Scheffler and Martin Dressel *Rev. Sci. Inst.* **76**, 074702 (2005).
- [128] M. L. Stutzman, Mark Lee, and R. F. Bradley, *Rev. Sci. Inst.* **71**, 4596 (2000).
- [129] See, for example, Hewlett Packard Applicaion Note **183**, p.39 (1978).
- [130] S. Ramo, J.R. Whinnery, and T. Van Duzer, "Fields and waves in Communication Electronics", Second Edition, John Wiley and Sons, New York, P.252 (1984).

- [131] W. E. Lawrence and S. Doniach, Proceedings of the twelfth International Conference on Low-Temperature Physics, Kyoto, 1970, edited by E. Kanda (Keigaku, Tokoyo, 1970), P. 361.
- [132] A. T. Dorsey, *Phys. Rev. B* **43** 7575 (1991).
- [133] J. Cardy, *Scaling and Renormalization in Stastical Physics* Cambridge University Press (1996).
- [134] N. W. Ashcroft and N. D. Mermin, *Solid State Physics*, Harcourt Brace College Publishers, Philadelphia (1976).
- [135] Zoran Trajanovic, *Studies of Anisotropic In-plane Aligned a-axis Oriented  $YBa_2Cu_3O_{7-\delta}$  Thin Films*, Ph. D. thesis, Univeristy of Maryland, 1997.
- [136] W. F. McClune, Powder Diffraction File (International Centre for Diffraction Data, Swarthmore PA, 1991).
- [137] Ramo, Whinnery, and Van Duzer, *Fields and Waves in Communication Electronics*, second edition, p. 190.
- [138] P. Minnhagen, *Rev. of Modern Physics*, Vol. 59, No.4. October 1987.
- [139] Su Li, *Phase Transitions of High-Temperature Superconductors*, Ph. D. thesis, University of Maryland, 2007.
- [140] George Gruner J. Mater. Chem. **16**,3533 (2006)
- [141] M. S. Fuhrer, J. Nygard, L. Shih, M. Forero, T. Yoon, M. S. C. Mazzoni, H. J. Choi, J. Ihm, S. G. Louie, A. Zettl and P. L. Mceuen, *Science* 288,**494**, (2000).
- [142] A. B. Kaiser, G. Dusberg and S. Roth, *Phys. Rev. B* **57**, 1418, (1998).

- [143] B. E. Kilbride, J. N. Coleman, J. Fraysse, P. Fournet, M. Cadek, A. Drury, S. Hutzler, S. Roth and W. J. Blau, J. Appl. Phys. **92**, 4024, (2002).
- [144] T. I. Jeon, K. Kim, C. Kang, I. H. Maeng, J. Son, K. H. An, J. Y. Lee and Y. H. Lee, J. Appl. Phys. **95**, 5736, (2004).
- [145] A. Ugawa, A. G. Rinzler and D. B. Tanner, Phys. Rev. B **60**, 11305, (1999); A. Ugawa, J. Hwang, H. Gommans, H. Tashiro, AG Rinzler and D. B. Tanner, Curr. Appl. Phys. **1**, 45 (2001); M. E. Itkis, S. Niyogi, M. E. Meng, M. A. Hamon, H. Hu and R. C. Haddon Nano Lett. **2**, 155 (2002); Y. Murakami, E. Einarsson, T. Edamura and S. Maruyama Phys. Rev. Lett. **94**. 087402 (2005).
- [146] F. Borondics, K. Kamaras, M. Nikolou, D. B. Tanner, Z. H. Chen and A. G. Rinzler, Phys. Rev. B, **74**, 045431 (2006).
- [147] B. Ruzicka, L. Degiorgi, R. Gaal, L. Thien-Nga, R. Bacsá, J. P. Salvetat and L. Forro, Phys. Rev. B **61**, 2468, (2000).
- [148] Z. Yu and P. J. Burke, Nano Lett. **5**, 1403 (2005); S. Li, Z. Yu, S. Yen, W. C. Tang and P. J. Burke, Nano Lett. **4**, 753 (2004).
- [149] P. J. Burke, IEEE Trans. on Nano. Tech. **2**, 55 (2003).
- [150] O. Hilt, H. B. Brom and M. Ahlskog, Phys. Rev. B **61**, 5129, (2000).
- [151] P. Peit, E. Jouguelet, J. E. Fischer, A. G. Rinzler and R. E. Smalley, Phys. Rev. B **56**, 9275, (1997).
- [152] D.D.L. Chung, Carbon **39**, 279, (2001).
- [153] C. Xiang, Y. Pan, X. Liu, X. Sun, X. Shi and J. Guo Appl. Phys. Lett. **87**,123103, (2005).
- [154] M. B. Bryning, M. F. Islam, J. M. Kikkawa and Arjun G. Yodh Adv. Mater. **17**, 1186, (2005).



- [155] N. Li, Y. Huang, F. Du, X. He, H. Gao, Y. Ma, F. Li, Y. Chen and P. C. Eklund Nano. Lett. **6**, 1141, (2006).
- [156] Y. Zhou, L. Hu and G. Gruner, Appl. Phys. Lett. **88**, 123109, (2006).
- [157] J. E. Fischer, H. Dai, A. Thess, R. Lee, N. M. Hanjani, D. L. Dehaas and R. E. Smalley, Phys. Rev. B **55**, 4921, (1997).
- [158] E. Bekyarova, M. E. Itkis, N. Cabrera, B. Zhao, A. Yu, J. Gao and R. C. Haddon, J. Am. Chem. Soc. **127**, 5990, (2005).
- [159] T. Taka, Synth. Met. **41-43**, 1177, (1991).
- [160] Z. Wu, Z. Chen, X. Du, J. M. Logan, J. Sippel, M. Nikolou, K. Kamaras, J. R. Reynolds, D. B. Tanner, A. F. Hebard and A. G. Rinzler, Science, **305**, 1273, (2004).
- [161] D. Hecht, L. Hu, G. Gruner Appl. Phys. Lett. **89**, 133112, (2006).
- [162] P. M. Ajayan and O. Z. Zhou, *Carbon Nanotubes: Synthesis, Structure, Properties and Application*, Springer: Berlin/Heidelberg, 2001.
- [163] Ray H. Baughman, Anvar A. Zakhidov and Walt A. de Heer, *Science* **297**, 787 (2002).
- [164] S.J. Kang, C. Kocabas, T. Ozel, M. Shim, N. Pimparkar, M.A. Alam, S.V. Rotkin and J.A. Rogers, *Nature Nanotechnology* **2**, 230 (2007).
- [165] E. S. Snow, J. P. Novak, P. M. Campbell, and D. Park , *Appl. Phys. Lett.* **82**, 2145, (2003).
- [166] S. Hur, M. Yoon, A. Gaur, M. Shim, A. Facchetti, T. J. Marks and John A. Rogers, *J. AM. CHEM. SOC.* **127**, 13808-13809, (2005).

- [167] M.W. Rowell, M.A. Topinka, M.D. McGehee, H. Prall, G. Dennler, N.S. Sariciftci, L. Hu, G. *Grüner*, *Appl. Phys. Lett.* **88**, 233506 (2006)
- [168] D. Zhang, K. Ryu, X. Liu, E. Polikarpov, J. Ly, M. E. Tompson, and Chongwu Zhou, *Nano Lett.* **6 (9)**, 1880, (2006)
- [169] J. Lagemaat, T. M. Barnes, G. Rumbles, S. E. Shaheen, and T. J. Coutts, C. Weeks, I. Levitsky, J. Peltola, and P. Glatkowski, *Appl. Phys. Lett.* **88**, 233503, (2006).
- [170] J. Li, L. Hu, L. Wang, Y. Zhou, G. Grner, T. J. Marks, *Nano Lett.* **6(11)** 2472 (2006)
- [171] A. Du Pasquier, H. E. Unalan, A. Kanwal, S. Miller, and M. Chowalla, *Appl. Phys. Lett.* **87**, 203511 (2005)
- [172] K. H. An, W. S. Kim, Y. S. Park, Y. C. Choi, S. M. Lee, D. C. Chung, D. J. Bae, S. C. Lim, Y. H. Lee, *Adv. Mater* **13**, 497, (2001).
- [173] F. Pic, J. M. Rojo, M. L. Sanjun, A. Ansn, A. M. Benito, M. A. Callejas, W. K. Maser, and M. T. Martnez, *J. Electrochem. Soc.* **151**, 831, (2004).
- [174] A. B. Kaiser, K. J. Challis, G. C. McIntosh, G. T. Kim, H. Y. Yu, J. G. Park, S. H. Jhang and Y. W. Park, *Curr. Appl. Phys.* **2**, 163 (2002)
- [175] D. S. Mclachlan, C. Chiteme, C. Park, K. E. Wise, S. E. Lowther, P. T. Lillehei, E. J. Siochi and J. S. Harrison, *J. of Polymer science, B* **43**, 3273 (2005)
- [176] Hua Xu, L. Hu, S. M. Anlage and G. Grüner, *Appl. Phys. Lett.* **90**, 183119 (2007).
- [177] M. S. Fuhrer, M. L. Cohen, A. Zettl, V. Crespi, *Solid. State Comm.* **109**, 105 (1999).

- [178] M. S. Fuhrer, W. Holmes, P. L. Richards, P. Delaney, S. G. Louie and A. Zettl, *Synthetic Metals* **103**, 2529 (1999)
- [179] L. Hu, G. Grüner, J. Gong, C-J Kim, B. Hornbostel, *Appl. Phys. Lett.*, **90**, 093124 (2007).
- [180] Jeppe C. Dyre *J. Appl. Phys.* **64**, 2456 (1988)
- [181] P. Dutta, S. Biswas, M. Ghosh, S. K. De and S. Chatterjee, *Synthetic metals* **122**, 455 (2001)
- [182] Jeppe C. Dyre and Thomas B. Schroder, *Rev. Mod. Phys.* **72**, 873 (2000)
- [183] L. Hu, D.S. Hecht and G. Grner, *Nano Letters*, **4**, 2513-2517, (2004).
- [184] K. Mortensen, M. L. W. Thewalt, Y. Tomkiewicz, T. C. Clarke, G. B. Street, *Phys. Rev. Lett.* **45**, 490 (1980)
- [185] N. Apsley and H. P. Hughes, *Phil. Mag.* **31**, 1327 (1975)
- [186] P. Minnhagen *Rev. Mod. Phys.* **59**, 1001 - 1066 (1987)

## List of Abbreviations

AFM	Atomic Force Microscope
AL	Aslamazov-Larkin
EMI	Electromagnetic interfere
FFH	Fisher Fisher and Huse
GL	Ginzburg-Landau
HTSC	High temperature superconductor
ITO	Indium tin oxide
LSCO	$La_{2-x}Sr_xCuO_4$
MT	Maki-Thompson
MWCNT	Multi-walled carbon nanotube
NGO	$NdGaO_3$
PCCO	$Pr_{2-x}Ce_xCuO_4$
PLD	Pulsed laser deposition
RBS	Rutherford Back Scattering
SE	Shielding effectiveness
SEM	Scanning electron microscope
STO	$SrTiO_3$
SWCNT	Single-walled carbon nanotube
TDGL	Time dependent Ginzburg-Landau
XRD	X-ray diffraction
YBCO	$YBa_2Cu_3O_{7-\delta}$
YSZ	Yttrium-stabilized Zirconia

# Curriculum Vitae

**Hua Xu**

## Personal Information

**Gender:** Male

**Citizenship:** P. R. China

**Birthplace:** Qianjiang City, Hubei Province, P. R. China

**Birthday:** 3/1982

**Phone:** 1-202-230-7779

**E-mail:** [oceanfly@gmail.com](mailto:oceanfly@gmail.com)

**Address:** 6002 Springhill Dr, Apt 204, Greenbelt, MD 20770

## Expertise

- Thin film coating, characterization and device fabrication
- Microwave engineering and test method development
- Electrical properties of superconductors and novel materials
- Superconductivity and cryogenic systems

## Education

**Ph. D in Experimental Physics,** 8/2007

University of Maryland, College Park, MD

**B.S. in Applied Physics (Minor in Computer Science and Mathematics)** 7/2002

Special Class for Gifted Young (SCGY), University of Science and Technology of China (USTC)

## Experience

**Graduate Research Assistant,** University of Maryland, High frequency lab 2002-Present

- Developed the state-of-the-art broadband frequency measurement system for electrical conductivity measurement (100 kHz to 50 GHz) from room temperature to cryogenic temperatures. Conducted research on the fluctuations at the superconductor to normal phase transition with the developed system.
- Studied the transparency and EM shielding effect of the nanotube films. Provided a guideline for applications of nanotube films as transparent shielding materials.
- Studied frequency, temperature and electric field dependent transport properties of SWNT networks of various thicknesses. Modeled the relation between frequency and electric field dependent conductivity. Revealed importance of the localization in SWNT networks.
- Grew high-quality high temperature superconducting (HTS) thin films with pulsed laser deposition. Investigated the local characterization of resistive microwave nonlinearities of HTS films.
- Fabricated HTS and Niobium superconducting split-ring resonators. Studied the tunability of superconducting metamaterials.

- Experienced with micro-fabrication of devices including mask design and excellent hands-on capability. Familiar with photolithography, electron beam lithography and different etching techniques, e.g. chemical etch, plasma etch and ion mill.
- Designed and built test fixtures and components in the RF and microwave frequency range. Experienced with design and simulation software such as Ansoft HFSS. Constructed different analog and digital circuits to meet specific experimental requirements.
- Developed software for automatic instrument control and data collection. Wrote programs for the microwave signal processing and data analysis.
- Designed, fabricated and operated vacuum, cryogenic, magnetic shielding and EM shielding systems. Good at mechanical design software, such as AutoCAD, Solidworks etc.

**Teaching Assistant**, University of Maryland, Department of Physics

2002-2003

- TA for PHYS401 Quantum Physics I
- TA for PHYS402 Quantum Physics II

**Research Assistant**, University of Science and Technology of China

1999-2002

- Simulated motion of the high energy particles with C and Mathematica. Developed math model and calculated the probability of particle collision.

## Computer skills

- Operation Systems: Windows, Linux, Macintosh
- Programming: MATLAB, Mathematica, Labview, C/C++, Fortran, Visual Basic, Assembly for Intel x86
- Software: Ansoft HFSS, Solid works, AutoCAD, Microsoft Office Suite, Origin, Photoshop

## Other Skills

- Thin film coating: thermal evaporation, pulse laser deposition, and sputtering.
- Test methods: broadband frequency measurement, cavity resonant measurement, I-V nonlinear characteristic, AC susceptibility, X-ray diffraction, atomic force microscopy and optical microscope.
- Electrical instruments: Agilent E8364B PNA, 8510C NWA, E4418 power meters, signal generators and oscilloscopes, Keithley DMM and current source, Lakeshore temperature controller etc.
- Other equipments: wire bonder, PEII-A Plasma Etcher, Quantum Design PPMS, Dektak 6M Stylus Profilometer, Ion Mill etc.

## Language skills

Fluent in English and Chinese

## Certification

- Certificate of radiation protection training for use of radiation-producing devices. The Radiation safety Office, University of Maryland, College Park, 2003.
- Certified in laboratory safety from Safety and Environment Health Department, University of Maryland, College Park, 2004.

## Honors

- Jacob K Goldhaber Travel Award (2007)
- Scholarship for the highest score on the Physics qualifying examination in UMCP (2003)
- Outstanding graduate in USTC (2002)
- Outstanding bachelor's thesis in USTC (2002)
- Outstanding Student Scholarship in USTC (1998/1999/2000/2001)

## Papers and Presentations

- **Hua Xu**, L. Hu, S. M. Anlage and G. Gruner, "Microwave shielding of transparent and conducting single-walled carbon nanotube films", Appl. Phys. Lett. 90, 183119 (2007)
- **Hua Xu**, L. Hu, S. Zhang, G. Grüner and S. M. Anlage "Density dependent transport properties of single walled carbon nanotube networks", International Conference on Nanoscience & Technology, China 2007.
- **Hua Xu**, S. Li, C. J. Lobb and S. M. Anlage, "Determination of the dynamical scaling exponent in the superconducting to normal metal phase transition", in preparation.
- M. C. Ricci, **Hua Xu**, S. M. Anlage, R. Prozorov, A. P. Zhuravel and A. V. Ustinov, "Tunability of Superconducting Metamaterials", IEEE Transactions on Applied Superconductivity. (in press)
- **Hua Xu**, Su Li, Christopher J. Lobb, Steven M. Anlage, "Fluctuations at the superconductor/normal phase transition of YBCO thin films", Presentation on APS March Meeting, 2006.
- D. I. Mircea, **Hua Xu**, S. Lee, M. C. Sullivan, B. Palmer, B. Maiorov, S. M. Anlage, "Local Characterization of Resistive Microwave Nonlinearities in HTS Films", Presentation on Applied Superconductivity Conference, 2006.
- **Hua Xu**, Su Li, Christopher J. Lobb, Steven M. Anlage, "Determination of the dynamical scaling exponent in the superconducting to normal metal phase transition", Presentation on APS March Meeting, 2007.
- Su Li, **Hua Xu**, S. M Anlage, C. J. Lobb, "Exploring the critical dynamic exponent using YBCO films and untwined crystal in normal-superconducting phase transition", Presentation on APS March Meeting, 2007.

## Activities

- Student member, American Physical Society.
- Committee of USTC Alumni Association in Maryland.
- Member of tennis club of University of Maryland.